



ATLAS Note

GROUP-2017-XX



11th May 2021

Draft version 0.1

1

2

3

4

5

6

**A Deep Learning Approach to Differential
Measurements of Higgs - Top Interactions in
Multilepton Final States using the ATLAS
Detector at the LHC**

The ATLAS Collaboration

7 Several theories Beyond the Standard Model predict a modification of the momentum spec-
8 trum of the Higgs Boson, without a significantly altered rate of Higgs produced in association
9 with top quark pairs ($t\bar{t}H$). This provides a physical observable that can be used to search
10 for new physics based on data collected by the LHC. This thesis presents techniques and
11 preliminary results for a differential measurement of the Higgs transverse momentum in $t\bar{t}H$
12 events with multiple leptons in the final state, using data collected at an energy of $\sqrt{s} = 13$
13 TeV by the ATLAS detector at the LHC.

14 This thesis also details a measurement of $WZ +$ heavy flavor production, a significant back-
15 ground to $t\bar{t}H$ that is poorly understood. This study targets events with three leptons and one
16 or two jets in the final state, using 140 fb^{-1} of $\sqrt{s} = 13 \text{ TeV}$ data. A measured cross-section
17 of $X \pm X \text{ fb}$ ($X \pm X \text{ fb}$) is observed for $WZ + b$ ($WZ + \text{charm}$) with 1 associated jet and $X \pm X$
18 fb ($X \pm X \text{ fb}$) for $WZ + b$ ($WZ + \text{charm}$) with 2 assoicated jets.

19 Because of the challenges inherent in reconstructing the Higgs in multilepton final states, a
20 deep learning approach is used to predict the momentum spectrum of the Higgs for these
21 events. The regressed Higgs p_T spectrum is fit to data for events with two same-sign leptons
22 or three leptons in the final state. The fit is used to extract normalization factors for high
23 ($p_T(H) > 150 \text{ GeV}$) and low ($p_T(H) < 150 \text{ GeV}$) momentum $t\bar{t}H$ events. Preliminary
24 results are presented for 80 fb^{-1} of data, with projected results shown for 140 fb^{-1} .

© 2021 CERN for the benefit of the ATLAS Collaboration.

25 Reproduction of this article or parts of it is allowed as specified in the CC-BY-4.0 license.

26 **Contents**

27	I Introduction	7
28	1 Introduction	7
29	II Theoretical Motivation	10
30	2 The Standard Model and the Higgs Boson	10
31	2.1 The Forces and Particles of the Standard Model	10
32	2.2 The Higgs Mechanism	13
33	2.2.1 The Higgs Field	13
34	2.2.2 Electroweak Symmetry Breaking	15
35	2.3 $t\bar{t}H$ Production	18
36	2.4 WZ + Heavy Flavor Production	21
37	2.5 Extensions to the Standard Model	22
38	III The LHC and the ATLAS Detector	27
39	3 The LHC	27
40	4 The ATLAS Detector	30
41	4.1 Inner Detector	31
42	4.2 Calorimeters	32
43	4.3 Muon Spectrometer	33
44	4.4 Trigger System	34
45	IV Measurement of WZ + Heavy Flavor	36
46	5 Introduction	36
47	6 Data and Monte Carlo Samples	37
48	6.1 Data Samples	37
49	6.2 Monte Carlo Samples	38
50	7 Object Reconstruction	39
51	7.1 Light leptons	39
52	7.2 Jets	40
53	7.3 B-tagged Jets	41
54	7.4 Missing transverse energy	42
55	7.5 Overlap removal	43

56	8 Event Selection and Signal Region Definitions	43
57	8.1 Event Preselection	44
58	8.2 Fit Regions	46
59	8.3 Non-Prompt Lepton Estimation	48
60	8.3.1 $t\bar{t}$ Validation	48
61	8.3.2 Z+jets Validation	49
62	9 tZ Separation Multivariate Analysis	50
63	10 Data and Monte Carlo Samples	54
64	10.1 Data Samples	54
65	10.2 Monte Carlo Samples	54
66	11 Object Reconstruction	55
67	11.1 Light leptons	56
68	11.2 Jets	57
69	11.3 B-tagged Jets	57
70	11.4 Missing transverse energy	59
71	11.5 Overlap removal	59
72	12 Event Selection and Signal Region Definitions	60
73	12.1 Event Preselection	60
74	12.2 Fit Regions	63
75	12.3 Non-Prompt Lepton Estimation	64
76	12.3.1 $t\bar{t}$ Validation	65
77	12.3.2 Z+jets Validation	66
78	13 tZ Interference Studies and Separation Multivariate Analysis	66
79	14 Systematic Uncertainties	70
80	15 Results	74
81	15.1 1-jet Fit Results	75
82	15.2 2-jet Fit Results	84
83	V Differential Studies of $t\bar{t}H$ Multilepton	93
84	16 Data and Monte Carlo Samples	93
85	16.1 Data Samples	93
86	16.2 Monte Carlo Samples	93
87	17 Object Reconstruction	96
88	17.1 Trigger Requirements	96
89	17.2 Light Leptons	96

90	17.3 Jets	97
91	17.4 B-tagged Jets	98
92	17.5 Missing Transverse Energy	98
93	17.6 Overlap removal	99
94	18 Higgs Momentum Reconstruction	99
95	18.1 Physics Object Truth Matching	101
96	18.2 Truth Level Studies	102
97	18.3 b-jet Identification	103
98	18.3.1 2lSS Channel	104
99	18.3.2 3l Channel	108
100	18.4 Higgs Reconstruction	111
101	18.4.1 2lSS Channel	112
102	18.4.2 3l Semi-leptonic Channel	116
103	18.4.3 3l Fully-leptonic Channel	120
104	18.5 p_T Prediction	124
105	18.5.1 2lSS Channel	125
106	18.5.2 3l Semi-leptonic Channel	128
107	18.5.3 3l Fully-leptonic Channel	130
108	18.6 3l Decay Mode	132
109	19 Signal Region Definitions	134
110	19.1 Pre-MVA Event Selection	134
111	19.2 Event MVA	138
112	19.3 Signal Region Definitions	145
113	20 Systematic Uncertainties	146
114	21 Results	150
115	21.1 Results - 79.8 fb^{-1}	151
116	21.2 Projected Results - 139 fb^{-1}	155
117	VI Conclusion	160
118	VII Appendices	168
119	Appendices	168
120	A Non-prompt lepton MVA	168
121	B Supplementary WZ + Heavy Flavor Studies	173
122	B.1 Non-prompt CR Modelling	173

123	B.2 tZ Interference Studies	178
124	B.3 Alternate tZ Inclusive Fit	182
125	B.3.1 tZ Inclusive Fit	183
126	B.3.2 Floating tZ	184
127	C Supplementary t̄tH Differential Analysis Studies	185
128	C.1 Higgs Reconstruction Model Details	185
129	C.1.1 b-jet Identification Features - 2ISS	185
130	C.1.2 b-jet Identification Features - 3l	189
131	C.1.3 Higgs Reconstruction Features - 2ISS	194
132	C.1.4 Higgs Reconstruction Features - 3IS	199
133	C.1.5 Higgs Reconstruction Features - 3IF	204
134	C.2 Background Rejection MVA Details	208
135	C.2.1 Background Rejection MVA Features - 2ISS	208
136	C.2.2 Background Rejection MVA Features - 3l	212
137	C.3 Truth Level Studies	217
138	C.4 Alternate b-jet Identification Algorithm	218
139	C.5 Binary Classification of the Higgs p _T	219
140	C.6 Impact of Alternative Jet Selection	221

141 Part I

142 Introduction

143 1 Introduction

144 Particle physics is an attempt to describe the fundamental building blocks of the universe and
145 their interactions. The Standard Model (SM) - our best current theory of fundamental particle
146 physics - does a remarkable job of that. All known fundamental particles and (almost) all of the
147 forces underlying their interactions can be explained by the SM, and the predictions from this
148 theory agree with experiment to an incredibly precise degree. This is especially true since the
149 Higgs Boson, the last piece of the SM predicted decades before, was finally discovered at the
150 Large Hadron Collider (LHC) in 2012 [1].

151 Despite the success of the SM, there remains significant work to be done. For one, the
152 SM is incomplete: it fails to provide a description of gravity, to give an explanation for the
153 observation of Dark Matter, or to provide a mechanism for neutrinos to gain mass. Further, a
154 Higgs Boson with a mass of around 125 GeV, as observed at the LHC, gives rise to what is
155 known a hierarchy problem - such a low mass Higgs requires a seemingly unnatural level of “fine
156 tuning” that is unexplained by the SM.

157 A promising avenue for addressing these problems is to study the properties of the Higgs
158 Boson and the way it interacts with other particles, in part simply because these interactions

159 have not been measured before. Its interactions with the Top Quark are a particularly promising
160 place to look. Because the Higgs Field is responsible for allowing particle to acquire mass, the
161 strength of a particle's interaction with the Higgs Boson is proportional to its mass. As the most
162 massive of the fundamental particles, the Top Quark has the strongest coupling to the Higgs
163 Boson, meaning any new physics in the Higgs sector is likely to present itself most prominently
164 in its interaction with the Top Quark.

165 These interactions can be measured by directly by studying the production of a Higgs
166 Boson in association with a pair of Top Quarks ($t\bar{t}H$). While studies have been done measuring
167 the overall rate of $t\bar{t}H$ production, there are several theories of physics Beyond the Standard
168 Model (BSM) that would affect the kinematics of $t\bar{t}H$ production without altering its overall
169 rate. This dissertation attempts to make a differential measurement of the kinematics of the
170 Higgs Boson in $t\bar{t}H$ events in order to search for these BSM effects.

171 The proton-proton collision data collected by the ATLAS detector at the LHC from 2015-
172 2018 provides the opportunity to make this measurement for the first time. The unprecedented
173 energy achieved by the LHC during this period greatly increase the rate at which $t\bar{t}H$ events are
174 produced, and the large amount of data collected provides the necessary statistics for a differential
175 measurement to be performed.

176 A study of $t\bar{t}H$ events with multiple leptons in the final state is performed, using 139 fb^{-1}
177 of data from proton-proton collisions at an energy $\sqrt{s} = 13 \text{ TeV}$ collected by the ATLAS detector
178 from 2015-2018. Events are separated into channels based on the number of light leptons in the

179 final state - either two same-sign leptons, or three leptons. A deep neural network is used to
180 reconstruct the momentum of the Higgs Boson in each event. This momentum spectrum is fit to
181 data for each analysis channel in order to search for evidence of these BSM effects.

182 An additional study of WZ produced in association with a heavy flavor jet (including both
183 b-jets and charm jets) is also included. This process mimics the final state of $t\bar{t}H$ multilpjet
184 events, making it an irreducible background for that analysis. However, this process is poorly
185 understood, and difficult to simulate accurately, introducing large systematic uncertainties for
186 analyses that include it as a background. A measurement of WZ + heavy flavor in the fully
187 leptonic decay mode is performed in an attempt to reduce this uncertainty.

188 This dissertation begins with a brief explanation of the SM, its limitations, and the theor-
189 etical motivation behind this work in Part II. This is followed by a description of the LHC and
190 the ATLAS detector in Part III. Part IV details a measurement of WZ + heavy flavor. Studies
191 of differential measurements of $t\bar{t}H$ are then described in Part V, and preliminary results are
192 presented. Finally, the results of these studies are summarized in the conclusion, Part VI.

193 Part II**194 Theoretical Motivation****195 2 The Standard Model and the Higgs Boson**

196 The Standard Model of particle physics (SM) is a Quantum Field Theory (QFT) describing the
197 known fundamental particles and their interactions. It accounts for three of the four known
198 fundamental force - electromagnetism, the weak nuclear force, and the strong nuclear force, but
199 not gravity. Further, the SM describes a mechanism for combining the weak and electromagnetic
200 forces into a singular interaction, known as the electroweak force. It is a non-Abelian gauge
201 theory, invariant under the Lie Group $SU(3)_C \otimes SU(2)_L \otimes U(1)_Y$, where C refers to color
202 charge, L, the helicity of the particle, and Y, the hypercharge.

203 2.1 The Forces and Particles of the Standard Model

204 The SM particles, summarized in Figure 2.1, can be classified into two general categories based
205 on their spin: fermions, and bosons.

Standard Model of Elementary Particles

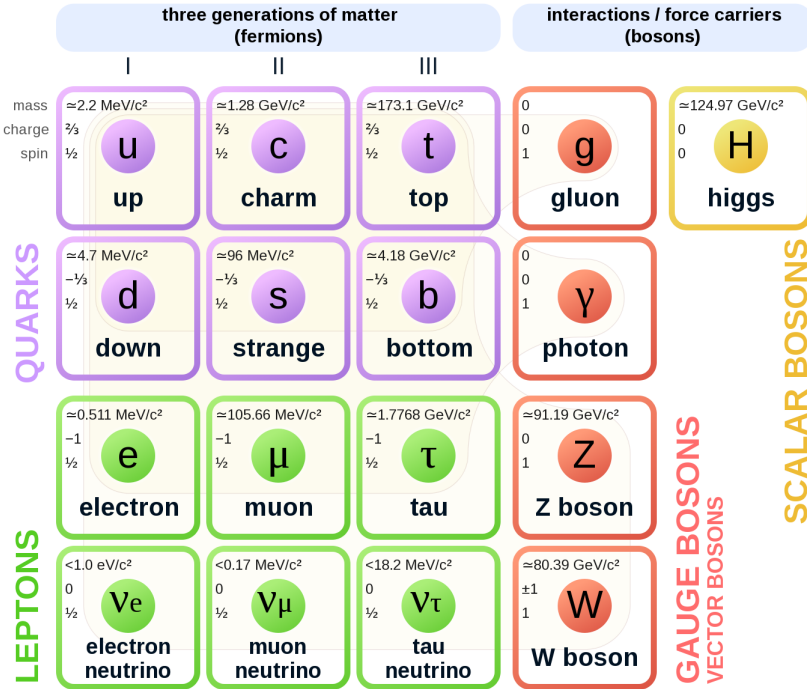


Figure 2.1: A summary of the particles of the Standard Model, including their mass, charge and spin, with the fermions listed on the left, and the bosons on the right. [2]

206 Fermions are particles with $\frac{1}{2}$ -integer spin, which according to the spin-statistics theorem,
 207 causes them to comply with the Pauli-exclusion principle. They can be separated into two groups,
 208 leptons and quarks, each of which consist of three generations of particles with increasing mass.

209 Leptons are fermions which interact via the electroweak force, but not the strong force.
 210 The three generation of leptons consist of the electron and electron neutrino, the muon and muon
 211 neutrino, the tau and tau neutrino. The quarks, by contrast, do interact via the strong force - which
 212 is to say they have color charge - in addition to the electroweak force. The three generations
 213 include the up and down quarks, the strange and charm quarks, and the top and bottom quarks.

214 Each of these generations form left-handed doublets invariant under SU(2) transfor-

215 mations. For the leptons these doublets are:

$$\begin{pmatrix} e^- \\ \nu_e \end{pmatrix}_L, \begin{pmatrix} \mu^- \\ \nu_\mu \end{pmatrix}_L, \begin{pmatrix} \tau^- \\ \nu_\tau \end{pmatrix}_L \quad (2.1)$$

216 And for the quarks:

$$\begin{pmatrix} u \\ d \end{pmatrix}_L, \begin{pmatrix} s \\ c \end{pmatrix}_L, \begin{pmatrix} t \\ b \end{pmatrix}_L \quad (2.2)$$

217 For both leptons and quarks, the heavier generations can decay into the lighter generation

218 of particles, while the first generation does not decay. Hence, ordinary matter generally consists

219 of this first generation of fermions - electrons, up quarks, and down quarks. Each of these

220 fermions has a corresponding anti-particle, which has an equal mass as its partner but opposite

221 charge. The fermions acquire their mass via the Higgs Mechanism, except for the neutrinos,

222 whose mass has been experimentally confirmed but is not accounted for in the SM.

223 Bosons, by contrast, have integer spin, and are therefore unconstrained by the Pauli-

224 exclusion principle. The SM includes two kinds of bosons: Gauge bosons, which are spin-1

225 particles that mediate the interactions between the fermions, and a single scalar, i.e. spin-0,

226 particle - the Higgs Boson. Of the gauge bosons, the W^+ , W^- and Z bosons - which are the

²²⁷ mass eigenstates of the electroweak bosons - mediate the weak interaction, while the photon
²²⁸ mediates the electric force, and the gluon mediates the strong force.

²²⁹ **2.2 The Higgs Mechanism**

²³⁰ A key feature of the SM is the gauge invariance of its Lagrangian. However, any terms added to
²³¹ the Lagrangian giving mass to the the gauge bosons would violate this underlying symmetry of
²³² the theory. This presents a clear problem with the theory: The experimental observation that the
²³³ W and Z bosons have mass seems to contradict the basic structure of the SM.

²³⁴ Rather than abandoning gauge invariance, an alternative way for particles to acquire mass
²³⁵ beyond adding a simple mass term to the Lagrangian was theorized by Higgs, Englert and Brout
²³⁶ in 1964 [3]. This procedure for introducing masses for the gauge bosons while preserving local
²³⁷ gauge invariance, known as the Higgs mechanism, was incorporated into the electroweak theory
²³⁸ by Weinberg in 1967 [4].

²³⁹ **2.2.1 The Higgs Field**

²⁴⁰ The Higgs mechanism introduces a complex scalar SU(2) doublet, Φ , with the form:

$$\Phi = \begin{pmatrix} \phi^+ \\ \phi^0 \end{pmatrix}_L \quad (2.3)$$

²⁴¹ This field introduces a scalar potential to the Lagrangian of the form:

$$V(\Phi) = \mu^2 |\Phi^\dagger \Phi| + \lambda (|\Phi^\dagger \Phi|)^2 \quad (2.4)$$

²⁴² Where μ and λ are free parameters of the new field. This represents the most general
²⁴³ potential allowed while preserving $SU(2)_L$ invariance and renormalizability. In the case that
²⁴⁴ $\mu^2 < 0$, this potential takes the form shown in Figure 2.2.

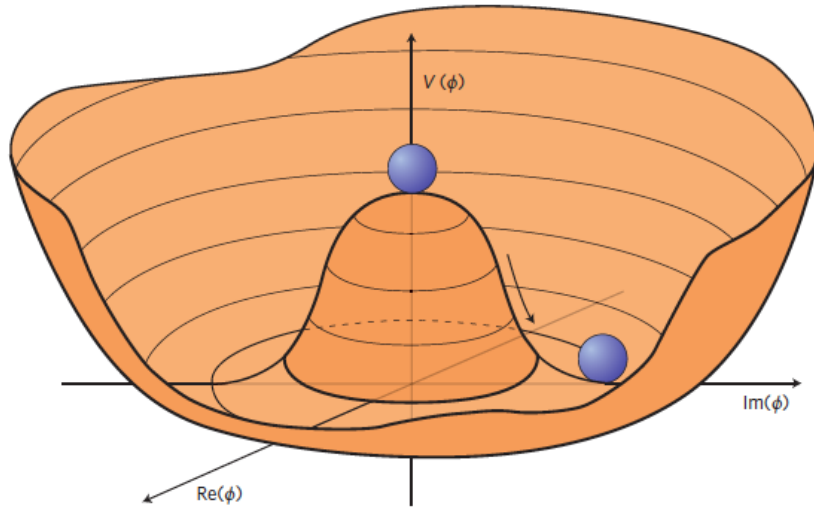


Figure 2.2: The value of the Higgs potential, $V(\Phi)$ as a function of Φ , for the case that $\mu^2 < 0$ [5].

²⁴⁵ The significant feature of this potential is that its minimum does not occur for a value of
²⁴⁶ $\Phi = 0$. Instead, it is minimized when $|\Phi^\dagger \Phi| = -\mu^2/\lambda$. This means that in its ground state, the
²⁴⁷ Higgs field takes on a non-zero value - referred to as a vacuum expectation value (VEV). So while
²⁴⁸ the Higgs potential is globally symmetric, about the minimum this symmetry is broken. Since

²⁴⁹ the minimum is determined only by $\Phi^\dagger \Phi$, there is some ambiguity in the particular definition of

²⁵⁰ the VEV, but it is generally represented as

$$\langle \Phi \rangle = \frac{1}{\sqrt{2}} \begin{pmatrix} 0 \\ v \end{pmatrix} \quad (2.5)$$

²⁵¹ The full value of Φ can be written as

$$\langle \Phi \rangle = \frac{1}{\sqrt{2}} \begin{pmatrix} 0 \\ v + H/\sqrt{2} \end{pmatrix} \quad (2.6)$$

²⁵² with v being the value of the VEV, and H being the real value of the scalar field.

²⁵³ 2.2.2 Electroweak Symmetry Breaking

²⁵⁴ The Electroweak (EWK) interaction is described in the SM by a $SU(2)_L \otimes U(1)_Y$ gauge theory.

²⁵⁵ This theory predicts three $SU(2)_L$ gauge boson, $W_\mu^1, W_\mu^2, W_\mu^3$, and a single $U(1)_Y$ gauge boson,

²⁵⁶ B_μ . The couplings of these bosons to the Higgs field show up in the kinetic terms of the scalar

²⁵⁷ field Φ in the Lagrangian:

$$(D_\mu \Phi)^\dagger (D^\mu \Phi) = |(\partial_\mu - \frac{i g}{2} W_\mu^a \sigma^a - \frac{i g'}{2} B_\mu Y) \phi|^2 \quad (2.7)$$

258 Here D_μ represents the covariant derivative required to preserve gauge invariance, g and
 259 g' represent coupling constant of the gauge bosons, σ^a denotes the Pauli matrices of $SU(2)$,
 260 and Y represents the hypercharge of $U(1)$. The terms in this interaction which contribute to the
 261 masses of the gauge bosons can be written as:

$$\frac{1}{2}(0, v)(\frac{g}{2}W_\mu^a \sigma^a - \frac{g'}{2}B_\mu)^2 \begin{pmatrix} 0 \\ v \end{pmatrix} \quad (2.8)$$

262 Expanding these terms into the mass eigenstates of the electroweak interaction yields four
 263 physical gauge bosons, two charged and two neutral, which are linear combinations of the fields
 264 W_μ^1 , W_μ^2 , W_μ^3 , and B_μ :

$$\begin{aligned} W_\mu^\pm &= \frac{1}{\sqrt{2}}(W_\mu^1 \pm iW_\mu^2) \\ Z^\mu &= \frac{1}{\sqrt{(g^2 + g'^2)}}(-g'B_\mu + gW_\mu^3) \\ A^\mu &= \frac{1}{\sqrt{(g^2 + g'^2)}}(gB_\mu + g'W_\mu^3) \end{aligned} \quad (2.9)$$

265 And the masses of these fields are given by:

$$\begin{aligned} M_W^2 &= \frac{1}{4}g^2v^2 \\ M_Z^2 &= \frac{1}{4}(g^2 + g'^2)v^2 \\ M_A^2 &= 0 \end{aligned} \quad (2.10)$$

266 This produces exactly the particles we observe - three massive gauge bosons and a single
 267 massless photon. The massless photon represents the portion of the gauge symmetry, a single
 268 $U(1)$ of the electromagnetic force, that remains unbroken by the VEV.

269 Interactions with the Higgs field also lead to the generation of the fermion masses, which
 270 in the Lagrangian take the form:

$$-\lambda_\psi(\bar{\psi}_L \phi \psi_R + \bar{\psi}_R \phi^\dagger \psi_L) \quad (2.11)$$

271 After symmetry breaking has occurred and ϕ has taken on the value of the VEV as written
 272 in equation 2.5, the mass terms of the fermions become $\lambda_\psi v$. Written this way, the fermion
 273 masses are proportional to their Yukawa coupling to the VEV, λ_ψ .

274 Based on the equation 2.6, an additional mass term, $\mu^2 H^2$ arises from the potential $V(\Phi)$.
 275 This term can be understood as an excitation of the Higgs field, a scalar boson with mass $M_H = \mu$.
 276 This is the Higgs boson, which comes about as a natural prediction of electroweak symmetry
 277 breaking.

278 The fermions' Yukawa couplings to the VEV take the same form as the fermions' coupling
 279 to the Higgs boson - λ_ψ . Therefore, the strength of a fermion's interaction with the Higgs is
 280 directly proportional to its mass. We now have a model that predicts a Higgs boson with mass
 281 $M_H = \mu$, which interacts with the fermions with coupling strength λ_ψ . Because μ and λ_ψ are

²⁸² free parameters of the theory, the mass of the Higgs boson and its interactions with the fermions

²⁸³ must be measured experimentally.

²⁸⁴ **2.3 $t\bar{t}H$ Production**

²⁸⁵ The strength of a particles interaction with the Higgs, given by its Yukawa coupling, is propor-
²⁸⁶ tionate to its mass. The top quark - as the heaviest known particle - has the strongest interaction,
²⁸⁷ making this interaction particularly interesting to study. While several processes involve interac-
²⁸⁸ tions between the Higgs and the top, some Higgs production modes include the top interaction
²⁸⁹ only as a part of a loop diagram, such as the gluon-gluon fusion diagram shown in Figure 2.3.

²⁹⁰ This process therefore only allows for an indirect probe of the Higgs-top Yukawa coupling, as
²⁹¹ the flavor of the quark in this diagram is not unique.

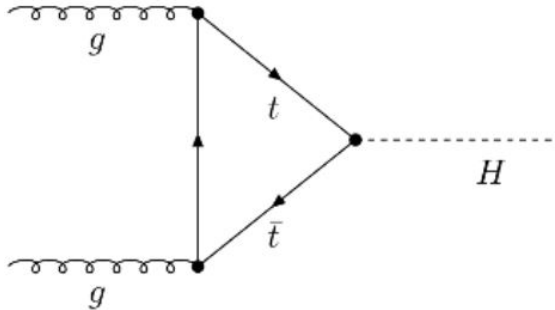


Figure 2.3: Diagram of a Higgs boson produced via gluon-gluon fusion.

²⁹² Studying the Higgs produced in association with top quark pairs, $t\bar{t}H$, allows this interac-
²⁹³ tion to be measured directly. This process, as shown in Figure 2.4, involves a unique coupling
²⁹⁴ between the Higgs and the top, which can be identified by the top quark pair in the final state.

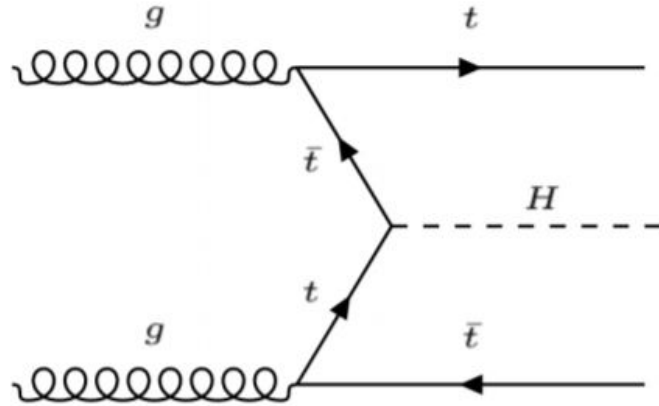


Figure 2.4: Diagram of a Higgs boson produced in association with a pair of top quarks.

295 The Higgs boson, as well as the top quarks, have very short lifetimes - on the order of
 296 10^{-22} s and 10^{-25} s respectively - meaning they can only be observed via their decay products.
 297 Measuring this process is therefore a matter of identifying events with final states consistent with
 298 $t\bar{t}H$ production.

299 Studies of $t\bar{t}H$ production have been reported by the ATLAS collaboration for $H \rightarrow b\bar{b}$,
 300 $H \rightarrow \gamma\gamma$ and multilepton (encompassing $H \rightarrow W^+W^-$, $H \rightarrow ZZ$ and $H \rightarrow \tau^-\tau^+$, with
 301 $H \rightarrow ZZ \rightarrow 4l$ as a separate analysis) decay modes. While the branching ratio of $H \rightarrow W^+W^-$
 302 is smaller than $H \rightarrow b\bar{b}$ (see Table 2.3), it produces a clearer signal, as $H \rightarrow b\bar{b}$ suffers from
 303 large $t\bar{t}$ backgrounds. On the other hand, $H \rightarrow \gamma\gamma$ produces the most easily identifiable signal,
 304 but has a much smaller branching ratio than $H \rightarrow W^+W^-$. Therefore, compared with other final
 305 states of $t\bar{t}H$, the $t\bar{t}H$ – ML channel is an attractive candidate for study, as it involves a good
 306 balance between statistical power and identifiability.

Decay Mode	Branching Ratio (%)
$H \rightarrow b\bar{b}$	58.2
$H \rightarrow WW^*$	21.4
$H \rightarrow gg$	8.19
$H \rightarrow \tau\tau$	6.27
$H \rightarrow c\bar{c}$	2.89
$H \rightarrow ZZ^*$	2.62
$H \rightarrow \gamma\gamma$	0.227

Table 1: Summary of the predominant SM Higgs ($m_H = 125$ GeV) branching ratios. Particles with a star imply off-shell decays.

307 Searches for $t\bar{t}H$ production typically target a measurement of the signal strength para-
 308 meter, $\mu_{t\bar{t}H}$, which measures the ratio of the observed cross-section and the expected cross-section
 309 according to the SM.

$$\mu_{t\bar{t}H} = \frac{\sigma_{t\bar{t}H}^{\text{obs.}}}{\sigma_{t\bar{t}H}^{\text{SM}}} \quad (2.12)$$

310 $t\bar{t}H$ production was observed by ATLAS using up to 79.8 fb^{-1} of data collected at \sqrt{s}
 311 $= 13 \text{ TeV}$, based on a combination of five Higgs decay modes: $b\bar{b}$, WW^* , $\tau^-\tau^+$, $\gamma\gamma$, and ZZ^*
 312 [6]. A significance of 5.8σ was observed, compared to a 4.9σ expected significance. Since then,
 313 two analyses have published updated results ($H \rightarrow \gamma\gamma$ and $H \rightarrow ZZ^* \rightarrow 4l$) with the full Run 2
 314 dataset, representing 139 fb^{-1} . Studies are still ongoing in the remaining channels.

315 This thesis focuses on $t\bar{t}H$ events with multiple leptons in the final state, $t\bar{t}H - ML$,
 316 specifically targeting events with two same-sign leptons (2lSS) or three leptons (3l) in the

317 final state. This includes $H \rightarrow W^+W^-$ events, where at least one of the W bosons decays
318 leptonically.

319 **2.4 WZ + Heavy Flavor Production**

320 Part IV is dedicated to a measurement of WZ produced in association with a heavy flavor jet
321 - namely, a charm or b-jet - in the fully leptonic channel. In the instance that both the W
322 and Z bosons decay leptonically, this process produces a final state similar to $t\bar{t}H$, making it
323 an irreducible background for $t\bar{t}H$ – ML specifically, and any analysis that includes multiple
324 leptons and b-tagged jets in the final state more broadly.

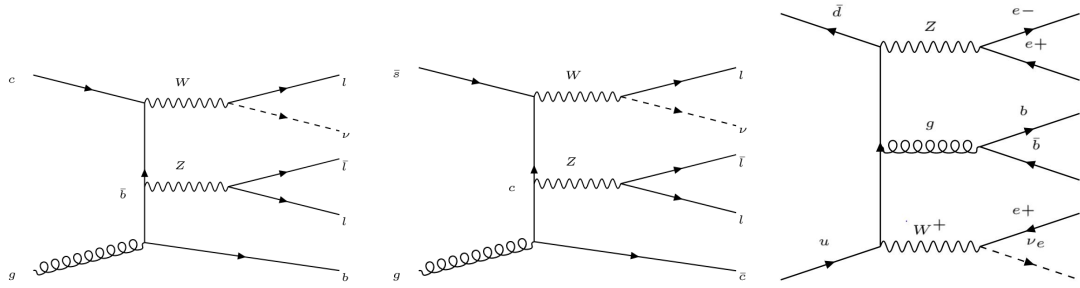


Figure 2.5: Example Feynman diagrams of $WZ +$ heavy flavor production

325 The b-jets produced in this process can be thought of in two different ways: either as
326 originating from the quark “sea” of the initial state hadrons, or as the result of a gluon from
327 one the colliding protons splitting into $b\bar{b}$ pairs. However, the heavy flavor contribution to the
328 parton distribution function (PDF) of the proton is uncertain, and simulations of this process
329 disagree depending on which of these two approaches one considers. This makes $WZ +$ heavy

330 flavor difficult to accurately simulate, and introduces a large uncertainty for any analysis which
331 includes it as a background, motivating a measurement of this process.

332 **2.5 Extensions to the Standard Model**

333 While the SM has been tested to great precision, particularly at the LHC, it is generally accepted
334 that it is only valid up to a certain energy scale. It is assumed that above a certain energy, at the
335 scale where something like a Grand Unified Theory (GUT) or quantum gravity become relevant,
336 the SM will not be applicable. Further, there are several experimental observations that the SM
337 fails to explain. For example, the SM predicts neutrinos to be massless, despite experimental
338 observation to the contrary, and fails to explain the observation of dark matter and dark energy.

339 Another example, relevant to the Higgs sector, is known as the hierarchy problem: large
340 quantum corrections to the Higgs mass from loop diagrams, such as those shown in Figure 2.6,
341 are many orders of magnitude larger than the Higgs mass itself. The observed value of the Higgs
342 mass therefore requires extremely precise cancellation between these corrections and the bare
343 mass of the Higgs, a cancellation which seems unnatural and suggests something missing in our
344 theoretical picture.

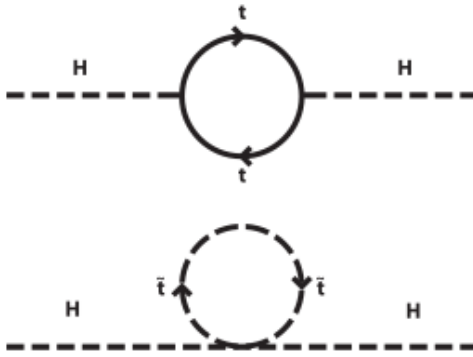


Figure 2.6: Above diagram is the leading order correction to the Higgs mass via a top quark loop, and below is the stop squark loop, coming from a supersymmetric extension of the SM, that provides a potential cancellation of the top diagram.

Because so many of the properties of the Higgs boson have not yet been studied, its interactions are a promising place to search for new physics that could resolve some of the limitations of the SM. As explained above, the interactions of the Higgs with the top quark, as in $t\bar{t}H$ production, are particularly interesting: As the most massive particle in the Standard Model, the top quark is the most strongly interacting with the Higgs. Therefore, any new physics effects are likely to be seen most prominently in this interaction.

These interactions can be measured directly by studying the production of a Higgs Boson in association with a pair of Top Quarks ($t\bar{t}H$). While this process has been observed by both the ATLAS [7] and CMS [8] collaborations, these analyses have focused on measuring the overall rate of $t\bar{t}H$ production. There are several theories of physics Beyond the Standard Model (BSM), however, that would affect the kinematics of $t\bar{t}H$ production without altering its overall rate [9].

357 An Effective Field Theory approach can be used to model the low energy effects of new,
 358 high energy physics, by parameterizing BSM effects as higher dimensional operators. These
 359 additional operators can then be added to the SM Lagrangian to write an effective Lagrangian
 360 that accounts for the effects of these higher energy physics. The lowest order of these that could
 361 contribute to Higgs-top couplings are dimension-six, as represented in Equation 2.13.

$$\mathcal{L}_{\text{eff}} = \mathcal{L}_{\text{SM}} + \frac{f}{\Lambda} O^6 \quad (2.13)$$

362 Here Λ represents the energy scale of the new physics, and f is a Wilson coefficient which
 363 represents the strength of the effective coupling. An experimental observation of any non-zero
 364 value of f would be a sign of BSM physics.

365 The addition of these operators can be shown to modify the transverse momentum (p_T)
 366 spectrum of the Higgs Boson in Higg-top interactions, without effecting the overall rate of $t\bar{t}H$
 367 production [10]. The possible impact of these higher order effects on the Higgs p_T spectrum are
 368 shown in Figure 2.7.

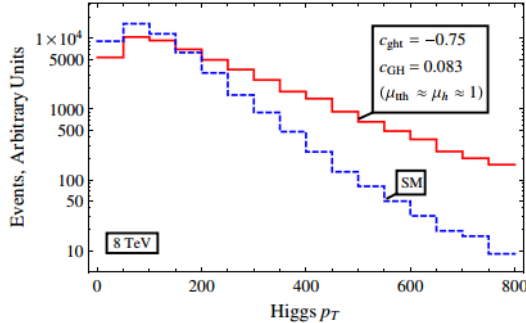


Figure 2.7: The momentum spectrum of the Higgs boson produced via top-quarks with (red) and without (blue) the presence of dimension-six operators.

369 This provides a clear, physics observable that could be used to search for evidence of
 370 BSM physics. The energy and luminosity produced by the LHC now make such a measurement
 371 possible. Reconstructing the momentum spectrum of the Higgs in $t\bar{t}H$ events therefore provides
 372 a means to search for new physics in the Higgs sector.

373 Reconstructing the Higgs is a particular challenge in the multilepton channels of $t\bar{t}H$, due
 374 to an ambiguity arising from multiple sources of missing energy. In the $H \rightarrow \gamma\gamma$ channel, the
 375 kinematics of the Higgs can be fully reconstructed from the two photons. The same is true of
 376 $H \rightarrow b\bar{b}$, though with the additional challenge of identifying which two of the four b-quarks in
 377 the final state originated from the Higgs. By contrast, the two channels (2lSS and 3l) targeted
 378 by this analysis include at least one neutrino originating from the Higgs decay.

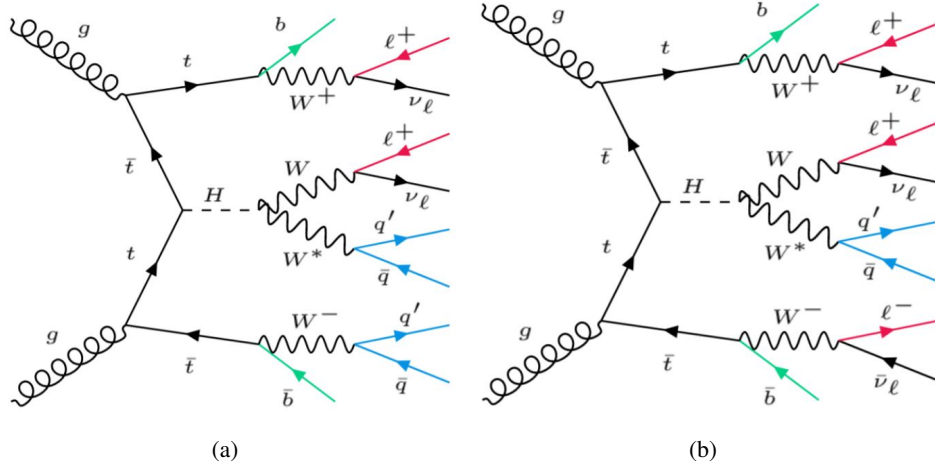


Figure 2.8: Feynman diagrams of $t\bar{t}H$ production with (a) two same-sign leptons and (b) three leptons in the final state.

379 Neutrinos are not detected by ATLAS; instead, their presence is inferred from missing
 380 transverse energy in the detector, E_{miss}^T . The two channels targeted here include not just a
 381 neutrino from the Higgs decay, but at least one additional neutrino from the decay of the top-
 382 quarks. This makes disentangling the contribution of the Higgs decay to E_{miss}^T , and thereby fully
 383 reconstructing the Higgs, impossible.

384 This challenge motivates the use of more sophisticated machine learning techniques when
 385 attempting to perform differential measurements of the Higgs p_T spectrum in the multi-lepton
 386 channels of $t\bar{t}H$.

Part III**388 The LHC and the ATLAS Detector****389 3 The LHC**

390 The Large Hadron Collider (LHC) is a particle accelerator consisting of a 27 km ring, designed
391 to collide protons at high energy. Located outside of Geneva, Switzerland and buried about 100
392 m underground, it consists of a ring of superconducting magnets which are used to accelerate
393 opposing beams of protons - or lead ions - which collide at the center of one of the various
394 detectors located around the LHC ring which record the result of these collisions. These
395 detectors include two general purpose detectors, ATLAS and CMS, which are designed to make
396 precision measurements of a broad range of physics phenomenon, and two more specialized
397 experiments, LHCb and ALICE, which are optimized to study b-quarks and heavy-ion physics,
398 respectively.

399 The LHC first began running in 2009 at a proton-proton center of mass energy of $\sqrt{s} = 8$
400 TeV. It operated at this energy from 2009 to 2012, known as Run 1, and data collected during
401 this period was used in discovering the Higgs Boson. The LHC began running again in 2015,
402 and collected data at an increased energy of $\sqrt{s} = 13$ TeV until 2018, a period referred to as Run
403 2.

404 The LHC consists of a chain of accelerators, which accelerate the protons to higher and

higher energies until they are injected into the main ring. This process is summarized in figure 3.1. Protons extracted from a tank of ionized hydrogen are fed into a linear accelerator, LINAC2, where they reach an energy of 50 MeV. From there, they enter a series of three separate circular accelerators, before being injected into the main accelerator ring at an energy of 450 GeV. Within the main ring protons are separated into two separate beams moving in opposite directions, and their energy is increased to their full collision energy. Radiofrequency cavities are used to accelerate these particles and sort them into bunches. From 2015-2018, these bunches consisted of around 100 billion protons each with an energy of 6.5 TeV per proton, which collided at a rate of 40 MHz, or every 25 ns.

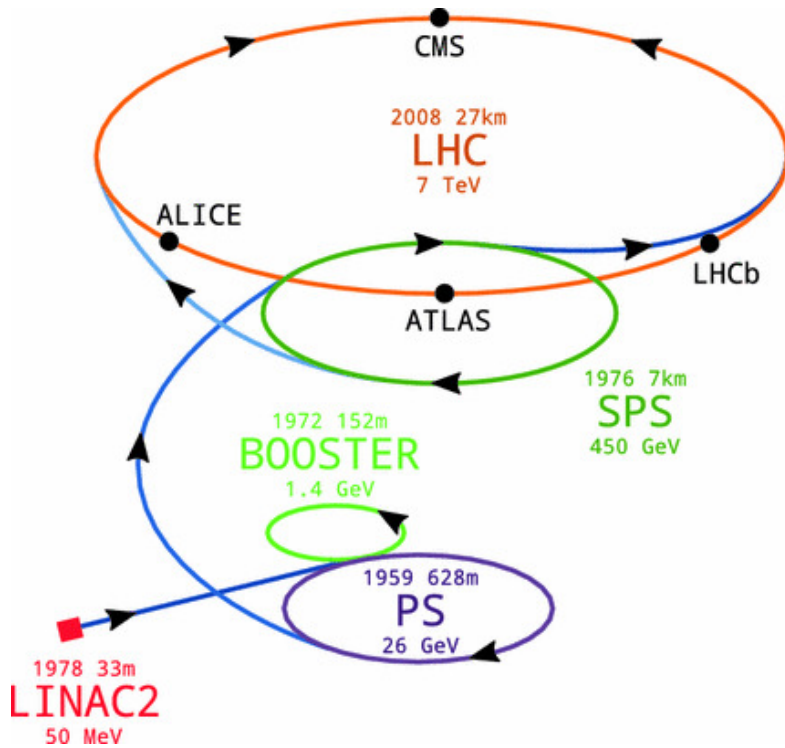


Figure 3.1: A summary of the accelerator chain used to feed protons into the LHC [11].

414 Because these proton bunches consist of a large number of particles, each bunch crossing
 415 consists of not just one, but several direct proton-proton collisions. The number of interactions
 416 that occur per bunch crossing, μ , is known as pileup. During Run 2, the average pileup for bunch
 417 crossings was around $\langle \mu \rangle = 35$, with values typically ranging between 10 and 70.

418 The amount of data collected by the LHC is measured in terms of luminosity, which is the
 419 ratio of the number of events detected per unit time, $\frac{dN}{dt}$, and the interaction cross-section, σ .

$$\mathcal{L} = \frac{1}{\sigma} \frac{dN}{dt} \quad (3.1)$$

420 The design luminosity of the LHC is $10^{34} \text{ cm}^{-2}\text{s}^{-1}$, however the LHC has achieved a
 421 luminosity of over $2 \times 10^{34} \text{ cm}^{-2}\text{s}^{-1}$. The total luminosity is then this instantaneous luminosity
 422 integrated over time.

$$\mathcal{L}_{\text{int}} = \int \mathcal{L} dt \quad (3.2)$$

423 The integrated luminosity collected by the ATLAS detector as of the end of 2018 is around
 424 140 fb^{-1} , exceeding the expected integrated luminosity of 100 fb^{-1} .

425 4 The ATLAS Detector

426 ATLAS (a not terribly natural acronym for “A Toroidal LHC Apparatus”) is a general purpose
 427 detector designed to maximize the detection efficiency of all physics objects, including leptons,
 428 jets, and photons. This means it is capable of measuring all SM particles, with the exception of
 429 neutrinos, the presence of which can be inferred based on missing transverse momentum. The
 430 detector measures 44 m long, and 25 m tall.

431 The ATLAS detector consists of multiple concentric layers, each of which serves a different
 432 purpose in reconstructing collisions. At the very center of the detector is the interaction point
 433 where the proton beams of the LHC collide.

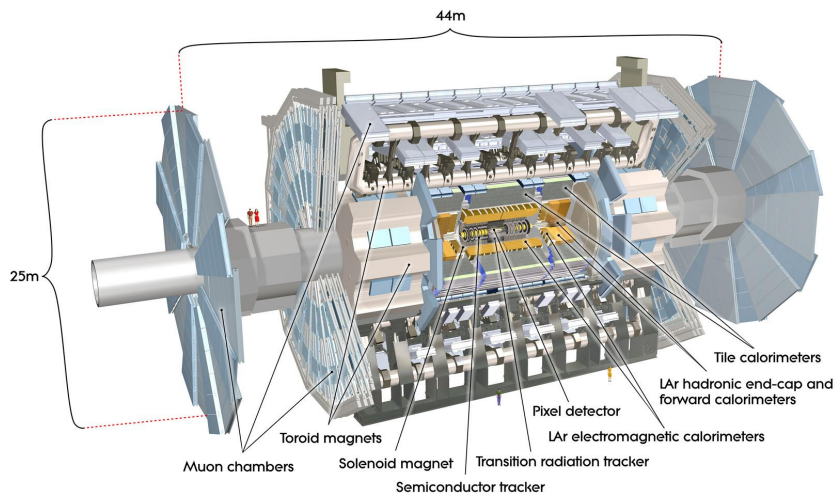


Figure 4.1: Cutaway view of the ATLAS detector, with labels of its major components [12].

434 **4.1 Inner Detector**

435 Just surrounding the interaction point is the Inner Detector, designed to track the path of charged
436 particles moving through the detector. An inner solenoid surrounding the Innder Detector is
437 used to produces a magnetic field of 2 T. This large magnetic field causes the path of charged
438 particles moving through the Inner Detector to bend. Because this magnetic field is uniform and
439 well known, it can be used in conjunction with the curvature of a particles path to measure its
440 charge and momentum.

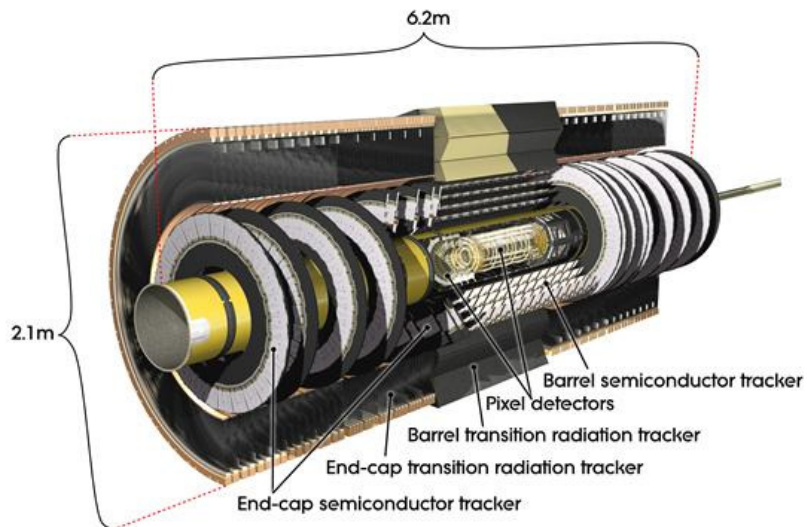


Figure 4.2: Cutaway view of the Inner Detector [13].

441 The Inner Detector consists of three components - the Pixel Detector, the Semi-Conductor
442 Tracker (SCT), and the Transition Radiation Tracker (TRT). The Pixel Detector is the innermost
443 of these, beginning just 33.25 mm away from the beam line. It consists of three silicon layers
444 along the barrel, as well as three endcap layers, covering a range of $|\eta| < 2.5$.

445 The Semiconductor Tracker (SCT) is similar to the Pixel detector, but uses long strips of
 446 silicon rather than small pixels to cover a larger spatial area. It includes over 6 million readout
 447 strips, allowing the position of charged particles to be measured to an accuracy of 17 μm .

448 The outermost component of the inner detector, the TRT consists of around 300,000 straw
 449 tubes filled with ionizable gas, which produces current through a wire in the center of each tube
 450 when a charged particle passes through. Between these staws are layers of material designed
 451 to produce transition radiation from ultrarelativistic particles as they pass through each material
 452 boundary, amplifying the signal. The position uncertainty in the TRT is higher than the other
 453 two, on the order of 200 μm , but covering a much larger area.

454 4.2 Calorimeters

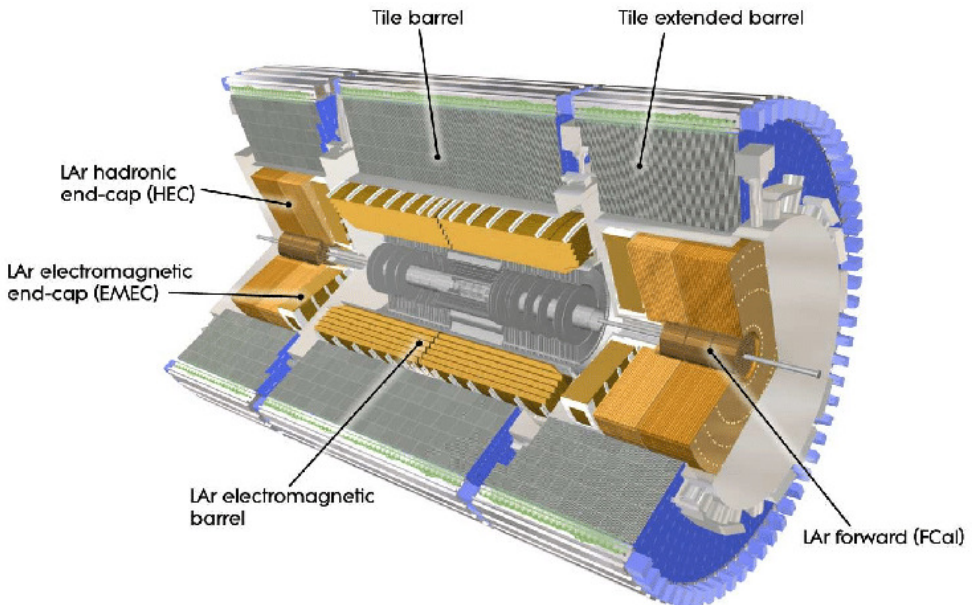


Figure 4.3: Cutaway view of the calorimeter system of the ATLAS detector [13].

455 Situated outside the Inner Detector are two concentric calorimeters. The inner calorimeter
456 uses liquid argon (LAr) to measure the energy of particles that interact electromagnetically,
457 which includes photons and any charged particle. The LAr calorimeter is made of heavy metals,
458 primarily lead and copper, which causes electromagnetically interacting particles to shower,
459 depositing their energy in the detector. The showering of the high energy particles that pass
460 through the calorimeter cause the liquid argon to ionize, and the ionized electrons are detected
461 by electronic readouts. The LAr calorimeter consists of around 180,000 readout channels.

462 The outer calorimeter measures the energy from particles that pass through the EM
463 calorimeter, and measures the energy of particles that interact via the strong force. This is
464 primarily hadrons. It is composed of steel plates designed to cause hadronic showering and
465 around 500,000 scintillating tiles as the active material. The signals from the hadronic calorimeter
466 are read out by photomultiplier tubes (PMTs).

467 **4.3 Muon Spectrometer**

468 Because muons are heavier than electrons and photons, and do not interact via the strong force,
469 they generally pass through the detector without being stopped by the calorimeters. The outermost
470 components of the detector are designed specifically to measure the energy and momentum of
471 muons produced in the LHC. The muon spectrometer consists of tracking and triggering systems.
472 The largest of the subdetectors, it extends from the outside of the calorimeter system, about a
473 4.25 m radius from the beam line, to a radius of 11 m. This large detector system is necessary

474 to accurately measure the momentum of muons, which is essential not only for measurements
475 involving the muons themselves, but also to accurately estimate the missing energy in each
476 event.

477 Two large toroidal magnets within the muon system generate a large magnetic field which
478 covers an area 26 m long with a radius of 10 m. Because the area covered by this magnet system
479 is so large, a uniform magnetic field like the one produced in the Inner Detector is impractical.
480 Instead, the magnetic field that exists in the muon spectrometer ranges between 2 T and 8 T, and
481 is much less uniform. The path of the muons passing through the spectrometer is bent by this
482 field, allowing their charge to be determined.

483 1200 tracking chambers are placed in the muon system in order to precisely measure the
484 tracks of muons with high spatial resolution. The path of the muons are tracked by Monitored
485 Drift Tubes, which are drift chambers formed by aluminum tubes and filled with ionizing gas.
486 These tubes produce a multi-layer spatial resolution on the order of 50 μm .

487 **4.4 Trigger System**

488 Because of the high collision rate and large amount of data collected by the various subdetectors,
489 ATLAS produces far more data than can actually be stored. Each event produces around 25 Mb
490 of raw data, which multiplied by the bunch crossing rate of 40 MHz, comes out to around a
491 petabyte of data every second. The information from every event cannot practically be stored,

492 therefore a sophisticated trigger system is employed in real time to determine whether events are
493 sufficiently interesting to be worth storing.

494 The trigger system in ATLAS involves multiple levels, each of which select out which
495 events move on to the next level of scrutiny. The level-1 trigger uses hardware information from
496 the calorimeters and muon spectrometer to select events that contain candidates for particles
497 commonly used in analysis, such as energetic leptons and jets. The level-1 trigger reduces the
498 rate of events from 40 MHz to around 100 kHz.

499 Events that pass the level-1 trigger move to the High-Level Trigger (HLT). The HLT takes
500 place outside of the detector in software, and looks for properties such as a large amount of
501 missing transverse energy, well defined leptons, and multiple high energy jets. Events that pass
502 the HLT are stored and used for analysis. Because the specifics of the HLT are determined by
503 software rather than hardware, the thresholds can be changed throughout the run of the detector
504 in response to run conditions such as changes to pileup and luminosity. After the HLT is applied,
505 the event rate is reduced to around 1000 per second, which are recorded for analysis.

506 Part IV**507 Measurement of WZ + Heavy Flavor****508 5 Introduction**

509 The production of WZ in association with a heavy flavor jet represents an important background
510 for many major analyses. This includes any process with leptons and b-jets in the final state,
511 such as $t\bar{t}H$, $t\bar{t}W$, and $t\bar{t}Z$. While precise measurements have been made of WZ production
512 [14], WZ + heavy flavor remains poorly understood. This is largely because the QCD processes
513 involved in the production of the b-jet make it difficult to simulate accurately. This introduces a
514 large uncertainty for analyses that include this process as a background.

515 Motivated by its relevance to the $t\bar{t}H$ multilepton analysis, we perform a study of the fully
516 leptonic decay mode of this channel; that is, events where both the W and Z decay leptonically.
517 Because WZ has no associated jets at leading order, while the major backgrounds for this channel
518 tend to have high jet multiplicity, events with more than two jets are rejected. This gives a final
519 state signature of three leptons and one or two jets.

520 Events that meet this selection criteria are sorted into pseudo-continuous b-tagging regions
521 based on the DL1r b-tag score of their associated jets. This is done to separate WZ + b-jet events
522 from WZ + charm and WZ + light jets. These regions are fit to data in order to make a more
523 accurate estimate of the contribution of WZ + heavy-flavor, where heavy-flavor jets include

524 b-jets and charm jets. The full Run-2 dataset collected by the ATLAS detector, representing 139
525 fb^{-1} of data from pp collisions at $\sqrt{s} = 13 \text{ TeV}$, is used for this study.

526 Section 10 details the data and Monte Carlo (MC) samples used in the analysis. The
527 reconstruction of various physics objects is described in Section 11. Section 12 describes the
528 event selection applied to these samples, along the definitions of the various regions used in
529 the fit. The multivariate analysis techniques used to separate the tZ background from WZ +
530 heavy flavor are described in Section 13. Section 20 describes the various sources of systematic
531 uncertainties considered in the fit. Finally, the results of the analysis are summarized in Section
532 21, followed by a brief conclusion in Section ??.

533 **The current state of the analysis shows blinded results for the full 2018 dataset.**
534 **Regions containing >5% WZ+b events are blinded, and results are from Asimov, MC only**
535 **fits.**

536 6 Data and Monte Carlo Samples

537 6.1 Data Samples

538 This study uses a sample of proton-proton collision data collected by the ATLAS detector from
539 2015 through 2018 at an energy of $\sqrt{s} = 13 \text{ TeV}$, which represents an integrated luminosity of
540 139 fb^{-1} . This data set was collected with a bunch crossing rate of 25 ns. All data used in this
541 analysis was verified by data quality checks.

542 **6.2 Monte Carlo Samples**

543 Several different generators were used to produce Monte Carlo simulations of the signal and
544 background processes. For all samples, the response of the ATLAS detector is simulated using
545 Geant4. The WZ signal samples are simulated using Sherpa 2.2.2 [15]. Specific information
546 about the Monte Carlo samples being used can be found in Table 22.

Table 2: The configurations used for event generation of signal and background processes, including the event generator, matrix element (ME) order, parton shower algorithm, and parton distribution function (PDF).

Process	Event generator	ME order	Parton Shower	PDF
WZ, VV	SHERPA 2.2.2	MEPS NLO	SHERPA	CT10
tZ	MG5_AMC	NLO	PYTHIA 8	CTEQ6L1
t̄tW	MG5_AMC (SHERPA 2.1.1)	NLO (LO multileg)	PYTHIA 8 (SHERPA)	NNPDF 3.0 NLO (NNPDF 3.0 NLO)
t̄t(Z/γ* → ll)	MG5_AMC	NLO	PYTHIA 8	NNPDF 3.0 NLO
t̄tH	MG5_AMC (MG5_AMC)	NLO (NLO)	PYTHIA 8 (HERWIG++)	NNPDF 3.0 NLO [16] (CT10 [17])
tHqb	MG5_AMC	LO	PYTHIA 8	CT10
tHW	MG5_AMC (SHERPA 2.1.1)	NLO (LO multileg)	HERWIG++ (SHERPA)	CT10 (NNPDF 3.0 NLO)
tWZ	MG5_AMC	NLO	PYTHIA 8	NNPDF 2.3 LO
t̄t̄t, t̄tt̄t̄t̄	MG5_AMC	LO	PYTHIA 8	NNPDF 2.3 LO
t̄tW+W-	MG5_AMC	LO	PYTHIA 8	NNPDF 2.3 LO
t̄t	POWHEG-BOX v2 [18]	NLO	PYTHIA 8	NNPDF 3.0 NLO
t̄t̄γ	MG5_AMC	LO	PYTHIA 8	NNPDF 2.3 LO
s-, t-channel, Wt single top	POWHEG-BOX v1 [19]	NLO	PYTHIA 6	CT10
qqVV, VVV Z → l+l-	SHERPA 2.2.1	MEPS NLO	SHERPA	NNPDF 3.0 NLO

547 7 Object Reconstruction

548 All regions defined in this analysis share a common lepton, jet, and overall event preselection.
 549 The selection applied to each physics object is detailed here; the event preselection, and the
 550 selection used to define the various fit regions, is described in Section 12.

551 All events are required to be selected by dilepton triggers. The p_T thresholds of the
 552 dilepton trigger on two electrons were 12 GeV in 2015, 17 GeV in 2016, and 24 GeV in 2017 and
 553 2018, while for the dimuon triggers the p_T thresholds on the leading (sub-leading) muon were
 554 18 GeV (8 GeV) in 2015, and 22 GeV (8 GeV) in 2016-2018. For the electron+muon triggers,
 555 the p_T thresholds on the electron (muon) were 17 GeV (14 GeV) for all datasets.

556 7.1 Light leptons

557 Electron candidates are reconstructed from energy clusters in the electromagnetic calorimeter
 558 that are associated with charged particle tracks reconstructed in the inner detector [20]. Electron
 559 candidates are required to have $p_T > 10$ GeV and $|\eta_{\text{cluster}}| < 2.47$. Muon candidates are
 560 reconstructed by combining inner detector tracks with track segments or full tracks in the muon
 561 spectrometer [21]. Muon candidates are required to have $p_T > 10$ GeV and $|\eta| < 2.5$. Candidates
 562 in the transition region between different electromagnetic calorimeter components, $1.37 <$
 563 $|\eta_{\text{cluster}}| < 1.52$, are rejected. A multivariate likelihood discriminant combining shower shape
 564 and track information is used to distinguish real electrons from hadronic showers (fake electrons).
 565 To further reduce the non-prompt electron contribution, the track is required to be consistent

566 with originating from the primary vertex; requirements are imposed on the transverse impact
 567 parameter significance ($|d_0|/\sigma_{d_0} < 5$) and the longitudinal impact parameter ($|\Delta z_0 \sin \theta_\ell| < 0.5$
 568 mm). Electron candidates are required to pass TightLH identification.

569 Muon candidates are reconstructed by combining inner detector tracks with track segments
 570 or full tracks in the muon spectrometer [21]. Muon candidates are required to have $p_T > 10$ GeV
 571 and $|\eta| < 2.5$. The longitudinal impact parameter is the same for both electrons and muons, while
 572 muons are required to pass a slightly tighter transverse impact parameter, $|d_0|/\sigma_{d_0} < 3$. Muons
 573 are also required to pass Medium ID requirements.

574 Leptons are additionally required to pass a non-prompt BDT selection developed by the
 575 $t\bar{t}H$ multilepton/ $t\bar{t}W$ analysis group. This BDT and the WPs used are summarized in Appendix
 576 A, and described in detail in [22]. Optimized working points and scale factors for this BDT are
 577 taken from that analysis.

578 7.2 Jets

579 Jets are reconstructed from calibrated topological clusters built from energy deposits in the
 580 calorimeters [23], using the anti- k_t algorithm with a radius parameter $R = 0.4$. Particle Flow, or
 581 PFlow, jets are used in the analysis, which are hadronic objects reconstructed using information
 582 from both the tracker and the calorimeter. Jets with energy contributions likely arising from noise
 583 or detector effects are removed from consideration [24], and only jets satisfying $p_T > 25$ GeV
 584 and $|\eta| < 2.5$ are used in this analysis. For jets with $p_T < 60$ GeV and $|\eta| < 2.4$, a jet-track

585 association algorithm is used to confirm that the jet originates from the selected primary vertex,
 586 in order to reject jets arising from pileup collisions [25].

587 **7.3 B-tagged Jets**

588 In order to make a measurement of $WZ +$ heavy flavor it is necessary to distinguish these events
 589 from $WZ +$ light jets. For this purpose, the DL1r b-tagging algorithm is used to distinguish
 590 heavy flavor jets from lighter ones. The DL1r algorithm uses jet kinematics, particularly jet
 591 vertex information, as input for a neural network which assigns each jet a score designed to
 592 reflect how likely that jet is to have originated from a b-quark.

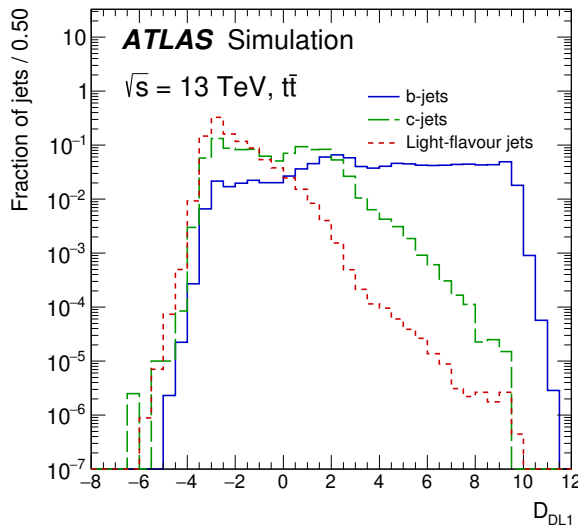


Figure 7.1: Output distribution of the DL1r algorithm for b-jets, charm jets, and light jets

593 From the output of the BDT, calibrated working points (WPs) are developed based on the
 594 efficiency of truth b-jets at particular values of the DL1r algorithm. The working points used in

595 this analysis are summarized in Table 9.

WP	none	loose	medium	tight	tightest
b eff.	-	85%	77%	70%	60%

Table 3: B-tagging Working Points by tightness and b-jet efficiency

596 A tighter WP will accept fewer b-jets, but reject a higher fraction of charm and light jets.

597 Generally, analyses that include b-jets will use a fixed working point, for example, requiring that
 598 a jet pass the 70% threshold. By instead treating these working point as bins, e.g. events with
 599 jets that fall between the 85% and 77% WPs fall into one bin, while events with jets passing the
 600 60% WP fall into another, and looking at the full psuedo-continuous DL1r spectrum of the jets,
 601 additional information can be gained. The psuedo-continuous b-tag spectrum is used in this case
 602 to separate out WZ + b, WZ + charm, and WZ + light.

603 7.4 Missing transverse energy

604 Missing transverse momentum (E_T^{miss}) is used as part of the event selection. The missing
 605 transverse momentum vector is defined as the inverse of the sum of the transverse momenta of
 606 all reconstructed physics objects as well as remaining unclustered energy, the latter of which is
 607 estimated from low- p_T tracks associated with the primary vertex but not assigned to a hard object,
 608 with object definitions taken from [26]. Light leptons considered in the E_T^{miss} reconstruction are
 609 required to have $p_T > 10 \text{ GeV}$, while jets are required to have $p_T > 20 \text{ GeV}$.

⁶¹⁰ **7.5 Overlap removal**

⁶¹¹ To avoid double counting objects and remove leptons originating from decays of hadrons, overlap
⁶¹² removal is performed in the following order: any electron candidate within $\Delta R = 0.1$ of another
⁶¹³ electron candidate with higher p_T is removed; any electron candidate within $\Delta R = 0.1$ of a muon
⁶¹⁴ candidate is removed; any jet within $\Delta R = 0.3$ of an electron candidate is removed; if a muon
⁶¹⁵ candidate and a jet lie within $\Delta R = \min(0.4, 0.04 + 10[\text{GeV}]/p_T(\text{muon}))$ of each other, the jet
⁶¹⁶ is kept and the muon is removed.

⁶¹⁷ This algorithm is applied to the preselected objects. The overlap removal procedure is
⁶¹⁸ summarized in Table 23.

Keep	Remove	Cone size (ΔR)
electron	electron (low p_T)	0.1
muon	electron	0.1
electron	jet	0.3
jet	muon	$\min(0.4, 0.04 + 10[\text{GeV}]/p_T(\text{muon}))$
electron	tau	0.2

Table 4: Summary of the overlap removal procedure between electrons, muons, and jets.

⁶¹⁹ **8 Event Selection and Signal Region Definitions**

⁶²⁰ Event are required to pass a preselection described in Section 12.1 and summarized in Table 11.
⁶²¹ Those that pass this preselection are divided into various fit regions described in Section 12.2,
⁶²² based on the number of jets in the event, and the b-tag score of those jets.

623 8.1 Event Preselection

624 Events are required to include exactly three reconstructed light leptons passing the requirement
 625 described in 11.1, which have a total charge of ± 1 .

626 The leptons are ordered in the analysis code as 0, 1, and 2. Lepton 0 is the lepton whose
 627 charge is opposite the other two. Lepton 1 is the lepton closest to the opposite charge lepton, i.e.
 628 the smallest ΔR , leaving lepton 2 as the lepton further from the opposite charge lepton. Lepton
 629 0 is required to have $p_T > 10$ GeV, while the same sign leptons, 1 and 2, are required to have
 630 $p_T > 20$ GeV to reduce the contribution of non-prompt leptons.

631 The invariant mass of at least one pair of opposite sign, same flavor leptons is required
 632 to fall within 10 GeV of the mass of the Z boson, 91.2 GeV. Events where one of the opposite
 633 sign pairs have an invariant mass less than 12 GeV are rejected in order to suppress low mass
 634 resonances.

635 An additional requirement is placed on the missing transverse energy, $E_T^{\text{miss}} > 20$ GeV,
 636 and the transverse mass of the W candidate, $m(E_T^{\text{miss}} + l_{\text{other}}) > 30$ GeV, where E_T^{miss} is the
 637 missing transverse energy, and l_{other} is the lepton not included in the Z-candidate.

638 Events are required to have one or two reconstructed jets passing the selection described
 639 in Section 11.2. Events with more than two jets are rejected in order to reduce the contribution
 640 of backgrounds such as $t\bar{t}Z$ and $t\bar{t}W$, which tend to have higher jet multiplicity.

Event Selection
Exactly three leptons with charge ± 1
Two same-charge leptons with $p_T > 20 \text{ GeV}$
One opposite charge lepton with $p_T > 10 \text{ GeV}$
$m(l^+l^-)$ within 10 GeV of 91.2 GeV
Transverse mass of W-candidate, $m_T(E_T^{\text{miss}} + \text{lep}_{\text{other}}) > 30 \text{ GeV}$
Missing transverse energy, $E_T^{\text{miss}} > 20 \text{ GeV}$
One or two jets with $p_T > 25 \text{ GeV}$

Table 5: Summary of the selection applied to events for inclusion in the fit

641 The event yields in the preselection region for both data and Monte Carlo are summarized
 642 in Table 12.1, which shows good agreement between data and Monte Carlo, and demonstrates
 643 that this region consists primarily of WZ events. The WZ events are split into WZ + b, WZ +
 644 c, and WZ + l based on the truth flavor of the associated jet in the event. In this ordering b-jet
 645 supersede charm, which supersides light. That is, WZ + l events contain no charm and no b jets
 646 at truth level, WZ + c contain at least one truth charm and no b-jets, and WZ + b contains at least
 647 one truth b-jet.

Process	Events
WZ + b	167.6 ± 6.5
WZ + c	1080 ± 40
WZ + l	7220 ± 310
Other VV	850 ± 140
t̄tW	16.8 ± 2.3
t̄tZ	115 ± 17
rare Top	2.2 ± 0.1
Single top	0.10 ± 0.45
Three top	0.01 ± 0.01
Four top	0.02 ± 0.01
t̄tWW	0.23 ± 0.05
Z + jets	600 ± 260
V + γ	37 ± 54
tZ	190 ± 70
tW	5.5 ± 1.2
WtZ	25.8 ± 1.1
VVV	26.2 ± 0.9
VH	94 ± 7
t̄t	108.68 ± 8
t̄tH	4.3 ± 0.5
Total	10600 ± 530
Data	10574

Table 6: Event yields in the preselection region at 139.0 fb^{-1}

648 Here Other VV represents diboson processes other than WZ, and consists predominantly
 649 of $ZZ \rightarrow ll\bar{l}\bar{l}$ events where one of the leptons is not reconstructed.

650 8.2 Fit Regions

651 Once preselection has been applied, the remaining events are categorized into one of twelve
 652 orthogonal regions. The regions used in the fit are summarized in Table 13.

Table 7: A list of the regions used in the fit and the selection used for each.

Region	Selection
1j, <85%	$N_{\text{jets}} = 1, n\text{Jets_DL1r_85} = 0$
1j, 85%-77%	$N_{\text{jets}} = 1, n\text{Jets_DL1r_85} = 1, n\text{Jets_DL1r_77}=0$
1j, 77%-70%	$N_{\text{jets}} = 1, n\text{Jets_DL1r_77} = 1, n\text{Jets_DL1r_70}=0$
1j, 70%-60%	$N_{\text{jets}} = 1, n\text{Jets_DL1r_70} = 1, n\text{Jets_DL1r_60}=0$
1j, >60%	$N_{\text{jets}} = 1, n\text{Jets_DL1r_60} = 1, tZ \text{ BDT} > 0.725$
1j tZ CR	$N_{\text{jets}} = 1, n\text{Jets_DL1r_60} = 1, tZ \text{ BDT} < 0.725$
2j, <85%	$N_{\text{jets}} = 2, n\text{Jets_DL1r_85} = 0$
2j, 85%-77%	$N_{\text{jets}} = 2, n\text{Jets_DL1r_85} >= 1, n\text{Jets_DL1r_77}=0$
2j, 77%-70%	$N_{\text{jets}} = 2, n\text{Jets_DL1r_77} >= 1, n\text{Jets_DL1r_70}=0$
2j, 70%-60%	$N_{\text{jets}} = 2, n\text{Jets_DL1r_70} >= 1, n\text{Jets_DL1r_60}=0$
2j, >60%	$N_{\text{jets}} = 2, n\text{Jets_DL1r_60} >= 1, tZ \text{ BDT} > 0.725$
2j tZ CR	$N_{\text{jets}} = 2, n\text{Jets_DL1r_60} >= 1, tZ \text{ BDT} < 0.725$

653 The working points discussed in Section 11.3 are used to separate events into fit regions
 654 based on the highest working point reached by a jet in each event. Because the background
 655 composition differs significantly based on the number of b-jets, events are further subdivided
 656 into 1-jet and 2-jet regions in order to minimize the impact of background uncertainties.

657 An unfolding procedure is performed to account for differences in the number of recon-
 658 structed jets compared to the number of truth jets in each event. In order to account for migration
 659 of WZ+1-jet and WZ+2-jet events between the 1-jet and 2-jet bins at reco level, the signal
 660 samples are separated based on the number of truth jets. Events with 0 jets or more than 3 jets at
 661 truth level, yet fall within one of the categories listed in Table 13, are categorized as WZ + other,
 662 and treated as a background. The composition of the number of truth jets in each reco jet bin is
 663 taken from MC, with uncertainties in these estimates described in detail in Section 20.

664 An additional tZ control region is created based on the BDT described in Section 13. The

665 region with 1-jet passing the 60% working point is split in two - a signal enriched region of
666 events with a BDT score greater than 0.03, and a tZ control region including events with less
667 than 0.03. This cutoff is arrived at by performing an Asimov fit with a variety of cutoffs, and
668 selecting the value that produces the highest significance for the measurement of WZ + b.

669 **8.3 Non-Prompt Lepton Estimation**

670 Two processes act as sources of non-prompt leptons appear in the analysis: $t\bar{t}$ and Z+jet
671 production both produce two prompt leptons, and each contribute to the 3l region when an
672 additional non-prompt lepton appears in the event. The contribution of these processes is
673 estimated with Monte Carlo simulations, which are validated using enriched control regions.

674 The modelling in the Z+jets and $t\bar{t}$ CRs is further validated for each of the pseudo-
675 continuous b-tag regions used in the analysis. The relevant lepton p_T spectrum in each b-tag
676 region is shown in Appendix B.1 for these CRs after the correction factors derived below have
677 been applied.

678 **8.3.1 $t\bar{t}$ Validation**

679 $t\bar{t}$ events can produce two prompt leptons from the decay of each of the tops. These top decays
680 produce two b-quarks, the decay of which can produce additional non-prompt leptons, which
681 occasionally pass the event preselection. In order to validate that the Monte Carlo accurately

682 simulates this process accurately, the MC prediction in a non-prompt $t\bar{t}$ enriched control region
 683 is compared to data.

684 The $t\bar{t}$ control region is similar to the preselection region - three leptons meeting the
 685 criteria described in Section 12 are required, and the requirements on E_T^{miss} remain the same.
 686 However, the selection requiring a lepton pair form a Z-candidate are reversed. Events where the
 687 invariant mass of any two opposite sign, same flavor leptons falls within 10 GeV of 91.2 GeV are
 688 rejected. This ensures the $t\bar{t}$ control region is orthogonal to the preselection region.

689 Further, because the jet multiplicity of $t\bar{t}$ events tends to be higher than WZ, the number
 690 of jets in each event is required to be greater than 1. As b-jets are almost invariably produced
 691 from top decays, at least one b-tagged jet passing the 70% DL1r WP in each event is required.

692 Data is compared to MC predictions in the region for a variety of kinematic variable, as well
 693 as various b-tag WPs. A constant normalization discrepancy between data and MC predictions
 694 of approximately 10% is found, which is accounted for by applying a constant correction factor
 695 of 0.9 to the $t\bar{t}$ MC prediction. As data and MC are found to agree within 20% for each of
 696 the b-tag WPs considered, a 20% systematic uncertainty on the $t\bar{t}$ prediction is included for the
 697 analysis.

698 **8.3.2 Z+jets Validation**

699 Similar to $t\bar{t}$, a non-prompt Z+jets control region is produced in order to validate the MC
 700 predictions. The lepton requirements remain the same as the preselection region. Because no

701 neutrinos are present for this process, the E_T^{miss} cut is reversed, requiring $E_T^{\text{miss}} < 30 \text{ GeV}$. This
 702 also ensures this control region is orthogonal to the preselection region. Further, the number of
 703 jets in each event is required to be greater than or equal to one.

704 While there is general agreement between data and MC within statistical uncertainty, the
 705 shape of the p_T spectrum of the lepton from the W is found to differ. To account for this
 706 discrepancy, a variable correction factor is applied to Z+jets. χ^2 minimization of the W lepton
 707 p_T spectrum is performed to derive a correction factor of $1.53 - 6.6 * 10^{-6}(\text{lep}_\text{Pt}_W)$.

708 The uncertainty in the Z + jets prediction is evaluated by comparing data to MC for each
 709 of the continuous b-tag WPs. For each of the regions considered, the data falls within 25% of
 710 the MC prediction once this correction factor has been applied. Therefore, a 25% systematic
 711 uncertainty is applied to Z + jets in the analysis.

712 9 tZ Separation Multivariate Analysis

713 An important process to consider in this analysis is tZ: the top almost always decays into a W
 714 boson and b-quark, and when both the W and Z decay leptonically, this gives three leptons and
 715 a heavy flavor jet in the final state. Because tZ can produce a final state identical to the signal,
 716 it represents a predominant background in the most signal enriched regions. That is, the region
 717 with one jet passing the 60% DL1r WP. Therefore, a boosted decision tree (BDT) algorithm is
 718 trained using XGBoost [27] to separate WZ + heavy flavor from tZ. The result of this BDT is

⁷¹⁹ used to create a tZ enriched region in the fit, reducing its impact on the measurement of WZ +
⁷²⁰ heavy flavor.

⁷²¹ The following kinematic variables are used as inputs to train this BDT:

- ⁷²² • The invariant mass of the reconstructed top candidate
- ⁷²³ • p_T of each of the leptons, jet
- ⁷²⁴ • The invariant mass of each combination of lepton pairs, $M(l\bar{l})$
- ⁷²⁵ • E_T^{miss}
- ⁷²⁶ • Distance between each combination of leptons, $\Delta R(l\bar{l})$
- ⁷²⁷ • Distance between each lepton and the jet, $\Delta R(lj)$

⁷²⁸ Here the top candidate is reconstructed based on the procedure described in section 6.1 of
⁷²⁹ [28]. Broadly, the mass of the top quark candidate is reconstructed from the jet, the lepton not
⁷³⁰ included in the Z-candidate, and a reconstructed neutrino. In the case that there is one jet in the
⁷³¹ event, there is only possible b-jet candidate. For events with two jets, the jet with the highest
⁷³² DL1r score is used.

⁷³³ The training samples included only events meeting the requirements of the 1-jet, >60%
⁷³⁴ region, i.e. passing all the selection described in section 12 and having exactly one jet which
⁷³⁵ passes the tightest (60%) DL1r working point. A sample of 20,000 background (tZ) and signal

736 (WZ+b) Monte Carlo events are used to train the BDT. And additional 5,000 events are reserved
 737 for testing the model, in order to prevent over-fitting. A total of 750 decision trees with a
 738 maximum depth of 6 branches are used to build the model. These parameters are chosen
 739 empirically, by training several models with different parameters and selecting the one that gave
 740 the best separation for the test sample.

741 The results of the BDT training are shown in figure 13.1. The output scores for both signal
 742 and background events is shown on the left. The right shows the receiving operating characteristic
 743 (ROC) curve that results from the MVA. The ROC curve represents the background rejection
 744 as a function of signal efficiency, where each point on the curve represents a different response
 745 score. The ROC curve of the BDT is compared to the performance of using an optimal set of flat
 746 selections on the same set of input variables.

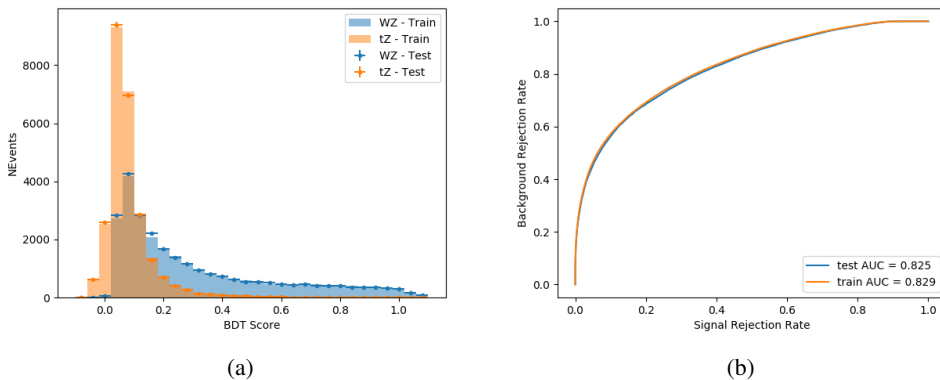


Figure 9.1: Distribution of the BDT response for signal and background events on the left, the ROC curve for the BDT on the right.

747 The relative important of each input feature in the model, measured by how often they
 748 appeared in the decision trees, is shown in figure 13.2.

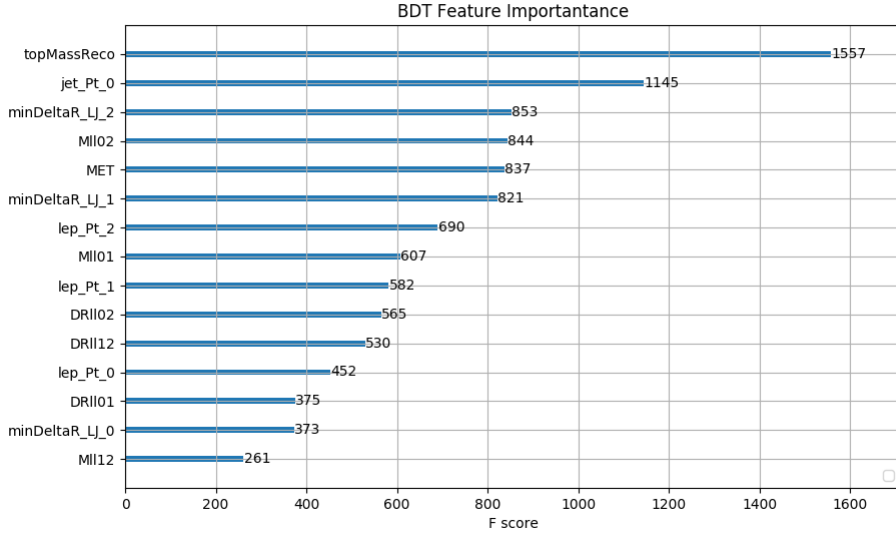


Figure 9.2: Relative importance of each input feature in the model.

749 These results suggest that some amount of separation can be achieved between these two
 750 processes, with a high BDT score selecting a set of events that is pure in $WZ + b$. A BDT score
 751 of 0.725 is selected as a cutoff, where events with scores higher than this form a signal enriched
 752 region, and events with scores lower than this form a $t\bar{Z}$ control region. This cutoff is selected by
 753 varying the value of this cutoff in stat-only Asimov fits, and selecting the value that minimizes
 754 the statistical uncertainty on $WZ + b$.

755 10 Data and Monte Carlo Samples**756 10.1 Data Samples**

757 This study uses a sample of proton-proton collision data collected by the ATLAS detector from
758 2015 through 2018 at an energy of $\sqrt{s} = 13$ TeV, which represents an integrated luminosity of
759 139 fb^{-1} . This data set was collected with a bunch crossing rate of 25 ns. All data used in this
760 analysis was verified by data quality checks.

761 10.2 Monte Carlo Samples

762 Several different generators were used to produce Monte Carlo simulations of the signal and
763 background processes. For all samples, the response of the ATLAS detector is simulated using
764 Geant4. The WZ signal samples are simulated using Sherpa 2.2.2 [15]. Specific information
765 about the Monte Carlo samples being used can be found in Table 22.

Table 8: The configurations used for event generation of signal and background processes, including the event generator, matrix element (ME) order, parton shower algorithm, and parton distribution function (PDF).

Process	Event generator	ME order	Parton Shower	PDF
WZ, VV	SHERPA 2.2.2	MEPS NLO	SHERPA	CT10
tZ	MG5_AMC	NLO	PYTHIA 8	CTEQ6L1
t̄tW	MG5_AMC (SHERPA 2.1.1)	NLO (LO multileg)	PYTHIA 8 (SHERPA)	NNPDF 3.0 NLO (NNPDF 3.0 NLO)
t̄t(Z/γ* → ll)	MG5_AMC	NLO	PYTHIA 8	NNPDF 3.0 NLO
t̄tH	MG5_AMC (MG5_AMC)	NLO (NLO)	PYTHIA 8 (HERWIG++)	NNPDF 3.0 NLO [16] (CT10 [17])
tHqb	MG5_AMC	LO	PYTHIA 8	CT10
tHW	MG5_AMC (SHERPA 2.1.1)	NLO (LO multileg)	HERWIG++ (SHERPA)	CT10 (NNPDF 3.0 NLO)
tWZ	MG5_AMC	NLO	PYTHIA 8	NNPDF 2.3 LO
t̄t̄t, t̄t̄t̄t	MG5_AMC	LO	PYTHIA 8	NNPDF 2.3 LO
t̄tW+W-	MG5_AMC	LO	PYTHIA 8	NNPDF 2.3 LO
t̄t	POWHEG-BOX v2 [18]	NLO	PYTHIA 8	NNPDF 3.0 NLO
t̄tγ	MG5_AMC	LO	PYTHIA 8	NNPDF 2.3 LO
s-, t-channel, Wt single top	POWHEG-BOX v1 [19]	NLO	PYTHIA 6	CT10
qqVV, VVV				
Z → l+l-	SHERPA 2.2.1	MEPS NLO	SHERPA	NNPDF 3.0 NLO

11 Object Reconstruction

All regions defined in this analysis share a common lepton, jet, and overall event preselection.

768 The selection applied to each physics object is detailed here; the event preselection, and the

⁷⁶⁹ selection used to define the various fit regions, is described in Section 12.

All events are required to be selected by dilepton triggers. The p_T thresholds of the

⁷⁷¹ dilepton trigger on two electrons were 12 GeV in 2015, 17 GeV in 2016, and 24 GeV in 2017 and

⁷⁷² 2018, while for the dimuon triggers the p_T thresholds on the leading (sub-leading) muon were

⁷⁷³ 18 GeV (8 GeV) in 2015, and 22 GeV (8 GeV) in 2016-2018. For the electron+muon triggers,
⁷⁷⁴ the p_T thresholds on the electron (muon) were 17 GeV (14 GeV) for all datasets.

⁷⁷⁵ **11.1 Light leptons**

⁷⁷⁶ Electron candidates are reconstructed from energy clusters in the electromagnetic calorimeter
⁷⁷⁷ that are associated with charged particle tracks reconstructed in the inner detector [20]. Electron
⁷⁷⁸ candidates are required to have $p_T > 10$ GeV and $|\eta_{\text{cluster}}| < 2.47$. Muon candidates are
⁷⁷⁹ reconstructed by combining inner detector tracks with track segments or full tracks in the muon
⁷⁸⁰ spectrometer [21]. Muon candidates are required to have $p_T > 10$ GeV and $|\eta| < 2.5$. Candidates
⁷⁸¹ in the transition region between different electromagnetic calorimeter components, $1.37 <$
⁷⁸² $|\eta_{\text{cluster}}| < 1.52$, are rejected. A multivariate likelihood discriminant combining shower shape
⁷⁸³ and track information is used to distinguish real electrons from hadronic showers (fake electrons).
⁷⁸⁴ To further reduce the non-prompt electron contribution, the track is required to be consistent
⁷⁸⁵ with originating from the primary vertex; requirements are imposed on the transverse impact
⁷⁸⁶ parameter significance ($|d_0|/\sigma_{d_0} < 5$) and the longitudinal impact parameter ($|\Delta z_0 \sin \theta_\ell| < 0.5$
⁷⁸⁷ mm). Electron candidates are required to pass TightLH identification.

⁷⁸⁸ Muon candidates are reconstructed by combining inner detector tracks with track segments
⁷⁸⁹ or full tracks in the muon spectrometer [21]. Muon candidates are required to have $p_T > 10$ GeV
⁷⁹⁰ and $|\eta| < 2.5$. The longitudinal impact parameter is the same for both electrons and muons, while

791 muons are required to pass a slightly tighter transverse impact parameter, $|d_0|/\sigma_{d_0} < 3$. Muons
792 are also required to pass Medium ID requirements.

793 Leptons are additionally required to pass a non-prompt BDT selection developed by the
794 $t\bar{t}H$ multilepton/ $t\bar{t}W$ analysis group. This BDT and the WPs used are summarized in Appendix
795 A, and described in detail in [22]. Optimized working points and scale factors for this BDT are
796 taken from that analysis.

797 11.2 Jets

798 Jets are reconstructed from calibrated topological clusters built from energy deposits in the
799 calorimeters [23], using the anti- k_t algorithm with a radius parameter $R = 0.4$. Particle Flow, or
800 PFlow, jets are used in the analysis, which are hadronic objects reconstructed using information
801 from both the tracker and the calorimeter. Jets with energy contributions likely arising from noise
802 or detector effects are removed from consideration [24], and only jets satisfying $p_T > 25$ GeV
803 and $|\eta| < 2.5$ are used in this analysis. For jets with $p_T < 60$ GeV and $|\eta| < 2.4$, a jet-track
804 association algorithm is used to confirm that the jet originates from the selected primary vertex,
805 in order to reject jets arising from pileup collisions [25].

806 11.3 B-tagged Jets

807 In order to make a measurement of $WZ +$ heavy flavor it is necessary to distinguish these events
808 from $WZ +$ light jets. For this purpose, the DL1r b-tagging algorithm is used to distinguish

809 heavy flavor jets from lighter ones. The DL1r algorithm uses jet kinematics, particularly jet
 810 vertex information, as input for a neural network which assigns each jet a score designed to
 811 reflect how likely that jet is to have originated from a b-quark.

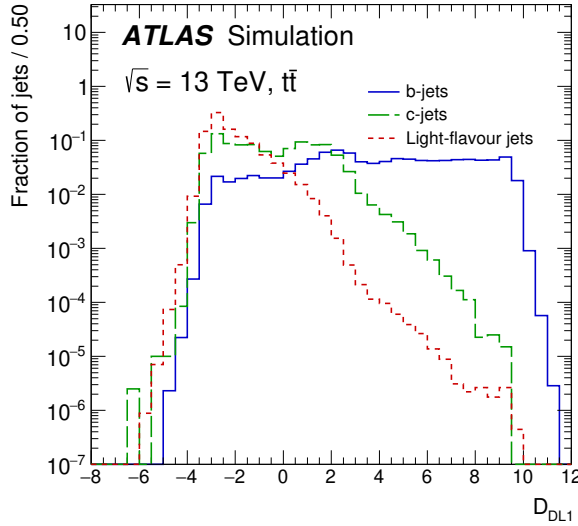


Figure 11.1: Output distribution of the DL1r algorithm for b-jets, charm jets, and light jets

812 From the output of the BDT, calibrated working points (WPs) are developed based on the
 813 efficiency of truth b-jets at particular values of the DL1r algorithm. The working points used in
 814 this analysis are summarized in Table 9.

WP	none	loose	medium	tight	tightest
b eff.	-	85%	77%	70%	60%

Table 9: B-tagging Working Points by tightness and b-jet efficiency

815 A tighter WP will accept fewer b-jets, but reject a higher fraction of charm and light jets.
 816 Generally, analyses that include b-jets will use a fixed working point, for example, requiring that

817 a jet pass the 70% threshold. By instead treating these working point as bins, e.g. events with
818 jets that fall between the 85% and 77% WPs fall into one bin, while events with jets passing the
819 60% WP fall into another, and looking at the full psuedo-continuous DL1r spectrum of the jets,
820 additional information can be gained. The psuedo-continuous b-tag spectrum is used in this case
821 to separate out $WZ + b$, $WZ + \text{charm}$, and $WZ + \text{light}$.

822 **11.4 Missing transverse energy**

823 Missing transverse momentum (E_T^{miss}) is used as part of the event selection. The missing
824 transverse momentum vector is defined as the inverse of the sum of the transverse momenta of
825 all reconstructed physics objects as well as remaining unclustered energy, the latter of which is
826 estimated from low- p_T tracks associated with the primary vertex but not assigned to a hard object,
827 with object definitions taken from [26]. Light leptons considered in the E_T^{miss} reconstruction are
828 required to have $p_T > 10$ GeV, while jets are required to have $p_T > 20$ GeV.

829 **11.5 Overlap removal**

830 To avoid double counting objects and remove leptons originating from decays of hadrons, overlap
831 removal is performed in the following order: any electron candidate within $\Delta R = 0.1$ of another
832 electron candidate with higher p_T is removed; any electron candidate within $\Delta R = 0.1$ of a muon
833 candidate is removed; any jet within $\Delta R = 0.3$ of an electron candidate is removed; if a muon

⁸³⁴ candidate and a jet lie within $\Delta R = \min(0.4, 0.04 + 10[\text{GeV}]/p_T(\text{muon}))$ of each other, the jet
⁸³⁵ is kept and the muon is removed.

⁸³⁶ This algorithm is applied to the preselected objects. The overlap removal procedure is
⁸³⁷ summarized in Table 23.

Keep	Remove	Cone size (ΔR)
electron	electron (low p_T)	0.1
muon	electron	0.1
electron	jet	0.3
jet	muon	$\min(0.4, 0.04 + 10[\text{GeV}]/p_T(\text{muon}))$
electron	tau	0.2

Table 10: Summary of the overlap removal procedure between electrons, muons, and jets.

⁸³⁸ 12 Event Selection and Signal Region Definitions

⁸³⁹ Event are required to pass a preselection described in Section 12.1 and summarized in Table 11.
⁸⁴⁰ Those that pass this preselection are divided into various fit regions described in Section 12.2,
⁸⁴¹ based on the number of jets in the event, and the b-tag score of those jets.

⁸⁴² 12.1 Event Preselection

⁸⁴³ Events are required to include exactly three reconstructed light leptons passing the requirement
⁸⁴⁴ described in 11.1, which have a total charge of ± 1 .

845 The leptons are ordered in the analysis code as 0, 1, and 2. Lepton 0 is the lepton whose
 846 charge is opposite the other two. Lepton 1 is the lepton closest to the opposite charge lepton, i.e.
 847 the smallest ΔR , leaving lepton 2 as the lepton further from the opposite charge lepton. Lepton
 848 0 is required to have $p_T > 10$ GeV, while the same sign leptons, 1 and 2, are required to have
 849 $p_T > 20$ GeV to reduce the contribution of non-prompt leptons.

850 The invariant mass of at least one pair of opposite sign, same flavor leptons is required
 851 to fall within 10 GeV of the mass of the Z boson, 91.2 GeV. Events where one of the opposite
 852 sign pairs have an invariant mass less than 12 GeV are rejected in order to suppress low mass
 853 resonances.

854 An additional requirement is placed on the missing transverse energy, $E_T^{\text{miss}} > 20$ GeV,
 855 and the transverse mass of the W candidate, $m(E_T^{\text{miss}} + l_{\text{other}}) > 30$ GeV, where E_T^{miss} is the
 856 missing transverse energy, and l_{other} is the lepton not included in the Z-candidate.

857 Events are required to have one or two reconstructed jets passing the selection described
 858 in Section 11.2. Events with more than two jets are rejected in order to reduce the contribution
 859 of backgrounds such as $t\bar{t}Z$ and $t\bar{t}W$, which tend to have higher jet multiplicity.

Event Selection

- Exactly three leptons with charge ± 1
 - Two same-charge leptons with $p_T > 20$ GeV
 - One opposite charge lepton with $p_T > 10$ GeV
 - $m(l^+l^-)$ within 10 GeV of 91.2 GeV
 - Transverse mass of W-candidate, $m_T(E_T^{\text{miss}} + \text{lep}_{\text{other}}) > 30$ GeV
 - Missing transverse energy, $E_T^{\text{miss}} > 20$ GeV
 - One or two jets with $p_T > 25$ GeV
-

Table 11: Summary of the selection applied to events for inclusion in the fit

860 The event yields in the preselection region for both data and Monte Carlo are summarized
 861 in Table 12.1, which shows good agreement between data and Monte Carlo, and demonstrates
 862 that this region consists primarily of WZ events. The WZ events are split into WZ + b, WZ +
 863 c, and WZ + l based on the truth flavor of the associated jet in the event. In this ordering b-jet
 864 supersede charm, which supersides light. That is, WZ + l events contain no charm and no b jets
 865 at truth level, WZ + c contain at least one truth charm and no b-jets, and WZ + b contains at least
 866 one truth b-jet.

Process	Events
WZ + b	167.6 ± 6.5
WZ + c	1080 ± 40
WZ + l	7220 ± 310
Other VV	850 ± 140
$t\bar{t}W$	16.8 ± 2.3
$t\bar{t}Z$	115 ± 17
rare Top	2.2 ± 0.1
Single top	0.10 ± 0.45
Three top	0.01 ± 0.01
Four top	0.02 ± 0.01
$t\bar{t}WW$	0.23 ± 0.05
Z + jets	600 ± 260
V + γ	37 ± 54
tZ	190 ± 70
tW	5.5 ± 1.2
WtZ	25.8 ± 1.1
VVV	26.2 ± 0.9
VH	94 ± 7
t \bar{t}	108.68 ± 8
t $\bar{t}H$	4.3 ± 0.5
Total	10600 ± 530
Data	10574

Table 12: Event yields in the preselection region at 139.0 fb^{-1}

867 Here Other VV represents diboson processes other than WZ, and consists predominantly

868 of $ZZ \rightarrow ll\bar{l}\bar{l}$ events where one of the leptons is not reconstructed.

869 12.2 Fit Regions

870 Once preselection has been applied, the remaining events are categorized into one of twelve
871 orthogonal regions. The regions used in the fit are summarized in Table 13.

Table 13: A list of the regions used in the fit and the selection used for each.

Region	Selection
1j, <85%	$N_{\text{jets}} = 1, n\text{Jets_DL1r_85} = 0$
1j, 85%-77%	$N_{\text{jets}} = 1, n\text{Jets_DL1r_85} = 1, n\text{Jets_DL1r_77}=0$
1j, 77%-70%	$N_{\text{jets}} = 1, n\text{Jets_DL1r_77} = 1, n\text{Jets_DL1r_70}=0$
1j, 70%-60%	$N_{\text{jets}} = 1, n\text{Jets_DL1r_70} = 1, n\text{Jets_DL1r_60}=0$
1j, >60%	$N_{\text{jets}} = 1, n\text{Jets_DL1r_60} = 1, tZ \text{ BDT} > 0.725$
1j tZ CR	$N_{\text{jets}} = 1, n\text{Jets_DL1r_60} = 1, tZ \text{ BDT} < 0.725$
2j, <85%	$N_{\text{jets}} = 2, n\text{Jets_DL1r_85} = 0$
2j, 85%-77%	$N_{\text{jets}} = 2, n\text{Jets_DL1r_85} >= 1, n\text{Jets_DL1r_77}=0$
2j, 77%-70%	$N_{\text{jets}} = 2, n\text{Jets_DL1r_77} >= 1, n\text{Jets_DL1r_70}=0$
2j, 70%-60%	$N_{\text{jets}} = 2, n\text{Jets_DL1r_70} >= 1, n\text{Jets_DL1r_60}=0$
2j, >60%	$N_{\text{jets}} = 2, n\text{Jets_DL1r_60} >= 1, tZ \text{ BDT} > 0.725$
2j tZ CR	$N_{\text{jets}} = 2, n\text{Jets_DL1r_60} >= 1, tZ \text{ BDT} < 0.725$

872 The working points discussed in Section 11.3 are used to separate events into fit regions
873 based on the highest working point reached by a jet in each event. Because the background
874 composition differs significantly based on the number of b-jets, events are further subdivided
875 into 1-jet and 2-jet regions in order to minimize the impact of background uncertainties.

876 An unfolding procedure is performed to account for differences in the number of recon-
877 structed jets compared to the number of truth jets in each event. In order to account for migration

878 of WZ+1-jet and WZ+2-jet events between the 1-jet and 2-jet bins at reco level, the signal
 879 samples are separated based on the number of truth jets. Events with 0 jets or more than 3 jets at
 880 truth level, yet fall within one of the categories listed in Table 13, are categorized as WZ + other,
 881 and treated as a background. The composition of the number of truth jets in each reco jet bin is
 882 taken from MC, with uncertainties in these estimates described in detail in Section 20.

883 An additional tZ control region is created based on the BDT described in Section 13. The
 884 region with 1-jet passing the 60% working point is split in two - a signal enriched region of
 885 events with a BDT score greater than 0.03, and a tZ control region including events with less
 886 than 0.03. This cutoff is arrived at by performing an Asimov fit with a variety of cutoffs, and
 887 selecting the value that produces the highest significance for the measurement of WZ + b.

888 **12.3 Non-Prompt Lepton Estimation**

889 Two processes act as sources of non-prompt leptons appear in the analysis: $t\bar{t}$ and Z+jet
 890 production both produce two prompt leptons, and each contribute to the 31 region when an
 891 additional non-prompt lepton appears in the event. The contribution of these processes is
 892 estimated with Monte Carlo simulations, which are validated using enriched control regions.

893 The modelling in the Z+jets and $t\bar{t}$ CRs is further validated for each of the pseudo-
 894 continuous b-tag regions used in the analysis. The relevant lepton p_T spectrum in each b-tag
 895 region is shown in Appendix B.1 for these CRs after the correction factors derived below have
 896 been applied.

897 **12.3.1 $t\bar{t}$ Validation**

898 $t\bar{t}$ events can produce two prompt leptons from the decay of each of the tops. These top decays
899 produce two b-quarks, the decay of which can produce additional non-prompt leptons, which
900 occasionally pass the event preselection. In order to validate that the Monte Carlo accurately
901 simulates this process accurately, the MC prediction in a non-prompt $t\bar{t}$ enriched control region
902 is compared to data.

903 The $t\bar{t}$ control region is similar to the preselection region - three leptons meeting the
904 criteria described in Section 12 are required, and the requirements on E_T^{miss} remain the same.
905 However, the selection requiring a lepton pair form a Z-candidate are reversed. Events where the
906 invariant mass of any two opposite sign, same flavor leptons falls within 10 GeV of 91.2 GeV are
907 rejected. This ensures the $t\bar{t}$ control region is orthogonal to the preselection region.

908 Further, because the jet multiplicity of $t\bar{t}$ events tends to be higher than WZ, the number
909 of jets in each event is required to be greater than 1. As b-jets are almost invariably produced
910 from top decays, at least one b-tagged jet passing the 70% DL1r WP in each event is required.

911 Data is compared to MC predictions in the region for a variety of kinematic variable, as well
912 as various b-tag WPs. A constant normalization discrepancy between data and MC predictions
913 of approximately 10% is found, which is accounted for by applying a constant correction factor
914 of 0.9 to the $t\bar{t}$ MC prediction. As data and MC are found to agree within 20% for each of
915 the b-tag WPs considered, a 20% systematic uncertainty on the $t\bar{t}$ prediction is included for the
916 analysis.

917 **12.3.2 Z+jets Validation**

918 Similar to $t\bar{t}$, a non-prompt Z +jets control region is produced in order to validate the MC
 919 predictions. The lepton requirements remain the same as the preselection region. Because no
 920 neutrinos are present for this process, the E_T^{miss} cut is reversed, requiring $E_T^{\text{miss}} < 30 \text{ GeV}$. This
 921 also ensures this control region is orthogonal to the preselection region. Further, the number of
 922 jets in each event is required to be greater than or equal to one.

923 While there is general agreement between data and MC within statistical uncertainty, the
 924 shape of the p_T spectrum of the lepton from the W is found to differ. To account for this
 925 discrepancy, a variable correction factor is applied to Z +jets. χ^2 minimization of the W lepton
 926 p_T spectrum is performed to derive a correction factor of $1.53 - 6.6 * 10^{-6}(\text{lep}_\text{Pt}_W)$.

927 The uncertainty in the $Z + \text{jets}$ prediction is evaluated by comparing data to MC for each
 928 of the continuous b-tag WPs. For each of the regions considered, the data falls within 25% of
 929 the MC prediction once this correction factor has been applied. Therefore, a 25% systematic
 930 uncertainty is applied to $Z + \text{jets}$ in the analysis.

931 **13 tZ Interference Studies and Separation Multivariate Analysis**

932 An important process to consider in this analysis is tZ : the top almost always decays into a W
 933 boson and b-quark, and when both the W and Z decay leptonically, this gives three leptons and
 934 a heavy flavor jet in the final state. Because tZ can produce a final state identical to the signal,

935 it represents a predominant background in the most signal enriched regions. That is, the region
 936 with one jet passing the 60% DL1r WP. Therefore, a boosted decision tree (BDT) algorithm is
 937 trained using XGBoost [27] to separate WZ + heavy flavor from tZ. The result of this BDT is
 938 used to create a tZ enriched region in the fit, reducing its impact on the measurement of WZ +
 939 heavy flavor.

940 The following kinematic variables are used as inputs to train this BDT:

- 941 • The invariant mass of the reconstructed top candidate
- 942 • p_T of each of the leptons, jet
- 943 • The invariant mass of each combination of lepton pairs, $M(l\bar{l})$
- 944 • E_T^{miss}
- 945 • Distance between each combination of leptons, $\Delta R(l\bar{l})$
- 946 • Distance between each lepton and the jet, $\Delta R(lj)$

947 Here the top candidate is reconstructed based on the procedure described in section 6.1 of
 948 [28]. Broadly, the mass of the top quark candidate is reconstructed from the jet, the lepton not
 949 included in the Z-candidate, and a reconstructed neutrino. In the case that there is one jet in the
 950 event, there is only possible b-jet candidate. For events with two jets, the jet with the highest
 951 DL1r score is used.

952 The training samples included only events meeting the requirements of the 1-jet, >60%
953 region, i.e. passing all the selection described in section 12 and having exactly one jet which
954 passes the tightest (60%) DL1r working point. A sample of 20,000 background (tZ) and signal
955 (WZ+b) Monte Carlo events are used to train the BDT. And additional 5,000 events are reserved
956 for testing the model, in order to prevent over-fitting. A total of 750 decision trees with a
957 maximum depth of 6 branches are used to build the model. These parameters are chosen
958 empirically, by training several models with different parameters and selecting the one that gave
959 the best separation for the test sample.

960 The results of the BDT training are shown in figure 13.1. The output scores for both signal
961 and background events is shown on the left. The right shows the receiving operating characteristic
962 (ROC) curve that results from the MVA. The ROC curve represents the background rejection
963 as a function of signal efficiency, where each point on the curve represents a different response
964 score. The ROC curve of the BDT is compared to the performance of using an optimal set of flat
965 selections on the same set of input variables.

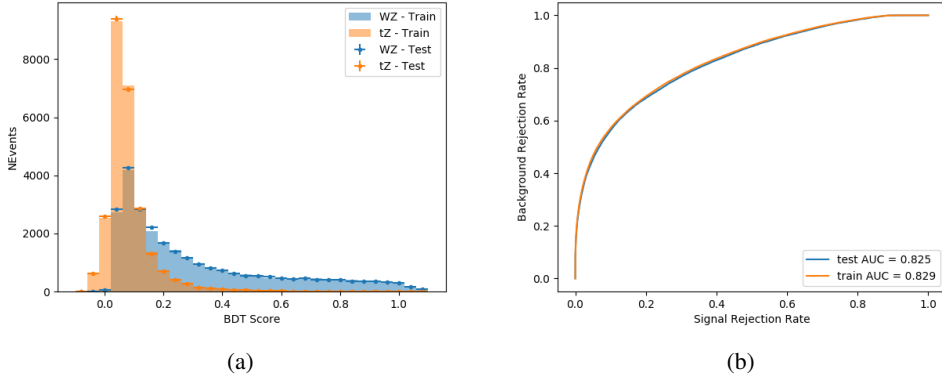


Figure 13.1: Distribution of the BDT response for signal and background events on the left, the ROC curve for the BDT on the right.

966 The relative important of each input feature in the model, measured by how often they
 967 appeared in the decision trees, is shown in figure 13.2.

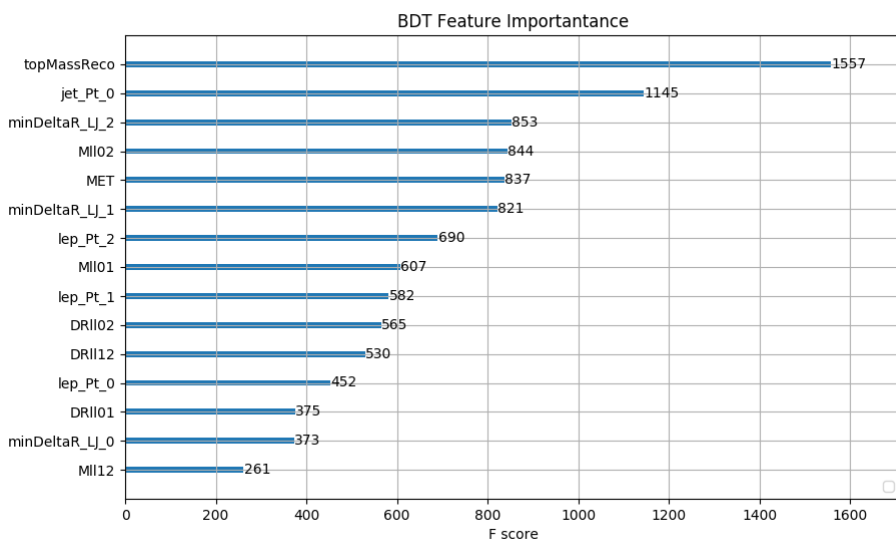


Figure 13.2: Relative importance of each input feature in the model.

968 These results suggest that some amount of separation can be achieved between these two
969 processes, with a high BDT score selecting a set of events that is pure in $WZ + b$. A BDT score
970 of 0.725 is selected as a cutoff, where events with scores higher than this form a signal enriched
971 region, and events with scores lower than this form a $t\bar{Z}$ control region. This cutoff is selected by
972 varying the value of this cutoff in stat-only Asimov fits, and selecting the value that minimizes
973 the statistical uncertainty on $WZ + b$.

974 **14 Systematic Uncertainties**

975 The systematic uncertainties that are considered are summarized in Table 43. These are imple-
976 mented in the fit either as a normalization factors or as a shape variation or both in the signal
977 and background estimations. The numerical impact of each of these uncertainties is outlined in
978 Section 21.

Table 14: Sources of systematic uncertainty considered in the analysis.

Systematic uncertainty	Components
Luminosity	1
Pileup reweighting	1
Physics Objects	
Electron	6
Muon	15
Jet energy scale	28
Jet energy resolution	8
Jet vertex fraction	1
Jet flavor tagging	131
E_T^{miss}	3
Total (Experimental)	194
Signal Modeling	
Shape modelling	3
Renormalization and factorization scales	5
nJet Migration	5
Background Modeling	
Cross section	15
Renormalization and factorization scales	12
Total (Signal and background modeling)	35
Total (Overall)	230

979 The uncertainty in the combined integrated luminosity is derived from a calibration of the
 980 luminosity scale performed for 13 TeV proton-proton collisions [29], [30].

981 The experimental uncertainties are related to the reconstruction and identification of light
 982 leptons and b-tagging of jets, and to the reconstruction of E_T^{miss} . The sources which contribute to
 983 the uncertainty in the jet energy scale (JES) [31] are decomposed into uncorrelated components
 984 and treated as independent sources of uncertainty in the analysis. These are treated as 30
 985 nuisance parameters included in the fit. A similar approach is used for the jet energy resolution

986 (JER) uncertainty, which is decomposed into 8 JER uncertainty components included as NPs in
987 the fit.

988 The uncertainties in the b-tagging efficiencies measured in dedicated calibration analyses
989 [32] are also decomposed into uncorrelated components. The large number of components for
990 b-tagging is due to the calibration of the distribution of the MVA discriminant.

991 Theoretical uncertainties applied to MC predictions, including cross section, PDF, and scale
992 uncertainties are taken from theory calculations, with the exception of non-prompt and dibo-
993 son backgrounds. The cross-section uncertainty on tZ is taken from [33]. Derivation of the
994 non-prompt background uncertainties, Z+jets and tt>, are explained in Section 12.3. These
995 normalization uncertainties are chosen so as to account for the complete uncertainty in the
996 non-prompt contribution, and therefore no additional modelling uncertainties are considered for
997 Z+jets and tt>.

998 The other VV + heavy flavor processes (namely VV+b and VV+charm, which primarily
999 consist of ZZ events) are also poorly understood, because these processes involve the same
1000 physics as WZ + heavy flavor, and have also not been measured. Therefore, a conservative 50%
1001 uncertainty is applied to those samples. While this uncertainty is large, it is found to have little
1002 impact on the significance of the final result.

1003 The theory uncertainties applied to the predominate background estimates are summarized
1004 in Table 45.

Process	X-section [%]
tZ	X-sec: ± 15.2 QCD Scale: $^{+5.2}_{-1.3}$ PDF($+\alpha_S$): ± 1.2
t̄t H (aMC@NLO+Pythia8)	QCD Scale: $^{+5.8}_{-9.2}$ PDF($+\alpha_S$): ± 3.6
t̄t Z (aMC@NLO+Pythia8)	QCD Scale: $^{+9.6}_{-11.3}$ PDF($+\alpha_S$): ± 4
t̄t W (aMC@NLO+Pythia8)	QCD Scale: $^{+12.9}_{-11.5}$ PDF($+\alpha_S$): ± 3.4
VV + b/charm (Sherpa 2.2.1)	± 50
VV + light (Sherpa 2.2.1)	± 6
t̄t	± 20
Z + jets	± 25
Others	± 50

Table 15: Summary of theoretical uncertainties for MC predictions in the analysis.

1005 Additional signal uncertainties are estimated by comparing estimates from the nominal Sherpa
 1006 WZ samples with alternate WZ samples generated with Powheg+PYTHIA8. Separate systemat-
 1007 ics are included in the fit for WZ + b, WZ + charm and WZ + light, where the distribution among
 1008 each of the fit regions is varied based on the prediction of the Powheg sample.

1009 A similar approach is taken to account for uncertainties in migrations between the number of
 1010 reco and truth jets. The fraction of events with 1 truth jet which fall into the 1 jet bin versus the
 1011 2 jet bin at reco level is compared for Sherpa and Powheg. The same is done for events with 2
 1012 truth jets. A systematic is included where events are shifted between the 1-jet and 2-jet regions
 1013 based on the differences between these two shapes. This is done independently for each of the
 1014 WZ + b, WZ + charm, and WZ + light templates.

1015 Additional systematics are included to account for the uncertainty in the contamination of
 1016 0 jet and 3 or more jet events (as defined at truth level) in the 1 and 2 reco jet bins. Because these
 1017 events fall outside the scope of this measurement, these events are included as a background.
 1018 As such, a normalization, rather than a shape, uncertainty is applied for this background. The
 1019 number of WZ events with 0-jets and $>=3$ -jets in the reconstructed 1-jet and 2-jet regions are
 1020 compared for Sherpa and Powheg, and these differences are taken as separate normalization
 1021 systematics on the yield of WZ+0-jet and WZ+ $>=3$ -jet events.

1022 15 Results

1023 A separate maximum-likelihood fit is performed over the 1-jet and 2-jet fit regions in order to
 1024 extract the best-fit value of the WZ + b-jet and WZ + charm jet contributions. The WZ + b,
 1025 WZ + charm and WZ + light contributions are allowed to float, with the remaining background
 1026 contributions are held fixed. **The current fit strategy treats the WZ + b-jet contribution as**
 1027 **the parameter of interest, with the normalization of the WZ + charm and the WZ + light**
 1028 **contributions taken as systematic uncertainties. This could however be adjusted, depending**
 1029 **on whether it is decided the goal of the analysis should be to measure WZ+b specifically or**
 1030 **WZ + heavy flavor overall.** The result of the fit is used to extract the cross-section of WZ +
 1031 heavy-flavor production.

1032 A maximum likelihood fit to data is performed simultaneously in the regions described
 1033 in Section 12. The parameters μ_{WZ+b} , $\mu_{WZ+charm}$, $\mu_{WZ+light}$, where $\mu = \sigma_{\text{observed}}/\sigma_{\text{SM}}$, are

1034 extracted from the fit.

1035 The Asimov fit for 1-jet events gives an expected μ value of $1.00^{+0.37}_{-0.35}(\text{stat})^{+0.24}_{-0.22}(\text{sys})$ for
 1036 WZ + b. The fitted cross-section modifiers for WZ + charm and WZ + light are $1.00 \pm 0.17 \pm 0.15$
 1037 and $1.00 \pm 0.04 \pm 0.07$, respectively.

1038 The expected cross-section of WZ+b with 1 associated jet obtained from the fit is
 1039 $1.74^{+0.65}_{-0.61}(\text{stat})^{+0.42}_{-0.37}(\text{sys})$ fb with an expected significance of 2.2σ . The expected cross-sectin
 1040 of WZ + charm is measured to be $14.6 \pm 2.5(\text{stat}) \pm 2.1(\text{sys})$ fb, with a correlation of -0.23.

1041 For 2-jet events, the fit gives an expected μ value of $1.00^{+0.34}_{-0.33}(\text{stat})^{+0.29}_{-0.28}(\text{sys})$ for WZ +
 1042 b. The fitted cross-section modifiers for WZ + charm and WZ + light are $1.00 \pm 0.17 \pm 0.15$ and
 1043 $1.00 \pm 0.04 \pm 0.08$, respectively.

1044 The expected WZ + b cross-section in the 2-jet region is $2.46^{+0.83}_{-0.81}(\text{stat})^{+0.073}_{-0.68}(\text{sys})$ fb
 1045 with an expected significance of 2.6σ . The 2-jet expected cross-section of WZ + charm is
 1046 $12.7 \pm 2.2(\text{stat}) \pm 2.0(\text{sys})$ fb, and the correlation between WZ + charm and WZ + b is -0.26.

1047 15.1 1-jet Fit Results

1048 **The results of the fit are currently blinded.**

1049 The pre-fit yields in each of the regions used in the fit are shown in Table 15.1, and
 1050 summarized in Figure 15.1.

Sample	1j, <85% WP	1j, 77%-85% WP	1j, 70%-77% WP	1j, 60%-70% WP	1j, >60% WP	tZ CR
WZ + b - 1j	8.1 ± 1.6	4.7 ± 0.5	4.6 ± 0.4	5.1 ± 0.4	18.2 ± 2.4	4.8 ± 0.6
WZ + c - 1j	260 ± 22	81 ± 6	43.1 ± 3.6	25.8 ± 2.6	9.4 ± 1.8	2.9 ± 0.6
WZ + l - 1j	3090 ± 250	91 ± 13	17 ± 3	4.9 ± 1.6	1.3 ± 0.4	0.2 ± 0.1
WZ + b - 2j	1.10 ± 0.37	0.44 ± 0.11	0.39 ± 0.06	0.62 ± 0.14	2.1 ± 0.5	0.59 ± 0.14
WZ + c - 2j	21 ± 5	5.6 ± 1.2	3.0 ± 0.7	2.0 ± 0.5	0.70 ± 0.20	0.30 ± 0.08
WZ + l - 2j	250 ± 60	5.7 ± 1.6	0.73 ± 0.53	0.31 ± 0.15	0.07 ± 0.06	0.01 ± 0.01
WZ - Other	13 ± 5	1.4 ± 0.4	0.42 ± 0.08	0.2 ± 0.01	0.30 ± 0.05	0.67 ± 0.15
Other VV	6.2 ± 0.6	0.2 ± 0.4	0.2 ± 0.04	0.07 ± 0.1	0.1 ± 0.1	0.1 ± 0.2
ZZ	336 ± 26	17.8 ± 2.1	4.3 ± 0.6	1.7 ± 0.5	0.36 ± 0.08	0.10 ± 0.03
t̄W	1.1 ± 0.2	0.2 ± 0.1	0.3 ± 0.1	0.4 ± 0.1	1.5 ± 0.3	0.7 ± 0.2
t̄Z	6.8 ± 1.2	1.4 ± 0.3	1.0 ± 0.2	1.2 ± 0.2	4.4 ± 0.8	3.2 ± 0.6
Z + jets	169 ± 38	8.9 ± 1.9	3.7 ± 0.8	3.3 ± 0.7	3.2 ± 0.7	0.8 ± 0.17
V + γ	45 ± 28	1.9 ± 2.4	0.1 ± 0.1	0.02 ± 0.01	1.0 ± 0.9	0.02 ± 0.03
tZ	24.3 ± 4.3	5.5 ± 1.1	4.1 ± 0.8	5.9 ± 1.1	10.7 ± 2.0	23 ± 4
tW	1.4 ± 0.8	0.2 ± 0.5	0.0 ± 0.2	0.7 ± 0.6	0.26 ± 0.42	0.39 ± 0.41
WtZ	2.3 ± 1.2	0.6 ± 0.3	0.3 ± 0.21	0.27 ± 0.2	1.1 ± 0.7	0.6 ± 0.5
VVV	12.4 ± 0.5	0.93 ± 0.06	0.35 ± 0.03	0.13 ± 0.02	0.14 ± 0.03	0.02 ± 0.01
VH	40 ± 6	2.6 ± 1.4	0.9 ± 0.8	0.7 ± 0.8	0.5 ± 0.6	0.0 ± 0.0
t̄t	12.1 ± 1.6	2.9 ± 0.6	2.5 ± 0.5	2.8 ± 0.5	11.2 ± 1.4	10.9 ± 1.5
t̄tH	0.24 ± 0.03	0.05 ± 0.01	0.04 ± 0.01	0.06 ± 0.01	0.20 ± 0.03	0.13 ± 0.02
Total	5010 ± 260	227 ± 24	88 ± 12	57 ± 8	76 ± 16	53 ± 8

Table 16: Pre-fit yields in each of the 1-jet fit regions.

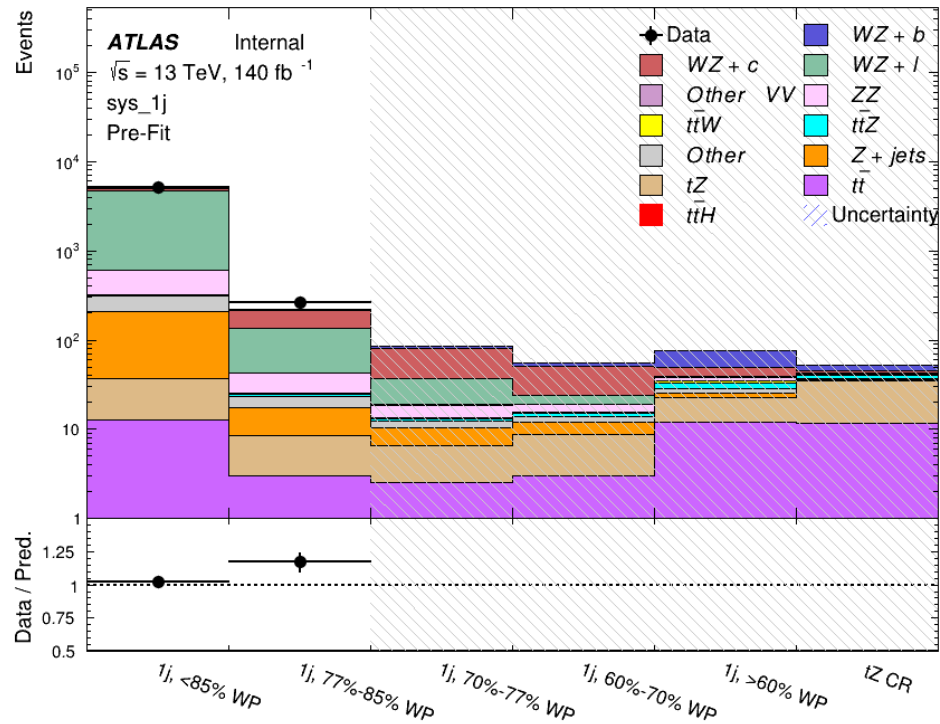


Figure 15.1: Pre-fit summary of the 1-jet fit regions.

1052

The post-fit yields in each region are summarized in Figure 15.1.

1053

	1j, <85% WP	1j, 77%-85% WP	1j, 70%-77% WP	1j, 60%-70% WP	1j, >60% WP	tZ CR
WZ + b	8.1 ± 4.9	4.7 ± 2.0	4.6 ± 2.0	5.1 ± 2.1	18 ± 10	5.0 ± 2.5
WZ + c	260 ± 60	80 ± 14	43 ± 7	26 ± 5	9.4 ± 2.3	2.9 ± 0.7
WZ + l	3090 ± 130	90 ± 11	17.3 ± 2.8	4.9 ± 1.6	1.3 ± 0.4	0.23 ± 0.1
WZ + b - 2j	1.10 ± 0.37	0.44 ± 0.11	0.39 ± 0.06	0.62 ± 0.14	2.1 ± 0.5	0.59 ± 0.1
WZ + c - 2j	21 ± 5	5.6 ± 1.2	3.0 ± 0.7	2.0 ± 0.5	0.70 ± 0.20	0.30 ± 0.0
WZ + l - 2j	250 ± 60	5.7 ± 1.6	0.73 ± 0.53	0.31 ± 0.15	0.07 ± 0.06	0.01 ± 0.0
WZ - Other	13 ± 5	1.4 ± 0.4	0.42 ± 0.08	0.2 ± 0.01	0.30 ± 0.05	0.67 ± 0.1
Other VV	6.2 ± 0.6	0.92 ± 0.07	0.02 ± 0.01	0.01 ± 0.01	0.01 ± 0.01	0.01 ± 0.0
ZZ	346 ± 57	19 ± 5	4.3 ± 0.8	2.7 ± 0.5	2.4 ± 0.1	2.1 ± 0.6
t̄tW	1.09 ± 0.21	0.2 ± 0.1	0.1 ± 0.1	0.4 ± 0.1	1.5 ± 0.3	0.1 ± 0.2
t̄tZ	6.8 ± 1.2	1.4 ± 0.3	1.0 ± 0.2	1.2 ± 0.2	4.4 ± 0.7	3.2 ± 0.5
rare Top	0.14 ± 0.04	0.04 ± 0.02	0.04 ± 0.0	0.1 ± 0.03	0.14 ± 0.04	0.15 ± 0.0
t̄tWW	0.04 ± 0.03	0.01 ± 0.02	0.01 ± 0.01	0.01 ± 0.01	0.01 ± 0.02	0.01 ± 0.0
Z + jets	169 ± 37	8.9 ± 1.9	3.7 ± 0.8	3.3 ± 0.7	3.2 ± 0.7	0.8 ± 0.2
W + jets	0.01 ± 0.01	0.01 ± 0.0				
V + γ	46 ± 28	1.9 ± 2.4	0.1 ± 0.1	0.0 ± 0.2	1.0 ± 0.9	0.0 ± 0.0
tZ	24 ± 4	5.5 ± 1.0	4.1 ± 0.8	5.9 ± 1.1	10.7 ± 1.8	23.3 ± 3.7
tW	1.37 ± 0.82	0.18 ± 0.26	0.01 ± 0.12	0.67 ± 0.64	0.26 ± 0.42	0.39 ± 0.4
WtZ	2.3 ± 1.2	0.6 ± 0.3	0.3 ± 0.2	0.3 ± 0.2	1.1 ± 0.6	0.6 ± 0.3
VVV	12.4 ± 0.4	0.9 ± 0.1	0.4 ± 0.1	0.13 ± 0.02	0.14 ± 0.03	0.02 ± 0.0
VH	40 ± 6	2.6 ± 1.4	0.9 ± 0.8	0.7 ± 0.8	0.4 ± 0.6	0.01 ± 0.0
t̄t	12.1 ± 1.6	2.9 ± 0.6	2.5 ± 0.5	2.8 ± 0.5	11.2 ± 1.5	10.9 ± 1.4
t̄tH	0.24 ± 0.03	0.05 ± 0.01	0.04 ± 0.01	0.06 ± 0.01	0.20 ± 0.03	0.13 ± 0.0
Total	5100 ± 110	227 ± 12	87 ± 6	56.7 ± 4.4	76 ± 9	52.5 ± 4.2

Table 17: Post-fit yields in each of the 1-jet fit regions.

1054

A post-fit summary plot of the 1-jet fitted regions is shown in Figure 15.2:

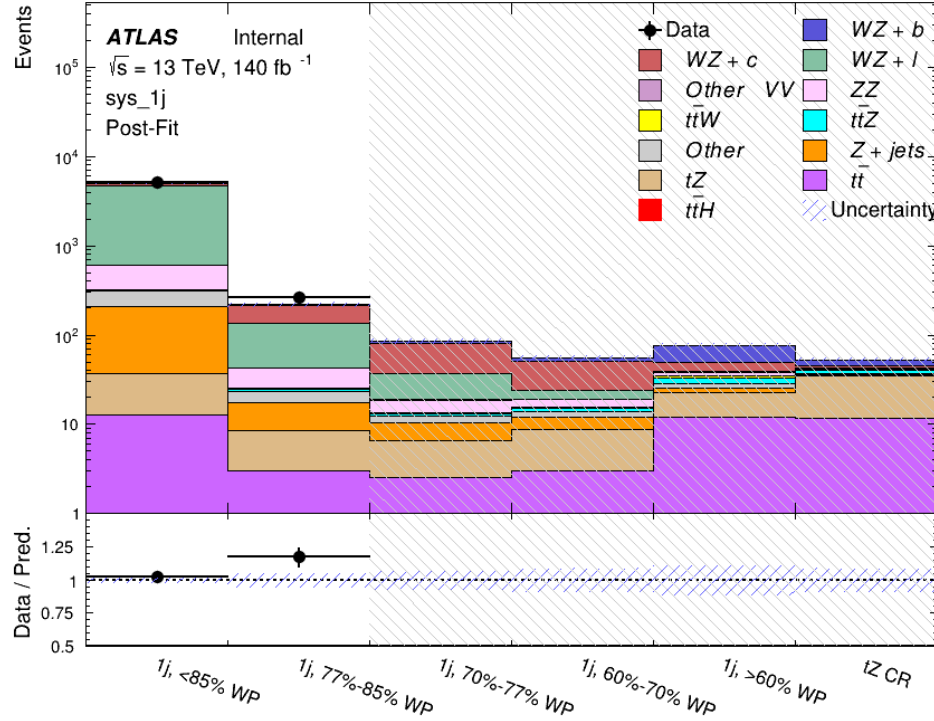


Figure 15.2: Post-fit summary of the 1-jet fit regions.

1055 As described in Section 20, there are 226 systematic uncertainties that are considered
 1056 as NPs in the fit. These NPs are constrained by Gaussian or log-normal probability density
 1057 functions. The latter are used for normalisation factors to ensure that they are always positive.
 1058 The expected number of signal and background events are functions of the likelihood. The prior
 1059 for each NP is added as a penalty term, decreasing the likelihood as it is shifted away from its
 1060 nominal value.

1061 The impact of each NP is calculated by performing the fit with the parameter of interest held
 1062 fixed, varied from its fitted value by its uncertainty, and calculating $\Delta\mu$ relative to the baseline

1063 fit. The impact of the most significant sources of systematic uncertainties is summarized in Table

1064 [18.](#)

Uncertainty Source	$\Delta\mu$	
WZ + light cross-section	0.13	-0.12
WZ + charm cross-section	-0.10	0.12
Jet Energy Scale	0.08	0.13
tZ cross-section	-0.10	0.10
Jet Energy Resolution	-0.10	0.10
Luminosity	-0.08	0.09
Other Diboson + b cross-section	-0.07	0.07
Flavor tagging	0.05	0.05
t <bar>t} cross-section</bar>	-0.05	0.05
WZ cross-section - QCD scale	-0.04	0.03
Total Systematic Uncertainty	0.28	0.32

Table 18: Summary of the most significant sources of systematic uncertainty on the measurement of WZ + b with exactly one associated jet.

1065 The ranking and impact of those nuisance parameters with the largest contribution to the

1066 overall uncertainty is shown in Figure [15.3](#).

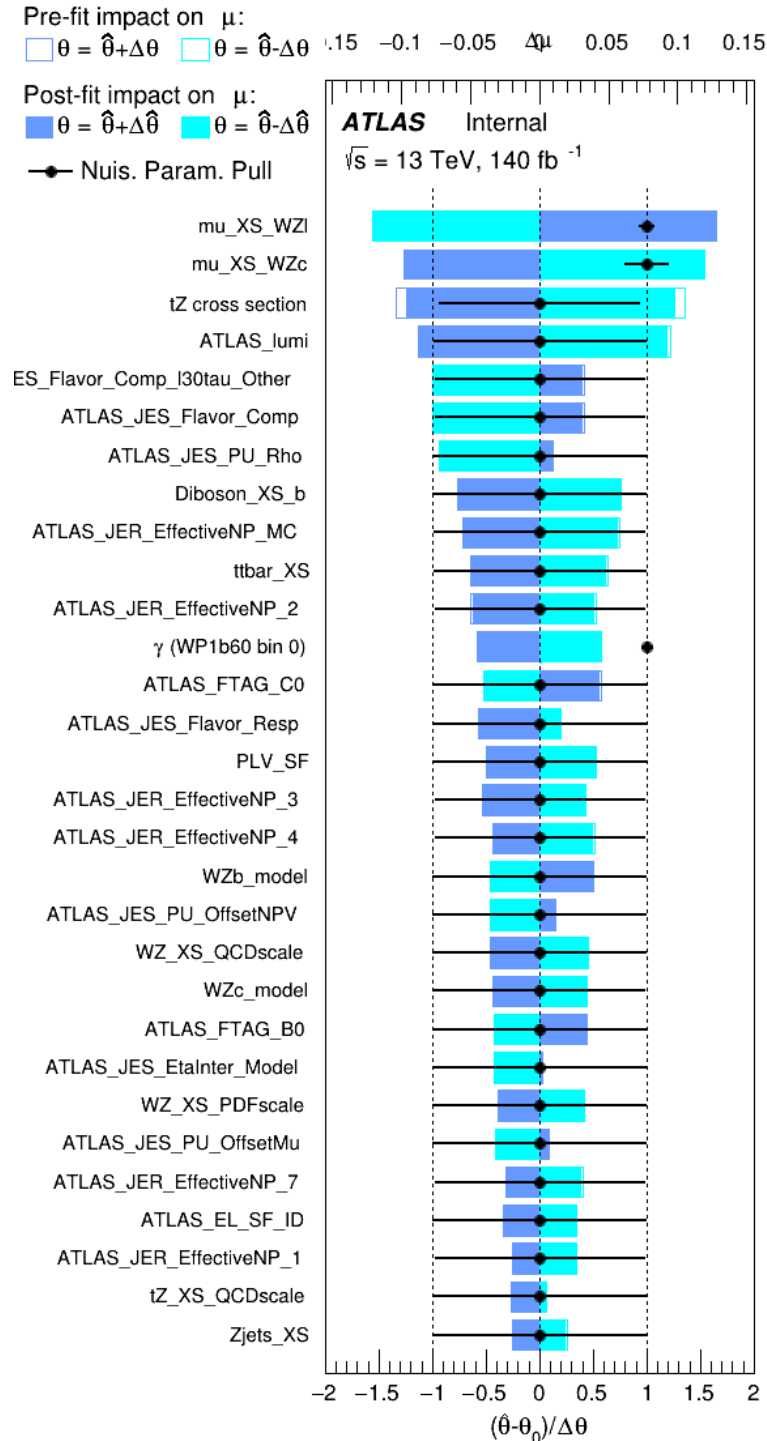


Figure 15.3: Impact of systematic uncertainties on the signal-strength of $WZ + b$ for events with exactly one jet

1067 The large impact of the Jet Energy Scale and Jet Flavor Tagging is unsurprising, as the
1068 shape of the fit regions depends heavily on the modeling of the jets. The other major sources
1069 of uncertainty come from background modelling and cross-section uncertainty. The pie charts
1070 in Figure 15.4 show that for the modelling uncertainties that contribute most correspond to the
1071 most significant backgrounds.

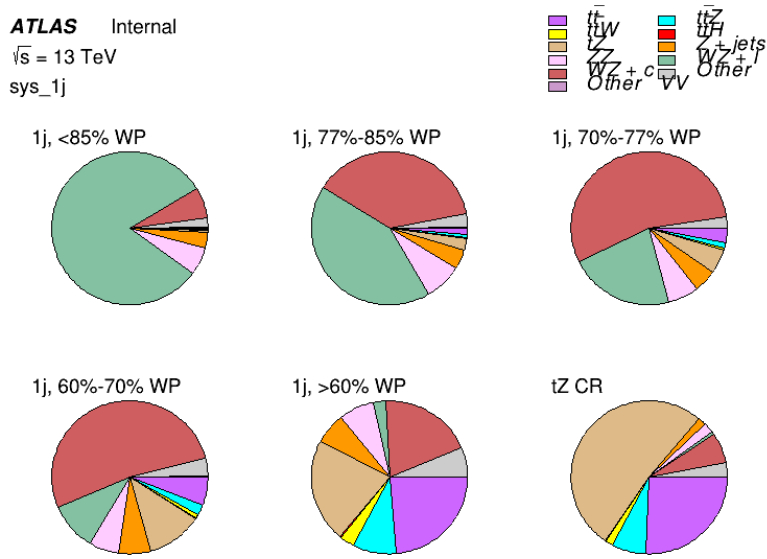


Figure 15.4: Post-fit background composition of the fit regions.

The correlations between these nuisance parameters are summarized in Figure 15.5.

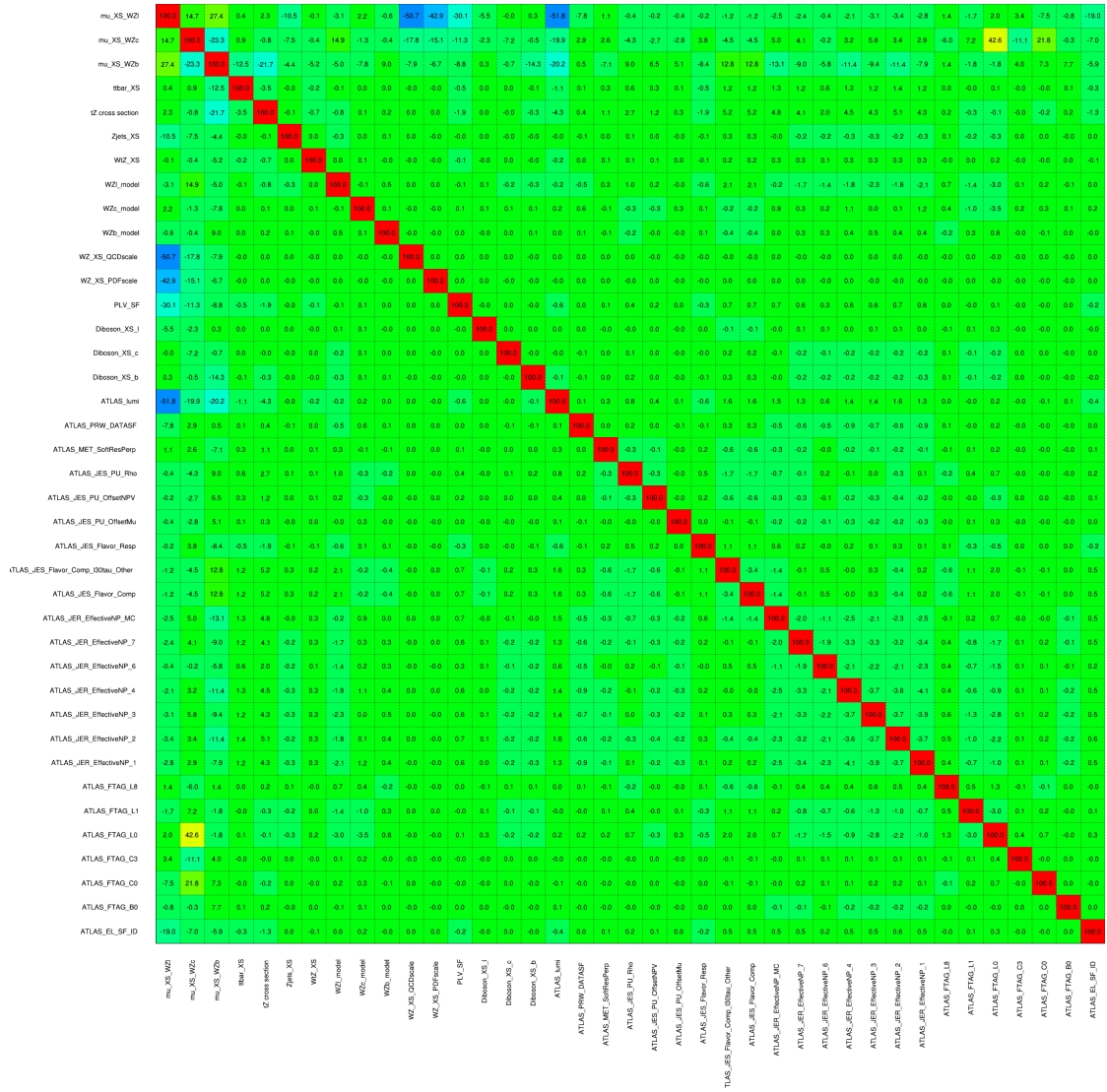


Figure 15.5: Correlations between nuisance parameters

1073 The negative correlations between $\mu_{WZ+charm}$ and μ_{WZ+b} and $\mu_{WZ+light}$ are expected:
1074 WZ + charm is present in both the WZ + b and WZ + light enriched regions, therefore increasing
1075 the fraction of charm requires increasing the fraction of WZ + b and WZ + light. This reasoning
1076 also explains the positive correlation between μ_{WZ+b} and $\mu_{WZ+light}$.

1077 Two of the major backgrounds in the region with the highest purity of WZ + b are tZ and
1078 Other VV + b, explaining the negative correlations between μ_{WZ+b} and the tZ cross section, and
1079 the VV + b cross section.

1080 The high correlation between the luminosity and $\mu_{WZ+light}$ arises from the fact that the
1081 uncertainty on $\mu_{WZ+light}$ is very low (around 4%). Small changes in luminosity cause a change
1082 in the yield of WZ + light that is large compared to its uncertainty, producing a large correlation
1083 between these two parameters.

1084 **15.2 2-jet Fit Results**

1085 **The results of the fit are currently blinded.**

1086 Pre-fit yields in each of the 2-jet fit regions are shown in Figure 15.2.

	2j, <85% WP	2j, 77%-85% WP	2j, 70%-77% WP	2j, 60%-70% WP	2j, >60% WP	tZ CR 2j
WZ + b - 2j	3.1 ± 1.6	6.7 ± 0.5	5.6 ± 0.4	8.0 ± 0.6	31 ± 2	14 ± 1
WZ + c - 2j	180 ± 20	54 ± 6	41 ± 3	24 ± 3	11 ± 2	4.8 ± 0.6
WZ + l - 2j	1250 ± 150	90 ± 14	18 ± 3	5.8 ± 1.4	1.4 ± 0.4	0.25 ± 0.1
WZ + b - 1j	3.4 ± 0.6	1.52 ± 0.35	1.58 ± 0.23	1.95 ± 0.39	6.7 ± 1.1	1.9 ± 0.6
WZ + c - 1j	56 ± 14	17.6 ± 4.0	8.6 ± 2.2	6.3 ± 1.8	3.0 ± 0.9	0.7 ± 0.2
WZ + l - 1j	427 ± 120	24 ± 7	4.7 ± 2.3	1.6 ± 0.7	0.3 ± 0.2	0.01 ± 0.0
WZ - Other	129 ± 29	6.1 ± 4.6	1.2 ± 0.3	0.3 ± 0.2	2.9 ± 0.5	3.6 ± 0.6
Other VV	7.63 ± 0.63	0.6 ± 0.5	0.16 ± 0.03	0.01 ± 0.01	0.1 ± 0.1	0.1 ± 0.1
ZZ	135 ± 20	14.1 ± 3.2	4.7 ± 0.8	4.0 ± 0.6	4.1 ± 0.7	3.1 ± 0.5
t̄tW	0.8 ± 0.2	0.4 ± 0.1	0.5 ± 0.1	0.7 ± 0.2	4.3 ± 0.6	3.9 ± 0.6
t̄tZ	14.7 ± 2.2	5.6 ± 0.8	4.5 ± 0.7	6.5 ± 1.1	25.4 ± 4.0	21.9 ± 3.4
rare Top	0.14 ± 0.04	0.07 ± 0.03	0.03 ± 0.02	0.09 ± 0.03	0.37 ± 0.07	0.6 ± 0.1
t̄tWW	0.04 ± 0.03	0.02 ± 0.02	0.01 ± 0.01	0.01 ± 0.00	0.03 ± 0.03	0.01 ± 0.0
Z + jets	110.0 ± 22.9	9.6 ± 2.0	2.1 ± 0.50	1.6 ± 0.4	5.1 ± 1.1	1.5 ± 0.3
W + jets	0.0 ± 0.0	0.0 ± 0.0	0.0 ± 0.0	0.0 ± 0.0	0.0 ± 0.0	0.0 ± 0.0
V + γ	25 ± 18	0.5 ± 0.2	0.1 ± 0.1	0.1 ± 0.1	0.0 ± 0.02	0.05 ± 0.0
tZ	15.9 ± 2.9	6.9 ± 1.3	5.1 ± 1.0	8.0 ± 1.5	18.7 ± 3.2	36.4 ± 6.1
tW	0.9 ± 0.7	0.2 ± 0.3	0.0 ± 0.1	0.0 ± 0.0	0.8 ± 0.6	0.2 ± 0.2
WtZ	4.9 ± 2.5	1.5 ± 0.8	1.1 ± 0.6	1.3 ± 0.7	4.6 ± 2.4	3.3 ± 1.7
VVV	7.4 ± 0.3	1.0 ± 0.1	0.4 ± 0.1	0.2 ± 0.1	0.13 ± 0.03	0.04 ± 0.0
VH	19.5 ± 4.2	2.8 ± 1.6	0.7 ± 0.7	0.1 ± 0.2	0.0 ± 0.0	0.0 ± 0.0
t̄t	0.7 ± 0.4	0.1 ± 0.1	0.05 ± 0.06	0.15 ± 0.13	0.8 ± 0.5	2.3 ± 1.2
t̄t	6.8 ± 1.0	2.4 ± 0.5	1.8 ± 0.4	3.3 ± 0.6	8.4 ± 1.2	13.6 ± 1.1
t̄tH	0.4 ± 0.1	0.2 ± 0.1	0.16 ± 0.02	0.23 ± 0.03	0.94 ± 0.11	1.03 ± 0.1
Total	2580 ± 160	229 ± 24	89 ± 13	69 ± 11	120 ± 15	108 ± 11

Table 19: Pre-fit yields in each of the 2-jet fit regions.

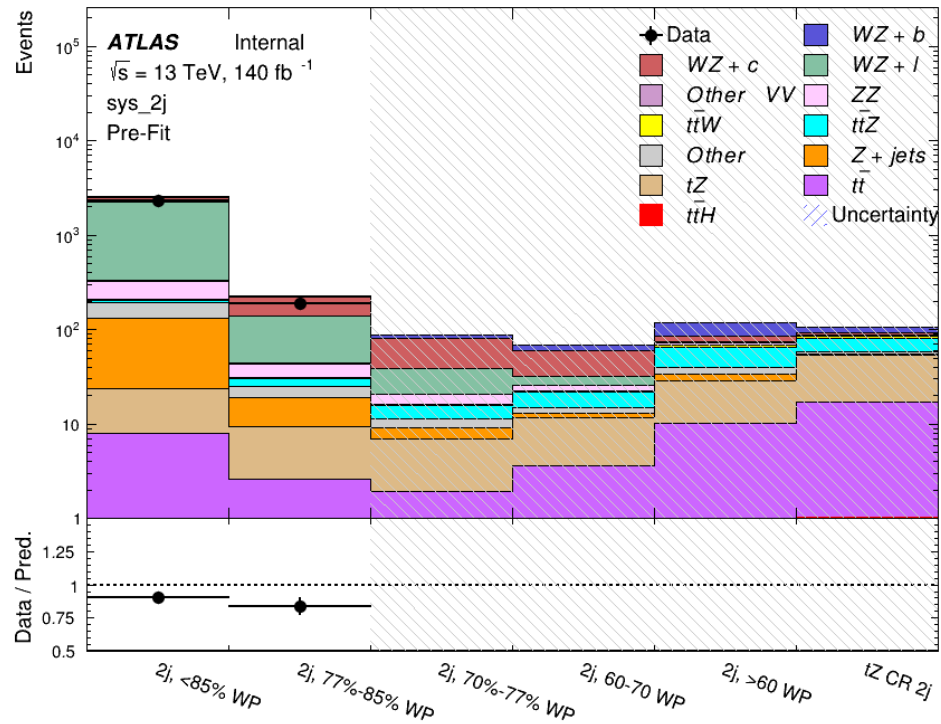


Figure 15.6: Pre-fit summary of the 2-jet fit regions.

1087

The post-fit yields in each region are summarized in Figure 15.2.

	2j, <85% WP	2j, 77%-85% WP	2j, 70%-77% WP	2j, 60%-70% WP	2j, >60% WP	tZ CR 2j
WZ + b	13 ± 6	6.7 ± 2.9	5.8 ± 2.5	8.0 ± 3.5	31 ± 13	14 ± 5
WZ + c	260 ± 60	77 ± 15	41 ± 8	26 ± 5	10.9 ± 2.4	4.8 ± 1.1
WZ + l	1860 ± 90	90 ± 12	17.6 ± 2.8	5.8 ± 1.3	1.4 ± 0.4	0.3 ± 0.2
WZ + b - 1j	3.4 ± 0.6	1.52 ± 0.35	1.58 ± 0.23	1.95 ± 0.39	6.7 ± 1.1	1.9 ± 0.6
WZ + c - 1j	56 ± 14	17.6 ± 4.0	8.6 ± 2.2	6.3 ± 1.8	3.0 ± 0.9	0.7 ± 0.2
WZ + l - 1j	427 ± 120	24 ± 7	4.7 ± 2.3	1.6 ± 0.7	0.3 ± 0.2	0.01 ± 0.0
WZ - Other	129 ± 29	6.1 ± 4.6	1.2 ± 0.3	0.3 ± 0.2	2.9 ± 0.5	3.6 ± 0.6
Other VV	7.6 ± 0.6	0.3 ± 0.3	0.3 ± 0.1	0.1 ± 0.06	0.03 ± 0.02	0.1 ± 0.1
ZZ	145 ± 30	11.3 ± 4.4	2.7 ± 1.6	1.0 ± 0.3	4.0 ± 0.1	2.4 ± 0.1
t̄tW	0.8 ± 0.2	0.4 ± 0.1	0.54 ± 0.12	0.74 ± 0.15	4.3 ± 0.6	3.9 ± 0.6
t̄tZ	14.7 ± 2.2	5.6 ± 0.8	4.5 ± 0.7	6.5 ± 1.0	25.4 ± 3.9	21.9 ± 3.0
rare Top	0.14 ± 0.04	0.07 ± 0.03	0.03 ± 0.02	0.09 ± 0.03	0.4 ± 0.1	0.6 ± 0.1
t̄tWW	0.04 ± 0.03	0.02 ± 0.02	0.01 ± 0.01	0.01 ± 0.01	0.03 ± 0.03	0.01 ± 0.0
Z + jets	110 ± 23	9.6 ± 2.0	2.1 ± 0.5	1.6 ± 0.4	5.1 ± 1.1	1.5 ± 0.3
W + jets	0.0 ± 0.0	0.0 ± 0.0				
V + γ	25 ± 19	0.5 ± 0.2	0.1 ± 0.1	0.13 ± 0.14	0.0 ± 0.02	0.05 ± 0.0
tZ	15.9 ± 2.7	6.9 ± 1.2	5.1 ± 0.9	8.0 ± 1.4	18.7 ± 3.0	36 ± 6
tW	0.1 ± 0.7	0.2 ± 0.3	0.0 ± 0.1	0.0 ± 0.0	0.8 ± 0.6	0.2 ± 0.2
WtZ	4.9 ± 2.5	1.5 ± 0.8	1.1 ± 0.6	1.3 ± 0.7	4.6 ± 2.3	3.3 ± 1.7
VVV	7.4 ± 0.3	1.0 ± 0.1	0.36 ± 0.03	0.19 ± 0.03	0.13 ± 0.03	0.04 ± 0.0
VH	19 ± 4	2.8 ± 1.6	0.7 ± 0.7	0.1 ± 0.2	0.0 ± 0.0	0.0 ± 0.0
t̄t	6.8 ± 1.0	2.4 ± 0.5	1.8 ± 0.4	3.3 ± 0.6	8.4 ± 1.2	13.6 ± 1.7
t̄tH	0.40 ± 0.05	0.19 ± 0.03	0.16 ± 0.02	0.23 ± 0.03	0.94 ± 0.11	1.03 ± 0.1
Total	2580 ± 60	229 ± 11	89 ± 6	69.1 ± 4.1	120 ± 10	108 ± 6

Table 20: Post-fit yields in each of the 2-jet fit regions.

1088

A post-fit summary of the fitted regions is shown in Figure 15.7:

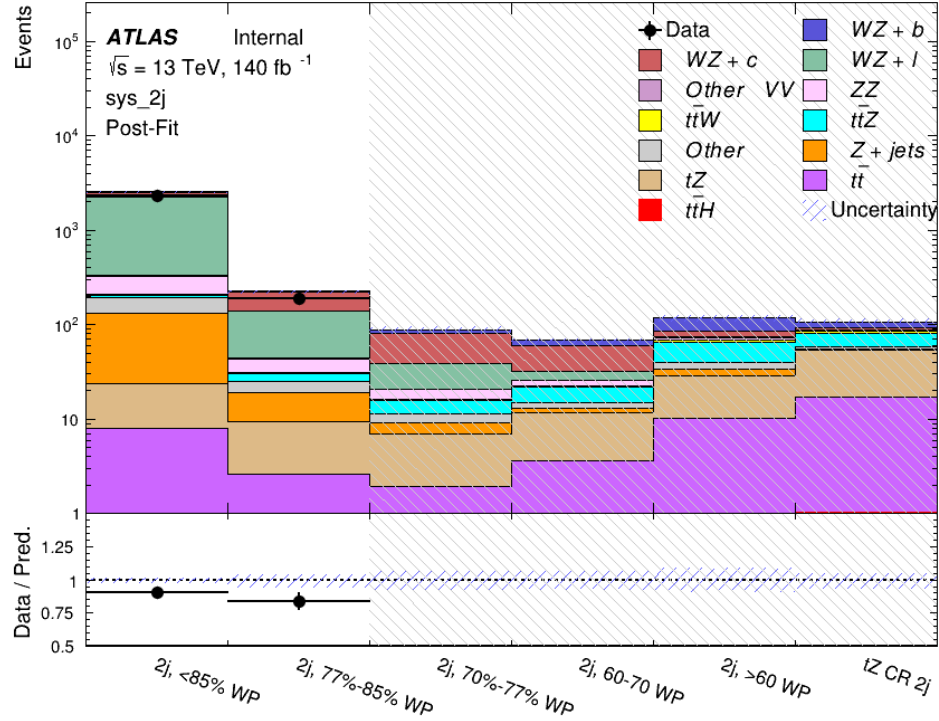


Figure 15.7: Post-fit summary of the fit over 2-jet regions.

1089 The same set of systematic uncertainties consider for the 1-jet fit are included in the 2-jet
 1090 fit as well. The impact of the most significant systematic uncertainties is summarized in Table
 1091 [21](#).

Uncertainty Source	$\Delta\mu$	
WZ + c cross-section	-0.1	0.14
Luminosity	-0.11	0.12
tZ cross-section	-0.11	0.11
Jet Energy Scale	-0.11	0.11
ttZ cross-section - QCD scale	-0.08	0.09
WZ + l cross-section	0.08	-0.07
WtZ cross-section	-0.07	0.07
Flavor tagging	0.05	0.05
Other VV + b cross-section	-0.05	0.05
Jet Energy Resolution	-0.04	0.04
Total	0.29	0.31

Table 21: Summary of the most significant sources of systematic uncertainty on the measurement of WZ + b 2-jet events.

1092 The ranking and impact of those nuisance parameters with the largest contribution to the
 1093 overall uncertainty is shown in Figure 15.8.

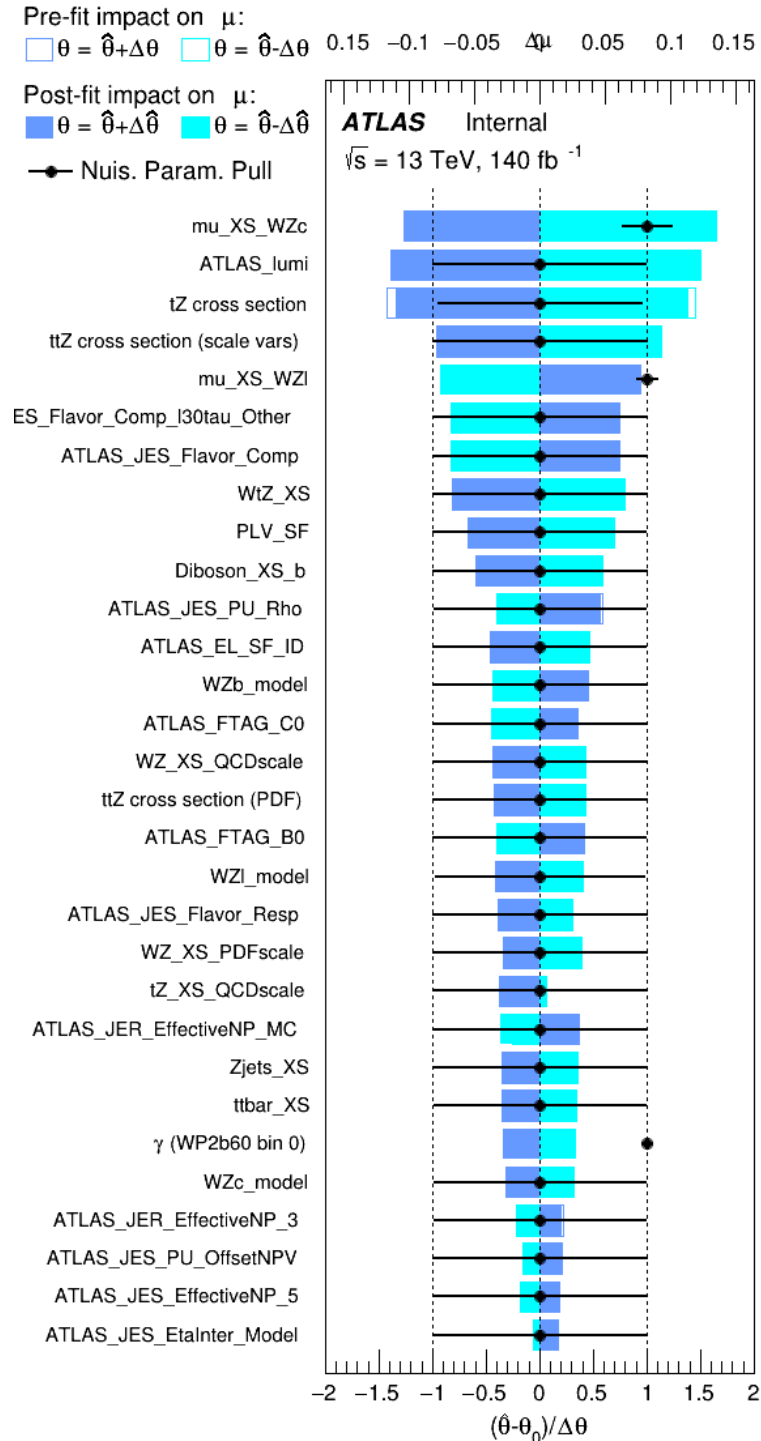


Figure 15.8: Impact of systematic uncertainties on the signal-strength of $WZ + b$ in 2-jet events.

1094 The large impact of the Jet Energy Scale and Jet Flavor Tagging is unsurprising, as the
 1095 shape of the fit regions depends heavily on the modeling of the jets. The other major sources
 1096 of uncertainty come from background modelling and cross-section uncertainty. The pie charts
 1097 in Figure 15.9 show that for the modelling uncertainties that contribute most correspond to the
 1098 most significant backgrounds.

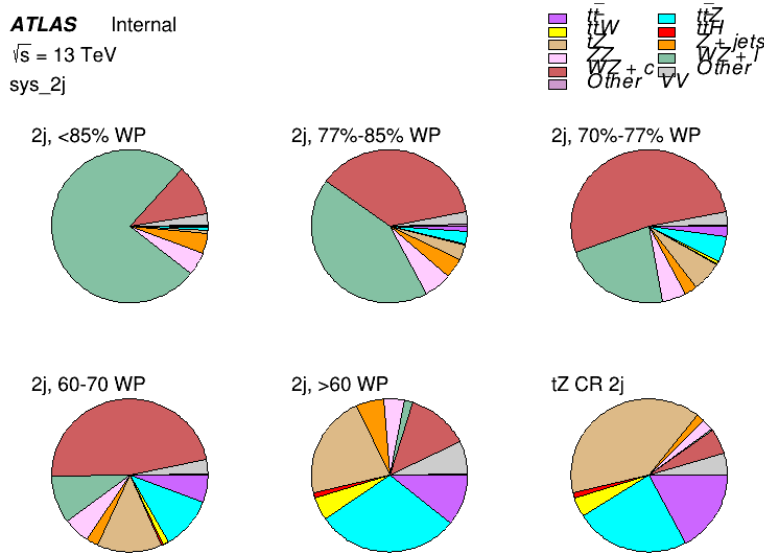


Figure 15.9: Post-fit background composition of the 2-jet fit regions.

1099 The correlations between these nuisance parameters are summarized in Figure 15.10.



Figure 15.10: Correlations between nuisance parameters in the 2-jet fit

1100 As in the 1-jet case, no significant, unexpected correlations are found between nuisance
parameters.

Part V**Differential Studies of $t\bar{t}H$ Multilepton****16 Data and Monte Carlo Samples****16.1 Data Samples**

The study uses proton-proton collision data collected by the ATLAS detector from 2015 through 2018, which represents an integrated luminosity of 139 fb^{-1} and an energy of $\sqrt{s} = 13 \text{ TeV}$. All data used in this analysis was included in one of the Good Run Lists verified by Data Quality checks.

16.2 Monte Carlo Samples

Several Monte Carlo (MC) generators were used to simulate both signal and background processes. For all of these, the effects of the ATLAS detector are simulated in Geant4. The specific event generator used for each of these MC samples is listed in Table 22. A Higgs mass of 125 GeV is assumed in all simulations.

Table 22: The configurations used for event generation of signal and background processes, including the event generator, matrix element (ME) order, parton shower algorithm, and parton distribution function (PDF).

Process	Event generator	ME order	Parton Shower	PDF
t̄H	MG5_AMC (MG5_AMC)	NLO (NLO)	PYTHIA 8 (HERWIG++)	NNPDF 3.0 NLO [16] (CT10 [17])
t̄W	MG5_AMC (SHERPA 2.1.1)	NLO (LO multileg)	PYTHIA 8 (SHERPA)	NNPDF 3.0 NLO (NNPDF 3.0 NLO)
t̄(Z/γ* → ll)	MG5_AMC	NLO	PYTHIA 8	NNPDF 3.0 NLO
VV	SHERPA 2.2.2	MEPS NLO	SHERPA	CT10
t̄t	POWHEG-BOX v2 [18]	NLO	PYTHIA 8	NNPDF 3.0 NLO
t̄γ	MG5_AMC	LO	PYTHIA 8	NNPDF 2.3 LO
tZ	MG5_AMC	LO	PYTHIA 6	CTEQ6L1
tHqb	MG5_AMC	LO	PYTHIA 8	CT10
tHW	MG5_AMC (SHERPA 2.1.1)	NLO (LO multileg)	HERWIG++ (SHERPA)	CT10 (NNPDF 3.0 NLO)
tWZ	MG5_AMC	NLO	PYTHIA 8	NNPDF 2.3 LO
t̄t̄, t̄t̄t̄	MG5_AMC	LO	PYTHIA 8	NNPDF 2.3 LO
t̄W+W-	MG5_AMC	LO	PYTHIA 8	NNPDF 2.3 LO
s-, t-channel, Wt single top	POWHEG-BOX v1 [19]	NLO	PYTHIA 6	CT10
qqVV, VVV				
Z → l+l-	SHERPA 2.2.1	MEPS NLO	SHERPA	NNPDF 3.0 NLO

1115 The signal sample ($t\bar{t}H$) is modelled at NLO with POWHEG-BOX v2 using the NNPDF2.0
 1116 parton distribution function (PDF) [34]. Parton showering and hadronisation were modelled
 1117 with PYTHIA 8.2 [35]. The $t\bar{t}H$ sample is normalized to a cross-section of 507^{+35}_{-50} fb based on
 1118 NLO calculations. Uncertainties are based on varying the QCD factorisation and renormalisation
 1119 scale, as well as uncertainties in the PDF and α_s .

1120 The $t\bar{t}W$ background is simulated using Sherpa 2.2.1 with the NNPDF3.0 NLO PDF. The
 1121 matrix element is calculated with up to one additional parton at NLO, and up to two at LO. As
 1122 explained in detail in [7], the $t\bar{t}W$ contribution predicted by MC is found disagree significantly

1123 with what is observed in data. While an effort is currently being undertaken to measure $t\bar{t}W$ more
 1124 accurately, the approach used by the 79.8 fb^{-1} $t\bar{t}H$ analysis is used here: A normalization
 1125 factor of 1.68 is applied to the MC estimate of $t\bar{t}W$ and additional systematic uncertainties on
 1126 $t\bar{t}W$ are included to account for this modelling discrepancy, as outlined in Section 20.

1127 The $t\bar{t}(Z/\gamma^*)$ process is simulated with the **MADGRAPH5_AMC@NLO** generator, using
 1128 NNPDF3.0. Diboson processes are generated with **SHERPA 2.2.2** at NLO precision for one extra
 1129 parton, and at LO for up to three extra partons.

1130 The estimation of the “fake” or non-prompt background - with leptons from hadron decays
 1131 or photon conversions - is done primarily using an inclusive $t\bar{t}$ sample. This sample is generated
 1132 using **POWHEG**, with **PYTHIA8** performing the parton shower and fragmentation.

1133 While the main $t\bar{t}H$ analysis is currently refining a data-driven approach for estimating
 1134 the contribution of events with non-prompt leptons, at the time of this note this strategy has not
 1135 been completely developed for the full Run-2 dataset. Therefore, the non-prompt contribution
 1136 is estimated with MC, while applying normalization corrections and systematic uncertainties
 1137 derived from data driven techniques developed for the 79.8 fb^{-1} $t\bar{t}H/t\bar{t}W$ analysis [7]. The
 1138 primary contribution to the non-prompt lepton background is from $t\bar{t}$ production, with V+jets
 1139 and single-top as much smaller sources. Likelihood fits over several control regions enriched with
 1140 these non-prompt backgrounds are fit to data in order to derive normalization factors for these
 1141 backgrounds. The specific normalization factors and uncertainties applied to the non-prompt
 1142 contributions are listed in Section 20.

1143 Other background processes, such as tH , tZ , $t\bar{t}WW$ and $t\bar{t}t\bar{t}$, are expected to make minor
1144 contributions to the total background. The generators and setting used for these backgrounds are
1145 summarized in Table 22.

1146 17 Object Reconstruction

1147 All analysis channels considered in this note share a common object selection for leptons and
1148 jets, as well as a shared trigger selection.

1149 17.1 Trigger Requirements

1150 Events are required to be selected by dilepton triggers. The p_T thresholds of the dilepton trigger
1151 on two electrons were 12 GeV in 2015, 17 GeV in 2016, and 24 GeV in 2017 and 2018, while for
1152 the dimuon triggers the p_T thresholds on the leading (sub-leading) muon were 18 GeV (8 GeV)
1153 in 2015, and 22 GeV (8 GeV) in 2016-2018. For the electron+muon triggers, the p_T thresholds
1154 on the electron (muon) were 17 GeV (14 GeV) for all datasets.

1155 17.2 Light Leptons

1156 Electron candidates are reconstructed from energy clusters in the electromagnetic calorimeter
1157 that are associated with charged particle tracks reconstructed in the inner detector [20]. Electron
1158 candidates are required to have $p_T > 10$ GeV and $|\eta_{\text{cluster}}| < 2.47$. Candidates in the transition

1159 region between different electromagnetic calorimeter components, $1.37 < |\eta_{\text{cluster}}| < 1.52$, are
 1160 rejected. A multivariate likelihood discriminant combining shower shape and track information
 1161 is used to distinguish prompt electrons from nonprompt leptons, such as those originating from
 1162 hadronic showers. Electron candidate are also required to pass TightLH identification.

1163 To further reduce the non-prompt contribution, the track of each electron is required to
 1164 originate from the primary vertex; requirements are imposed on the transverse impact parameter
 1165 significance ($|d_0|/\sigma_{d_0}$) and the longitudinal impact parameter ($|\Delta z_0 \sin \theta_\ell|$).

1166 Muon candidates are reconstructed by combining inner detector tracks with track segments
 1167 or full tracks in the muon spectrometer [21]. Muon candidates are required to have $p_T > 10 \text{ GeV}$
 1168 and $|\eta| < 2.5$. Muons are required to Medium ID requirements.

1169 All leptons are required to pass a non-prompt BDT selection developed by the main
 1170 $t\bar{t}H/t\bar{t}W$ analysis, described in detail in [7]. Optimized working points and scale factors for this
 1171 BDT are taken from that analysis. This BDT and the WPs used are summarized in Appendix
 1172 **A**,

1173 **17.3 Jets**

1174 Jets are reconstructed from calibrated topological clusters built from energy deposits in the
 1175 calorimeters [23], using the anti- k_t algorithm with a radius parameter $R = 0.4$. Particle Flow, or
 1176 PFlow, jets are used in the analysis, which are hadronic objects reconstructed using information

1177 from both the tracker and the calorimeter. Jets with energy contributions likely arising from noise
1178 or detector effects are removed from consideration [24], and only jets satisfying $p_T > 25$ GeV
1179 and $|\eta| < 2.5$ are used in this analysis. For jets with $p_T < 60$ GeV and $|\eta| < 2.4$, a jet-track
1180 association algorithm is used to confirm that the jet originates from the selected primary vertex,
1181 in order to reject jets arising from pileup collisions [25].

1182 **17.4 B-tagged Jets**

1183 Each analysis channel used in this analysis includes b-jets in the final state. These are identified
1184 using the DL1r b-tagging algorithm, which uses jet vertex and kinematic information to distin-
1185 guish heavy and light flavored jets. These features are used as inputs to a neural network, the
1186 output of which is used to form calibrated working points (WPs) based on how likely a jet is to
1187 have originated from a b-quark. This analysis uses the 70% DL1r WP - implying an efficiency of
1188 70% for truth b-jets - for selecting b-tagged jets.

1189 **17.5 Missing Transverse Energy**

1190 Because all $t\bar{t}H - ML$ channels considered include multiple neutrinos, missing transverse
1191 energy (E_T^{miss}) is present in each event. The missing transverse momentum vector is defined as
1192 the inverse of the sum of the transverse momenta of all reconstructed physics objects as well
1193 as remaining unclustered energy, the latter of which is estimated from low- p_T tracks associated
1194 with the primary vertex but not assigned to a hard object [26].

1195 17.6 Overlap removal

1196 To avoid double counting objects and remove leptons originating from decays of hadrons, overlap
 1197 removal is performed in the following order: any electron candidate within $\Delta R = 0.1$ of another
 1198 electron candidate with higher p_T is removed; any electron candidate within $\Delta R = 0.1$ of a muon
 1199 candidate is removed; any jet within $\Delta R = 0.3$ of an electron candidate is removed; if a muon
 1200 candidate and a jet lie within $\Delta R = \min(0.4, 0.04 + 10[\text{GeV}]/p_T(\text{muon}))$ of each other, the jet
 1201 is kept and the muon is removed.

1202 This algorithm is applied to the preselected objects. The overlap removal procedure is
 1203 summarized in Table 23.

Keep	Remove	Cone size (ΔR)
electron	electron (low p_T)	0.1
muon	electron	0.1
electron	jet	0.3
jet	muon	$\min(0.4, 0.04 + 10[\text{GeV}]/p_T(\text{muon}))$
electron	tau	0.2

Table 23: Summary of the overlap removal procedure between electrons, muons, and jets.

1204 18 Higgs Momentum Reconstruction

1205 Reconstructing the momentum of the Higgs boson is a particular challenge for channels with
 1206 leptons in the final state: Because all channels include at least two neutrinos in the final state, the
 1207 Higgs can never be fully reconstructed. However, the momentum spectrum can be well predicted
 1208 by a neural network when provided with the kinematics of the Higgs Boson decay products - as

1209 verified by studies detailed in Appendix C.3. With this in mind, several layers of MVAs are used
1210 to reconstruction the Higgs momentum:

1211 The first layer is a model designed to select which jets are most likely to be the b-jets that
1212 came from the top decay, detailed in Section 18.3. As described in Section 18.4, the kinematics
1213 of these jets and possible Higgs decay products are fed into the second layer, which is designed
1214 to identify the decay products of the Higgs Boson itself. The kinematics of the particles this
1215 layer identifies as most likely to have originated from the Higgs decay are then fed into yet
1216 another neural-network, which predicts the momentum of the Higgs (18.5). For the 3l channel,
1217 an additional MVA is used to determine the decay mode of the Higgs boson in the 3l channel
1218 (18.6).

1219 Models are trained on Monte Carlo simulations of $t\bar{t}H$ events generated using MG5_AMC.
1220 Specifically, events DSIDs 346343-5, 345873-5, and 345672-4 are used for training in order to
1221 increase the statistics of the training sample.

1222 For all of these models, the Keras neural network framework, with Tensorflow 2.0 as the
1223 backend, is used, and the number of hidden layers and nodes are determined using grid search
1224 optimization. Each neural network uses the LeakyReLU activation function, a learning rate of
1225 0.01, and the Adam optimization algorithm, as alternatives are found to either decrease or have
1226 no impact on performance. Batch normalization is applied after each layer in order to stabilize
1227 the model and decrease training time. For the classification algorithms (b-jet matching, Higgs
1228 reconstruction, and 3l decay identification) binary-cross entropy is used as the loss function,

1229 while the p_T reconstruction algorithm uses MSE.

1230 The specific inputs features used for each model are arrived at through a process of trial
1231 and error - features considered potentially useful are tried, and those that are found to increase
1232 performance are included. While each model includes a relatively large number of features,
1233 some using upwards of 30, this inclusive approach is found to maximize the performance of
1234 each model while decreasing the variance compared to a reduced number of inputs. Each input
1235 feature is validated by comparing MC simulations to 79.8 fb^{-1} of data, as shown in the sections
1236 below.

1237 **18.1 Physics Object Truth Matching**

1238 Machine Learning algorithms are trained to identify the decay products of the Higgs Boson using
1239 MC simulations of $t\bar{t}H$ events. The kinematics of the reconstructed physics objects, as well as
1240 event level variables, are used as inputs, with the parent ID taken from the truth record used to
1241 label the data. The objects considered include light leptons and jets.

1242 Reconstructed physics objects are matched to particle level objects, in order to identify the
1243 parent particle of these reconstructed objects. Reconstructed jets are matched to truth jets based
1244 on the requirements that the reco jet and truth jet fall within $\Delta R < 0.4$, and the two objects have
1245 a p_T that agrees within 10%. Truth level and reco level leptons are required to have the same
1246 flavor, a $\Delta R < 0.1$, and p_T that agree within 10%. Events where no match can be found between

1247 the particle level decay products of the Higgs and the reconstructed objects are not included in
1248 training.

1249 Leptons considered as possible Higgs and top decay candidates are required to pass the
1250 selection described in Section 17.2. For jets, however, it is found that a large fraction that
1251 originate from either the top decay or the Higgs decay fall outside the selection described in
1252 Section 17.3. Specifically, jets from the Higgs decay tend to be soft, with 32% having $p_T <$
1253 25 GeV. Therefore jets with $p_T < 15$ GeV are considered as possible candidates in the models
1254 described below. By contrast, less than 5% of the jets originating from the Higgs fall below this
1255 p_T threshold. The jets are found to be well modeled even down to this low p_T threshold, as shown
1256 in Section 19.1. The impact of using different p_T selection for the jet candidates is considered
1257 in detail in Section C.6. As they are expected to originate from the primary vertex, jets are also
1258 required to pass a JVT cut.

1259 18.2 Truth Level Studies

1260 Attempts to identify the decay products of the Higgs are motivated by the ability to reconstruct
1261 the Higgs momentum based on their kinematics. In order to demonstrate that this is case, the
1262 kinematics of reconstructed objects that are truth matched to the Higgs decay are used as inputs
1263 to a neural network which is designed to predict of the momentum of the Higgs. This is done in
1264 the 2lSS channel -

1265 18.3 b-jet Identification

1266 Including the kinematics of the b-jets that originate from the top decay is found to improve the
1267 identification of the Higgs decay products, and improve the accuracy with which the Higgs
1268 momentum can be reconstructed. Because these b-jets are reconstructed by the detector with
1269 high efficiency (just over 90% of the time), and can be identified relatively consistently, the first
1270 step in reconstructing the Higgs is selecting the b-jets from the top decay.

1271 Exactly two b-jets are expected in the final state of $t\bar{t}H - \text{ML}$ events. However, in both
1272 the 3l and 2lSS channels, only one or more b-tagged jets are required (where the 70% DL1r b-tag
1273 working point is used). Therefore, for events which have exactly one, or more than two, b-tagged
1274 jets, deciding which combination of jets correspond to the top decay is non-trivial. Further,
1275 events with 1 b-tagged jet represent just over half of all $t\bar{t}H - \text{ML}$ events. Of those, both b-jets
1276 are reconstructed by the detector 75% of the time. Therefore, rather than adjusting the selection
1277 to require exactly 2 b-tagged jets, and losing more than half of the signal events, a neural network
1278 is used to predict which pair of jets is most likely to correspond to truth b-jets.

1279 Once the network is trained, all possible pairings of jets are fed into the model, and the pair
1280 of jets with the highest output score are taken to be b-jets in successive steps of the analysis.

1281 **18.3.1 2lSS Channel**

1282 For the 2lSS channel, the input features shown in Table 24 are used for training. Here j_0 and j_1
1283 are the two jet candidates, while l_0 and l_1 are the two leptons in the event, both ordered by p_T . jet
1284 DL1r is an integer corresponding to the calibrated b-tagging working points reached by each jet,
1285 where 5 represents the tightest working point and 1 represents the loosest. The variables nJets
1286 DL1r 60% and nJets DL1r 85% represent the number of jets in the event passing the 60% and
1287 85% b-tag working points, respectively.

jet p_T 0	jet p_T 1	Lepton p_T 0
Lepton p_T 1	jet η 0	jet η 1
$\Delta R(j_0)(j_1)$	$M(j_0 j_1)$	$\Delta R(l_0)(j_0)$
$\Delta R(l_0)(j_1)$	$\Delta R(l_1)(j_0)$	$\Delta R(l_1)(j_1)$
$M(l_0 j_0)$	$M(l_0 j_1)$	$M(l_1 j_0)$
$M(l_1 j_1)$	jet DL1r 0	jet DL1r 1
nJets OR DL1r 85	nJets OR DL1r 60	$\Delta R(j_0 l_0)(j_1 l_1)$
$\Delta R(j_0 l_1)(j_1 l_0)$	$p_T(j_0 j_1 l_0 l_1 E_T^{\text{miss}})$	$M(j_0 j_1 l_0 l_1 E_T^{\text{miss}})$
$\Delta\phi(j_0)(E_T^{\text{miss}})$	$\Delta\phi(j_1)(E_T^{\text{miss}})$	HT jets
nJets	E_T^{miss}	

Table 24: Input features used in the b-jet identification algorithm for the 2lSS channel

1288 As there are far more incorrect combinations than correct ones, by a factor of more than
1289 20:1, the training set is resampled to reduce the fraction of incorrect combinations. A random
1290 sample of 5 million incorrect entries are used for training, along with close 1 million correct
1291 entries. 10% of the dataset is set aside for testing, leaving around 5 million datapoints for
1292 training.

1293 The difference between the distributions for a few of these features for the "correct" (i.e.

1294 both jets are truth b-jets), and "incorrect" combinations are shown in Figure 18.1. The correct and
 1295 incorrect contributions are scaled to the same integral, so as to better demonstrate the differences
 1296 in the distributions.

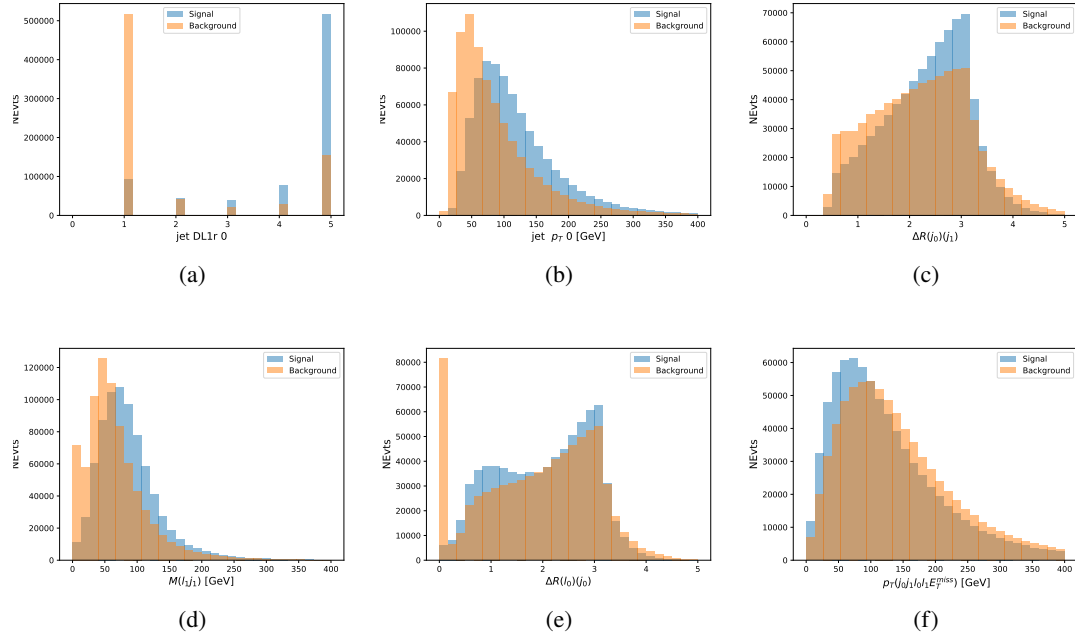


Figure 18.1: Input features for top2ISS training. The signal in blue represents events where both jet candidates are truth b-jets from top decays, and the orange is all other combinations. Each are scaled to the same number of events. (a) shows the DL1r working point of leading jet, (b) shows the p_T of the leading jet, (c) shows the ΔR of the two jets, (d) the invariant mass of lepton 1 and jet 1, (e) the ΔR of lepton 0 and jet 0, and (f) the p_T of both leptons, and the E_T^{miss} .

1297 The modeling of these inputs is validated against data, with Figure 18.2 showing good
 1298 general agreement between data and MC. Plots for the complete list of features can found in
 1299 Section C.

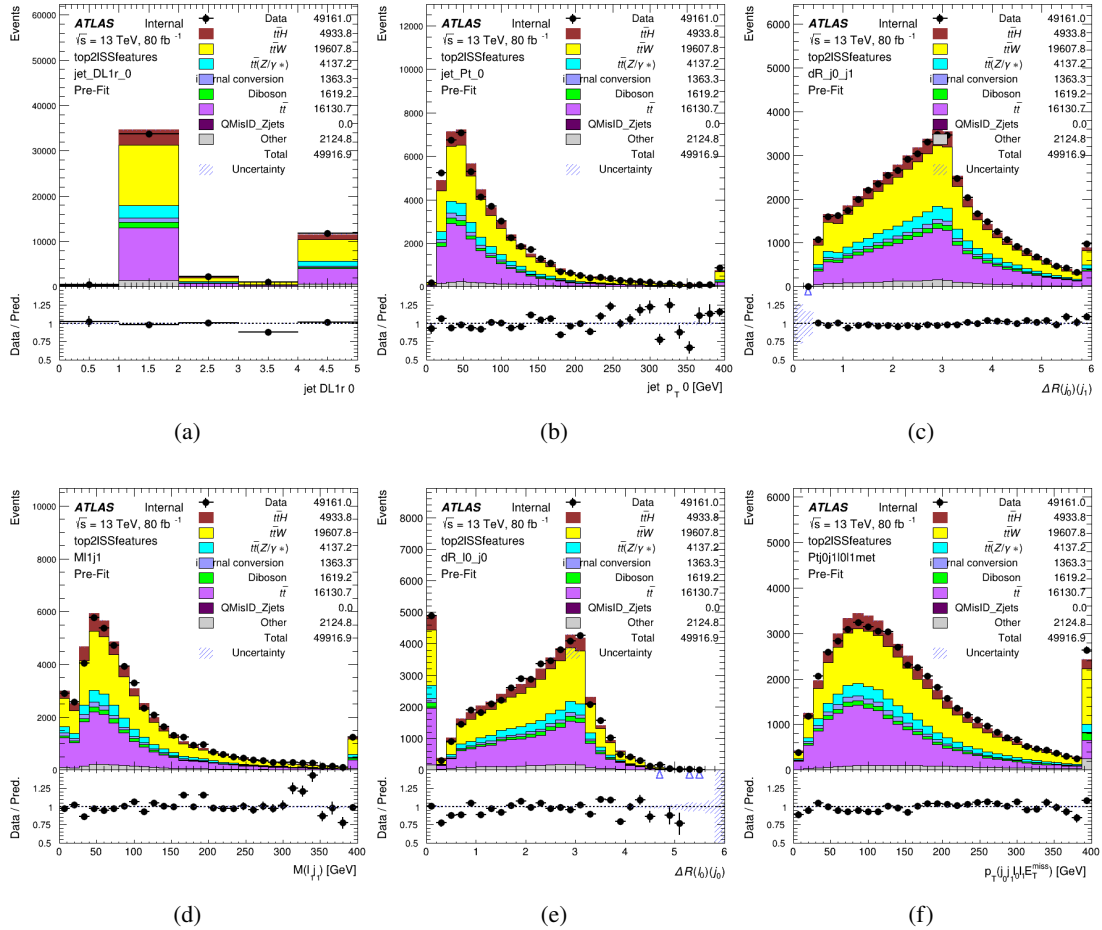


Figure 18.2: Data/MC comparisons of input features for top2ISS training for 79.8 fb^{-1} of data. (a) shows the DL1r working point of leading jet, (b) shows the p_T of the leading jet, (c) shows the ΔR of the two jets, (d) the invariant mass of lepton 1 and jet 1, (e) the ΔR of lepton 0 and jet 0, and (f) the p_T of both jets, both leptons, and the E_T^{miss} .

Based on the results of grid search evaluation, the optimal architecture is found to include
 1300 5 hidden layers with 40 nodes each. No regularizer or dropout is added to the network, as
 1301 overfitting is found to not be an issue. The output score distribution as well as the ROC curve for
 1302 the trained model are shown in Figure 18.3.1. The model is found to identify the correct pairing
 1303 of jets for 73% of 2ISS signal events on test data.
 1304

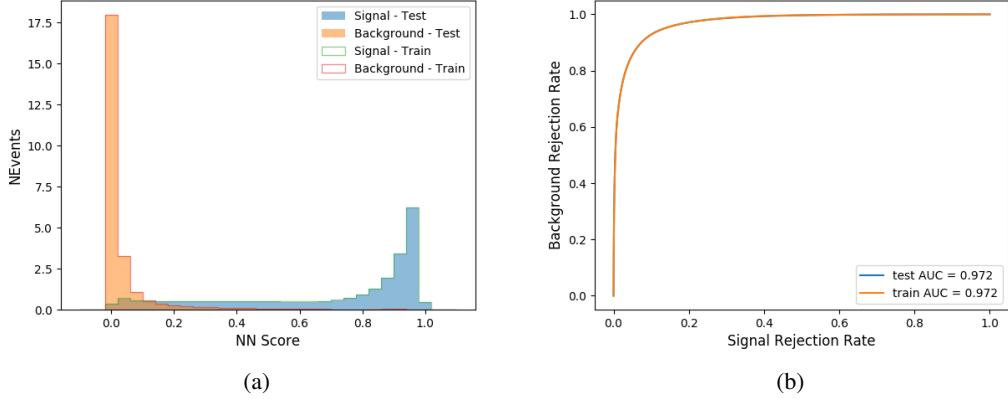


Figure 18.3: Results of the b-jet identification algorithm for the 2lSS channel, showing (a) the output score of the NN for correct and incorrect combinations of jets. (b) the ROC curve of the output, showing background rejection as a function of signal efficiency

1305 For point of comparison, a "naive" approach to identify b-jets is used as well: The two
 1306 jets which pass the highest DL1r b-tag working point are assumed to be the b-jets from the top
 1307 decay. In the case that multiple jets meet the same b-tag working point, the jet with higher p_T is
 1308 used. This method identifies the correct jet pair 65% of the time.

1309 The accuracy of the model for different values of n-bjets, compared to this naive approach,
 1310 is shown in Table 25.

b-jet Selection	Neural Network	Naive
1 b-jet	58.6%	42.1%
2 b-jets	88.4%	87.1%
≥ 3 b-jets	61.7%	53.3%
Overall	73.9%	67.2%

Table 25: Accuracy of the NN in identifying b-jets from tops in 2lSS events, overall and split by the number of b-tagged jets in the event, compared to the accuracy of taking the two highest b-tagged jets.

¹³¹¹ **18.3.2 3l Channel**

¹³¹² The input features used in the 3l channel are listed in Table 26, with the same naming convention
¹³¹³ as the 2lSS channel.

jet p_T 0	jet p_T 1	jet η 0
jet η 1	Lepton p_T 0	Lepton p_T 1
Lepton p_T 2	$\Delta R(j_0)(j_1)$	$M(j_0 j_1)$
$\Delta R(l_0)(j_0)$	$\Delta R(l_1)(j_0)$	$\Delta R(l_2)(j_0)$
$\Delta R(l_0)(j_1)$	$\Delta R(l_1)(j_1)$	$\Delta R(l_2)(j_1)$
$M(l_0 j_0)$	$M(l_1 j_0)$	$M(l_2 j_0)$
$M(l_0 j_1)$	$M(l_1 j_1)$	$M(l_2 j_1)$
$\Delta R(j_0 l_0)(j_1 l_1)$	$\Delta R(j_0 l_0)(j_1 l_2)$	$\Delta R(j_0 l_1)(j_1 l_0)$
$\Delta R(j_0 l_2)(j_1 l_0)$	jet DL1r 0	jet DL1r 1
$p_T(j_0 j_1 l_0 l_1 l_2 E_T^{\text{miss}})$	$M(t j_0 j_1 l_0 l_1 l_2 E_T^{\text{miss}})$	$\Delta\phi(j_0)(E_T^{\text{miss}})$
$\Delta\phi(j_1)(E_T^{\text{miss}})$	HT Lepton	HT jets
nJets	E_T^{miss}	nJets OR DL1r 85
nJets OR DL1r 60		

Table 26: Input features for the b-jet identification algorithm in the 3l channel.

¹³¹⁴ A few of these features are shown in Figure 18.4, comparing the distributions for correct
¹³¹⁵ and incorrect combinations of jets.

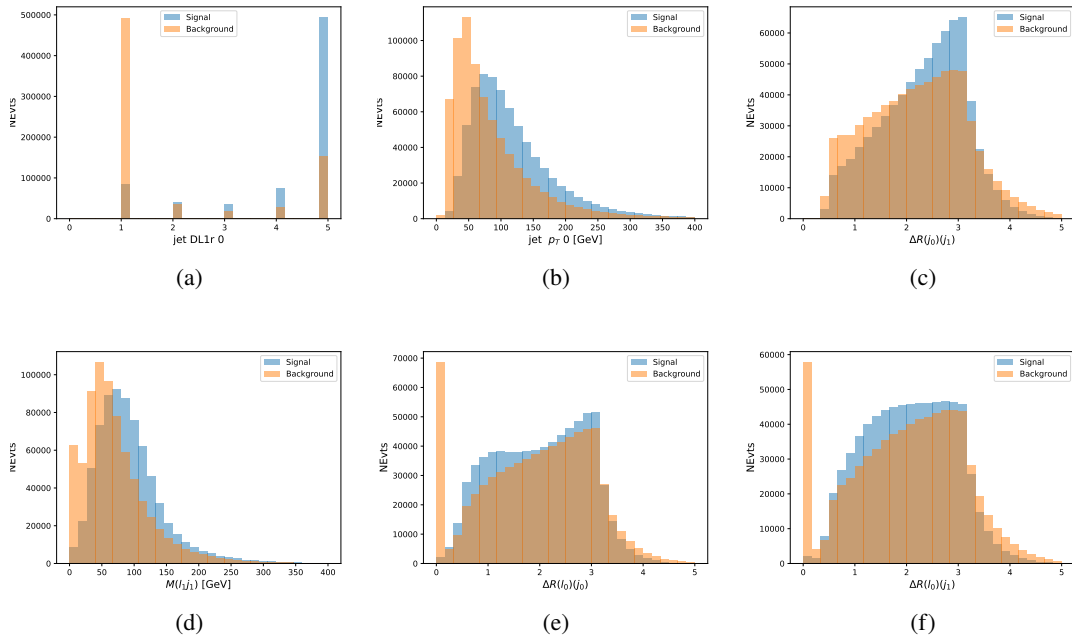


Figure 18.4: Input features for top3l training. The signal in blue represents events where both jet candidates are truth b-jets from top decays, and the orange is all other combinations. Scaled to the same number of events. (a) show the DL1r WP of jet 0, (b) the p_T of jet 0, (c) ΔR between jet 0 and jet 1, (d) the invariant mass of lepton 1 and jet 1, (e) ΔR between lepton 0 and jet 0, and (f) ΔR between lepton 0 and jet 1

1316 The modeling of these inputs is validated against data, with Figure 18.5 showing good
 1317 general agreement between data and MC. Plots for the complete list of features can found in
 1318 Section C.

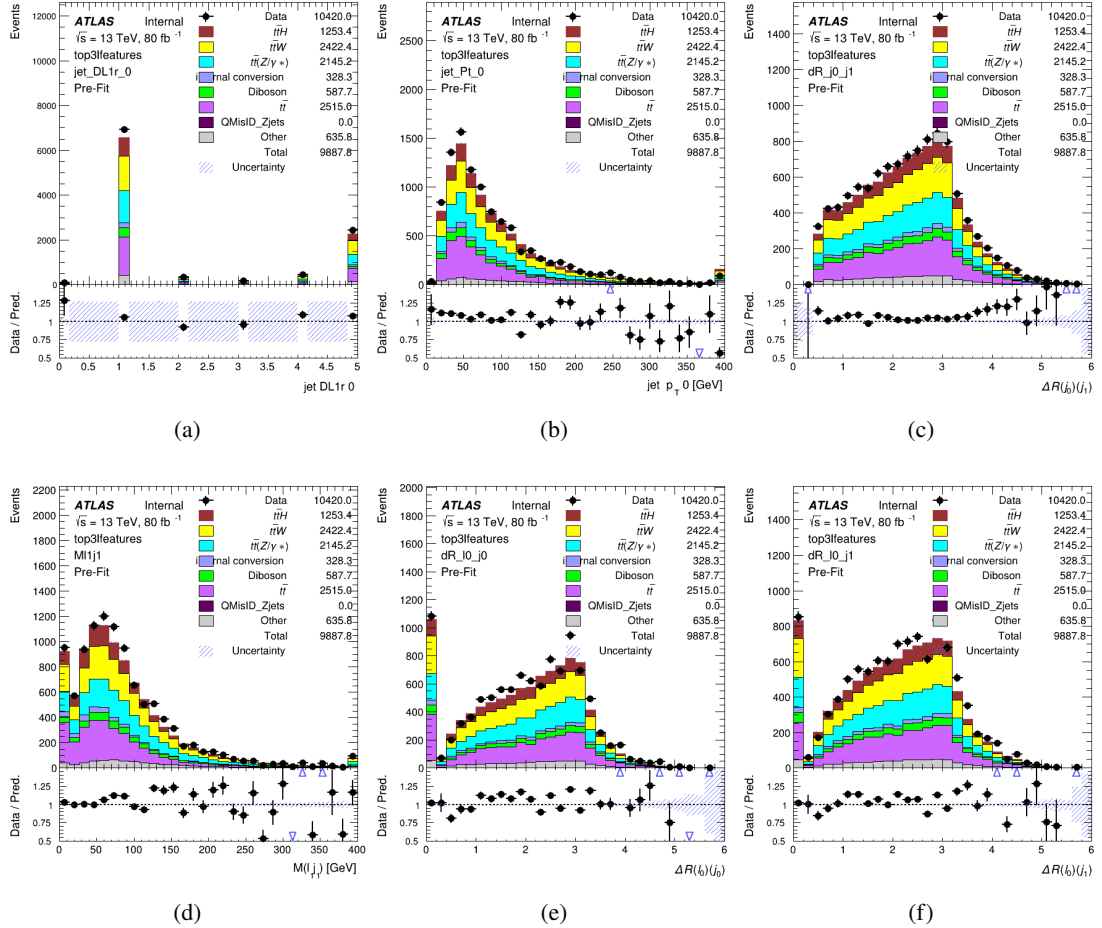


Figure 18.5: Data/MC comparisons of input features for top3l training for 79.8 fb^{-1} of data. (a) show the DL1r WP of jet 0, (b) the p_T of jet 0, (c) ΔR between jet 0 and jet 1, (d) the invariant mass of lepton 1 and jet 1, (e) ΔR between lepton 0 and jet 0, and (f) ΔR between lepton 0 and jet 1

Again, the dataset is downsized to reduce the ratio of correct and incorrect combination from 20:1, to 5:1. Around 7 million events are used for training, with 10% set aside for testing. Based on the results of grid search evaluation, the optimal architecture is found to include 5 hidden layers with 60 nodes each. The output score distribution as well as the ROC curve for the trained model are shown in Figure 18.3.2.

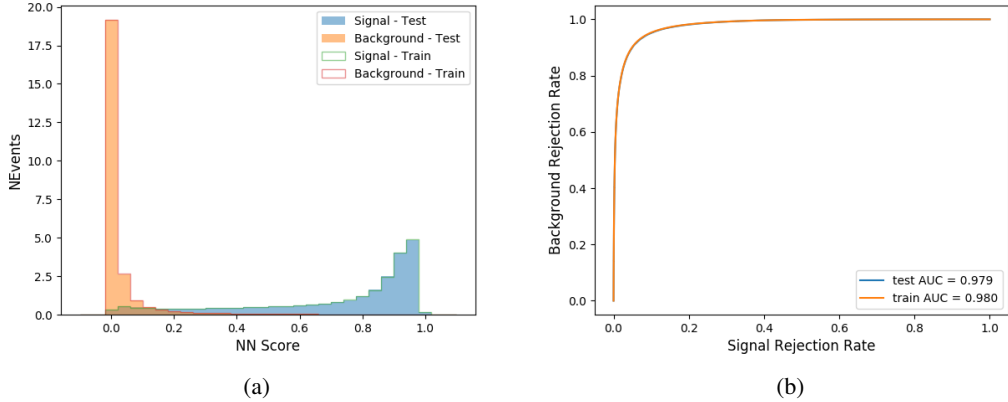


Figure 18.6: Results of the b-jet identification algorithm for the 3l channel, showing (a) the output score of the NN for correct and incorrect combinations of jets. (b) the ROC curve of the output, showing background rejection as a function of signal efficiency

1324 This procedure is found to identify the correct pairing of jets for nearly 80% of 3l signal
 1325 events. The accuracy of the model is summarized in Table 27.

Table 27: Accuracy of the NN in identifying b-jets from tops, compared to the naive method of taking the highest b-tagged jets.

	NN	Naive
1 b-jet	69.0%	48.9%
2 b-jets	89.6%	88.3%
≥ 3 b-jets	55.7%	52.3%
Overall	79.8%	70.2%

1326 18.4 Higgs Reconstruction

1327 Techniques similar to the b-jet identification algorithms are employed to select the decay products
 1328 of the Higgs: kinematics of all possible combinations of reconstructed objects are fed into a neural
 1329 network to determine which of those is most likely to be the decay products of the Higgs.

1330 Again separate models are used for the 2lSS and 3l channels, while the 3l channel has now
1331 been split into two: $t\bar{t}H$ events with three leptons in the final state include both instances where
1332 the Higgs decays into a lepton (and a neutrino) and a pair of jets, and instances where the Higgs
1333 decays to two leptons.

1334 3l events are therefore categorized as either semi-leptonic (3lS) or fully-leptonic (3lF). In
1335 the semi-leptonic case the reconstructed decay products consist of two jets and a single lepton.
1336 For the fully-leptonic case, the decay products include 2 of the three leptons associated with the
1337 event. For training the models, events are separated into these two categories using truth level
1338 information. A separate MVA, described in Section 18.6, is used to make this distinction at reco
1339 level and determine which model to use.

1340 For all channels, the models described in Section 18.3 are used to identify b-jet candidates,
1341 whose kinematics are used to identify the Higgs decay products. These jets are not considered
1342 as possible candidates for the Higgs decay, justified by the fact that these models are found to
1343 misidentify jets from the Higgs decay as jets from the top decay less than 1% of the time.

1344 **18.4.1 2lSS Channel**

1345 For the 2lSS channel, the Higgs decay products include one light lepton and two jets. The neural
1346 network is trained on the kinematics of different combinations of leptons and jets, as well as the
1347 b-jets identified in Section 18.3, with the specific input features listed in Table 28.

Lepton p_T H	Lepton p_T T	jet p_T 0
jet p_T 1	top p_T 0	top p_T 1
top η 0	top η 1	jet η 0
jet η 1	jet Phi 0	jet Phi 1
Lepton η H	Lepton heta T	$\Delta R(j_0)(j_1)$
$\Delta R(l_H)(j_0)$	$\Delta R(l_H)(j_1)$	$M(j_0 j_1)$
$M(l_H j_0)$	$M(l_H j_1)$	$\Delta R(l_H)(b_0)$
$\Delta R(l_H)(b_1)$	$\Delta R(l_T)(b_0)$	$\Delta R(l_T)(b_1)$
$\Delta R(j_0 j_1)(l_H)$	$\Delta R(j_0 j_1)(l_T)$	$\Delta R(j_0 j_1)(b_0)$
$\Delta R(j_0 j_1)(b_1)$	$\Delta R(j_0)(b_0)$	$\Delta R(j_0)(b_1)$
$\Delta R(j_1)(b_0)$	$\Delta R(j_1)(b_1)$	$M(j_0 j_1 l_H)$
$p_T(j_0 j_1 l_H l_T b_0 b_1 E_T^{\text{miss}})$	topScore	E_T^{miss}
nJets	HT jets	

Table 28: Input features used to identify the Higgs decay products in 2ISS events

1348 Here j_0 and j_1 , and l_H are the jet and lepton decay candidates, respectively. The other
 1349 lepton in the event is labeled l_T , as it is assumed to have come from the decay of one of the top
 1350 quarks. b_0 and b_1 are the two b-jets identified by the b-jet identification algorithm. The b-jet
 1351 Reco Score is the output of the b-jet reconstruction algorithm.

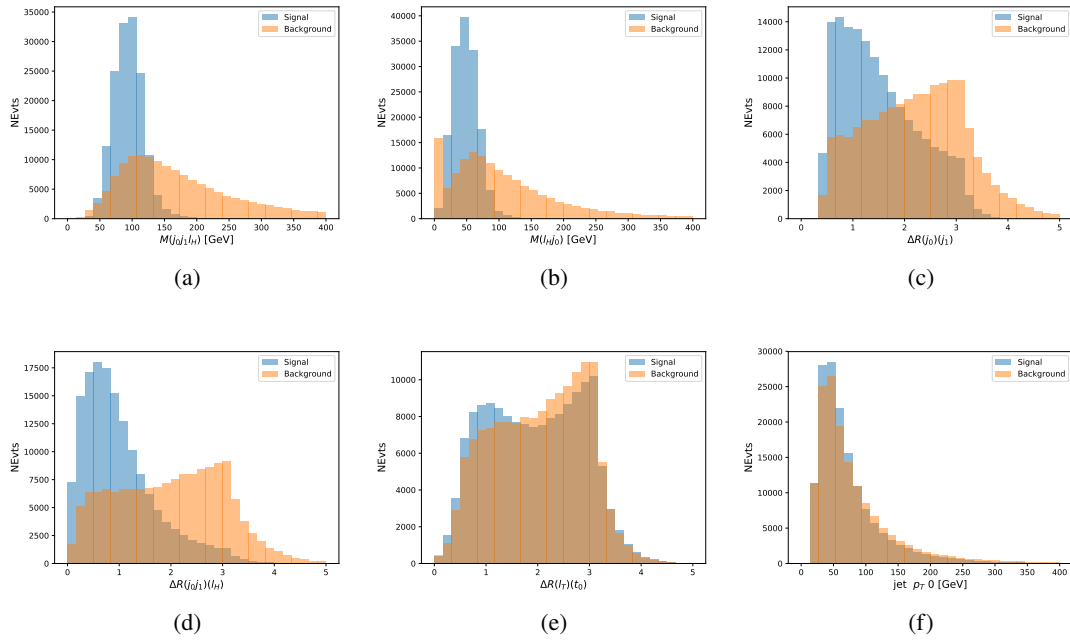


Figure 18.7: Input features for higgs2lSS training. The signal in blue represents events where both jet candidates are truth b-jets from top decays, and the orange is all other combinations. Scaled to the same number of events. (a) shows the invariant mass of the two jet candidates and the lepton candidate, (b) the invariant mass of jet 0 and the lepton candidate, (c) ΔR between the jet candidates, (d) ΔR between jet 0 + jet 1 and the lepton candidate, (e) ΔR between the lepton from the top and the leading b-jet, (f) the p_T of jet 0.

1352 The modeling of these inputs is validated against data, with Figure 18.2 showing good
 1353 general agreement between data and MC. Plots for the complete list of features can found in
 1354 Section C.

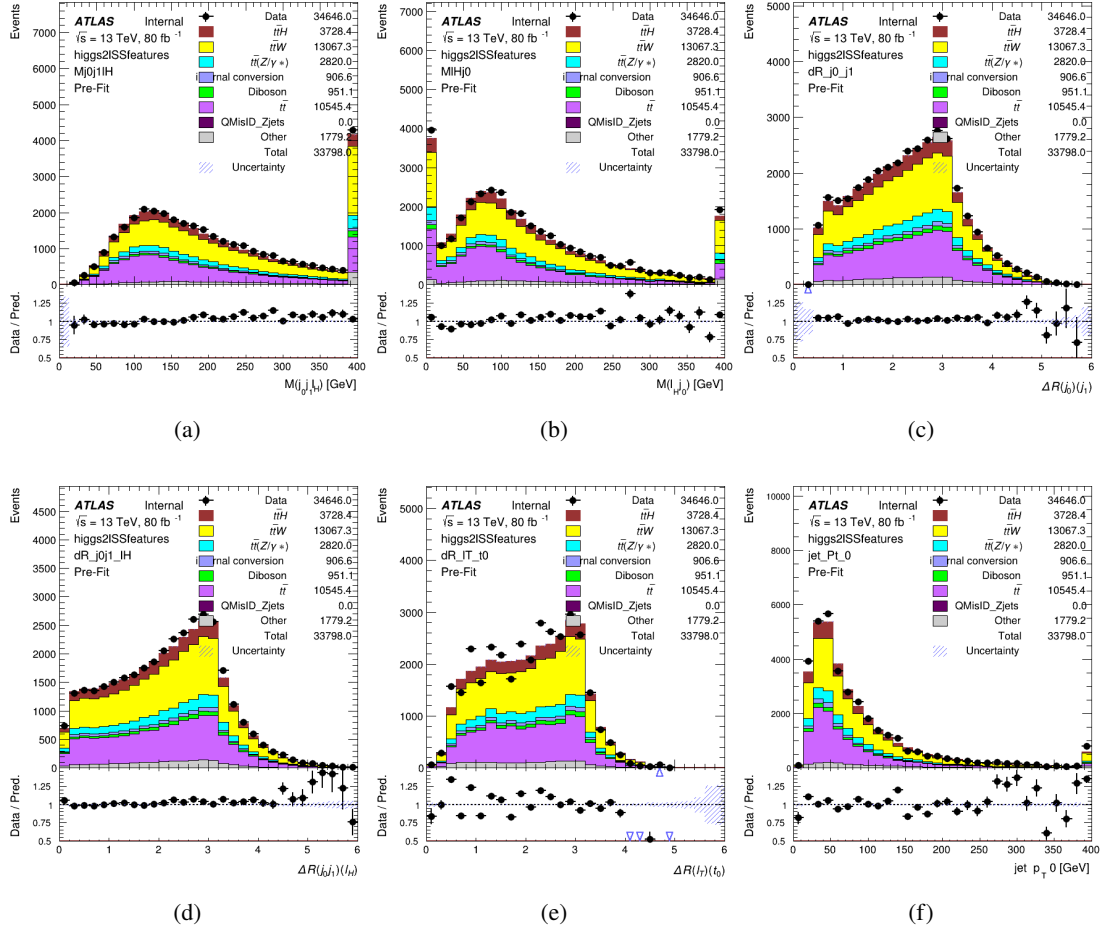


Figure 18.8: Data/MC comparisons of input features for higgs2ISS training for 79.8 fb^{-1} of data. (a) shows the invariant mass of the two jet candidates and the lepton candidate, (b) the invariant mass of jet 0 and the lepton candidate, (c) ΔR between the jet candidates, (d) ΔR between jet 0 + jet 1 and the lepton candidate, (e) ΔR between the lepton from the top and the leading b-jet, (f) the p_T of jet 0.

1355 A neural network consisting of 7 hidden layers with 60 nodes each is trained on around 2
 1356 million events, with an additional 200,000 reserved for testing the model. In order to compensate
 1357 for large number of incorrect combinations, these have been downsampled such that the correct
 1358 combinations represent over 10% of the training set. The output of the NN is summarized in
 1359 Figure 18.4.1.

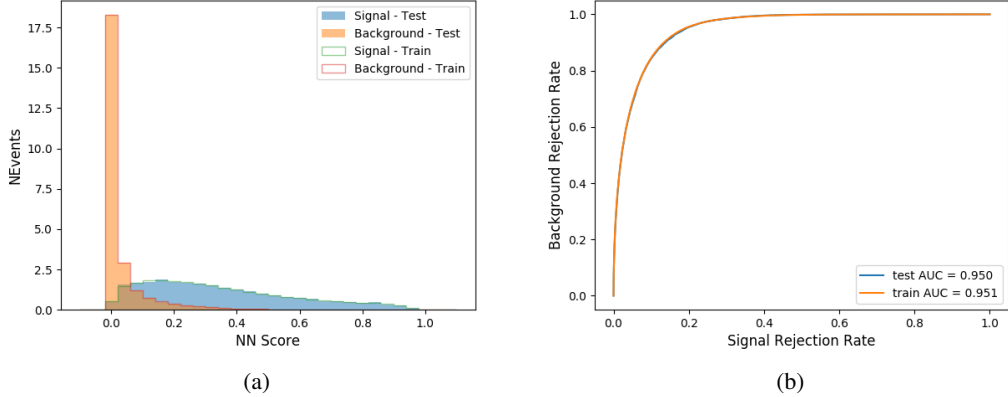


Figure 18.9: Result of the Higgs reconstruction algorithm in the 2lSS channel, showing (a) the output score of the NN for correct and incorrect combinations of jets scaled to an equal number of events, and (b) the ROC curve of the output, showing background rejection as a function of signal efficiency

1360 The neural network identifies the correct combination 55% of the time. It identifies the
 1361 correct lepton 85% of the time, and selects the correct lepton and at least one of the correct jets
 1362 81% of the time.

1363 **18.4.2 3l Semi-leptonic Channel**

1364 For 3l $t\bar{t}H$ where the Higgs decay semi-leptonically, the decay products include one of the three
 1365 leptons and two jets. In this case, the other two leptons originated from the decay of the tops,
 1366 meaning the opposite-sign (OS) lepton cannot have come from the Higgs. This leaves only the two
 1367 same-sign (SS) leptons as possible Higgs decay products.

Lepton $p_T H$	Lepton $p_T T_0$	Lepton $p_T T_1$
jet $p_T 0$	jet $p_T 1$	top $p_T 0$
top $p_T 1$	jet $\eta 0$	jet $\eta 1$
jet $\phi 0$	jet $\phi 1$	$\Delta R(j_0)(j_1)$
$M(j_0 j_1)$	$\Delta R(l_H)(j_0)$	$\Delta R(l_H)(j_1)$
$\Delta R(j_0 j_1)(l_H)$	$\Delta R(j_0 j_1)(l_{T_1})$	$\Delta R(l_{T_0})(l_{T_1})$
$\Delta R(l_H)(l_{T_1})$	$M(j_0 j_1 l_{T_0})$	$M(j_0 j_1 l_{T_1})$
$M(j_0 j_1 l_H)$	$\Delta R(j_0 j_1 l_H)(l_{T_0})$	$\Delta R(j_0 j_1 l_H)(l_{T_1})$
$\Delta\phi(j_0 j_1 l_H)(E_T^{\text{miss}})$	$p_T(j_0 j_1 l_H l_{T_0} l_{T_1} b_0 b_1 E_T^{\text{miss}})$	$M(j_0 j_1 b_0)$
$M(j_0 j_1 b_1)$	$\Delta R(l_{T_0})(b_0)$	$\Delta R(l_{T_0})(b_1)$
$\Delta R(l_{T_1})(b_0)$	$\Delta R(l_{T_1})(b_1)$	$\Delta R(j_0)(b_0)$
$\Delta R(j_0)(b_1)$	$\Delta R(j_1)(b_0)$	$\Delta R(j_1)(b_1)$
topScore	MET	HT jets
nJets		

Table 29: Input features used to identify the Higgs decay products in 31 semi-leptonic events

1368 Here j_0 and j_1 , and l_H are the jet and lepton decay candidates, respectively. The other
 1369 two leptons in the event are labeled as l_{T_0} and l_{T_1} . b_0 and b_1 are the two b-jets identified by
 1370 the b-jet identification algorithm. The b-jet Reco Score is the output of the b-jet identification
 1371 algorithm.

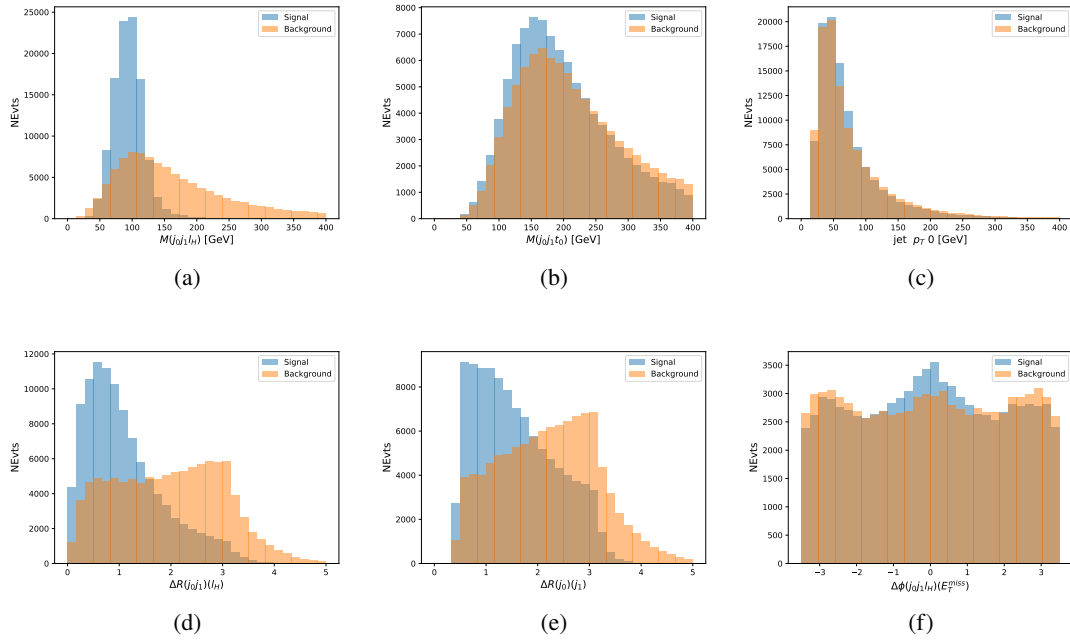


Figure 18.10: Input features for higgs3lS training. The signal in blue represents events where both jet candidates are truth b-jets from top decays, and the orange is all other combinations. Scaled to the same number of events.

1372 The modeling of these inputs is validated against data, with Figure 18.11 showing good
 1373 general agreement between data and MC. Plots for the complete list of features can found in
 1374 appendix C.1.

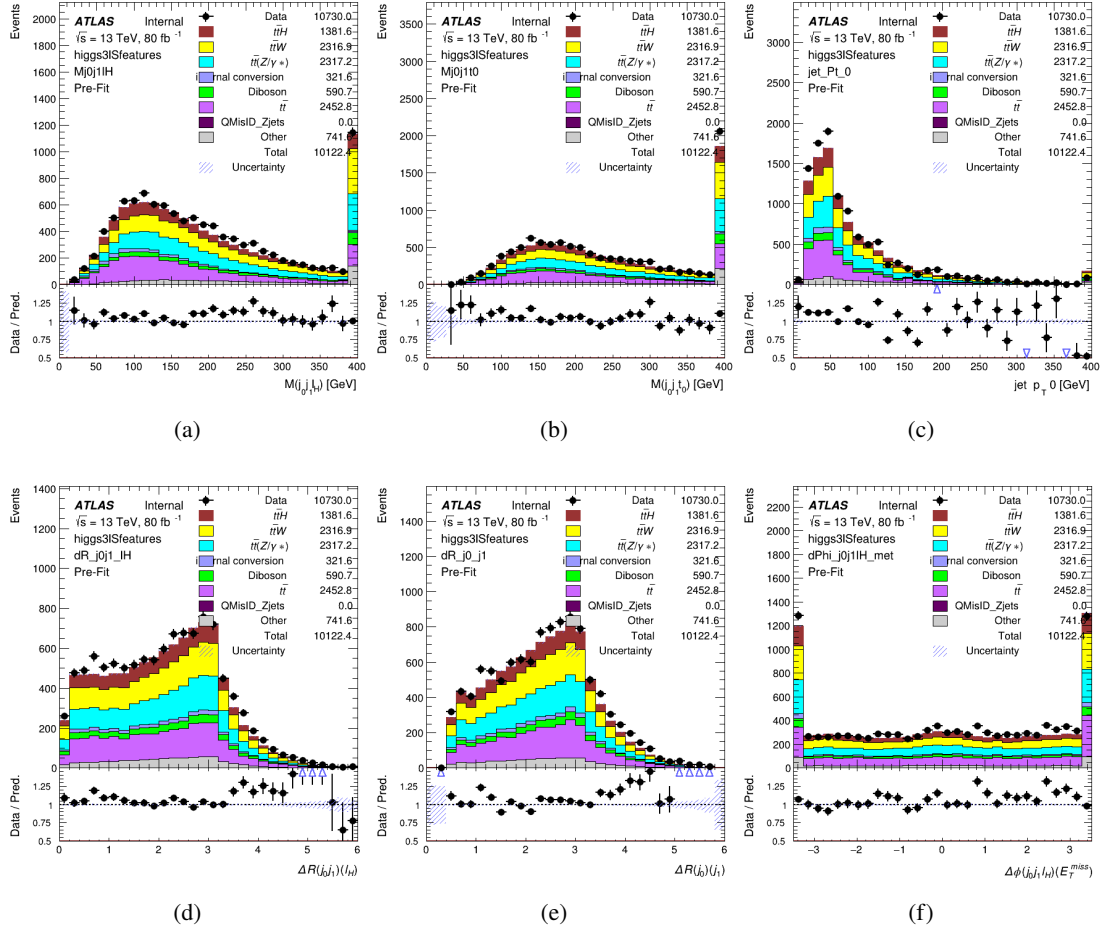


Figure 18.11: Data/MC comparisons of input features for higgs3lS training for 79.8 fb^{-1} of data.

1375 A neural network of 7 hidden layers with 70 nodes each is trained on 1.8 million events.
 1376 Once again, incorrect combinations are downsampled, such that the correct combinations are
 1377 around 10% of the training set. 10% of the dataset is reserved for testing. The output of the NN
 1378 is summarized in Figure 18.4.2.

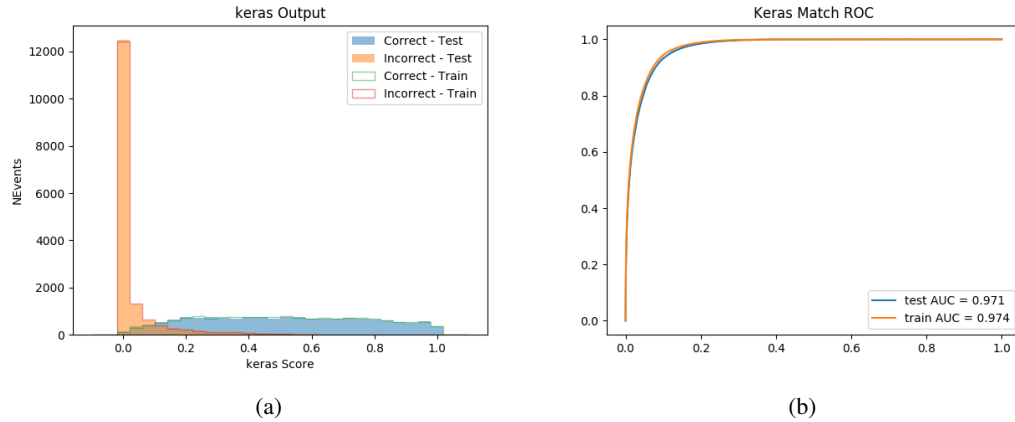


Figure 18.12: Results of the Higgs reconstruction algorithm in the 3lS channel, showing (a) the output score of the NN for correct and incorrect combinations of jets, scaled to an equal number of entries., (b) the ROC curve of the output, showing background rejection as a function of signal efficiency

1379 The neural network identifies the correct combination 64% of the time. It identifies the
1380 correct lepton 85% of the time, and selects the correct lepton and at least one of the correct jets
1381 83% of the time.

1382 18.4.3 3l Fully-leptonic Channel

In the fully-leptonic 3l case, the goal is identify which two of the three leptons originated from the Higgs decay. Since one of these two must be the OS lepton, this problem is reduced to determining which of the two SS leptons originated from the Higgs. The kinematics of both possibilities are used for training, one where the SS lepton from the Higgs is correctly labeled, and one where it is not.

Lepton $p_T H_1$	Lepton $p_T H_0$	Lepton $p_T T$
top $p_T 0$	top $p_T 1$	$\Delta\phi(l_{H_1})(E_T^{\text{miss}})$
$\Delta\phi(l_T)(E_T^{\text{miss}})$	$M(l_{H_0}l_{H_1})$	$M(l_{H_1}l_T)$
$M(l_{H_0}l_T)$	$\Delta R(l_{H_0})(l_{H_1})$	$\Delta R(l_{H_1})(l_T)$
$\Delta R(l_{H_0})(l_T)$	$\Delta R(l_{H_0}l_{H_1})(l_T)$	$\Delta R(l_{H_0}l_T)(l_{H_1})$
$\Delta R(l_{H_0}l_{H_1})(b_0)$	$\Delta R(l_{H_0}l_{H_1})(b_1)$	$\Delta R(l_{H_0}b_0)$
$M(l_{H_0}b_0)$	$\Delta R(l_{H_0}b_1)$	$M(l_{H_0}b_1)$
$\Delta R(l_{H_1}b_0)$	$M(l_{H_1}b_0)$	$\Delta R(l_{H_1}b_1)$
$M(l_{H_1}b_1)$	E_T^{miss}	topScore

Table 30: Input features used to identify the Higgs decay products in 3lF events

Table 31: Input features used to identify the Higgs decay products in 3l fully leptonic events

1388 Here l_{H_0} and l_{H_1} are the Higgs decay candidates. The other lepton in the event is labeled
 1389 l_T . b_0 and b_1 are the two b-jets identified by the b-jet identification algorithm. The b-jet Reco
 1390 Score is the output of the Higgs reconstruction algorithm.

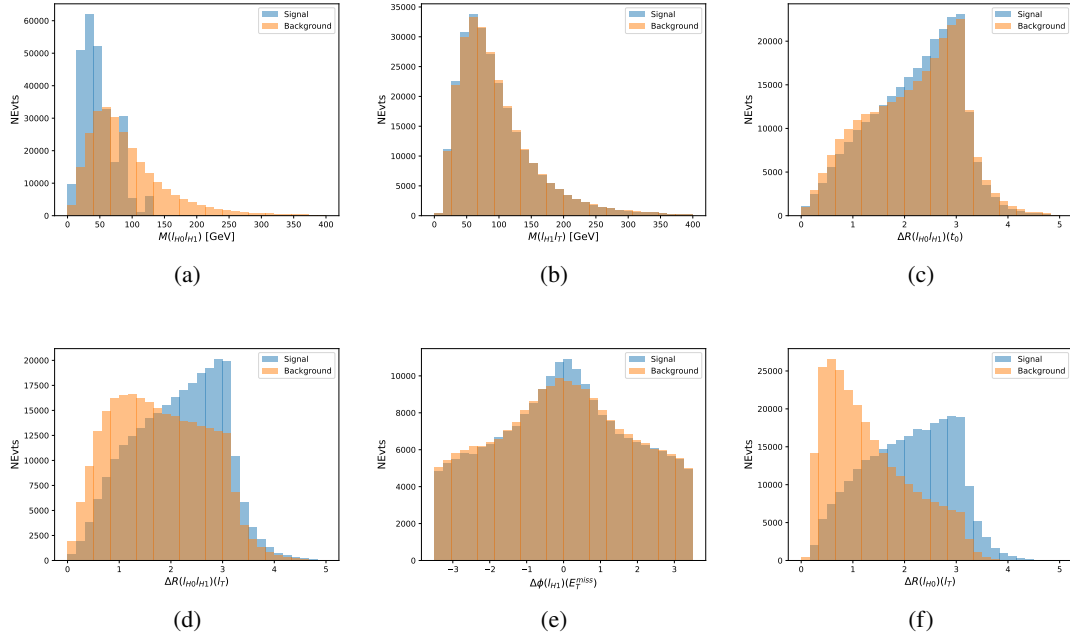


Figure 18.13: Input features for higgs3lF training. The signal in blue represents events where both jet candidates are truth b-jets from top decays, and the orange is all other combinations. Scaled to the same number of events.

1391 The modeling of these inputs is validated against data, with Figure 18.14 showing good
 1392 general agreement between data and MC. Plots for the complete list of features can found in
 1393 Section C.

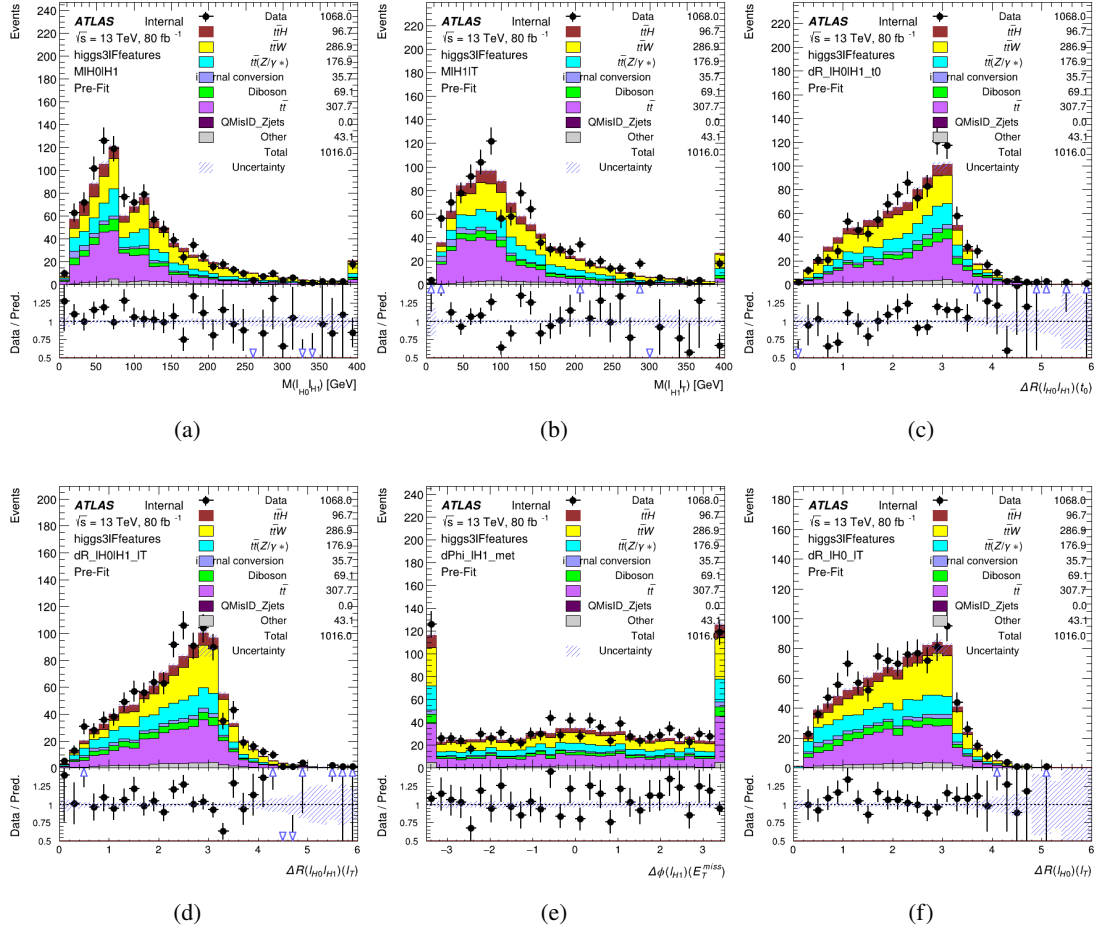


Figure 18.14: Data/MC comparisons of input features for higgs3lF training for 79.8 fb^{-1} of data.

1394 A neural network consisting of 5 nodes and 60 hidden units is trained on 800,000 events,

1395 with 10% of the dataset reserved for testing. The output of the model is summarized in Figure

1396 **18.4.3.**

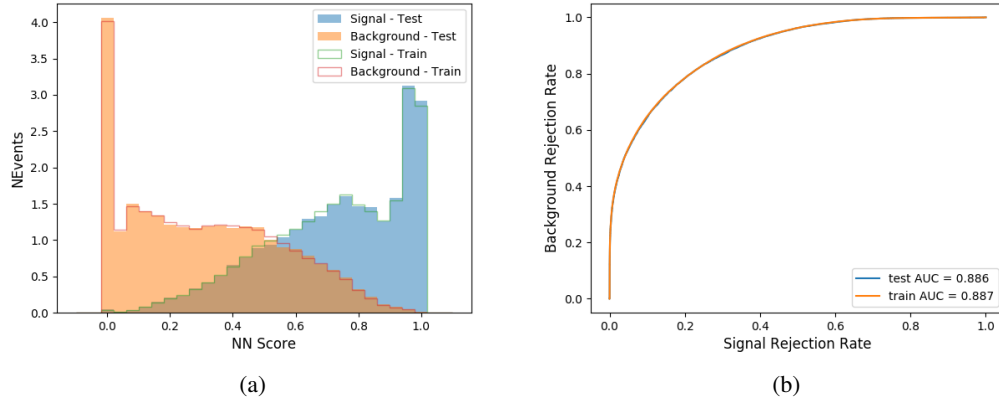


Figure 18.15: (a) the output score of the NN for correct and incorrect combinations of jets. (a) the ROC curve of the output, showing background rejection as a function of signal efficiency

1397 The correct lepton is identified by the model for 80% of events in the testing data set.

1398 18.5 p_T Prediction

1399 Once the most probable decay products have been identified, their kinematics are used as inputs
 1400 to a regression model which attempts to predict the momentum of the Higgs Boson. Once again,
 1401 a DNN is used. Input variables representing the b-jets and leptons not from the Higgs decay
 1402 are included as well, as these are found to improve performance. The truth p_T of the Higgs,
 1403 as predicted by MC, are used as labels. Separate models are built for each channel - 2lSS, 3l
 1404 Semi-leptonic and 3l Fully-leptonic.

1405 As a two-bin fit is targeted for the final result, some metrics evaluating the performance
 1406 of the models aim to show how well it distinguished between "high p_T " and "low p_T " events. A

1407 cutoff point of 150 GeV is used to define these two categories.

1408 Because the analysis uses a two bin fit of the Higgs p_T , the momentum reconstruction
1409 could be treated as a binary classification problem, rather than a regression problem. This
1410 approach is explored in detail in Section C.5, and is found not to provide any significant increase
1411 in sensitivity. The regression approach is used because it provides more flexibility for future
1412 analyses, as it is independent of the cutoff between high and low p_T , as well as the number of
1413 bins. Further, a regression allows the output of the neural network to be more clearly understood,
1414 as it can be directly compared to a physics observable.

1415 18.5.1 2lSS Channel

1416 The input variables listed in Table 32 are used to predict the Higgs p_T in the 2lSS channel. Here
1417 j_0 and j_1 are the two jets identified as Higgs decay products. The lepton identified as originating
1418 from the Higgs is labeled l_H , while the other lepton is labeled l_T , as it is assumed to have come
1419 from the decay of one of the top quarks. b_0 and b_1 are the two b-jets identified by the b-jet
1420 identification algorithm. The Higgs Reco Score and b-jet Reco Score are the outputs of the Higgs
1421 reconstruction algorithm, and the b-jet identification algorithm, respectively.

HT	$M(j_0 j_1)$	$M(j_0 j_1 l_H)$
$M(l_H j_0)$	$M(l_H j_1)$	$p_T(b_0 b_1)$
$p_T(j_0 j_1 l_H)$	$\Delta\phi(j_0 j_1 l_H)(E_T^{\text{miss}})$	$\Delta R(j_0)(j_1)$
$\Delta R(j_0 j_1)(l_H)$	$\Delta R(j_0 j_1 l_H)(l_T)$	$\Delta R(j_0 j_1 l_H)(b_0)$
$\Delta R(j_0 j_1 l_H)(b_1)$	$\Delta R(l_H)(j_0)$	$\Delta R(l_H)(b_0)$
$\Delta R(l_H)(b_1)$	$\Delta R(l_T)(b_0)$	$\Delta R(l_T)(b_1)$
$\Delta R(b_0)(b_1)$	Higgs Reco Score	jet η 0
jet η 1	jet Phi 0	jet Phi 1
jet p_T 0	jet p_T 1	Lepton η H
Lepton ϕ H	Lepton p_T H	Lepton p_T T
E_T^{miss}	nJets	b-jet Reco Score
b-jet p_T 0	b-jet p_T 1	

Table 32: Input features for reconstructing the Higgs p_T spectrum for 2lSS events

1422 The optimal neural network architecture for this channel is found to consist of 7 hidden
 1423 layers with 60 nodes each. The input data set includes 1.2 million events, 10% of which is used
 1424 for testing, the other 90% for training. Training is found to converge after around 150 epochs.

1425 To evaluate the performance of the model, the predicted p_T spectrum is compared to the
 1426 truth Higgs p_T in Figure 18.16. In order to visualize the model performance more clearly, in (a)
 1427 of that figure, the color of each point is determined by Kernel Density Estimation (KDE). The
 1428 color shown represents the logarithm of the output from KDE, to counteract the large number of
 1429 low p_T events. For that same reason, each column of the histogram shown in (b) of Figure 18.16
 1430 is normalized to unity. This plot therefore demonstrates what the model predicts for each slice
 1431 of truth p_T .

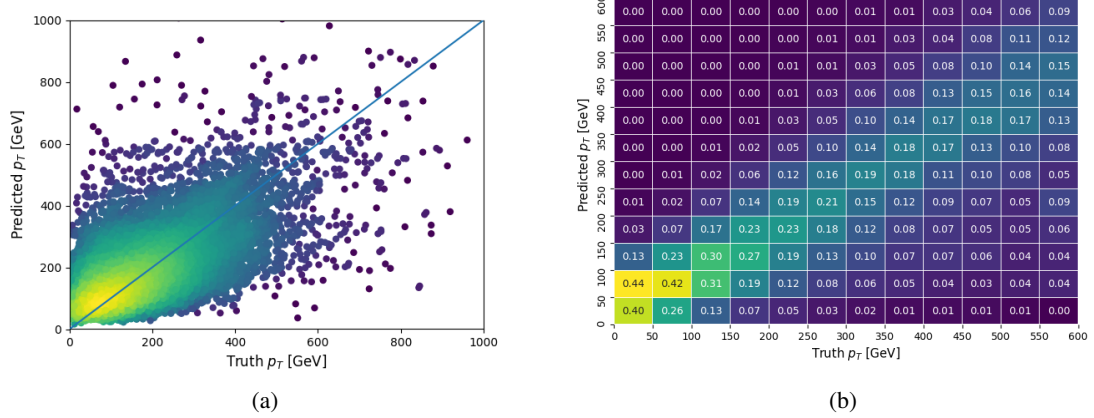


Figure 18.16: The regressed Higgs momentum spectrum as a function of the truth p_T for 2lSS $t\bar{t}H$ events in (a) a scatterplot, where the color of each point represents the log of the point density, based on Gaussian Kernel Density Estimation, and (b) a histogram where each column has been normalized to one.

1432 We are also interested in how well the model distinguishes between events with $p_T < 150$
 1433 GeV and > 150 GeV. Figure 18.17 demonstrates the NN output for high and low p_T events based
 1434 on this cutoff.

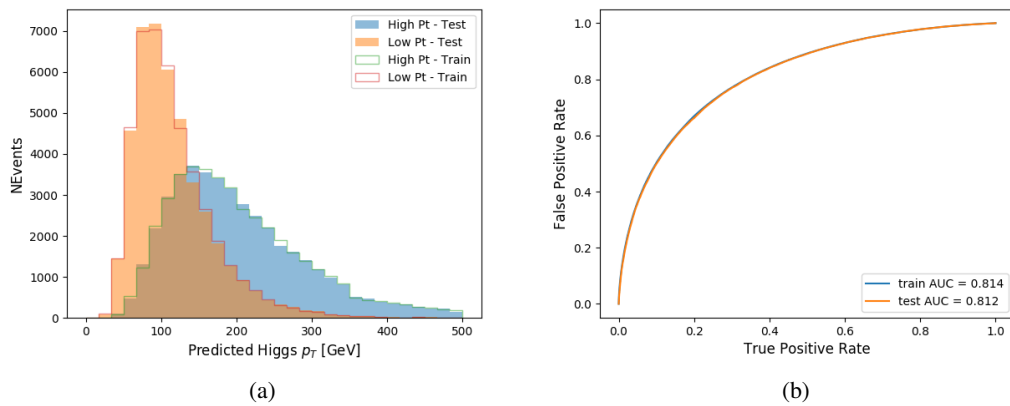


Figure 18.17: (a) shows the reconstructed Higgs p_T for 2lSS events with truth $p_T > 150$ GeV and < 150 GeV, while (b) shows the ROC curve for those two sets of events.

¹⁴³⁵ **18.5.2 3l Semi-leptonic Channel**

¹⁴³⁶ The following input features are used to predict the Higgs p_T for events in the 3lS channel:

HT jets	MET	$M(j_0 j_1)$
$M(j_0 j_1 l_H)$	$M(j_0 j_1 l_{T0})$	$M(j_0 j_1 l_{T1})$
$M(j_0 j_1 b_0)$	$M(j_0 j_1 b_1)$	$M(b_0 l_{T0})$
$M(b_0 l_{T1})$	$M(b_1 l_{T0})$	$M(b_1 l_{T1})$
$\Delta\phi(j_0 j_1 l_H)(E_T^{\text{miss}})$	$\Delta R(j_0)(j_1)$	$\Delta R(j_0 j_1)(l_H)$
$\Delta R(j_0 j_1)(l_{T1})$	$\Delta R(j_0 j_1)(b_0)$	$\Delta R(j_0 j_1)(b_1)$
$\Delta R(j_0 j_1 l_H)(l_{T0})$	$\Delta R(j_0 j_1 l_H)(l_{T1})$	$\Delta R(j_0 j_1 l_H)(b_0)$
$\Delta R(j_0 j_1 l_H)(b_1)$	$\Delta R(l_H)(j_0)$	$\Delta R(l_H)(j_1)$
$\Delta R(l_H)(l_{T1})$	$\Delta R(l_{T0})(l_{T1})$	$\Delta R(l_{T0})(b_0)$
$\Delta R(l_{T0})(b_1)$	$\Delta R(l_{T1})(b_0)$	$\Delta R(l_{T1})(b_1)$
higgsScore	jet η 0	jet η 1
jet ϕ 0	jet ϕ 1	jet p_T 0
jet p_T 1	Lepton η H	Lepton ϕ H
Lepton p_T H	Lepton p_T T0	Lepton p_T T1
nJets	topScore	b-jet p_T 0
b-jet p_T 1		

Table 33: Input features for reconstructing the Higgs p_T spectrum for 3lS events

¹⁴³⁷ Again, j_0 and j_1 are the two jets identified as Higgs decay products, ordered by p_T . The

¹⁴³⁸ lepton identified as originating from the Higgs is labeled l_H , while the other two leptons are

¹⁴³⁹ labeled l_{T0} and l_{T1} . b_0 and b_1 are the two b-jets identified by the b-jet identification algorithm.

¹⁴⁴⁰ The Higgs Reco Score and b-jet Reco Score are the outputs of the Higgs reconstruction algorithm,

¹⁴⁴¹ and the b-jet identification algorithm, respectively.

¹⁴⁴² The optimal neural network architecture for this channel is found to consist of 7 hidden

¹⁴⁴³ layers with 80 nodes each. The inputdata set includes one million events, 10% of which is used

¹⁴⁴⁴ for testing, the other 90% for training. Training is found to converge after around 150 epochs.

1445 To evaluate the performance of the model, the predicted p_T spectrum is compared to the
 1446 truth Higgs p_T in Figure 18.18. Once again, (a) of 18.18 shows a scatterplots of predicted vs
 1447 truth p_T , where the color of each point corresponds to the log of the relative KDE at that point.
 1448 Each column of the the histogram in (b) is normalized to unity, to better demonstrate the output
 1449 of the NN for each slice of truth p_T .

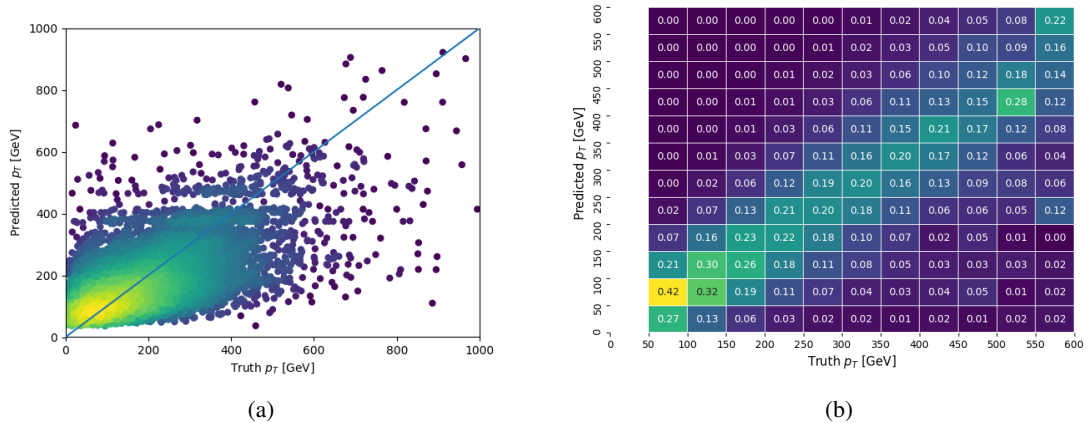


Figure 18.18: The regressed Higgs momentum spectrum as a function of the truth p_T for 3lS $t\bar{t}H$ events in (a) a scatterplot, where the color of each point represents the log of the point density, based on Gaussian Kernel Density Estimation, and (b) a histogram where each column has been normalized to one.

1450 Figure 18.19 shows (a) the output of the NN for events with truth p_T less than and greater
 1451 than 150 GeV and (b) the ROC curve demonstrating how well the NN distinguishes high and low
 1452 p_T events.

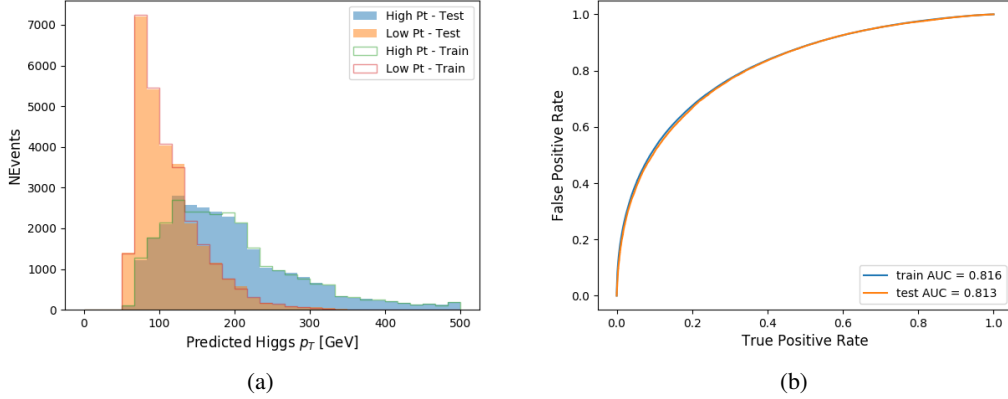


Figure 18.19: (

a) shows the reconstructed Higgs p_T for 3lS events with truth $p_T > 150$ GeV and < 150 GeV, while (b) shows the ROC curve for those two sets of events.

1453 18.5.3 3l Fully-leptonic Channel

1454 The features listed in 34 are used to construct a model for predictin the Higgs p_T for 3lF events.

HT	$M(l_{H0}l_{H1})$	$M(l_{H0}l_T)$
$M(l_{H0}b_0)$	$M(l_{H0}b_1)$	$M(l_{H1}l_T)$
$M(l_{H1}b_0)$	$M(l_{H1}b_1)$	$\Delta R(l_{H0})(l_{H1})$
$\Delta R(l_{H0})(l_T)$	$\Delta R(l_{H0}l_{H1})(l_T)$	$\Delta R(l_{H0}l_T)(l_{H1})$
$\Delta R(l_{H1})(l_T)$	$\Delta R(l_{H0}b_0)$	$\Delta R(l_{H0}b_1)$
$\Delta R(l_{H1}b_1)$	$\Delta R(l_{H1}b_0)$	higgsScore
Lepton η H_0	Lepton η H_1	Lepton η T
Lepton p_T H_0	Lepton p_T H_1	Lepton p_T T
E_T^{miss}	topScore	b-jet p_T 0
b-jet p_T 1		

Table 34: Input features for reconstructing the Higgs p_T spectrum for 3lF events

1455 l_{H0} and l_{H1} respresent the two leptons identified by the Higgs reconstruction model as

1456 originating from the Higgs, while l_T is the other lepton in the event. The Higgs Reco Score and
 1457 b-jet Reco Score are the outputs of the Higgs reconstruction algorithm, and b-jet identification
 1458 algorithm, respectively.

1459 The optimal neural network architecture for this channel is found to consist of 5 hidden
 1460 layers with 40 nodes each. The input data set includes 400,000 events, 10% of which is used for
 1461 testing, the other 90% for training. Training is found to converge after around 150 epochs.

1462 The predicted transverse momentum, as a function of the truth p_T , is shown in Figure
 1463 [18.20](#).

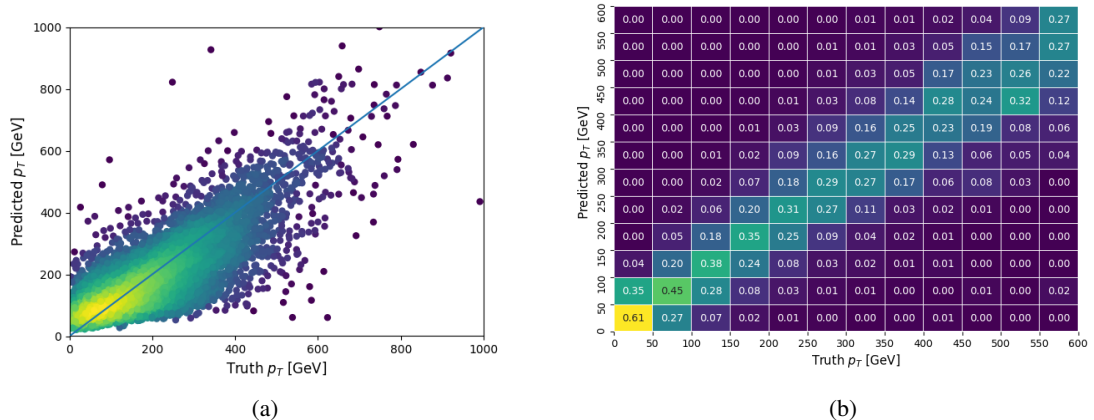


Figure 18.20: The regressed Higgs momentum spectrum as a function of the truth p_T for 3lF $t\bar{t}H$ events in (a) a scatterplot, where the color of each point represents the log of the point density, based on Gaussian Kernel Density Estimation, and (b) a histogram where each column has been normalized to one.

1464 When split into high and low p_T , based on a cutoff of 150 GeV, the

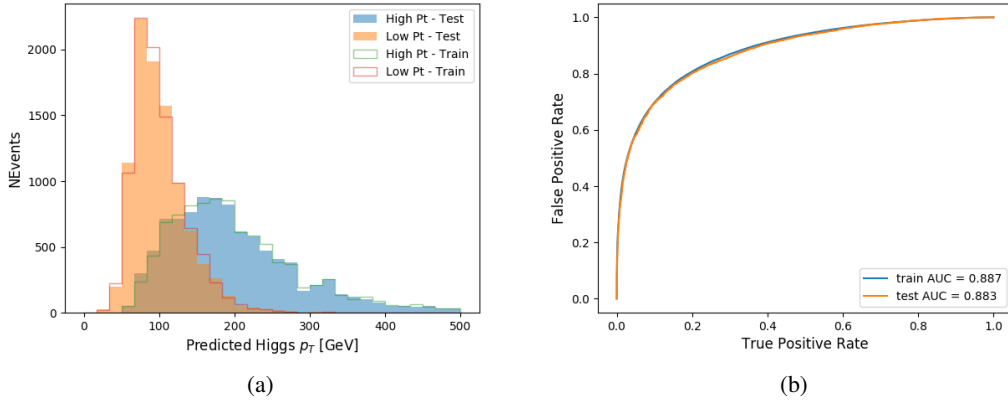


Figure 18.21: (a) shows the reconstructed Higgs p_T for 3lF events with truth $p_T > 150$ GeV and < 150 GeV, while (b) shows the ROC curve for those two sets of events.

1465 18.6 3l Decay Mode

1466 In the 3l channel, there are two possible ways for the Higgs to decay, both involving intermediate
 1467 W boson pairs: Either both W bosons decay leptonically, in which case the reconstructed decay
 1468 consists of two leptons (referred as the fully-leptonic 3l channel), or one W decays leptonically
 1469 and the other hadronically, giving two jets and one lepton in the final state (referred to as the
 1470 semi-leptonic 3l channel). In order to accurately reconstruct the Higgs, it is necessary to identify
 1471 which of these decays took place for each 3l event.

1472 The kinematics of each event, along with the output scores of the Higgs and top recon-
 1473 struction algorithms, are used to distinguish these two possible decay modes. The particular
 1474 inputs used are listed in Table 35.

HT jets	$M(l_0 t_0)$	$M(l_0 t_1)$
$M(l_1 t_0)$	$M(l_1 t_1)$	$M(l_0 l_1)$
$M(l_0 l_2)$	$M(l_1 l_2)$	$\Delta R(l_0 t_0)$
$\Delta R(l_0 t_1)$	$\Delta R(l_1 t_0)$	$\Delta R(l_1 t_1)$
$\Delta R(l l_0 1)$	$\Delta R(l l_0 2)$	$\Delta R(l l_1 2)$
Lepton η 0	Lepton η 1	Lepton η 2
Lepton ϕ 0	Lepton ϕ 1	Lepton ϕ 2
Lepton p_T 0	Lepton p_T 1	Lepton p_T 2
E_T^{miss}	nJets	nJets OR DL1r 60
nJets OR DL1r 85	score3lF	score3lS
topScore	total charge	

Table 35: Input features used to distinguish semi-leptonic and fully-leptonic Higgs decays in the 3l channel.

1475 Here l_0 is the opposite charge lepton, l_1 and l_2 are the two SS leptons order by ΔR
 1476 from lepton 0. score3lF and score3lS are the outputs of the 3lS and 3lF Higgs reconstruction
 1477 algorithms, while topScore is the output of the b-jet identification algorithm.

1478 A neural network with 5 hidden layers, each with 50 nodes, is trained to distinguish these
 1479 two decay modes. The output of the model is summarized in Figure 18.22.

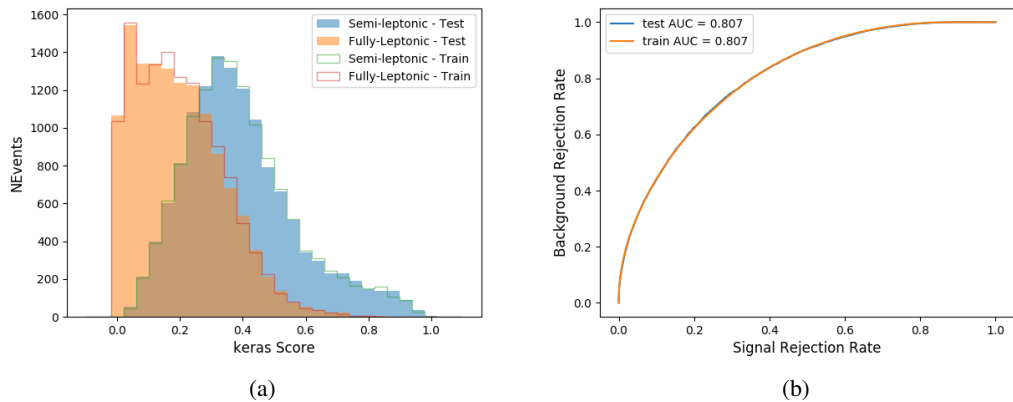


Figure 18.22: (a) shows the output of the decay separation NN for Semi-leptonic (blue) and Fully-leptonic (orange) 3l events, scaled to equal area. (b) shows the ROC curve for those two sets of events.

1480 A cutoff of 0.23 is determined to be optimal for separating 3lS and 3lF in the fit.

1481 19 Signal Region Definitions

1482 Events are divided into two channels based on the number of leptons in the final state: one with
1483 two same-sign leptons, the other with three leptons. The 3l channel includes events where both
1484 leptons originated from the Higgs boson as well as events where only one of the leptons

1485 19.1 Pre-MVA Event Selection

1486 A preselection is applied to define orthogonal analysis channels based on the number of leptons
1487 in each event. For the 2lSS channel, the following preselection is used:

- 1488 • Two very tight, same-charge, light leptons with $p_T > 20$ GeV
- 1489 • ≥ 4 reconstructed jets, ≥ 1 b-tagged jets
- 1490 • No reconstructed tau candidates

1491 The event yield after the 2lSS preselection has been applied, for MC and data at 79.8 fb^{-1} ,
1492 is shown in Table 19.1.

Process	Yield
t̄tH high p _T	41 ± 5
t̄tH low p _T	71 ± 8
t̄tW	450 ± 70
t̄t(Z/γ*)	91 ± 11
t̄tll low mass	10 ± 6
Rare Top	20 ± 12
VV	42 ± 22
tZ	10 ± 5
QMisID	44.7 ± 2.7
Fakes int. conv	47 ± 26
Fakes ext. conv	46 ± 44
Fakes HF e	45 ± 23
Fakes HF μ	250 ± 50
Three top	2.2 ± 1.1
Four top	5.64 ± 0.31
t̄tWW	10.9 ± 0.6
tW	0.0 ± 0.0
WtZ	9.1 ± 0.8
VVV	0.30 ± 0.05
VH	0.6 ± 1.0
Total	1170 ± 120
Data	1108

Table 36: Yields of the 2lSS preselection region

1493

Figure 19.1. Good general agreement is found.

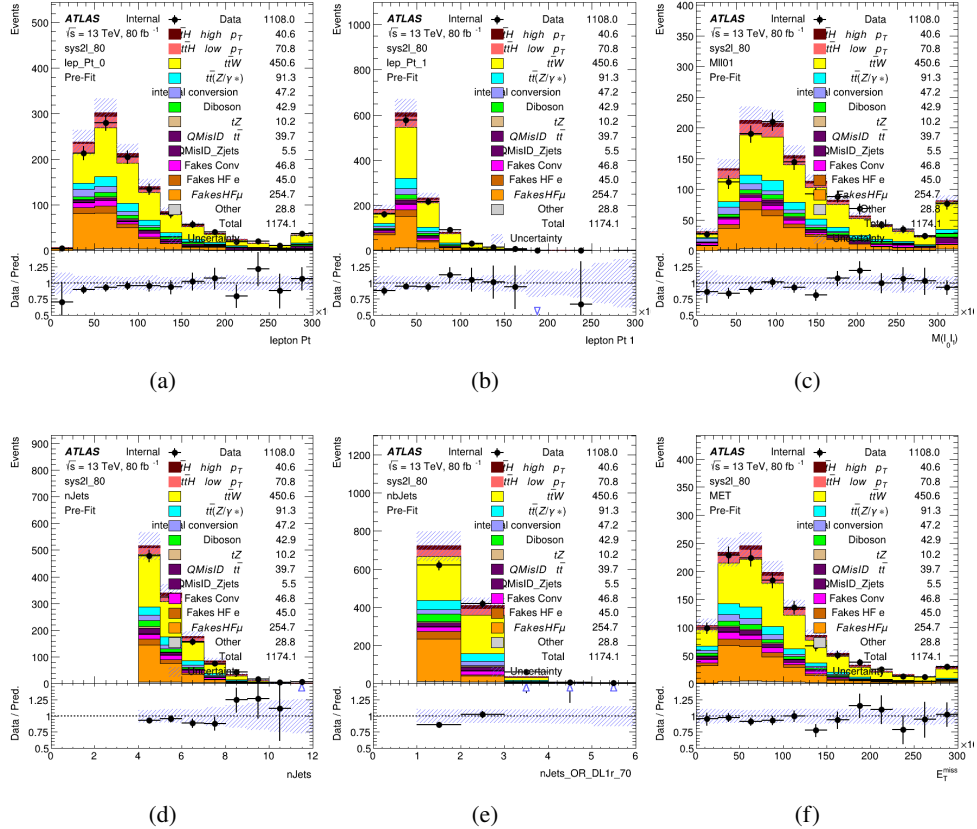


Figure 19.1: Data/MC comparisons of the 2LSS pre-selection region. (a) and (b) show the p_T of leptons 0 and 1, (c) shows the invariant mass of lepton 0 and 1, (d) shows the jet multiplicity, (e) the b-tagged jet multiplicity, and (f) the missing transverse energy.

1494

For the 3l channel, the following selection is applied:

1495

- Three light leptons with total charge ± 1
- Same charge leptons are required to be very tight, with $p_T > 20 \text{ GeV}$
- Opposite charge lepton must be loose, with $p_T > 10 \text{ GeV}$
- ≥ 2 reconstructed jets, ≥ 1 b-tagged jets

1497

- 1499 • No reconstructed tau candidates
- 1500 • $|M(l^+l^-) - 91.2 \text{ GeV}| > 10 \text{ GeV}$ for all opposite-charge, same-flavor lepton pairs
- 1501 The event yield after the 3l preselection has been applied, for MC and data at 79.8 fb^{-1} ,
- 1502 is shown in Table 19.1.

Process	Yield
t̄tH high p _T	20.5 ± 2.3
t̄tH low p _T	33.6 ± 3.8
t̄tW	138 ± 18
t̄tZ/γ	80 ± 9
t̄tlllowmass	3.5 ± 2.0
rareTop	22 ± 12
VV	39 ± 19
tZ	9.2 ± 4.5
QMisID	1.8 ± 0.6
Fakes int. conv	31 ± 17
Fakes ext. conv	14 ± 11
Fakes HF e	20 ± 10
Fakes HF μ	102 ± 22
Three top	0.96 ± 0.48
Four top	6.17 ± 0.35
t̄tWW	5.46 ± 0.33
tW	0.0 ± 0.0
WtZ	8.7 ± 0.6
VVV	0.81 ± 0.11
VH	0.0 ± 0.0
Total	512 ± 48
Data	535

Table 37: Yields of the 3l preselection region.

Table 38: Yields of the 3l preselection region.

1503 Comparisons of kinematic distributions for data and MC in this region are shown in Figure

1504 19.2.

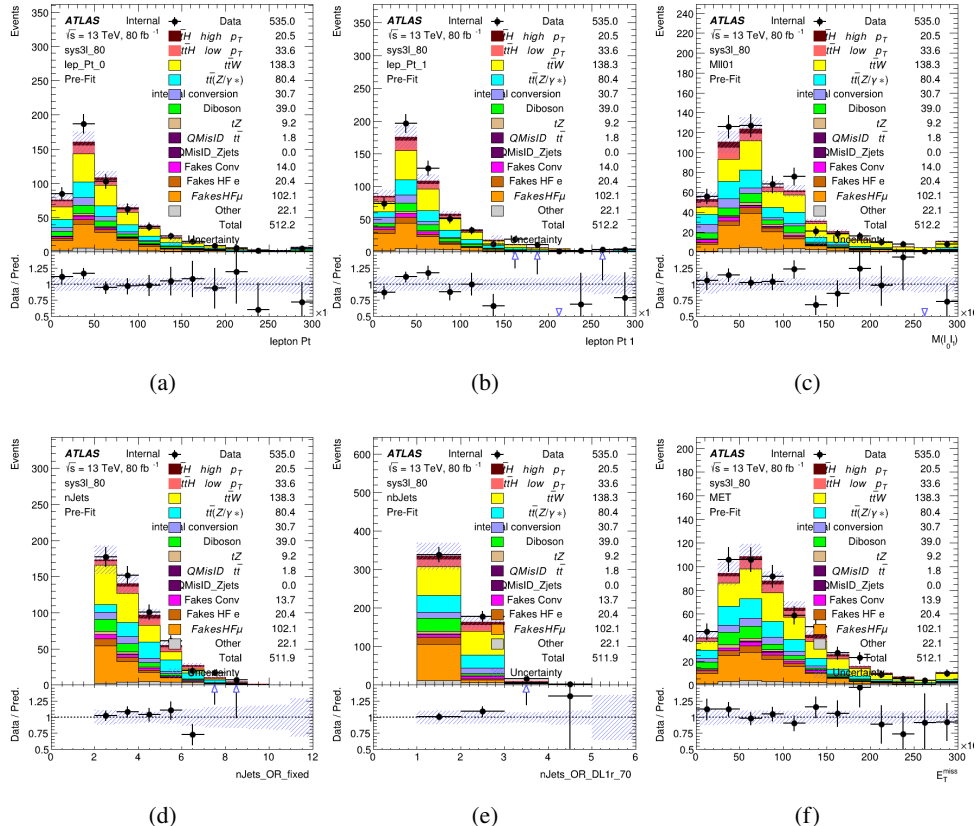


Figure 19.2: Data/MC comparisons of the 3l pre-selection region. (a) and (b) show the p_T of leptons 0 and 1, (c) shows the invariant mass of lepton 0 and 1, (d) shows the jet multiplicity, (e) the b-tagged jet multiplicity, and (f) the missing transverse energy.

1505 19.2 Event MVA

1506 Separate multi-variate analysis techniques (MVAs) are used in order to distinguish signal events
 1507 from background for each analysis channel - 2lSS, 3l semi-leptonic (3lS), and 3l fully leptonic
 1508 (3lF). Here events with three leptons are split into 3lS and 3lF based on the model described
 1509 in 18.6. In particular, Boosted Decision Tree (BDT) algorithms are produced with XGBoost

1510 [xgboost] are trained using the kinematics of signal and background events derived from Monte
 1511 Carlo simulations. Events are weighted in the BDT training by the weight of each Monte Carlo
 1512 event.

1513 Because the background composition differs for events with a high reconstructed Higgs p_T
 1514 compared to events with low reconstructed Higgs p_T , separate MVAs are produced for high and
 1515 low p_T regions. This is found to provide better significance than attempting to build an inclusive
 1516 model, as demonstrated in appendix C.2. A cutoff of 150 GeV is used. This gives a total of 6
 1517 background rejection MVAs - explicitly, 2lSS high p_T , 2lSS low p_T , 3lS high p_T , 3lS low p_T ,
 1518 3lF high p_T , and 3lF low p_T .

1519 The following features are used in both the high and low p_T 2lSS BDTs:

HT	$M(\text{lep}, E_T^{\text{miss}})$	$M(l_0 l_1)$
binHiggs p_T 2lSS	$\Delta R(l_0)(l_1)$	diLepton type
higgsRecoScore	jet η 0	jet η 1
jet ϕ 0	jet ϕ 1	jet p_T 0
jet p_T 1	Lepton η 0	Lepton η 1
Lepton ϕ 0	Lepton ϕ 1	Lepton p_T 0
Lepton p_T 1	E_T^{miss}	$\min \Delta R(l_0)(\text{jet})$
$\min \Delta R(l_1)(\text{jet})$	$\min \Delta R(\text{Lepton})(\text{bjet})$	mjjMax frwdJet
nJets	nJets OR DL1r 60	nJets OR DL1r 70
nJets OR DL1r 85	topRecoScore	

Table 39: Input features used to distinguish signal and background events in the 2lSS channel.

1520 While for each of the 3l BDTs, the features listed below are used for training:

$M(\text{lep}, E_T^{\text{miss}})$	$M(l_0 l_1)$	$M(l_0 l_1 l_2)$
$M(l_0 l_2)$	$M(l_1 l_2)$	$\text{binHiggs } p_T \text{ 3lS}$
$\Delta R(l_0)(l_2)$	$\Delta R(l_0)(l_1)$	$\Delta R(l_0)(l_2)$
higgsRecoScore3lS	decayScore	higgsRecoScore3lF
$\text{jet } \eta \text{ 0}$	$\text{jet } \eta \text{ 1}$	$\text{jet } \eta \text{ 1}$
$\text{jet } \phi \text{ 0}$	$\text{jet } \phi \text{ 1}$	$\text{jet } p_T \text{ 0}$
$\text{jet } p_T \text{ 1}$	$\text{Lepton } \eta \text{ 0}$	$\text{Lepton } \eta \text{ 1}$
$\text{Lepton } \eta \text{ 2}$	$\text{Lepton } \phi \text{ 0}$	$\text{Lepton } \phi \text{ 1}$
$\text{Lepton } \phi \text{ 2}$	$\text{Lepton } p_T \text{ 0}$	$\text{Lepton } p_T \text{ 1}$
$\text{Lepton } p_T \text{ 2}$	E_T^{miss}	$\min \Delta R(l_0)(\text{jet})$
$\min \Delta R(l_1)(\text{jet})$	$\min \Delta R(l_2)(\text{jet})$	$\min \Delta R(\text{Lepton})(\text{bjet})$
$mjj\text{Max frwdJet}$	$n\text{Jets}$	$n\text{Jets OR DL1r 60}$
$n\text{Jets OR DL1r 70}$	$n\text{Jets OR DL1r 85}$	topScore

Table 40: Input features used to distinguish signal and background events in the 3l channel.

1521 Modelling of each of these input features is verified in Appendix C.2 by comparing data
 1522 and MC for 79.8 fb^{-1} . The BDTs are produced with a maximum tree depth of 6, using AUC as
 1523 the target loss function. The BDT response distribution and ROC curve for each model is shown
 1524 in Figures 19.3-19.5.

2LSS

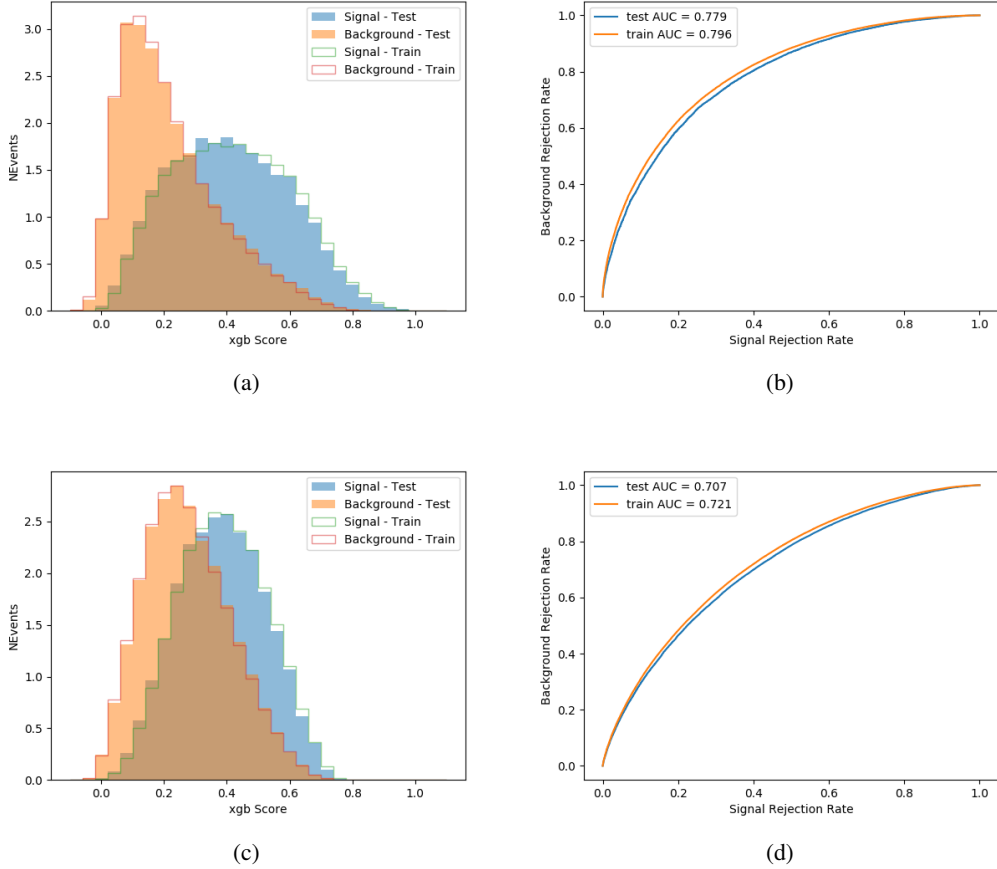


Figure 19.3: Output BDT scores of training and testing data for signal (blue) and background (orange) for 2LSS events with (a) high regressed Higgs p_T and (b) low regressed Higgs p_T . (b) and (d) show the ROC curve for the 2LSS high and low p_T models, respectively.

3l - Semileptonic

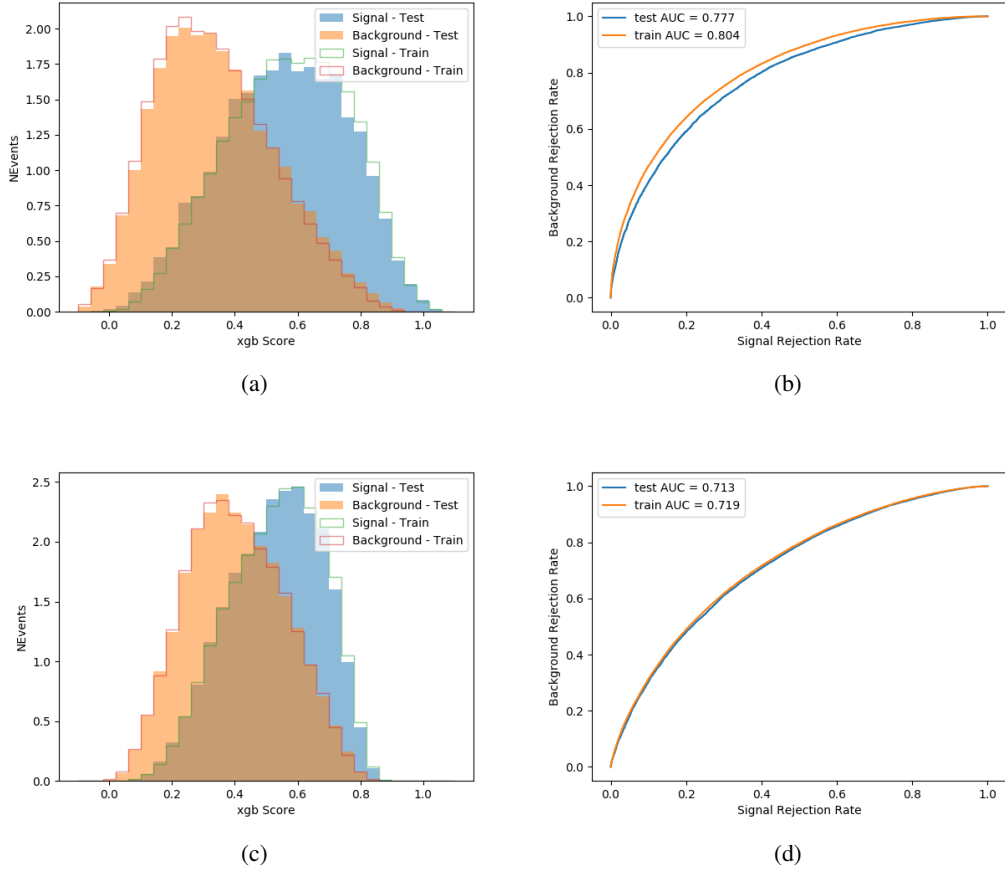


Figure 19.4: Output BDT scores of training and testing data for signal (blue) and background (orange) for 3lS events with (a) high regressed Higgs p_T and (b) low regressed Higgs p_T . (b) and (d) show the ROC curve for the 3lS high and low p_T models, respectively.

3l - Fully Leptonic

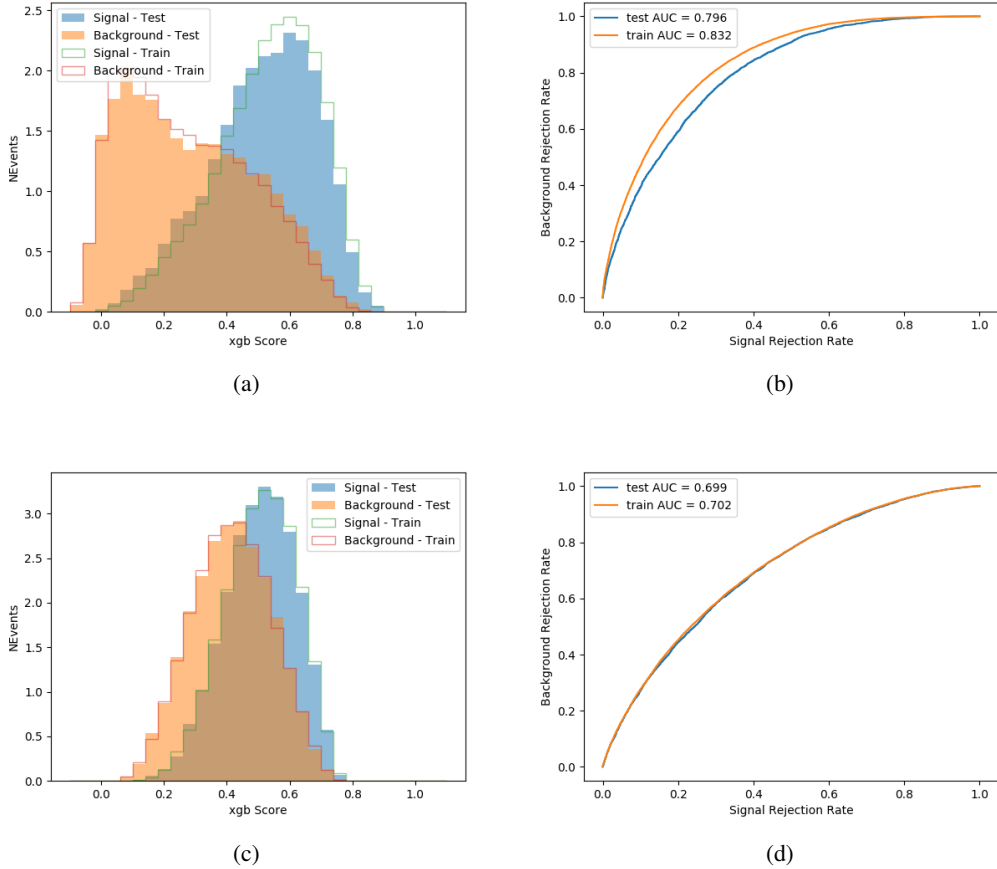


Figure 19.5: Output BDT scores of training and testing data for signal (blue) and background (orange) for 3lF events with (a) high regressed Higgs p_T and (b) low regressed Higgs p_T . (b) and (d) show the ROC curve for the 3lF high and low p_T models, respectively.

1525 Output distributions of each MVA, comparing MC predictions to data at 79.8 fb^{-1} are
 1526 shown in figures 19.6-19.2.

High p_T Background Rejection BDTs

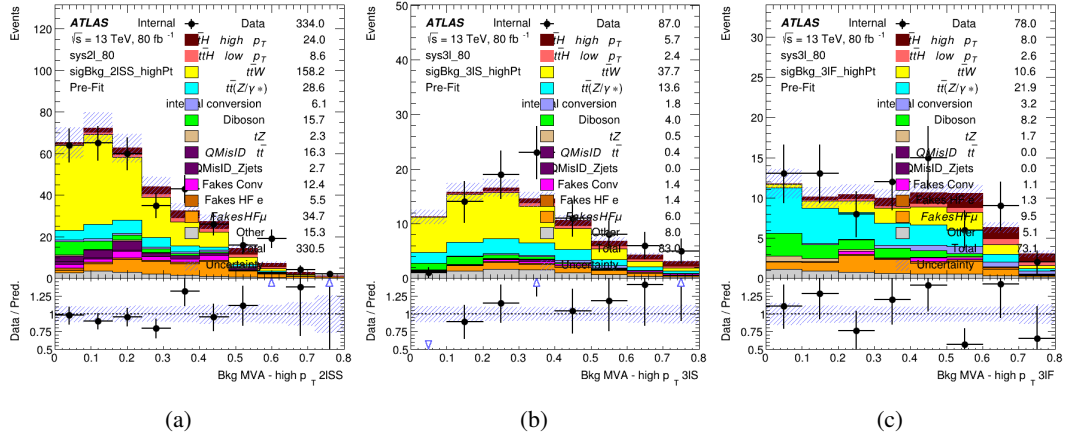


Figure 19.6: Output score of the high p_T BDTs in the (a) 2ISS, (b) 3IS, and (c) 3IF channels

Low p_T Background Rejection BDTs

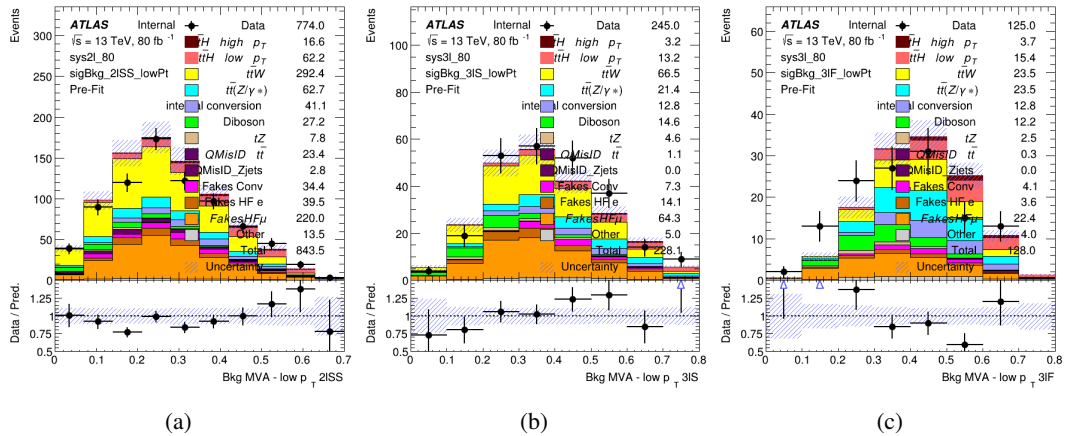


Figure 19.7: Output score of the low p_T BDTs in the (a) 2ISS, (b) 3IS, and (c) 3IF channels

1527 **19.3 Signal Region Definitions**

1528 Once pre-selection has been applied, channels are further refined based on the MVAs described
 1529 above. The output of the model described in Section 18.6 is used to separate the three channel
 1530 into two - Semi-leptonic and Fully-leptonic - based on the predicted decay mode of the Higgs
 1531 boson. This leaves three orthogonal signal regions - 2lSS, 3lS, and 3lF.

1532 For each event, depending on the number of leptons as well as whether the p_T of the Higgs
 1533 is predicted to be high (> 150 GeV) or low (< 150 GeV), a cut on the appropriate background
 1534 rejection MVA is applied. The particular cut values, listed in Table 41, are determined by
 1535 maximizing S/\sqrt{B} in each region.

Channel	BDT Score
2lSS high p_T	0.36
2lSS low p_T	0.34
3lS high p_T	0.51
3lS low p_T	0.43
3lF high p_T	0.33
3lF low p_T	0.41

Table 41: Cutoff values on background rejection MVA score applied to signal regions.

1536 The event preselection and MVA selection listed in Table 41 are used define the three
 1537 signal regions used in the fit. These signal region definitions are summarized in Table 42.

Region	Selection
2ISS	Two same charge tight leptons with $p_T > 20 \text{ GeV}$ $N_{\text{jets}} \geq 4, N_{\text{b-jets}} \geq 1$ b-tagged jets Zero τ_{had} $H_{p_T}^{\text{pred}} > 150 \text{ GeV}$ and BDT score > 0.36 or $H_{p_T}^{\text{pred}} < 150 \text{ GeV}$ and BDT score > 0.34
3IS	Three light leptons with total charge ± 1 Two tight SS leptons, $p_T > 20 \text{ GeV}$ One loose OS lepton, $p_T > 10 \text{ GeV}$ $N_{\text{jets}} \geq 2, N_{\text{b-jets}} \geq 1$ b-tagged jets Zero τ_{had} $ M(l^+l^-) - 91.2 \text{ GeV} > 10 \text{ GeV}$ for all OSSF lepton pairs Decay NN Score < 0.23 $H_{p_T}^{\text{pred}} > 150 \text{ GeV}$ and BDT score > 0.51 or $H_{p_T}^{\text{pred}} < 150 \text{ GeV}$ and BDT score > 0.43
3IF	Three light leptons with total charge ± 1 Two tight SS leptons, $p_T > 20 \text{ GeV}$ One loose OS lepton, $p_T > 10 \text{ GeV}$ $N_{\text{jets}} \geq 2, N_{\text{b-jets}} \geq 1$ b-tagged jets Zero τ_{had} $ M(l^+l^-) - 91.2 \text{ GeV} > 10 \text{ GeV}$ for all OSSF lepton pairs Decay NN Score > 0.23 $H_{p_T}^{\text{pred}} > 150 \text{ GeV}$ and BDT score > 0.33 or $H_{p_T}^{\text{pred}} < 150 \text{ GeV}$ and BDT score > 0.41

Table 42: Selection applied to define the three signal regions used in the fit.

20 Systematic Uncertainties

1538 The systematic uncertainties that are considered are summarized in Table 43. These are imple-
 1539 mented in the fit either as a normalization factors or as a shape variation or both in the signal
 1540 and background estimations. The numerical impact of each of these uncertainties is outlined in
 1541 section 21.
 1542

Table 43: Sources of systematic uncertainty considered in the analysis. Some of the systematic uncertainties are split into several components, as indicated by the number in the rightmost column.

Systematic uncertainty	Components
Luminosity	1
Pileup reweighting	1
Physics Objects	
Electron	6
Muon	15
Jet energy scale and resolution	28
Jet vertex fraction	1
Jet flavor tagging	131
E_T^{miss}	3
Total (Experimental)	186
Background Modeling	
Cross section	24
Renormalization and factorization scales	10
Parton shower and hadronization model	2
Shower tune	4
Total (Signal and background modeling)	40
Background Modeling	
Cross section	24
Renormalization and factorization scales	10
Parton shower and hadronization model	2
Shower tune	4
Total (Signal and background modeling)	40
Total (Overall)	226

¹⁵⁴³ The uncertainty in the combined integrated luminosity is derived from a calibration of the

¹⁵⁴⁴ luminosity scale using x-y beam-separation scans performed for 13 TeV proton-proton data [29],

¹⁵⁴⁵ [30].

¹⁵⁴⁶ The experimental uncertainties are related to the reconstruction and identification of light

¹⁵⁴⁷ leptons and b-tagging of jets, and to the reconstruction of E_T^{miss} .

1548 The sources which contribute to the uncertainty in the jet energy scale [31] are decomposed
 1549 into uncorrelated components and treated as independent sources in the analysis. This method
 1550 decomposes the uncertainties into 30 nuisance parameters included in the fit. A similar method
 1551 is used to account for jet energy resolution (JER) uncertainties, and 8 JER uncertainty components
 1552 are included as NPs in the fit.

1553 The uncertainties in the b-tagging efficiencies measured in dedicated calibration analyses
 1554 [32] are also decomposed into uncorrelated components. The large number of components for
 1555 b-tagging is due to the calibration of the distribution of the BDT discriminant.

1556 As mentioned in Section 16.2, a normalization corrections and uncertainties on the estim-
 1557 ates of non-prompt leptons backgrounds are derived using data driven techniques, described in
 1558 detail in [7]. These are derived from a likelihood fit over various non-prompt enriched control
 1559 regions, targeting several sources of non-prompt light leptons separately: external conversion
 1560 electrons, internal conversion electrons, electrons from heavy flavor decays, and muons from
 1561 heavy flavor decays.

1562 The normalization factor and uncertainty applied to each source of non-prompt leptons is
 1563 summarized in Table 20

Process	Normalization Factor
NF_e^{ExtCO}	1.70 ± 0.51
NF_e^{IntCO}	0.75 ± 0.26
NF_e^{HF}	1.09 ± 0.32
NF_{μ}^{HF}	1.28 ± 0.17

Table 44: Normalization factors - with statistical and systematic uncertainties - derived from the fit over fake control regions for each source of non-prompt leptons considered.

1564 In addition to those derived from the control regions, several additional uncertainties are
1565 assigned to the non-prompt lepton background. An additional 25% uncertainty on material
1566 conversions is assigned, based on the comparison between data and MC in a region where a
1567 loose electron fails the photon conversion veto. A shape uncertainty of 15% (6%) is assigned to
1568 the HF non-prompt electron (muon) background based on a comparison between data and MC
1569 where the second leading electron (muon) is only required to be loose. As the contribution from
1570 light non-prompt leptons is small, about 10% percent of the contribution from HF non-prompt
1571 leptons, it is derived from the agreement between data and simulation in a LF enriched region at
1572 low values of the non-prompt lepton BDT. The resulting uncertainty is 100%, and is taken to be
1573 uncorrelated between internal and material conversions.

1574 Theoretical uncertainties applied to MC predictions, including cross section, PDF, and
1575 scale uncertainties are taken from theory calculations for the predominate prompt backgrounds.
1576 Following the nominal $t\bar{t}H - ML$ analysis, a 50% uncertainty is applied to Diboson to account
1577 for the large uncertainty in estimating $VV +$ heavy flavor. The other “rare” background processes
1578 - including tZ , rare top processes, $ttWW$, WtZ , VVV , $tHjb$ and WtH - are assigned an overall
1579 50% normalization uncertainty as well. The theory uncertainties applied to the MC estimates
1580 are summarized in Table 45.

Process	X-section [%]
t̄H (aMC@NLO+Pythia8)	QCD Scale: $^{+5.8}_{-9.2}$ PDF($+\alpha_S$): ± 3.6
t̄Z (aMC@NLO+Pythia8)	QCD Scale: $^{+9.6}_{-11.3}$ PDF($+\alpha_S$): ± 4
t̄W (aMC@NLO+Pythia8)	QCD Scale: $^{+12.9}_{-11.5}$ PDF($+\alpha_S$): ± 3.4
tHjb (aMC@NLO+Pythia8)	QCD Scale: $^{+6.5}_{-14.9}$ PDF($+\alpha_S$): ± 3.7
WtH (aMC@NLO+Pythia8)	QCD Scale: $^{+5.0}_{-6.7}$ PDF($+\alpha_S$): ± 6.3
VV (Sherpa 2.2.1)	± 50
Others	± 50

Table 45: Summary of theoretical uncertainties for MC predictions in the analysis.

1581 Additional uncertainties to account for t̄W mismodelling are also applied. These include
 1582 a “Generator” uncertainty, based on a comparison between the nominal Sherpa 2.2.5 sample,
 1583 and the formerly used aMC@NLO sample, and an “Extra radiation” uncertainty, which includes
 1584 renormalisation and factorisation scale variations of the Sherpa 2.2.5 sample.

1585 21 Results

1586 A maximum likelihood fit is performed simultaneously over the reconstructed Higgs p_T spectrum
 1587 in the three signal regions, 2lSS, 3lS, and 3lF. The signal is split into high and low p_T samples,
 1588 based on whether the truth p_T of the Higgs is above or below 150 GeV. The parameters $\mu_{t\bar{t}H\text{high}p_T}$
 1589 and $\mu_{t\bar{t}H\text{low}p_T}$, where $\mu = \sigma_{\text{observed}}/\sigma_{\text{SM}}$, are extracted from the fit, signifying the difference
 1590 between the observed value and the theory prediction. Unblinded results are shown for the 79.8
 1591 fb⁻¹ data set, as well as MC only projections of results using the full Run-2, 139 fb⁻¹ dataset.

1592 As described in Section 20, there are 229 systematic uncertainties that are considered
 1593 as NPs in the fit. These NP s are constrained by Gaussian or log-normal probability density
 1594 functions. The latter are used for normalisation factors to ensure that they are always positive.
 1595 The expected number of signal and background events are functions of the likelihood. The prior
 1596 for each NP is added as a penalty term, decreasing the likelihood as it is shifted away from its
 1597 nominal value.

1598 21.1 Results - 79.8 fb^{-1}

1599 As the data collected from 2015-2017 has been unblinded for $t\bar{t}H$ – ML channels, represent-
 1600 ing 79.8 fb^{-1} , those events are unblinded. The predicted Higgs p_T spectrum is fit to data
 1601 simultaneously in each of the three signal regions shown in Figure 21.1.

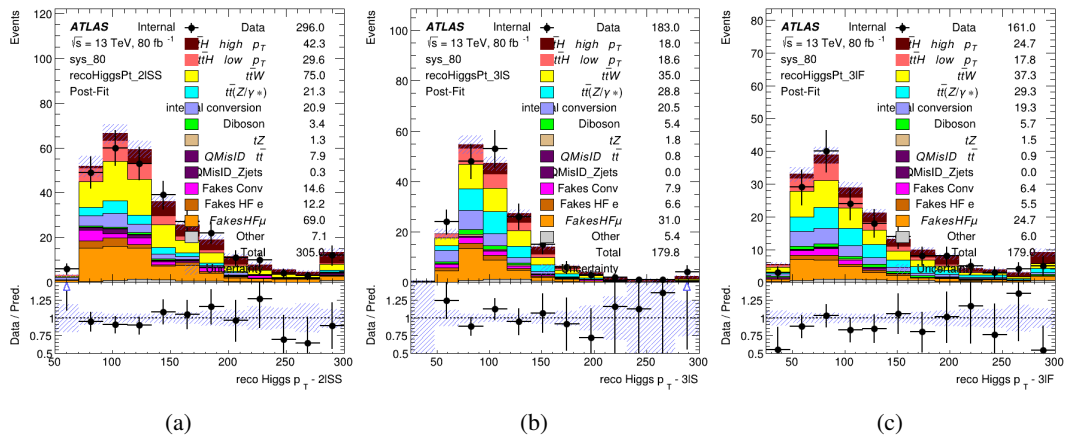


Figure 21.1: Post-fit distributions of the reconstructed Higgs p_T in the three signal regions, (a) 2ISS, (b) 3IS, and (c) 3IF, for 79.8 fb^{-1} of MC

1602 A post-fit summary of the fitted regions is shown in Figure 21.2.

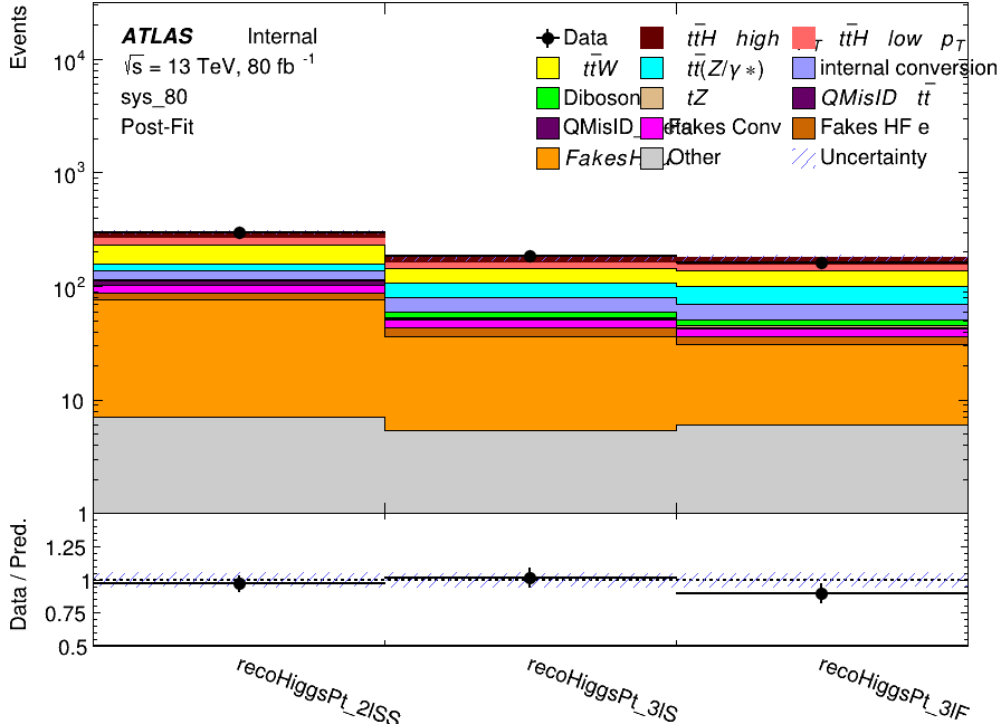


Figure 21.2: Post-fit summary of the yields in each signal region.

1603 The the measured μ values for high and low p_T Higgs production obtained from the fit
 1604 are shown in 46. A significance of 1.7σ is observed for $t\bar{t}H$ high p_T , and 2.1σ is measured for
 1605 $t\bar{t}H$ low p_T .

$$\mu_{t\bar{t}H \text{ high } p_T} = 2.1^{+0.62}_{-0.59} (\text{stat})^{+0.40}_{-0.43} (\text{sys})$$

$$\mu_{t\bar{t}H \text{ low } p_T} = 0.83^{+0.39}_{-0.40} (\text{stat})^{+0.51}_{-0.53} (\text{sys})$$

Table 46: Best fit μ values for $t\bar{t}H$ high p_T and $t\bar{t}H$ low p_T , where $\mu = \sigma_{\text{obs}}/\sigma_{\text{pred}}$

1606 The most prominent sources of systematic uncertainty, as measured by their impact on
 1607 $\mu_{t\bar{t}H \text{ high } p_T}$, are summarized in Table 47.

Uncertainty Source	$\Delta\mu$	
Jet Energy Scale	0.25	0.23
t̄H cross-section (QCD scale)	-0.11	0.21
Luminosity	-0.13	0.14
Flavor Tagging	0.14	0.13
t̄W cross-section (QCD scale)	-0.12	0.11
Higgs Branching Ratio	-0.1	0.11
t̄H cross-section (PDF)	-0.07	0.08
Electron ID	-0.06	0.06
Non-prompt Muon Normalization	-0.05	0.06
t̄Z cross-section (QCD scale)	-0.05	0.05
Diboson cross-section	-0.05	0.05
Fake muon modelling	-0.04	0.04
Total	0.40	0.43

Table 47: Summary of the most significant sources of systematic uncertainty on the measurement of t̄H high p_T.

¹⁶⁰⁸ The most significant sources of uncertainty on the measurement of t̄H - low p_T are shown
¹⁶⁰⁹ in Table 48.

Uncertainty Source	$\Delta\mu$	
Internal Conversions	-0.26	0.26
Luminosity	-0.16	0.17
Non-prompt Muon Normalization	-0.16	0.16
t̄W cross-section (QCD scale)	-0.17	0.15
Jet Energy Scal	0.15	0.15
Non-prompt Electron Modelling	-0.13	0.14
Flavor Tagging	0.13	0.13
Non-prompt Muon Modelling	-0.12	0.13
Non-prompt Electron Normalization	-0.11	0.11
t̄Z cross-section (QCD scale)	-0.08	0.09
Diboson Cross-section	-0.07	0.07
Total	0.51	0.53

Table 48: Summary of the most significant sources of systematic uncertainty on the measurement of t̄H low p_T.

¹⁶¹⁰ The ranking and impact of those nuisance parameters with the largest contribution to the

1611 overall uncertainty is shown in Figure 21.3.

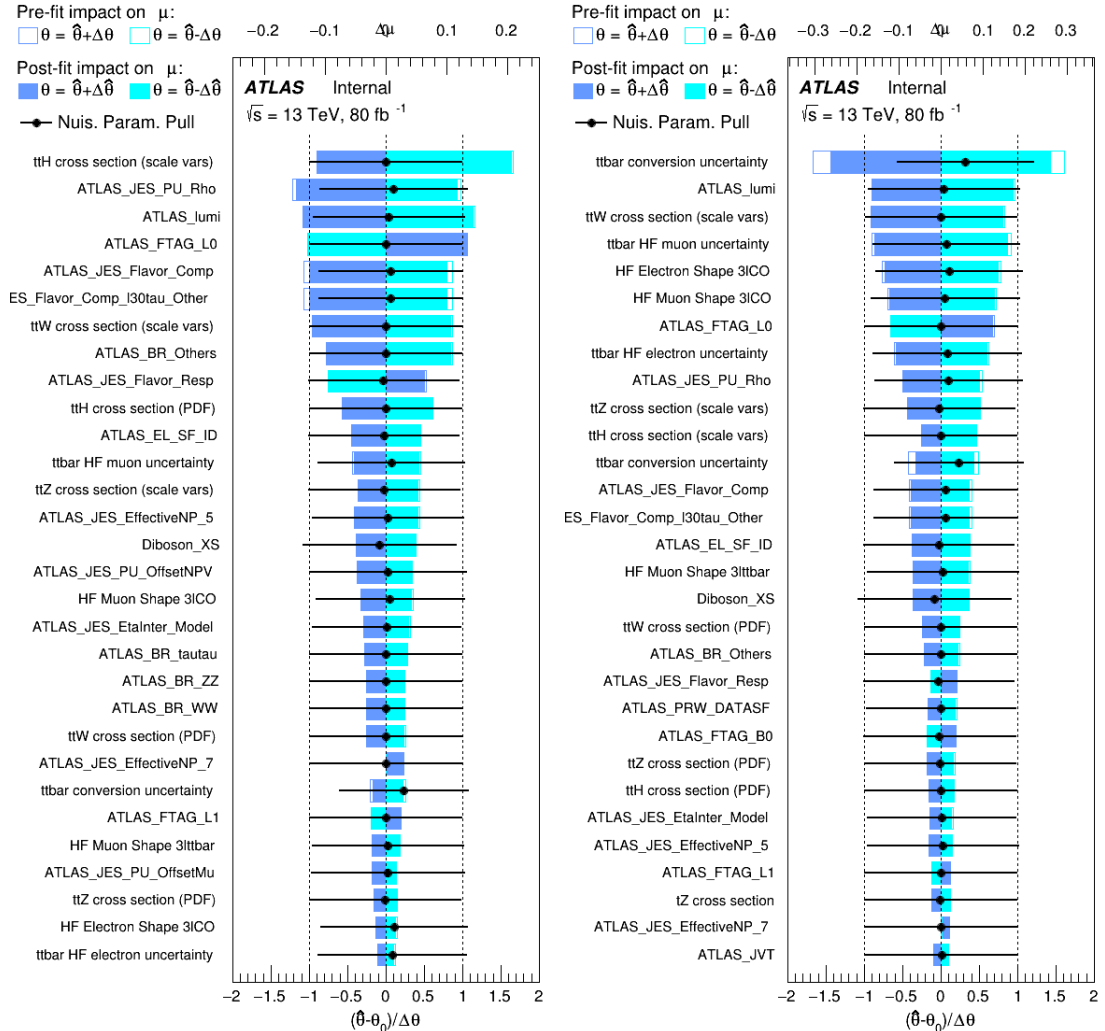


Figure 21.3: Impact of systematic uncertainties on the measurement of high p_T (left) and low p_T (right) $t\bar{t}H$ events

1612

The background composition of each of the fit regions is shown in Figure 21.4.

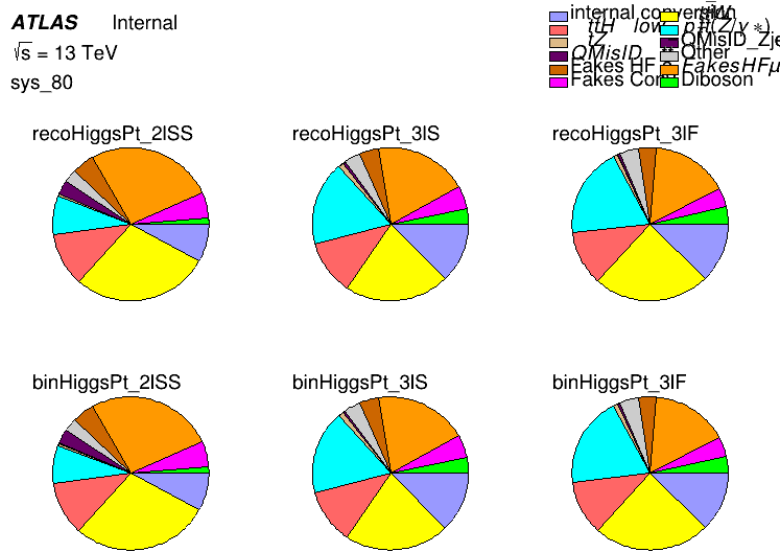


Figure 21.4: Background composition of the fit regions.

1613 21.2 Projected Results - 139 fb^{-1}

1614 As data collected in 2018 has not yet been unblinded for $t\bar{t}H$ – ML at the time of this note, data
 1615 from that year remains blinded. Instead, an Asimov fit is performed - with the MC prediction
 1616 being used both as the SM prediction as well as the data in the fit - in order to give expected
 1617 results.

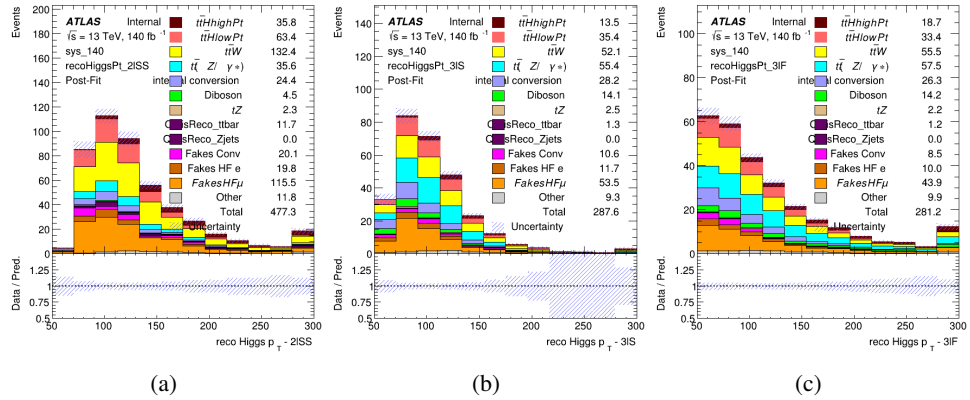


Figure 21.5: Blinded post-fit distributions of the reconstructed Higgs p_T in the three signal regions, (a) 2lSS, (b) 3lS, and (c) 3lF, for 139 fb^{-1} of data

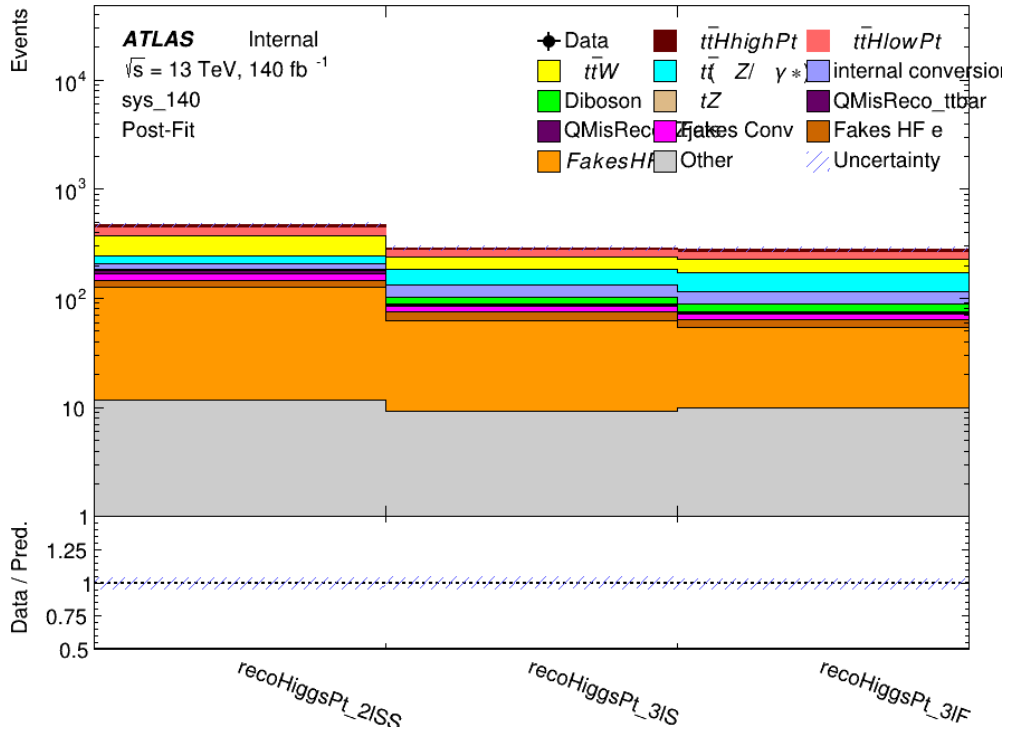


Figure 21.6: Post-fit summary of fit.

1618

Projected uncertainties on the μ values extracted from the fit for high and low p_T Higgs are

¹⁶¹⁹ shown in 49. A significance of 2.0σ is expected for $t\bar{t}H$ high p_T , and a projected significance

¹⁶²⁰ 2.3σ is extracted for $t\bar{t}H$ low p_T .

$$\mu_{t\bar{t}H \text{ high } p_T} = 1.00^{+0.45}_{-0.43}(\text{stat})^{+0.30}_{-0.31}(\text{sys})$$

$$\mu_{t\bar{t}H \text{ low } p_T} = 1.00^{+0.29}_{-0.30}(\text{stat})^{+0.48}_{-0.50}(\text{sys})$$

Table 49: Best fit μ values for $t\bar{t}H$ high p_T and $t\bar{t}H$ low p_T , where $\mu = \sigma_{\text{obs}}/\sigma_{\text{pred}}$

¹⁶²¹ The most prominent sources of systematic uncertainty, as measured by their impact on

¹⁶²² $\mu_{t\bar{t}H \text{ high } p_T}$, are summarized in Table 50.

Uncertainty Source	$\Delta\mu$	
Jet Energy Scale	0.19	0.17
$t\bar{t}W$ Cross-section (QCD Scale)	-0.12	0.11
Luminosity	-0.1	0.11
Flavor Tagging	0.1	0.1
$t\bar{t}H$ Cross-section (QCD Scale)	-0.05	0.1
$t\bar{t}Z$ Cross-section (QCD Scale)	-0.05	0.06
Non-prompt Muon Normalization	-0.05	0.05
Higgs Branching Ratio	-0.05	0.05
Diboson Cross-section	-0.04	0.05
Non-prompt Muon Modelling	-0.04	0.04
$t\bar{t}H$ Cross-section (PDF)	-0.03	0.04
Electron ID	-0.04	0.04
$t\bar{t}W$ Cross-section (PDF)	-0.03	0.03
Total	0.30	0.31

Table 50: Summary of the most significant sources of systematic uncertainty on the measurement of $t\bar{t}H$ high p_T .

¹⁶²³ The most significant sources of systematic uncertainty on $t\bar{t}H$ low p_T are summarized in

¹⁶²⁴ Table 51.

Uncertainty Source	$\Delta\mu$	
Internal Conversions	-0.18	0.2
Jet Energy Scale	0.19	0.16
Non-prompt Muon Normalization	-0.16	0.17
Luminosity	-0.15	0.17
t̄tW Cross-section (QCD Scale)	-0.17	0.15
Non-prompt Electron Modelling	-0.13	0.14
Non-prompt Muon Modelling	-0.13	0.13
Flavor Tagging	0.13	0.12
Non-prompt Electron Normalization	-0.1	0.11
t̄tZ Cross-section (QCD Scale)	-0.07	0.09
t̄tH Cross-section (QCD Scale)	-0.05	0.1
Total	0.48	0.50

Table 51: Summary of the most significant sources of systematic uncertainty on the measurement of t̄tH low p_T.

¹⁶²⁵ The ranking and impact of those nuisance parameters with the largest contribution to the
¹⁶²⁶ overall uncertainty is shown in Figure 21.7.

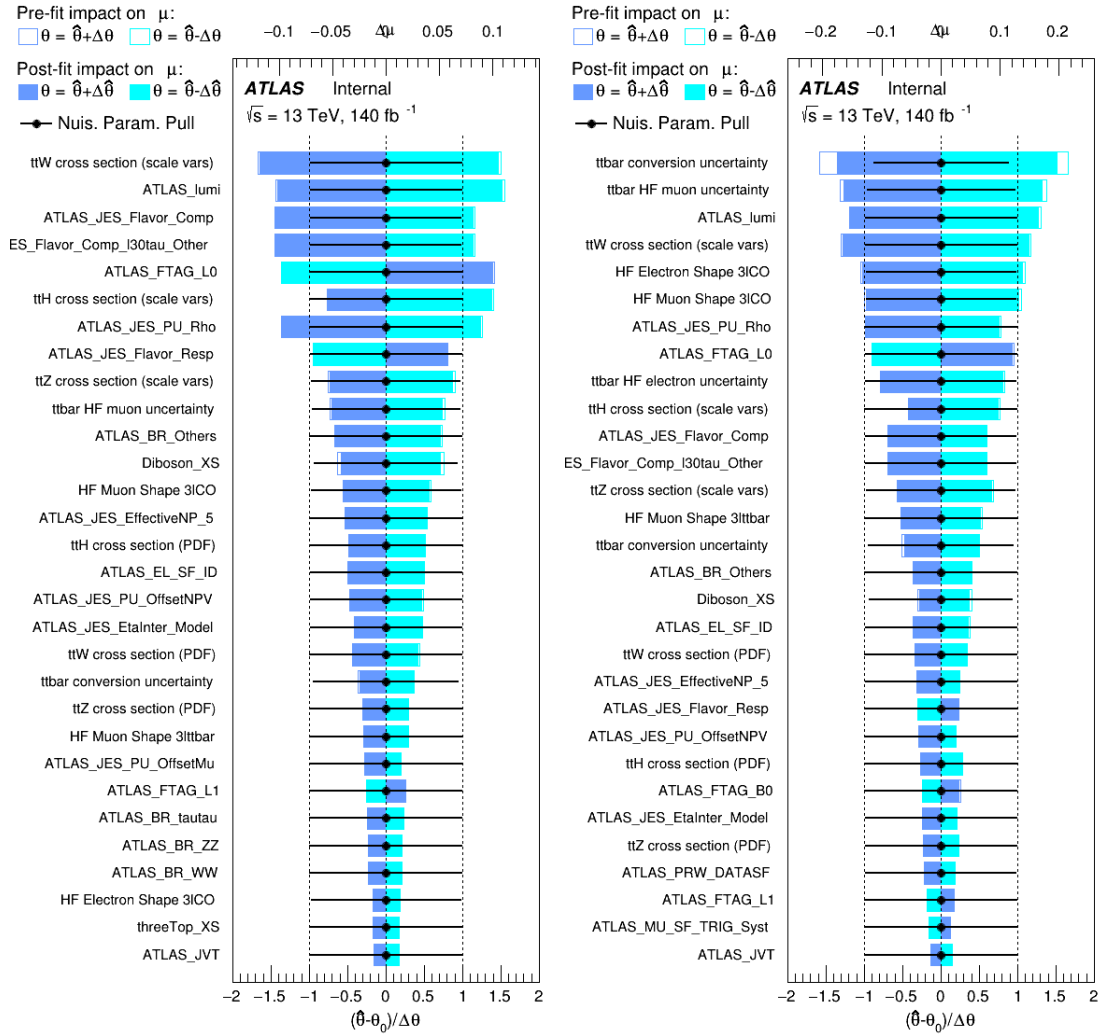


Figure 21.7: Impact of systematic uncertainties on the measurement of high p_T (left) and low p_T (right) ttH events

1627

The background composition of each of the fit regions is shown in Figure 21.8.

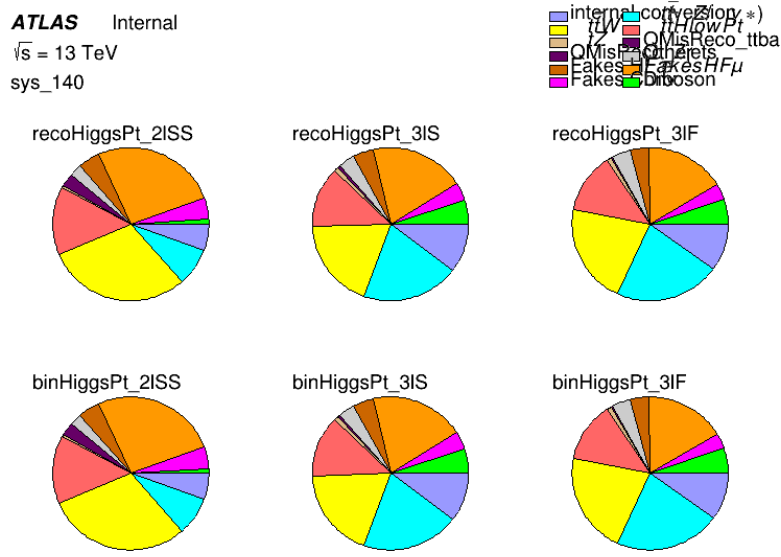


Figure 21.8: Background composition of the fit regions.

1628 Part VI

1629 Conclusion

1630 As search for the effects of dimension-six operators on $t\bar{t}H$ production is performed. An effective
 1631 field theory approached is used to parameterize the effects of high energy physics on the Higgs
 1632 momentum spectrum. The momentum spectrum is reconstructed using various MVA techniques,
 1633 and the limits on dimension-six operators are limited to X.

References

- 1634 [1] ATLAS Collaboration, *Observation of a new particle in the search for the Standard*
1635 *Model Higgs boson with the ATLAS detector at the LHC*, Phys. Lett. B **716** (2012) 1,
1636 arXiv: [1207.7214 \[hep-ex\]](https://arxiv.org/abs/1207.7214).
- 1637 [2] R. Oerter, *The theory of almost everything : the Standard Model, the unsung triumph of*
1638 *modern physics*, Pi Press, 2006, ISBN: 978-0-13-236678-6.
- 1639 [3] P. W. Higgs, *Broken Symmetries and the Masses of Gauge Bosons*,
1640 Phys. Rev. Lett. 13 (Oct, 1964) 508-509 ().
- 1641 [4] J. Goldstone, A. Salam and S. Weinberg, *Broken Symmetries*,
1642 Phys. Rev. **127** (3 1962) 965,
1643 URL: <https://link.aps.org/doi/10.1103/PhysRev.127.965>.
- 1644 [5] J. Ellis, *Higgs Physics*,
1645 (2013) 117, 52 pages, 45 figures, Lectures presented at the ESHEP 2013 School of
1646 High-Energy Physics, to appear as part of the proceedings in a CERN Yellow Report,
1647 URL: <https://cds.cern.ch/record/1638469>.
- 1648 [6] T. A. Collaboration, *Observation of Higgs boson production in association with a top*
1649 *quark pair at the LHC with the ATLAS detector*, Physics Letters B **784** (2018) 173,
1650 ISSN: 0370-2693, URL:
1651 <https://www.sciencedirect.com/science/article/pii/S0370269318305732>.

- 1653 [7] *Evidence for the associated production of the Higgs boson and a top quark pair with the*
1654 *ATLAS detector*, tech. rep. ATLAS-CONF-2017-077, CERN, 2017,
1655 URL: <https://cds.cern.ch/record/2291405>.
- 1656 [8] A. M. Sirunyan et al., *Observation of $t\bar{t}H$ Production*,
1657 *Physical Review Letters* **120** (2018), ISSN: 1079-7114,
1658 URL: <http://dx.doi.org/10.1103/PhysRevLett.120.231801>.
- 1659 [9] B. Dumont, S. Fichet and G. von Gersdorff,
1660 *A Bayesian view of the Higgs sector with higher dimensional operators*,
1661 *Journal of High Energy Physics* **2013** (2013), ISSN: 1029-8479,
1662 URL: [http://dx.doi.org/10.1007/JHEP07\(2013\)065](http://dx.doi.org/10.1007/JHEP07(2013)065).
- 1663 [10] S. Banerjee, S. Mukhopadhyay and B. Mukhopadhyaya,
1664 *Higher dimensional operators and the LHC Higgs data: The role of modified kinematics*,
1665 *Physical Review D* **89** (2014), ISSN: 1550-2368,
1666 URL: <http://dx.doi.org/10.1103/PhysRevD.89.053010>.
- 1667 [11] M. Zinser, ‘The Large Hadron Collider’, *Search for New Heavy Charged Bosons and*
1668 *Measurement of High-Mass Drell-Yan Production in Proton—Proton Collisions*,
1669 Springer International Publishing, 2018 47, ISBN: 978-3-030-00650-1,
1670 URL: https://doi.org/10.1007/978-3-030-00650-1_4.
- 1671 [12] *Detector and Technology*, URL: <https://atlas.cern/discover/detector>.
- 1672 [13] M. Marjanovic, *ATLAS Tile calorimeter calibration and monitoring systems*, 2018.

- 1673 [14] M. Aaboud et al., *Observation of electroweak $W^\pm Z$ boson pair production in association*
 1674 *with two jets in pp collisions at $\sqrt{s} = 13$ TeV with the ATLAS detector,*
 1675 **Phys. Lett. B** **793** (2019) 469, arXiv: [1812.09740 \[hep-ex\]](#).
- 1676 [15] T. Gleisberg et al., *Event generation with SHERPA 1.1*, **JHEP** **02** (2009) 007,
 1677 arXiv: [0811.4622 \[hep-ph\]](#).
- 1678 [16] R. D. Ball et al., *Parton distributions for the LHC Run II*, **JHEP** **04** (2015) 040,
 1679 arXiv: [1410.8849 \[hep-ph\]](#).
- 1680 [17] H.-L. Lai et al., *New parton distributions for collider physics*,
 1681 **Phys. Rev. D** **82** (2010) 074024, arXiv: [1007.2241 \[hep-ph\]](#).
- 1682 [18] S. Frixione, G. Ridolfi and P. Nason,
 1683 *A positive-weight next-to-leading-order Monte Carlo for heavy flavour hadroproduction*,
 1684 **JHEP** **09** (2007) 126, arXiv: [0707.3088 \[hep-ph\]](#).
- 1685 [19] E. Re, *Single-top Wt-channel production matched with parton showers using the*
 1686 *POWHEG method*, **Eur. Phys. J. C** **71** (2011) 1547, arXiv: [1009.2450 \[hep-ph\]](#).
- 1687 [20] ATLAS Collaboration, *Electron efficiency measurements with the ATLAS detector using*
 1688 *the 2015 LHC proton–proton collision data*, ATLAS-CONF-2016-024, 2016,
 1689 URL: <https://cds.cern.ch/record/2157687>.
- 1690 [21] ATLAS Collaboration, *Measurement of the muon reconstruction performance of the*
 1691 *ATLAS detector using 2011 and 2012 LHC proton–proton collision data*,
 1692 **Eur. Phys. J. C** **74** (2014) 3130, arXiv: [1407.3935 \[hep-ex\]](#).

- 1693 [22] R. Narayan et al., *Measurement of the total and differential cross sections of a*
1694 *top-quark-antiquark pair in association with a W boson in proton-proton collisions at a*
1695 *centre-of-mass energy of 13 TeV with ATLAS detector at the Large Hadron Collider,*
1696 tech. rep. ATL-COM-PHYS-2020-217, CERN, 2020,
1697 URL: <https://cds.cern.ch/record/2712986>.
- 1698 [23] ATLAS Collaboration, *Jet Calibration and Systematic Uncertainties for Jets*
1699 *Reconstructed in the ATLAS Detector at $\sqrt{s} = 13 \text{ TeV}$* , ATL-PHYS-PUB-2015-015,
1700 2015, URL: <https://cds.cern.ch/record/2037613>.
- 1701 [24] ATLAS Collaboration,
1702 *Selection of jets produced in 13 TeV proton–proton collisions with the ATLAS detector,*
1703 ATLAS-CONF-2015-029, 2015, URL: <https://cds.cern.ch/record/2037702>.
- 1704 [25] ATLAS Collaboration, *Performance of pile-up mitigation techniques for jets in pp*
1705 *collisions at $\sqrt{s} = 8 \text{ TeV}$ using the ATLAS detector*, Eur. Phys. J. C **76** (2016) 581,
1706 arXiv: [1510.03823 \[hep-ex\]](https://arxiv.org/abs/1510.03823).
- 1707 [26] ATLAS Collaboration, *Performance of missing transverse momentum reconstruction*
1708 *with the ATLAS detector in the first proton–proton collisions at $\sqrt{s} = 13 \text{ TeV}$* ,
1709 ATL-PHYS-PUB-2015-027, 2015, URL: <https://cds.cern.ch/record/2037904>.
- 1710 [27] T. Chen and C. Guestrin, ‘XGBoost: A Scalable Tree Boosting System’,
1711 *Proceedings of the 22nd ACM SIGKDD International Conference on Knowledge*
1712 *Discovery and Data Mining*, KDD ’16, ACM, 2016 785, ISBN: 978-1-4503-4232-2,
1713 URL: <http://doi.acm.org/10.1145/2939672.2939785>.

- 1714 [28] F. Cardillo et al., *Measurement of the fiducial and differential cross-section of a top*
1715 *quark pair in association with a Z boson at 13 TeV with the ATLAS detector*, (2019),
1716 URL: <https://cds.cern.ch/record/2672207>.
- 1717 [29] ATLAS Collaboration, *Luminosity determination in pp collisions at $\sqrt{s} = 7$ TeV using*
1718 *the ATLAS detector at the LHC*, *Eur. Phys. J. C* **71** (2011) 1630,
1719 arXiv: [1101.2185 \[hep-ex\]](https://arxiv.org/abs/1101.2185).
- 1720 [30] G. Avoni et al.,
1721 *The new LUCID-2 detector for luminosity measurement and monitoring in ATLAS*,
1722 *JINST* **13** (2018) P07017.
- 1723 [31] G. Aad, T. Abajyan, B. Abbott and etal, *Jet energy resolution in proton-proton collisions*
1724 *at $\sqrt{s} = 7$ TeV recorded in 2010 with the ATLAS detector*,
1725 *The European Physical Journal C* **73** (2013) 2306, ISSN: 1434-6052,
1726 URL: <https://doi.org/10.1140/epjc/s10052-013-2306-0>.
- 1727 [32] A. Collaboration, *Performance of b -jet identification in the ATLAS experiment*,
1728 *Journal of Instrumentation* **11** (2016) P04008,
1729 URL: <http://stacks.iop.org/1748-0221/11/i=04/a=P04008>.
- 1730 [33] *Observation of the associated production of a top quark and a Z boson at 13 TeV with*
1731 *ATLAS*, (2020), URL: <https://cds.cern.ch/record/2722504>.
- 1732 [34] ATLAS Collaboration, *Comparison of Monte Carlo generator predictions from Powheg*
1733 *and Sherpa to ATLAS measurements of top pair production at 7 TeV*,
1734 ATL-PHYS-PUB-2015-011, 2015, URL: <https://cds.cern.ch/record/2020602>.

- ¹⁷³⁵ [35] ATLAS Collaboration, *ATLAS tunes of PYTHIA 6 and Pythia 8 for MC11*,
¹⁷³⁶ ATL-PHYS-PUB-2011-009, 2011, URL: <https://cds.cern.ch/record/1363300>.

1737 List of contributions

1738

¹⁷³⁹ **Part VII**

¹⁷⁴⁰ **Appendices**

¹⁷⁴¹ **A Non-prompt lepton MVA**

1742 A lepton MVA has been developed to better reject non-prompt leptons than standard cut
1743 based selections based upon impact parameter, isolation and PID. The name of this MVA is
1744 **PromptLeptonIso**. The full set of studies and detailed explanation can be found in [22].

1745 The decays of W and Z bosons are commonly selected by the identification of one or two
1746 electrons or muons. The negligible lifetimes of these bosons mean that the leptons produced in the
1747 decay originate from the interaction vertex and are thus labelled “prompt”. Analyses using these
1748 light leptons impose strict reconstruction quality, isolation and impact parameter requirements
1749 to remove “fake” leptons. A significant source of the fake light leptons are non-prompt leptons
1750 produced in decays of hadrons that contain bottom (b) or charm (c) quarks. Such hadrons
1751 typically have microscopically significant lifetimes that can be detected experimentally.

1752 These non-prompt leptons can also pass the tight selection criteria. In analyses that
1753 involve top (t) quarks, which decay almost exclusively into a W boson and a b quark, non-
1754 prompt leptons from the semileptonic decay of bottom and charm hadrons can be a significant
1755 source of background events. This is particularly the case in the selection of same-sign dilepton
1756 and multilepton final states.

1757 The main idea is to identify non-prompt light leptons using lifetime information associated
1758 with a track jet that matches the selected light lepton. This lifetime information is computed
1759 using tracks contained within the jet. Typically, lepton lifetime is determined using the impact
1760 parameter of the track reconstructed by the inner tracking detector which is matched to the recon-
1761 structed lepton. Using additional reconstructed charged particle tracks increases the precision of

1762 identifying the displaced decay vertex of bottom or charm hadrons that produced a non-prompt
 1763 light lepton. The MVA also includes information related to the isolation of the lepton to reject
 1764 non-prompt leptons.

1765 **PromptLeptonIso** is a gradient boosted BDT. The training of the BDT is performed on
 1766 leptons selected from the PowHEG+PYTHIA6 non-allhad $t\bar{t}$ MC sample. Eight variables are used
 1767 to train the BDT in order to discriminate between prompt and non-prompt leptons. The track
 1768 jets that are matched to the non-prompt leptons correspond to jets initiated by b or c quarks, and
 1769 may contain a displaced vertex. Consequently, three of the selected variables are used to identify
 1770 b-tag jets by standard ATLAS flavour tagging algorithms. Two variables use the relationship
 1771 between the track jet and lepton: the ratio of the lepton p_T with respect to the track jet p_T and
 1772 ΔR between the lepton and the track jet axis. Finally three additional variables test whether the
 1773 reconstructed lepton is isolated: the number of tracks collected by the track jet and the lepton
 1774 track and calorimeter isolation variables. Table 52 describes the variables used to train the BDT
 1775 algorithm. The choice of input variables has been extensively discussed with Egamma, Muon,
 1776 Tracking, and Flavour Tagging CP groups.

Variable	Description
N_{track} in track jet	Number of tracks collected by the track jet
$\text{IP2 log}(P_b/P_{\text{light}})$	Log-likelihood ratio between the b and light jet hypotheses with the IP2D algorithm
$\text{IP3 log}(P_b/P_{\text{light}})$	Log-likelihood ratio between the b and light jet hypotheses with the IP3D algorithm
N_{TrkAtVtx} SV + JF	Number of tracks used in the secondary vertex found by the SV1 algorithm in addition to the number of tracks from secondary vertices found by the JetFitter algorithm with at least two tracks
$p_T^{\text{lepton}}/p_T^{\text{track jet}}$	The ratio of the lepton p_T and the track jet p_T
$\Delta R(\text{lepton}, \text{track jet})$	ΔR between the lepton and the track jet axis
$p_T^{\text{VarCone30}}/p_T$	Lepton track isolation, with track collecting radius of $\Delta R < 0.3$
$E_T^{\text{TopoCone30}}/p_T$	Lepton calorimeter isolation, with topological cluster collecting radius of $\Delta R < 0.3$

Table 52: A table of the variables used in the training of **PromptLeptonIso**.

1777 The output distribution of the BDT is shown in Figure A.

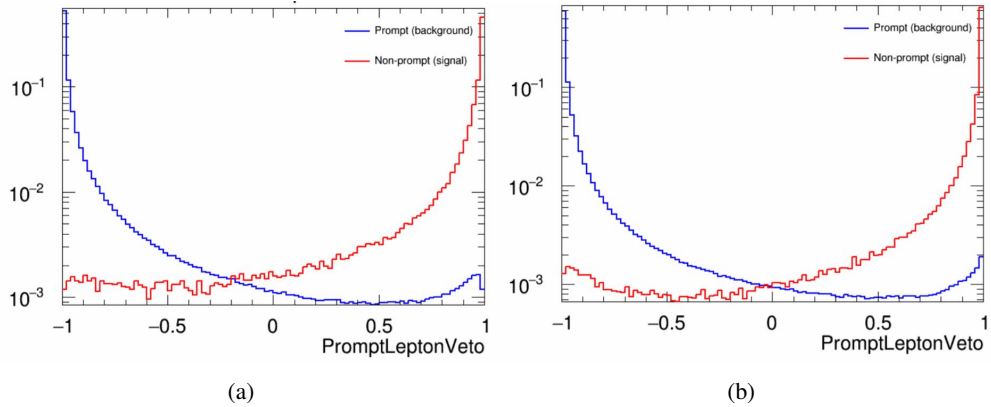


Figure A.1: Distribution of the PLV BDT discriminant for (a) electrons and (b) muons

1778 The ROC curve for the BDT response, compared to the standard `FixedCutTight` WP, is
1779 shown in figure A, which shows a clear improvement when using this alternate training.

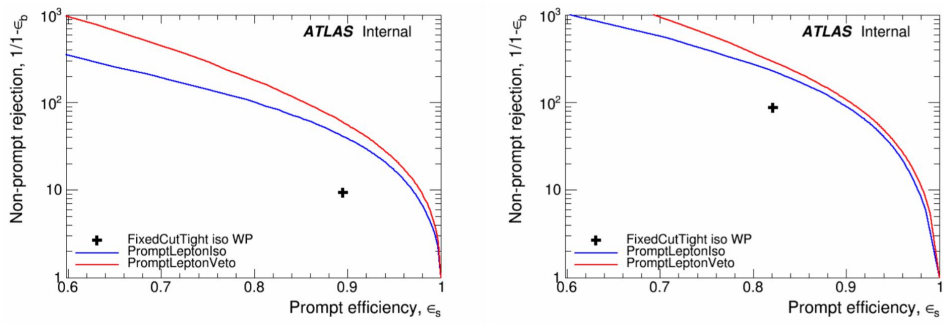


Figure A.2: ROC curves for the PLV as well as the performance of the standard FixedCutTight WP for (left) electrons and (right) muons

A cutoff value of -0.7 for electrons and -0.5 for muons are chosen as the WPs for this
 MVA, based on an optimisation of S/\sqrt{B} performed in the preselection regions of the $t\bar{t}H - ML$
 analysis, which have a signature similar to that of this analysis.

1783 The efficiency of the tight `PromptLeptonIso` working point is measured using the tag
1784 and probe method with $Z \rightarrow \ell^+ \ell^-$ events. Such calibration are performed by analysers from
1785 this analysis in communication with the Egamma and Muon combined performance groups. The
1786 scale factor are approximately 0.92 for $10 < p_T < 15$ GeV, and averaging at 0.98 to 0.99 for
1787 higher p_T leptons. An extra systematic is applied to muons within $\Delta R < 0.6$ of a calorimeter
1788 jet, since there is a strong dependence on the scale factor due to the presence of these jets. For
1789 electrons, the dominant systematics is coming from pile-up dependence. Overall the systematics
1790 are a maximum of 3% at low p_T and decreasing at a function of p_T .

¹⁷⁹¹ **B Supplementary WZ + Heavy Flavor Studies**

¹⁷⁹² **B.1 Non-prompt CR Modelling**

1793 In order to further validate the modeling in each of the non-prompt CRs, additional
 1794 kinematic plots are made in the Z+jets CR and $t\bar{t}$ CR in each of the continuous b-tag regions,
 1795 after the correction factors detailed in Section 12.3 have been applied.

1796 In the case of the Z+jets CR, the p_T spectrum of the lepton originating from the W
 1797 candidate is shown, as this is the distribution used to extract the scale factor applied to Z+jets.
 1798 These plots are shown in Figures B.1 and B.2.

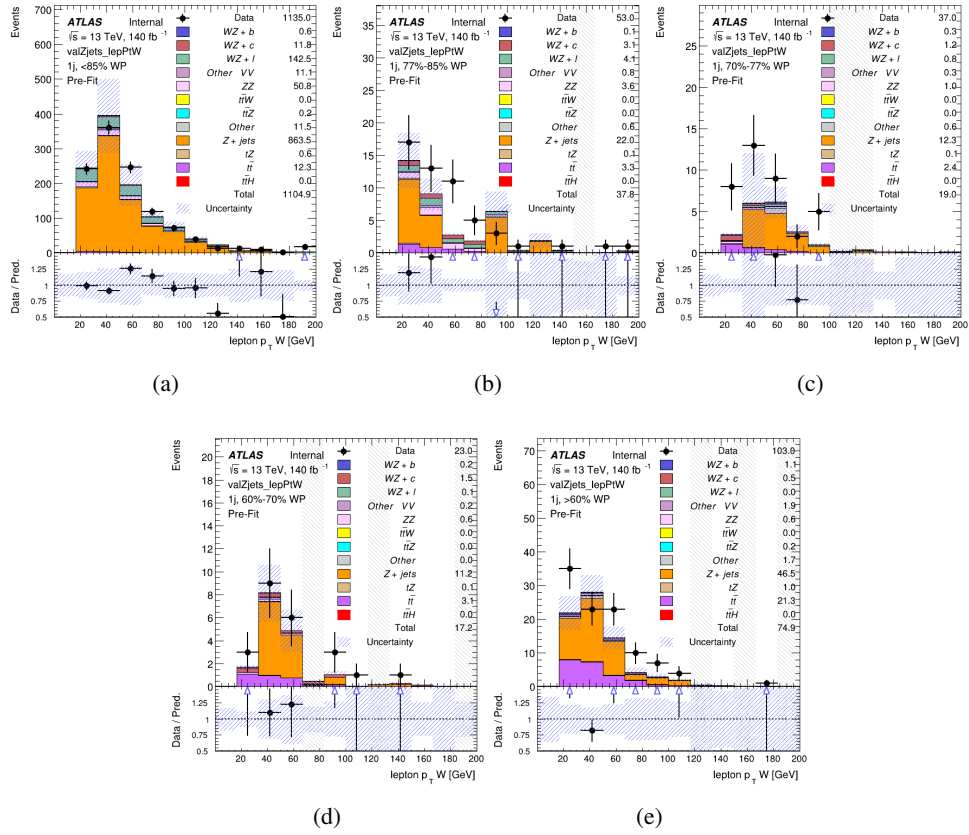


Figure B.1: Comparisons between the data and MC distributions of the p_T of the lepton originating from the W-candidate in the Z+jets CR for each of the 1-jet b-tag working point regions

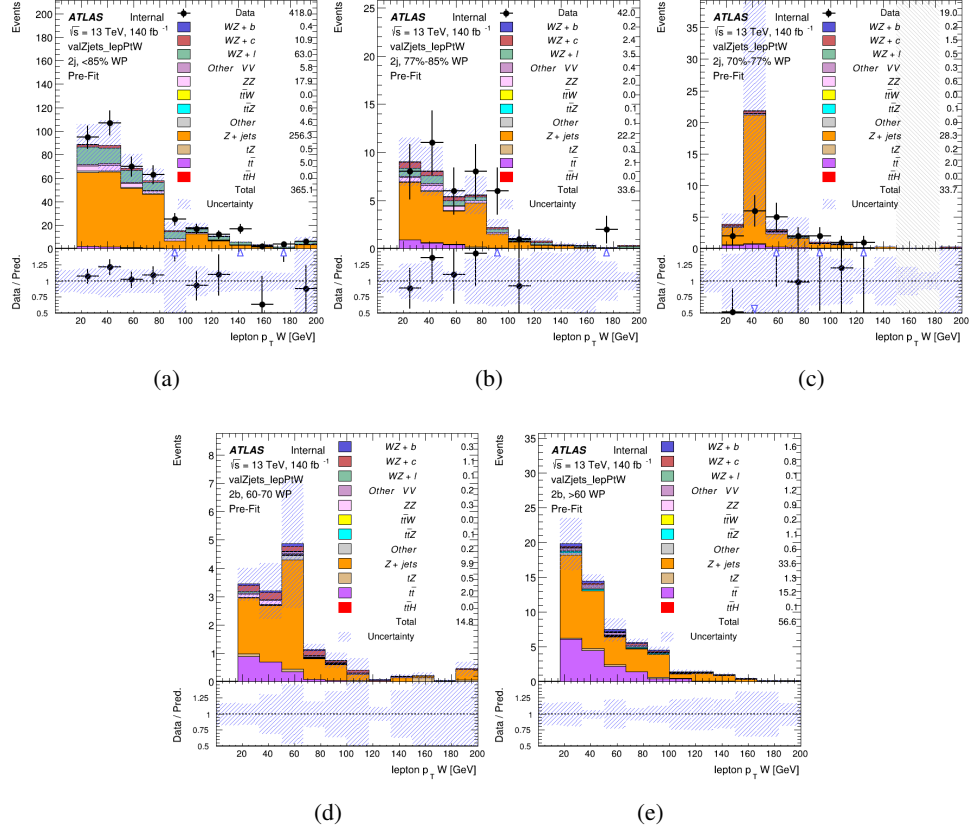


Figure B.2: Comparisons between the data and MC distributions of the p_T of the lepton originating from the W-candidate in the Z+jets CR for each of the 2-jet b-tag working point regions

1799 The same is shown for the $t\bar{t}$ CR, but the p_T of the OS lepton is used instead as a
 1800 representation of the modeling, as the lepton from the W is not well defined for $t\bar{t}$ events. These
 1801 plots are shown in Figures B.3 and B.4.

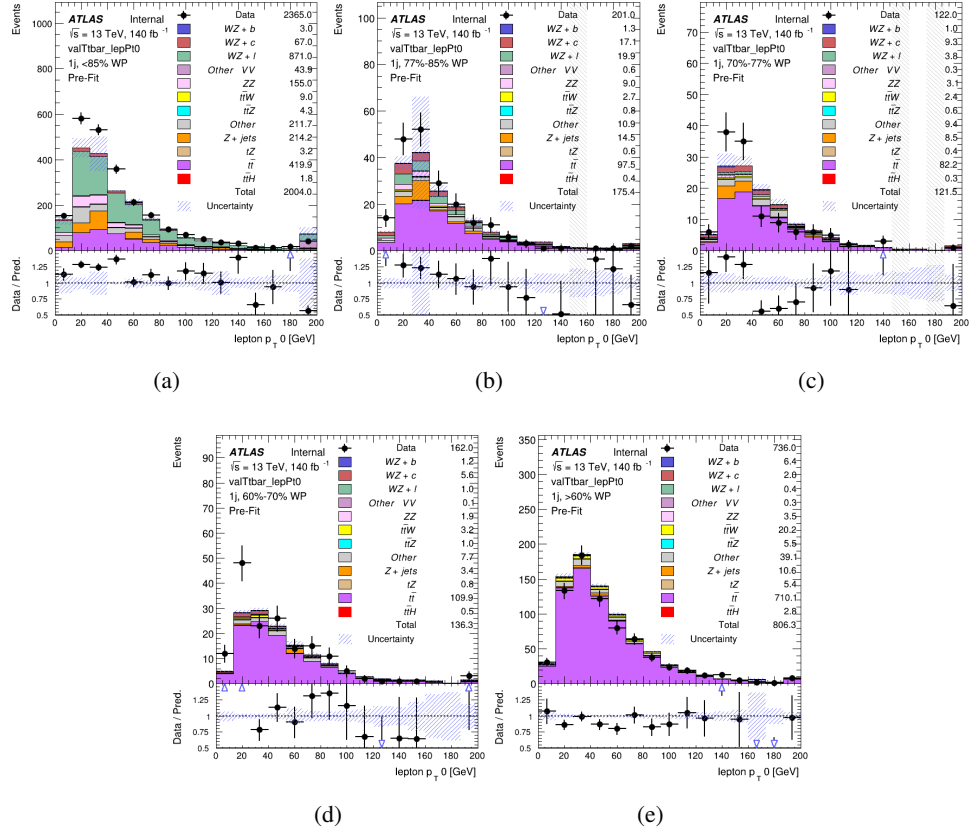


Figure B.3: Comparisons between the data and MC distributions of the p_T of the OS lepton in the $t\bar{t}$ CR for each of the 1-jet b-tag working point regions

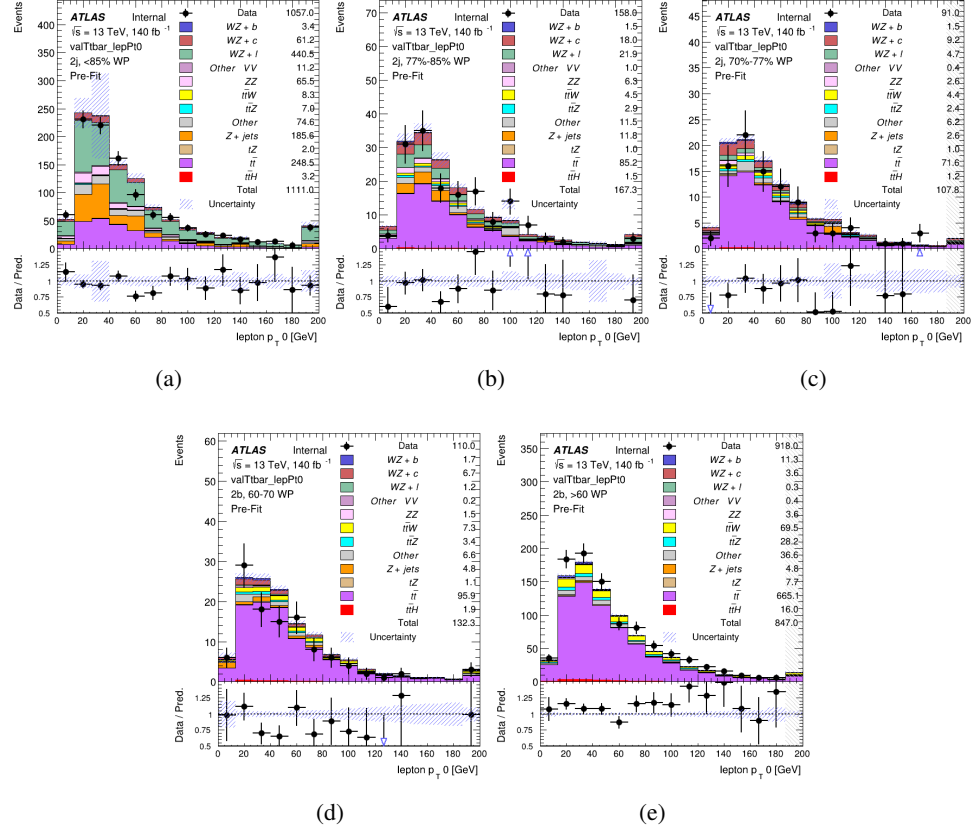


Figure B.4: Comparisons between the data and MC distributions of the p_T of the OS lepton in the $t\bar{t}$ CR for each of the 2-jet b-tag working point regions

1802 **B.2 tZ Interference Studies**

1803 Because it includes an on-shell Z boson as well as a b-jet and W from the top decay, tZ
1804 production represents an identical final state to WZ + b-jet. This implies the possibility of matrix
1805 level interference between these two processes not accounted for in the Monte Carlo simulations,
1806 which consider the two processes independently. Truth level studies are performed in order to
1807 estimate the impact of these interference effects.

1808 In order to estimate the matrix level interference effects between tZ and WZ + b-jet, two
1809 different sets of simulations are produced using MadGraph 5 [**Madgraph**] - one which simulates
1810 these two processes independently, and another where they are produced simultaneously, such
1811 that interference effects are present. These two sets of samples are then compared, and the
1812 difference between them can be taken to represent any interference effects.

1813 MadGraph simulations of 10,000 tZ and 10,000 WZ + b-jet events are produced, along
1814 with 20,000 events where both are present, in the fiducial region where three leptons and at least
1815 one jet are produced.

1816 A selection mimicking the preselection used in the main analysis is applied to the samples:
1817 The SS leptons are required to have $p_T > 20$ GeV, and > 10 GeV is required for the OS lepton.
1818 The associated b-jet is required to have $p_T > 25$ GeV, and all physics objects are required to fall
1819 in a range of $|\eta| < 2.5$.

1820 The kinematics of these samples after the selection has been applied are shown below:

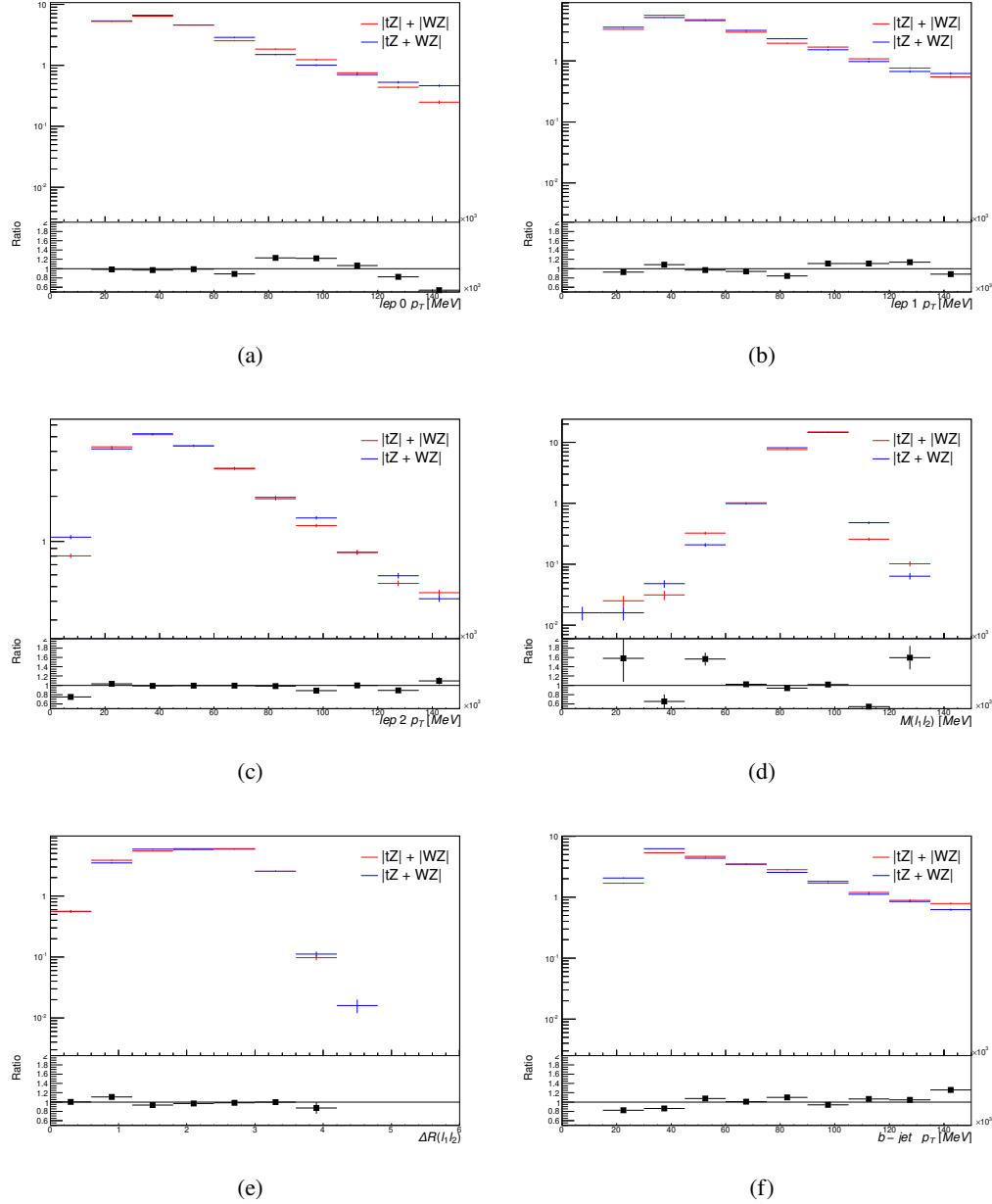


Figure B.5: Comparisons between (a) the p_T of the lepton from the W, (b) and (c) show the p_T of the lepton from the Z, (d) the invariant mass of the Z-candidate, (e) ΔR of the leptons from the Z, and (f) the p_T of the b-jet, for WZ and tZ events generated with interference effects (blue) and without interference effects (red).

1821 The overall cross-section of the two methods agree within error, and no significant differ-
1822 ences in the kinematic distributions are seen. It is therefore concluded that interference effects
1823 do not significantly impact the results.

1824 **B.3 Alternate tZ Inclusive Fit**

1825 **B.3.1 tZ Inclusive Fit**

1826 While tZ is often considered as a distinct process from WZ + b, this could also be considered part
 1827 of the signal. Alternate studies are performed where, using the same framework as the nominal
 1828 analysis, a measurement of WZ + b is performed that includes tZ as part of WZ+b.

1829 Because of this change, the tZ CR is no longer necessary, and only the five pseudo-
 1830 continuous b-tag regions are used in the fit. Further, systematics related to the tZ cross-section
 1831 are removed from the fit, as they are now encompassed by the normalization measurement of
 1832 WZ + b. All other systematic uncertainties are carried over from the nominal analysis.

1833 An expected WZ + b cross-section of $4.1^{+0.78}_{-0.74}(\text{stat})^{+0.53}_{-0.52}(\text{sys}) \text{ fb}$ is extracted from the fit,
 1834 with an expected significance of 4.0σ .

1835 The impact of the predominate systematics are summarized in Table 53.

Uncertainty Source	$\Delta\mu$	
WZ + light cross-section	0.08	-0.08
Jet Energy Scale	-0.06	0.08
Luminosity	-0.05	0.06
WZ + charm cross-section	-0.04	0.05
Other Diboson + b cross-section	-0.04	0.04
WZ cross-section - QCD scale	-0.04	0.03
t̄t cross-section	-0.03	0.03
Jet Energy Resolution	-0.03	0.03
Flavor tagging	-0.03	0.03
Z+jets cross section	-0.02	0.02
Total Systematic Uncertainty	-0.15	0.16

Table 53: Summary of the most significant sources of systematic uncertainty on the measurement of WZ + b with exactly one associated jet.

1836 **B.3.2 Floating tZ**

1837 In order to quantify the impact of the tZ uncertainty on the fit, an alternate fit strategy is used
1838 where the tZ normalization is allowed to float. This normalization factor replaces the cross-
1839 section uncertainty on tZ, and all other parameters of the fit remain the same.

1840 An uncertainty of 17% on the normalization of tZ is extracted from the fit, compared to a
1841 theory uncertainty of 15% applied to the tZ cross-section. The measured uncertainties on WZ
1842 remain the same.

C Supplementary $t\bar{t}H$ Differential Analysis Studies

¹⁸⁴³ The following section provides details of the various MVAs as well as a few studies performed
¹⁸⁴⁴ in support of this analysis, exploring alternate decisions and strategies.

¹⁸⁴⁵ **C.1 Higgs Reconstruction Model Details**

¹⁸⁴⁶ **C.1.1 b-jet Identification Features - 2lSS**

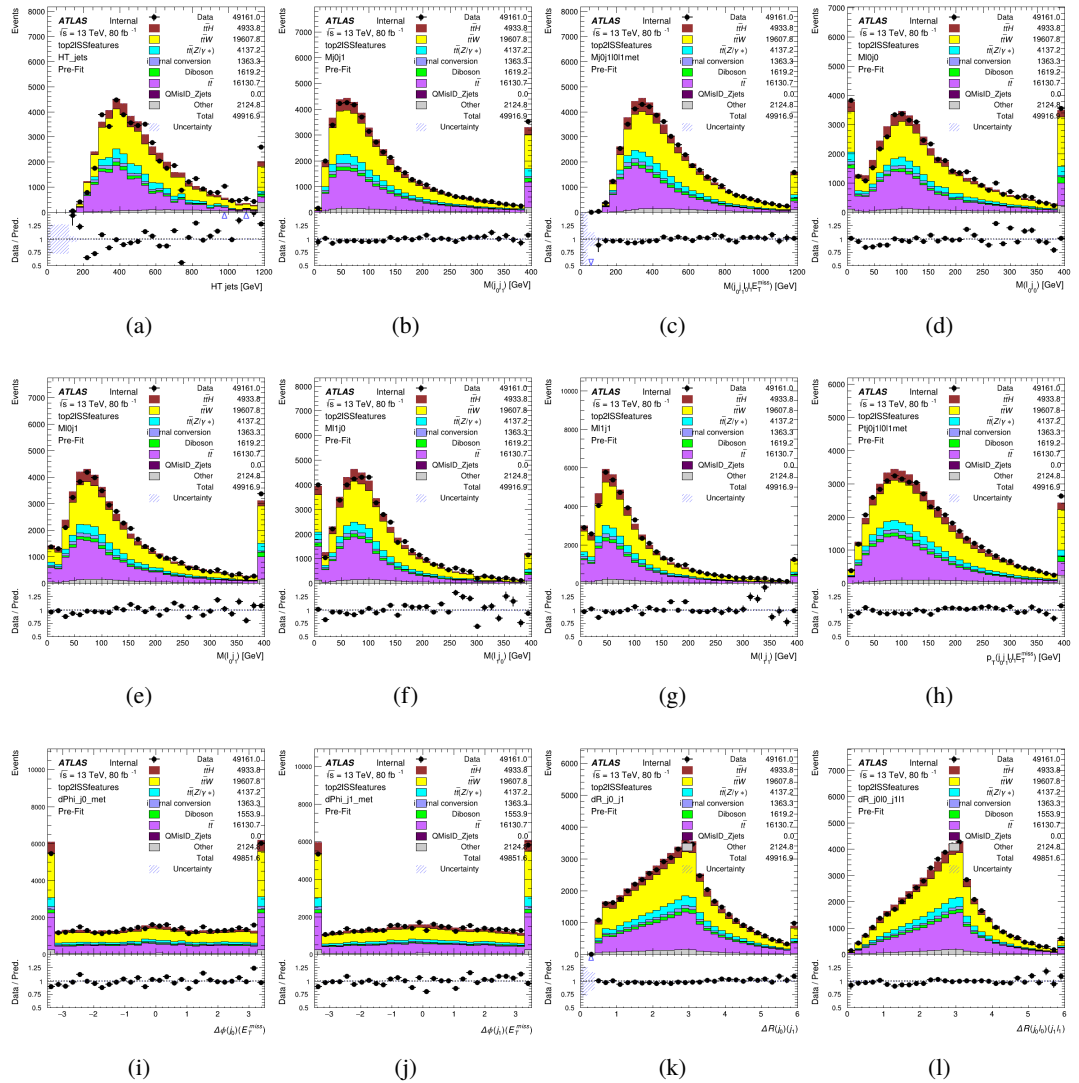


Figure C.1: Input features for top21SS

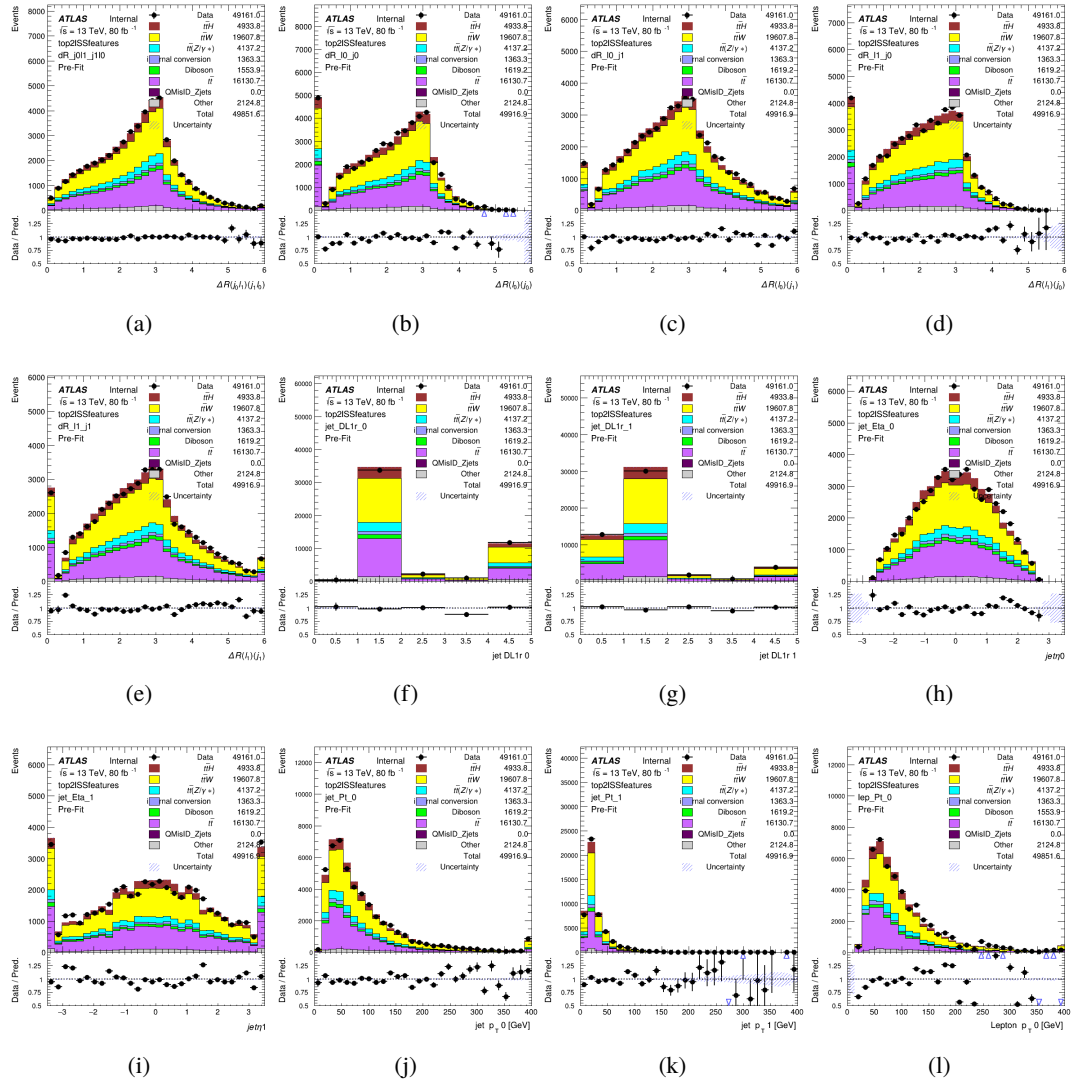


Figure C.2: Input features for top2lSS

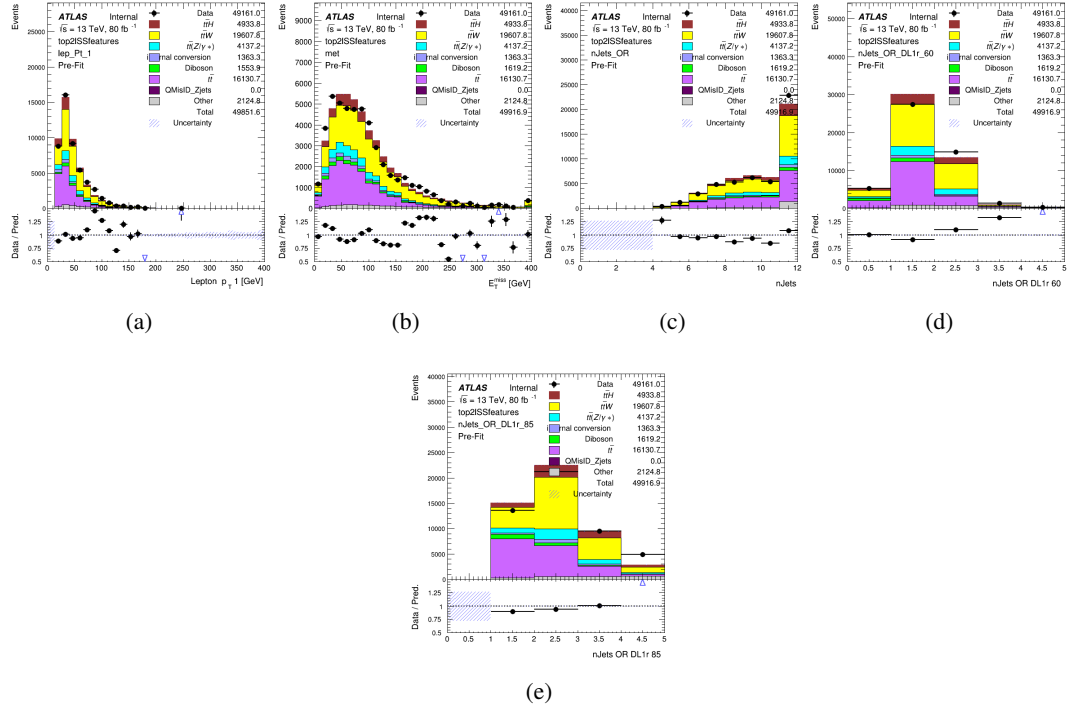


Figure C.3: Input features for top2ISS

1848 **C.1.2 b-jet Identification Features - 3l**

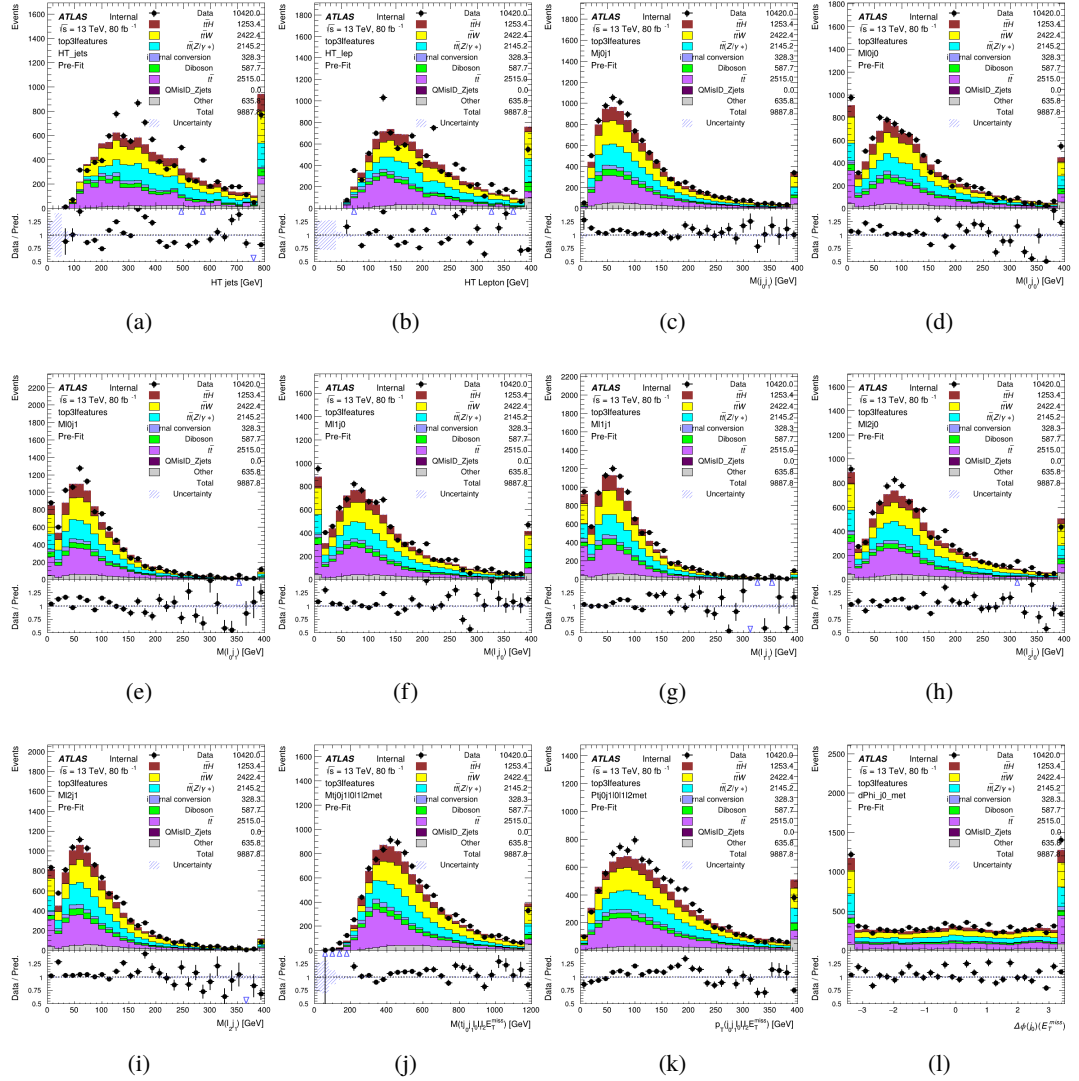


Figure C.4: Input features for top31

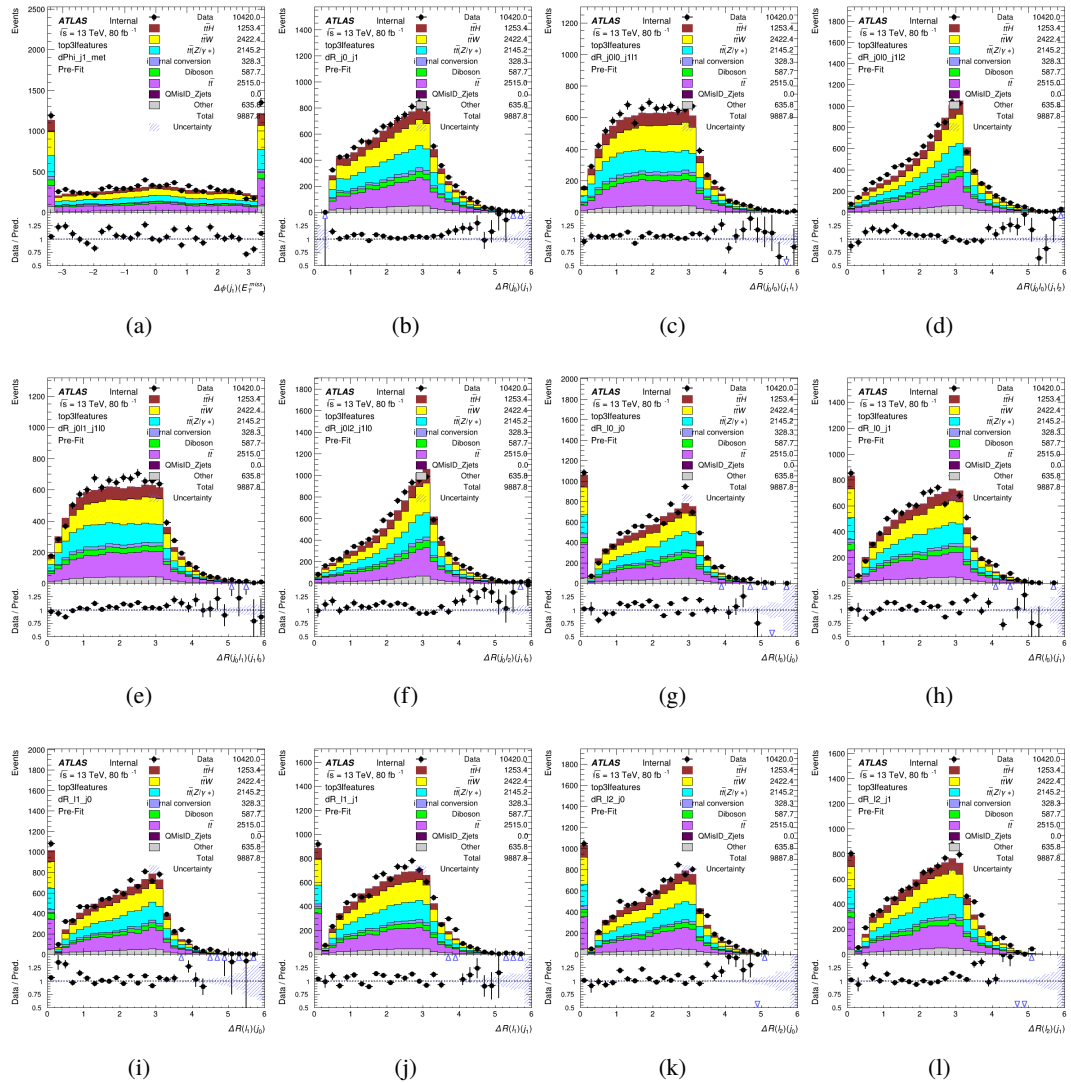


Figure C.5: Input features for top31

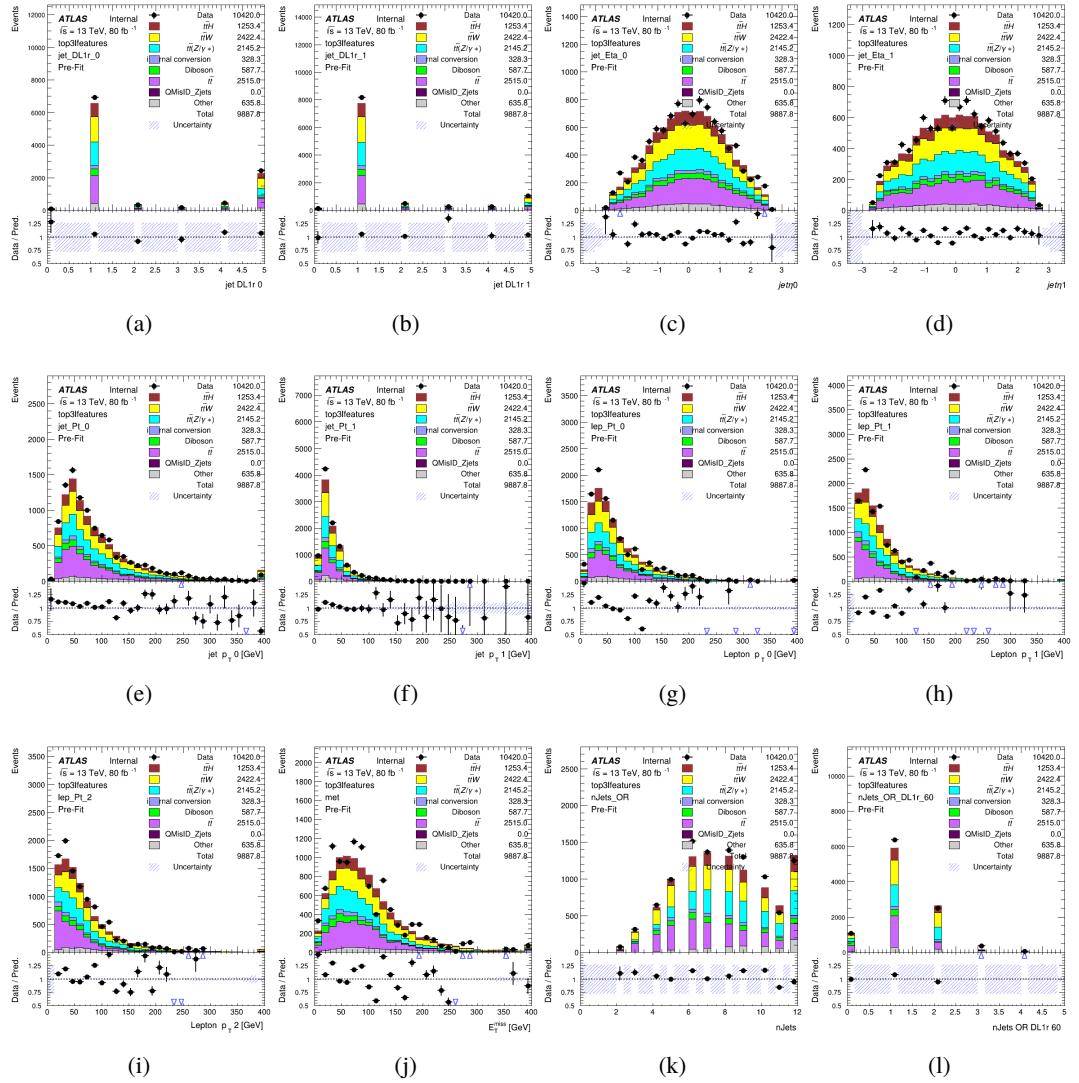
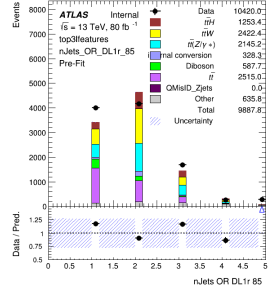


Figure C.6: Input features for top3l



(a)

Figure C.7: Input features for top3l

1849 **C.1.3 Higgs Reconstruction Features - 2lSS**

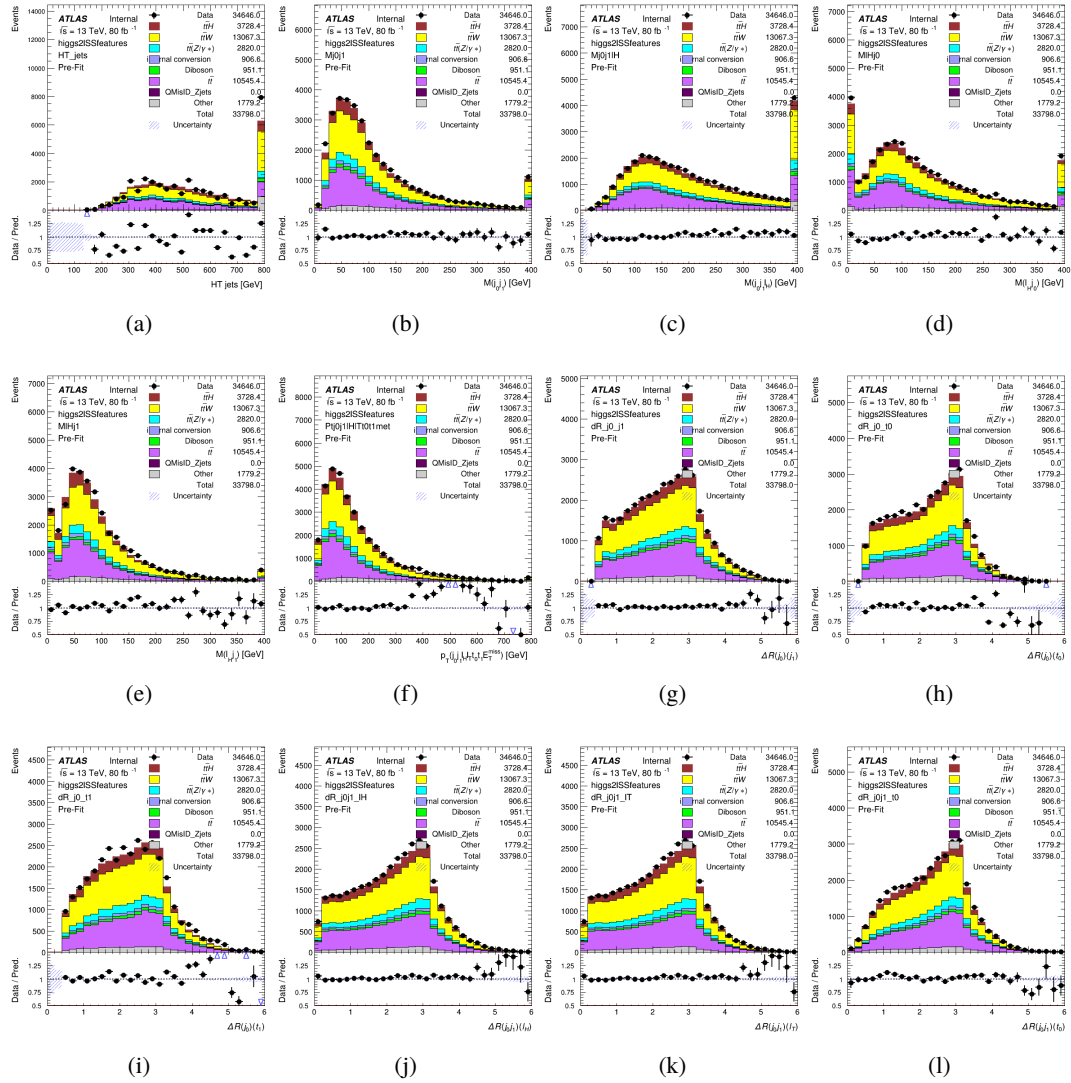


Figure C.8: Input features for higgs2lSS

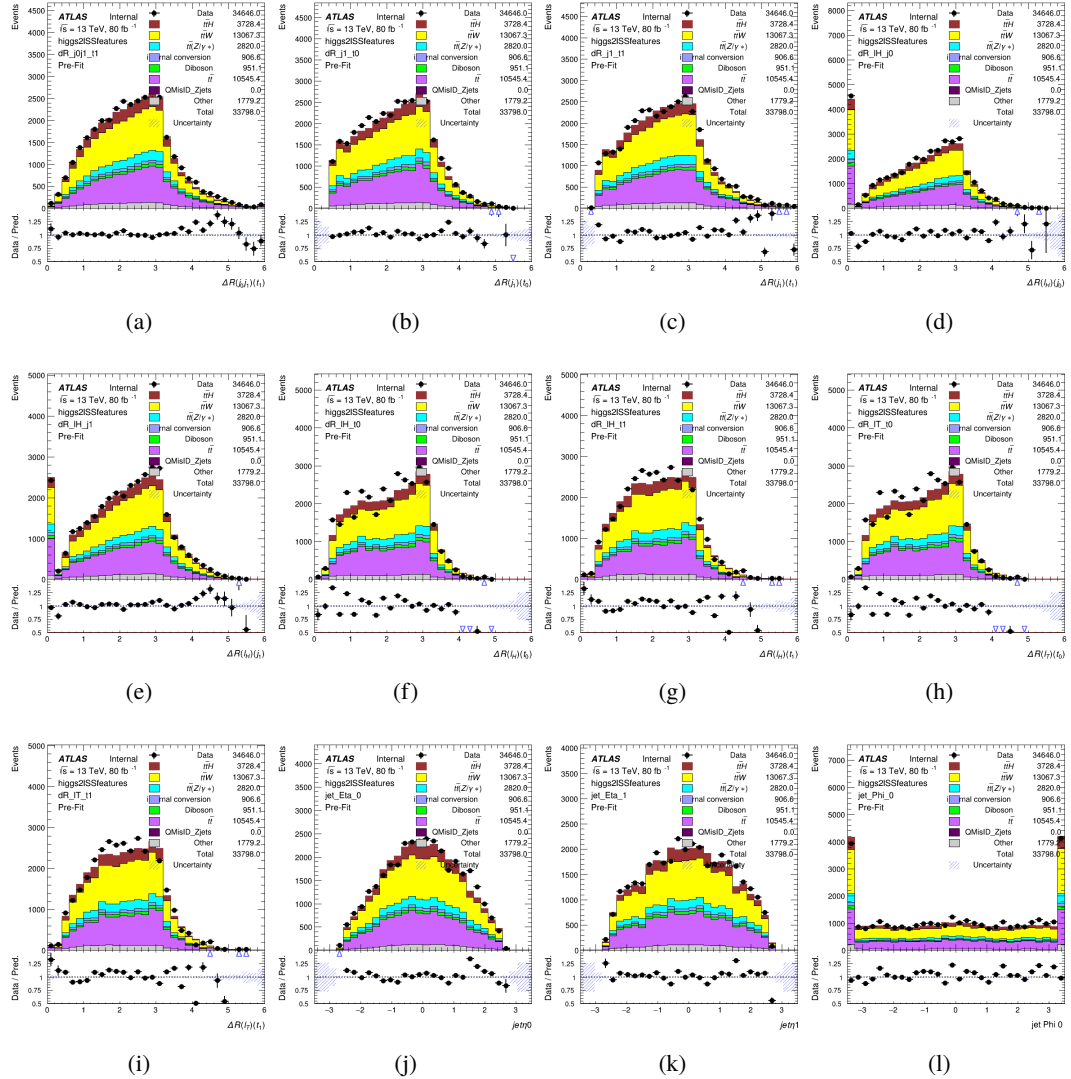


Figure C.9: Input features for higgs2lSS

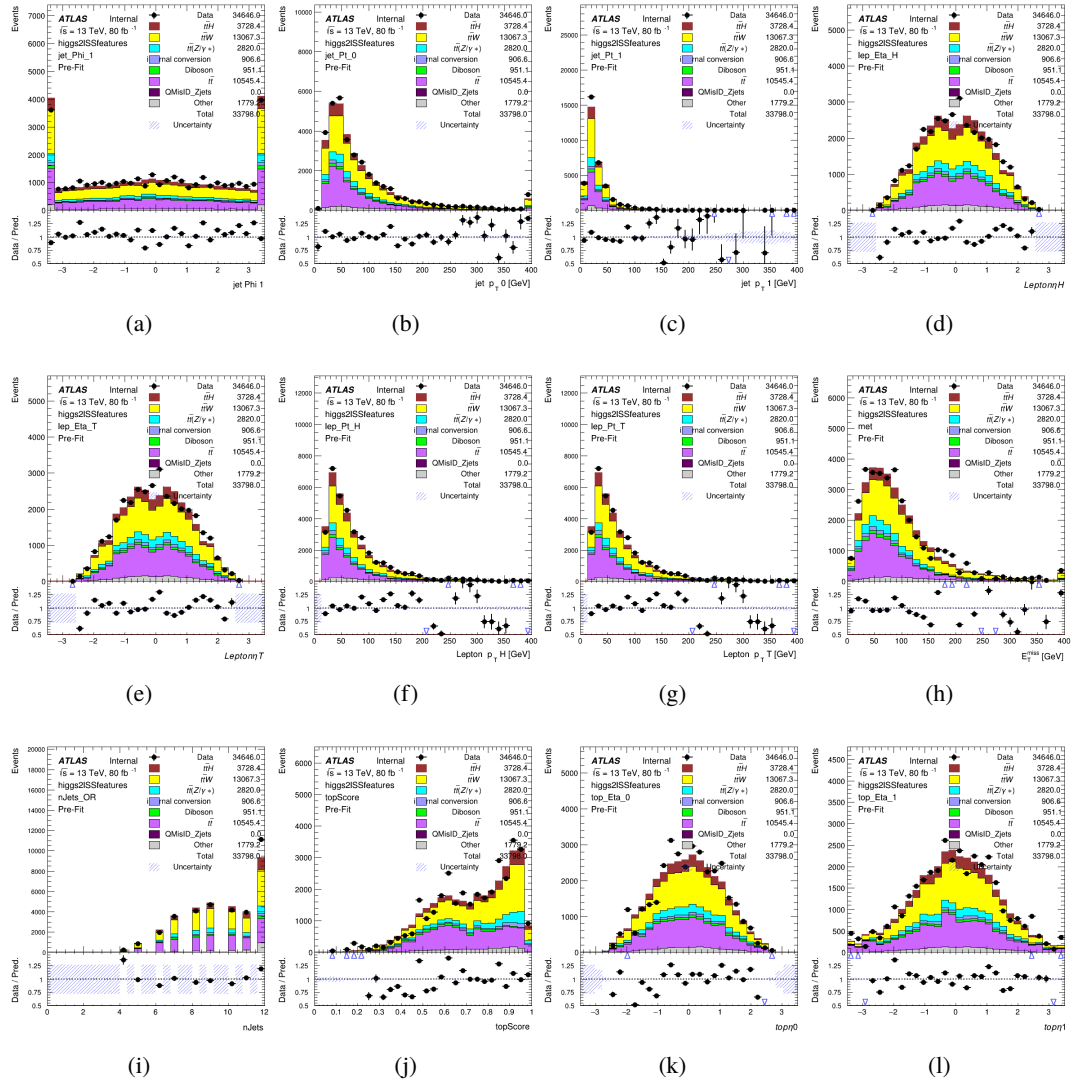


Figure C.10: Input features for higgs2lSS

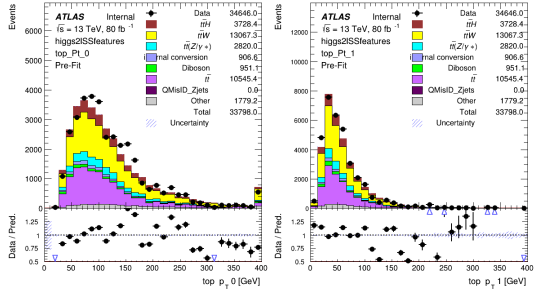


Figure C.11: Input features for higgs2lSS

1850 **C.1.4 Higgs Reconstruction Features - 3lS**

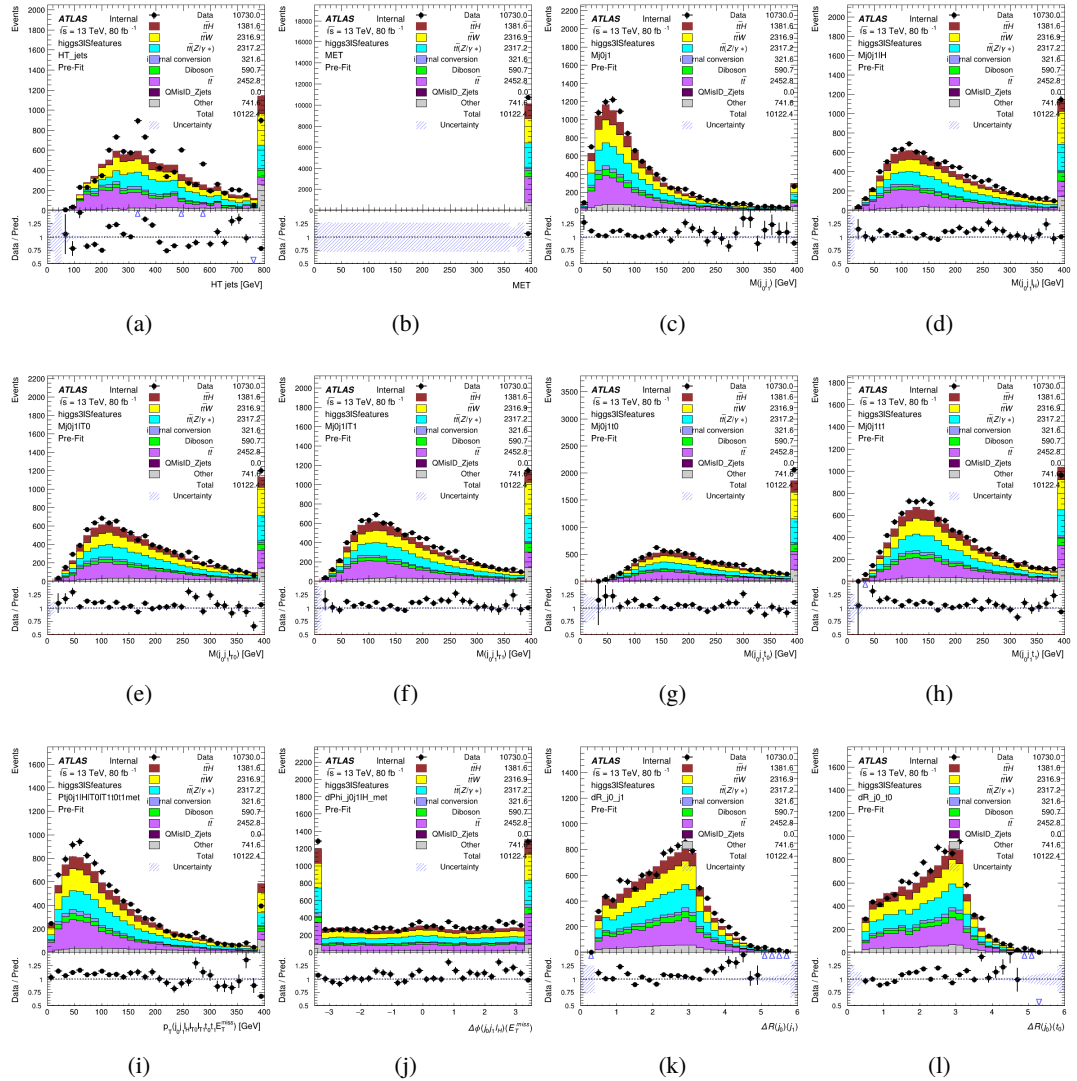


Figure C.12: Input features for higgs3IS

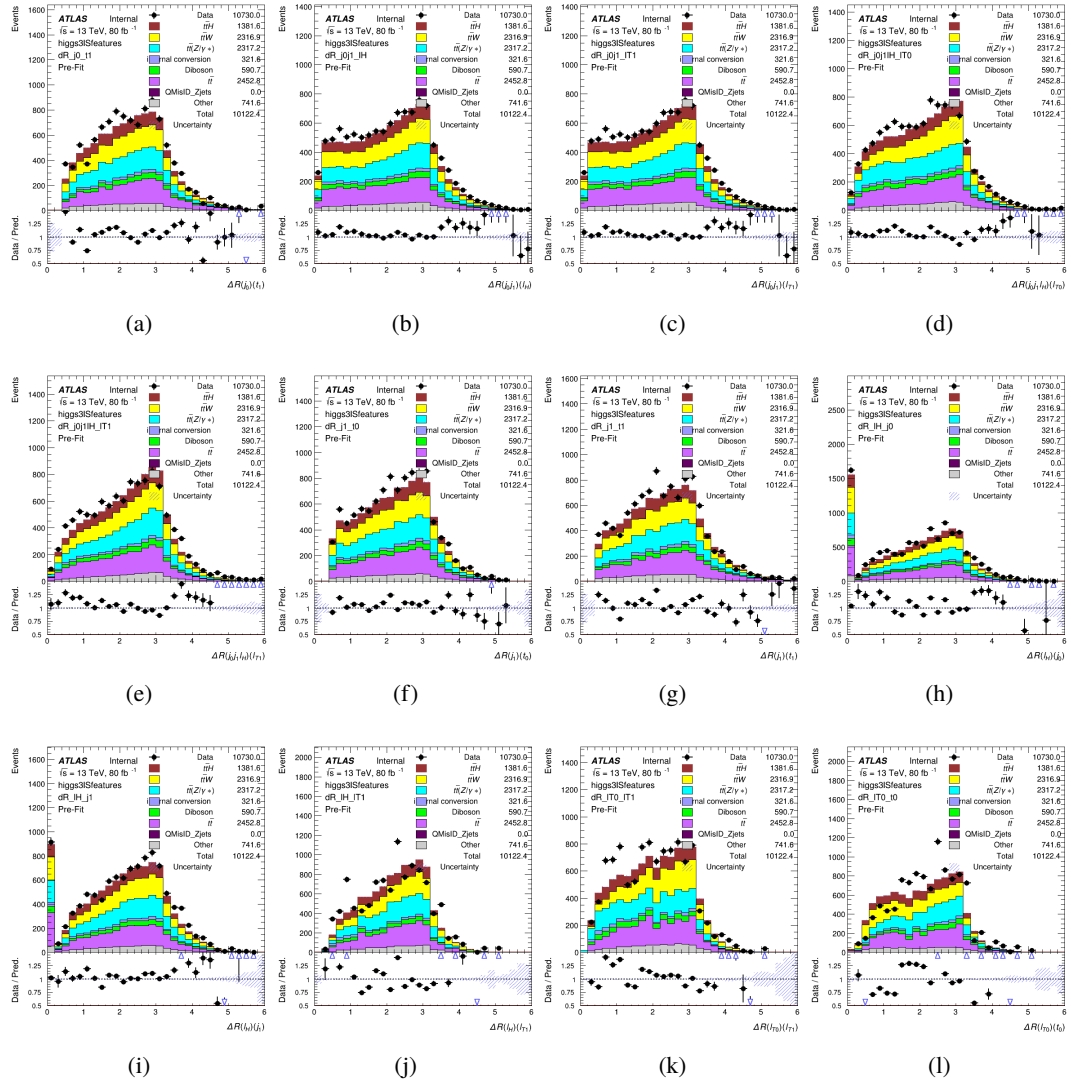


Figure C.13: Input features for higgs3lS

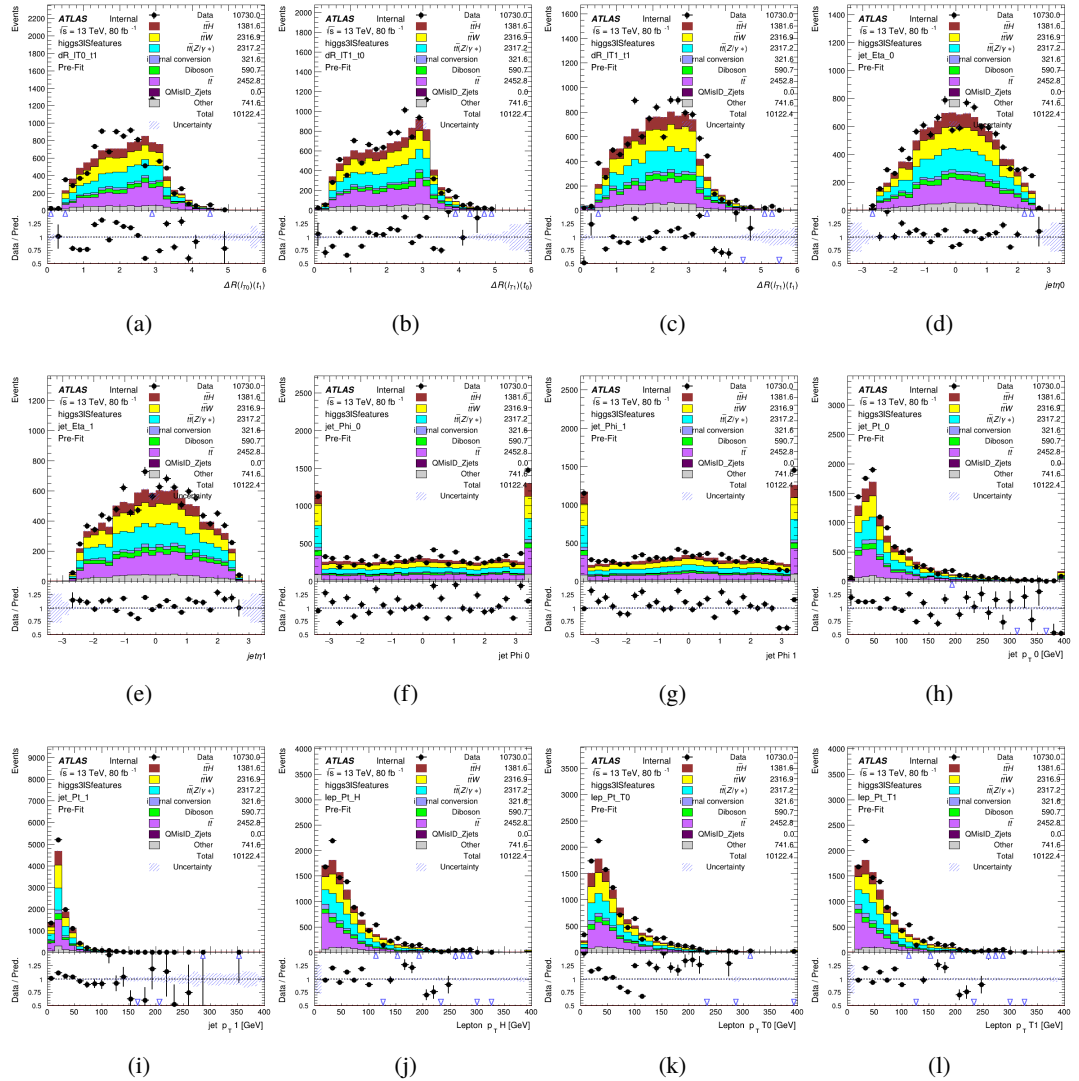


Figure C.14: Input features for higgs3lS

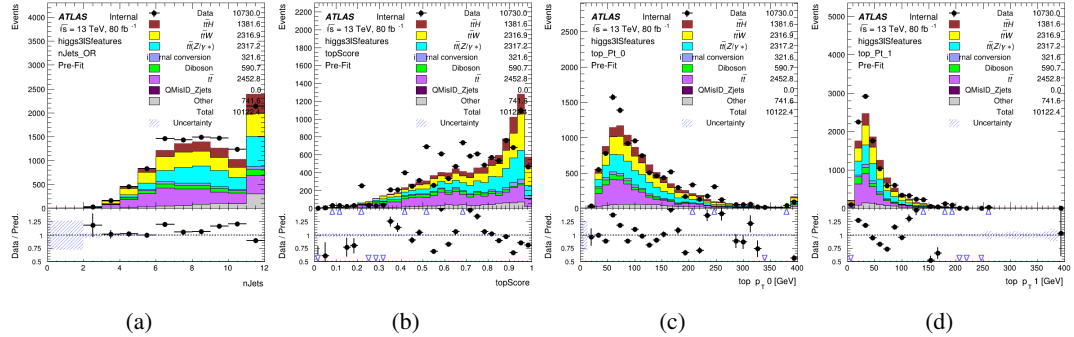


Figure C.15: Input features for higgs3IS

1851 **C.1.5 Higgs Reconstruction Features - 3lF**

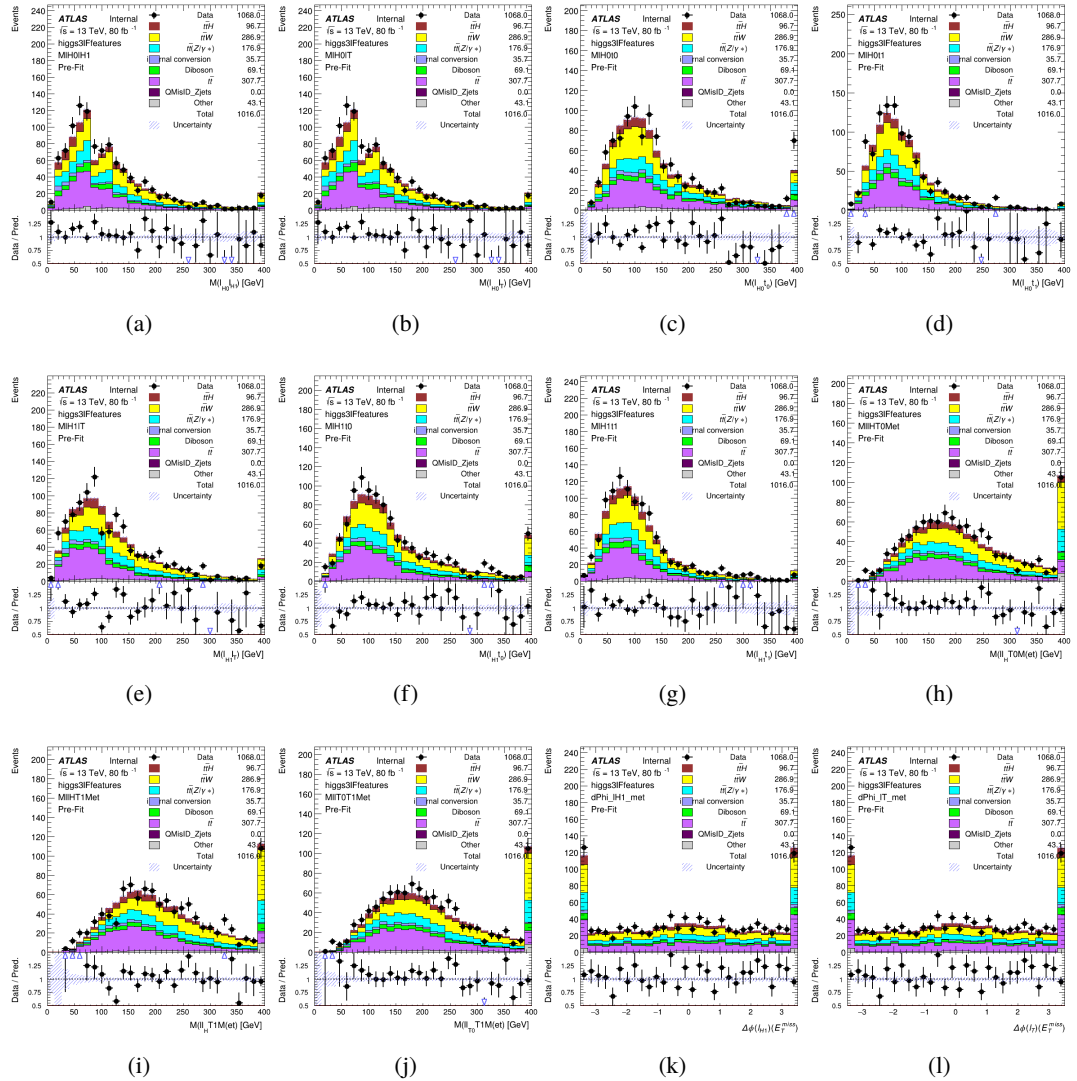


Figure C.16: Input features for higgs3lF

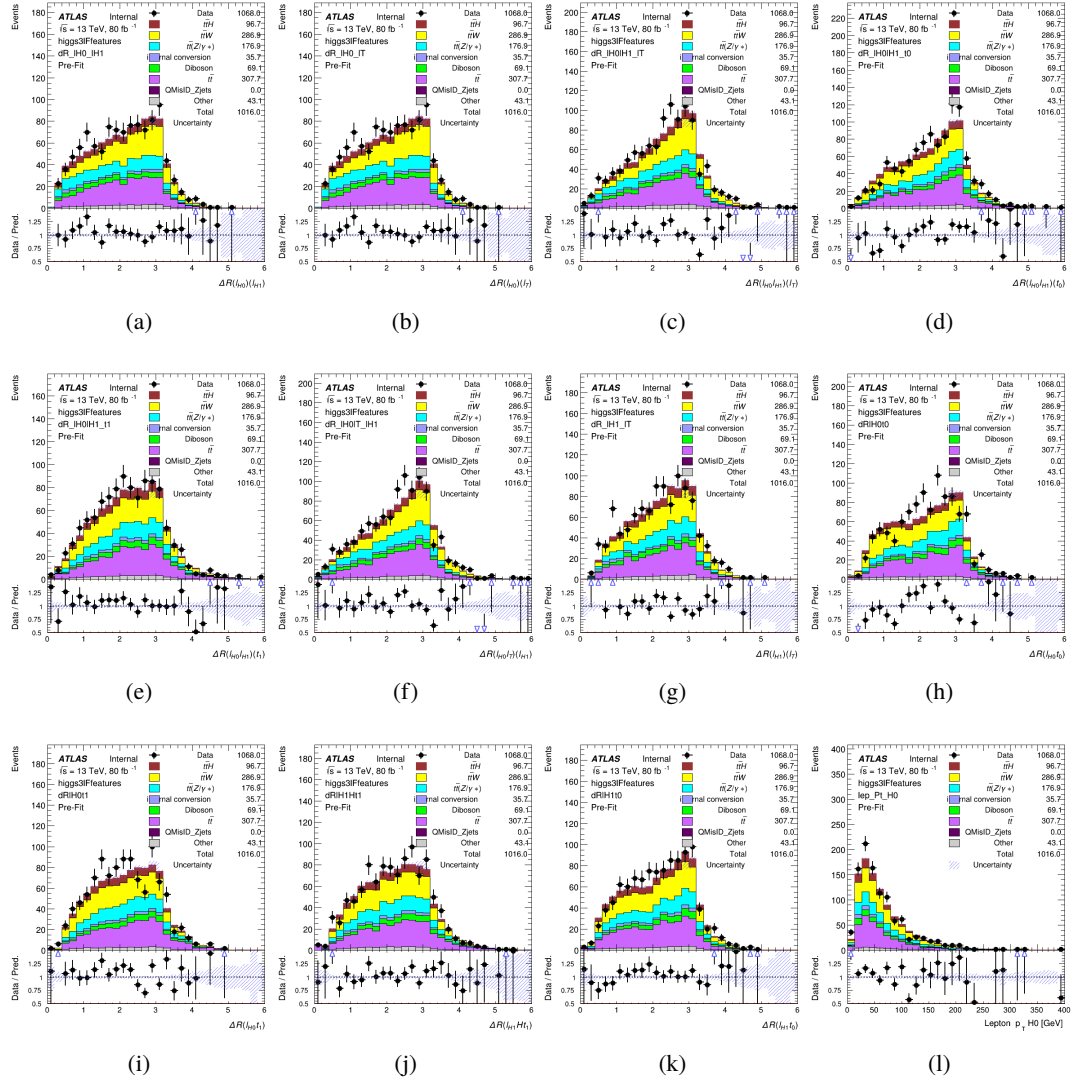


Figure C.17: Input features for higgs3IF

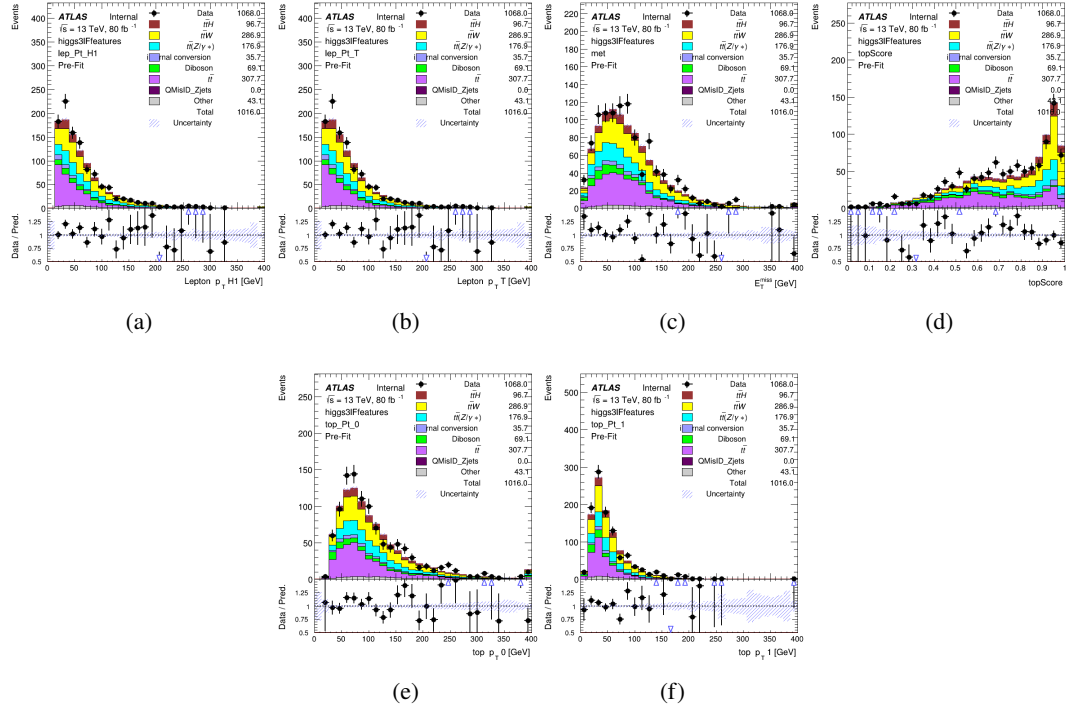


Figure C.18: Input features for higgs3lF

1852 **C.2 Background Rejection MVA Details**

1853 **C.2.1 Background Rejection MVA Features - 2ISS**

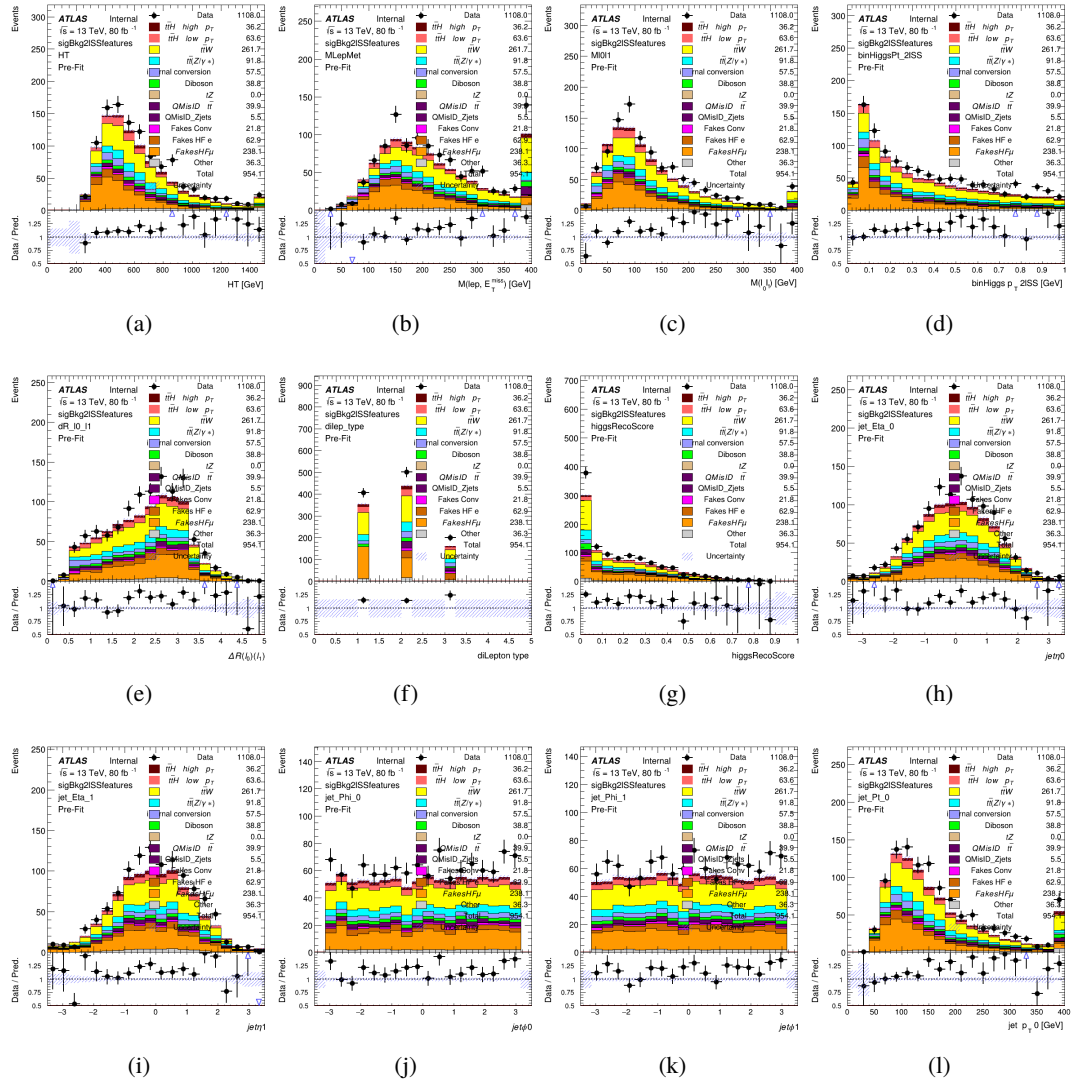
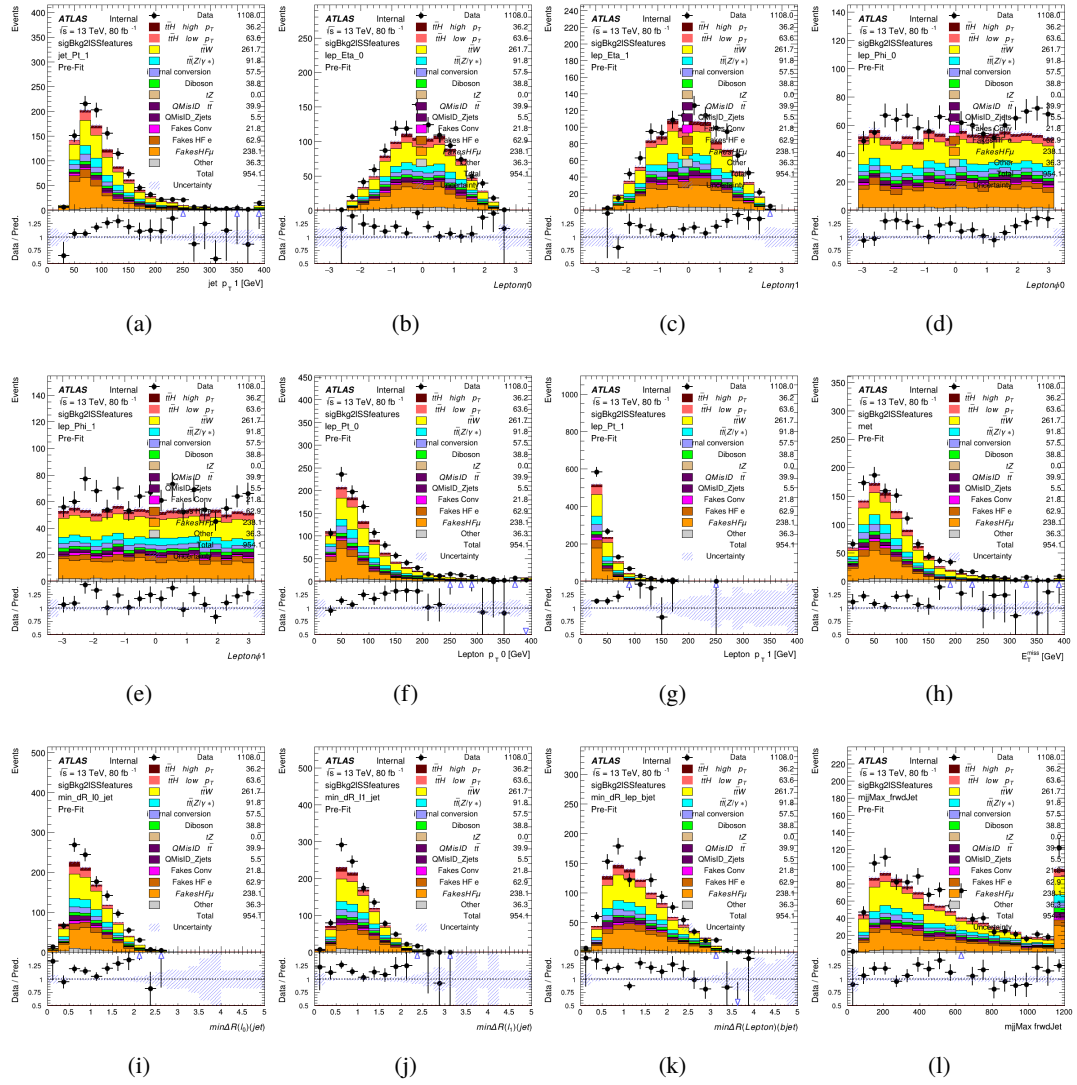


Figure C.19: Input features for sigBkg2ISS

Figure C.20: Input features for `sigBkg2lSS`

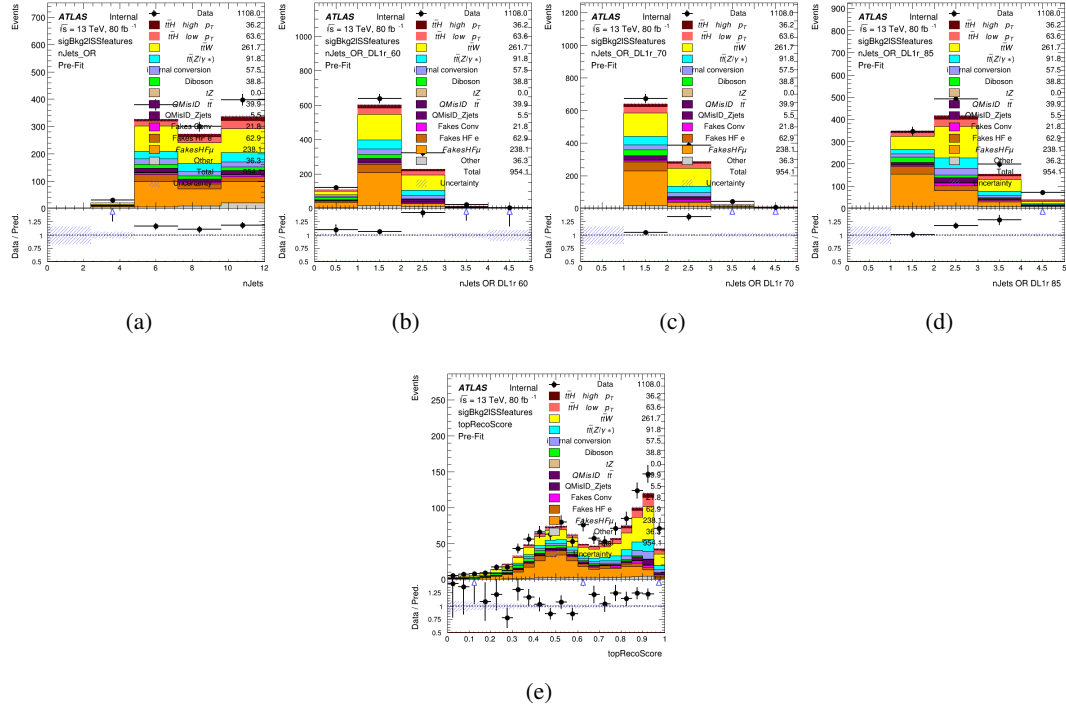


Figure C.21: Input features for sigBkg2lSS

1854 **C.2.2 Background Rejection MVA Features - 3l**

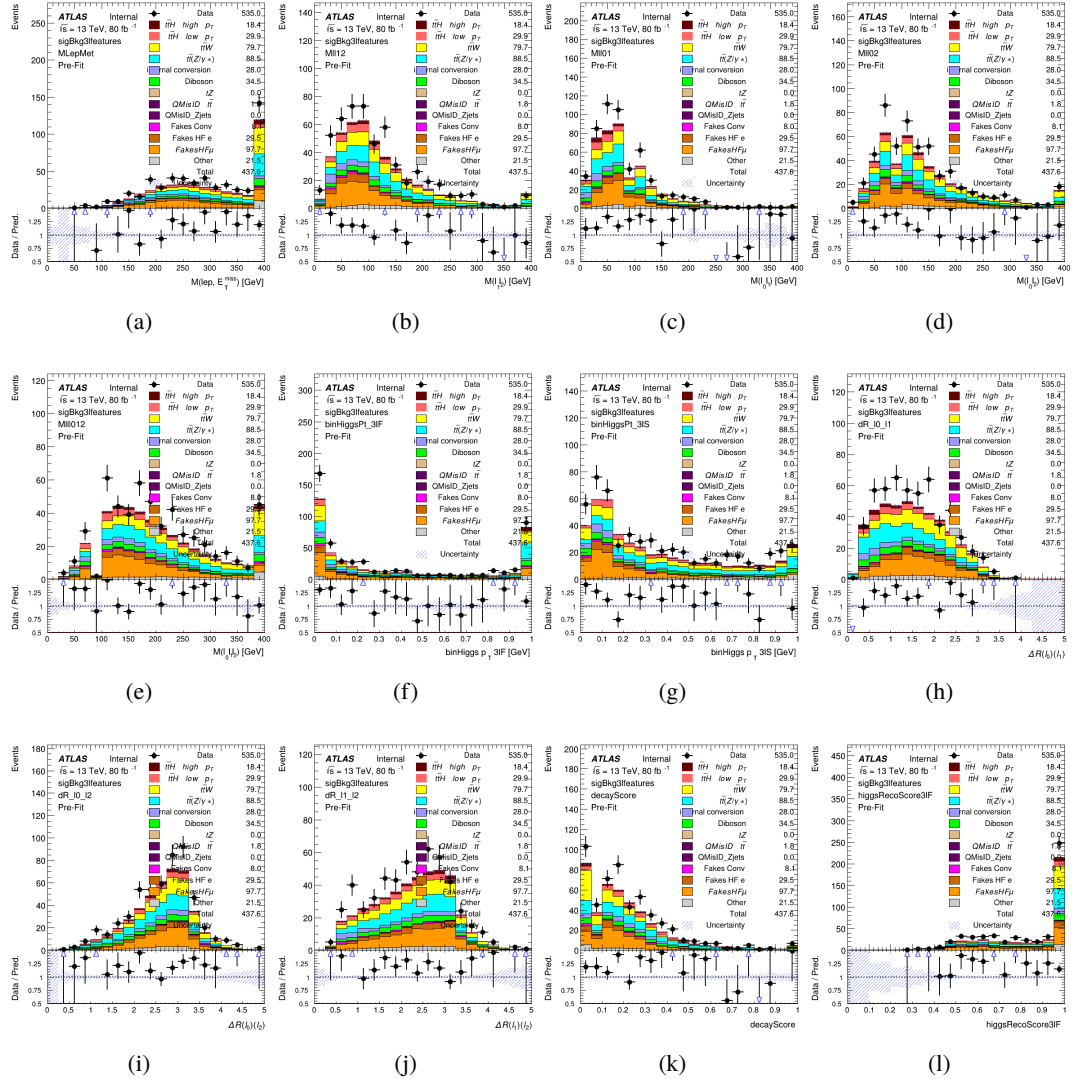


Figure C.22: Input features for sigBkg3l

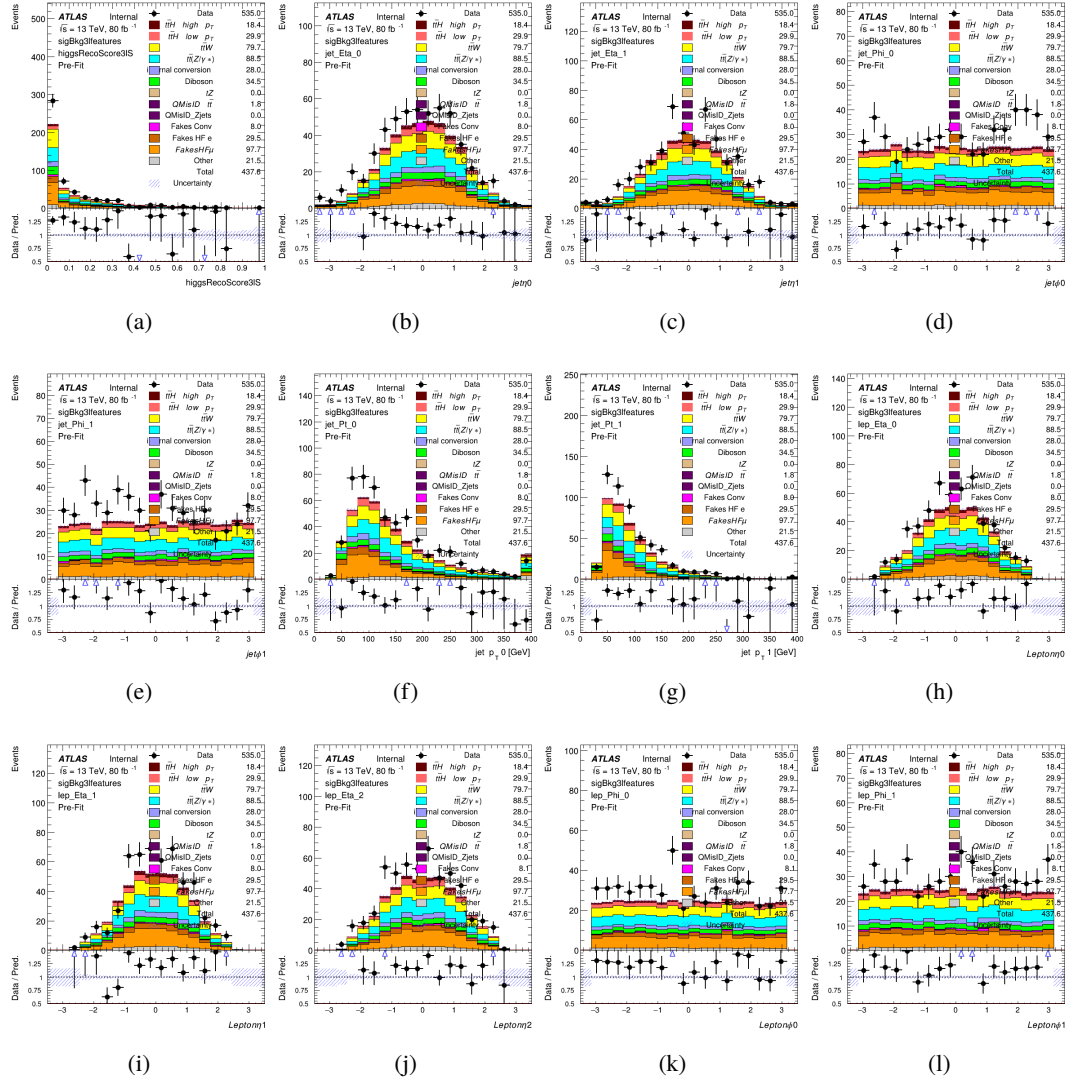


Figure C.23: Input features for sigBkg3l

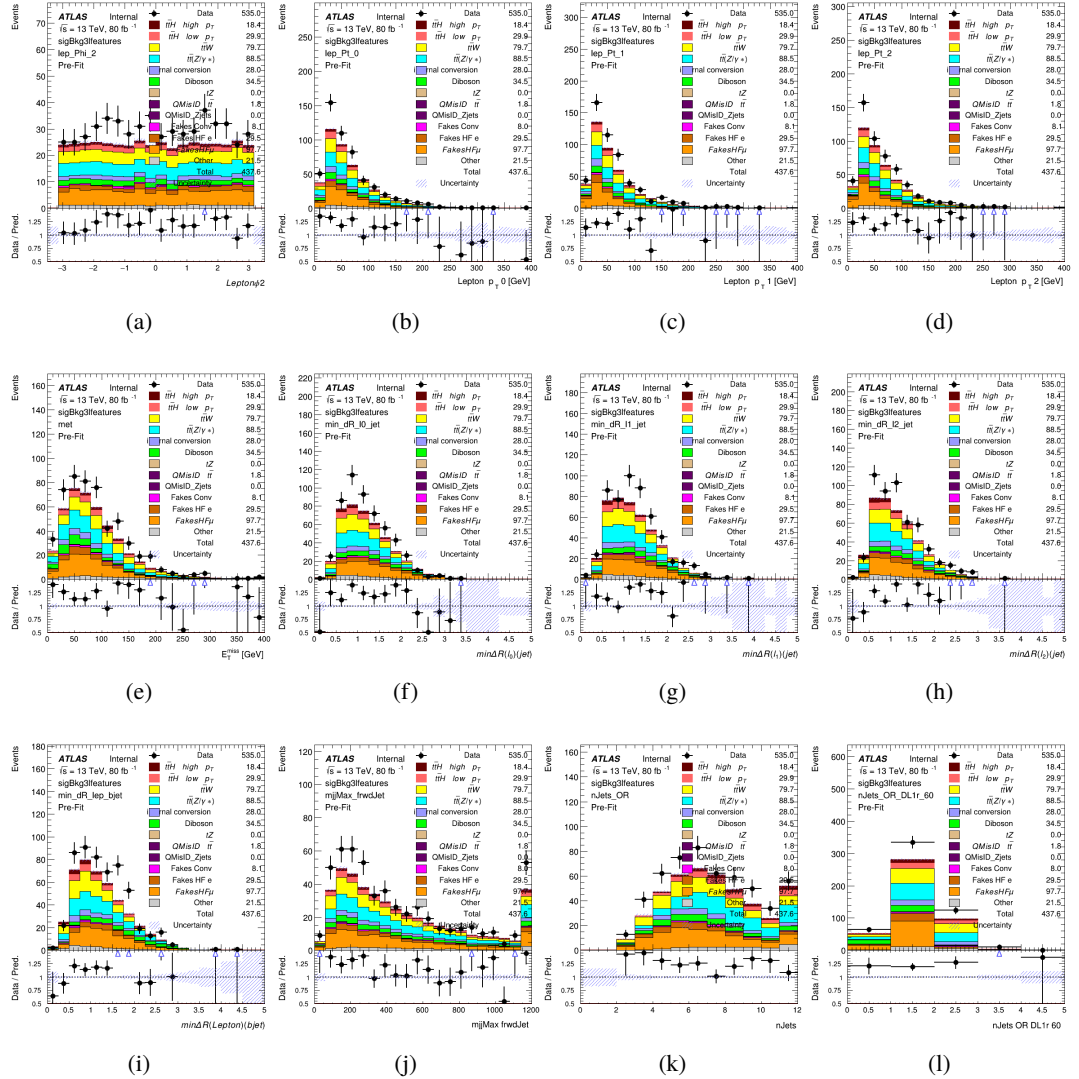


Figure C.24: Input features for sigBkg3l

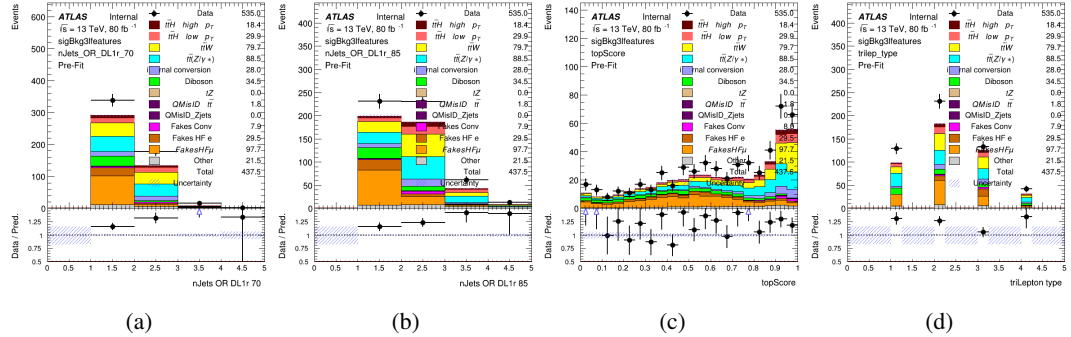


Figure C.25: Input features for sigBkg3l

1855 C.3 Truth Level Studies

1856 Attempts to identify the decay products of the Higgs are motivated by the ability to reconstruct
 1857 the Higgs momentum based on their kinematics. In order to demonstrate that this is case, the
 1858 kinematics of reconstructed objects that are truth matched to the Higgs decay are used as inputs
 1859 to a neural network which is designed to predict of the momentum of the Higgs. This is done in
 1860 the 2lSS channel, as it proves to be the most challenging for p_T reconstruction.

1861 Only leptons and jets which are truth matched to the Higgs are used as inputs for the
 1862 model; events where the lepton and both jets are not reconstructed are not included. The model
 1863 uses the same feature set and network architecture as the p_T prediction model used in the main
 1864 analysis, as described in Section 18.5.1.

1865 The results of the model are summarized below:

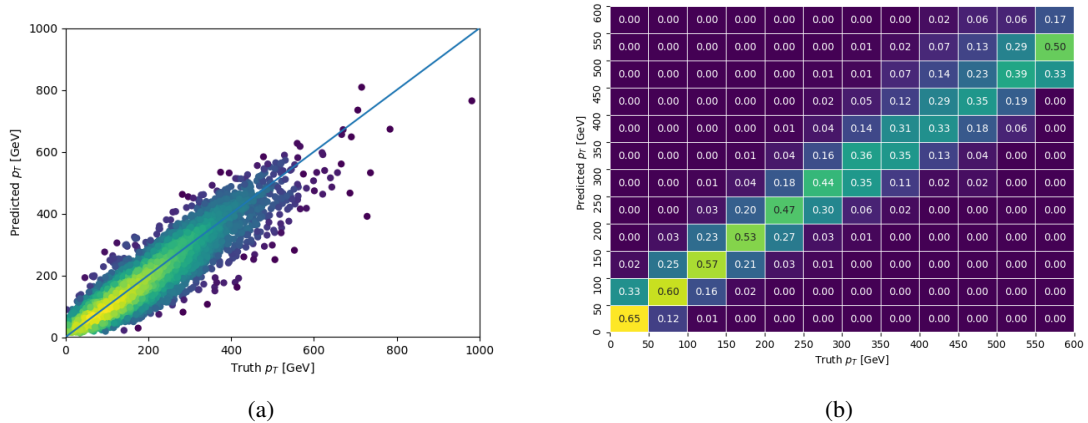


Figure C.26: The regressed Higgs momentum spectrum as a function of the truth p_T for 2lSS $t\bar{H}$ events in (a) a scatterplot, where the color of each point represents the log of the point density, based on Gaussian Kernel Density Estimation, and (b) a histogram where each column has been normalized to one.

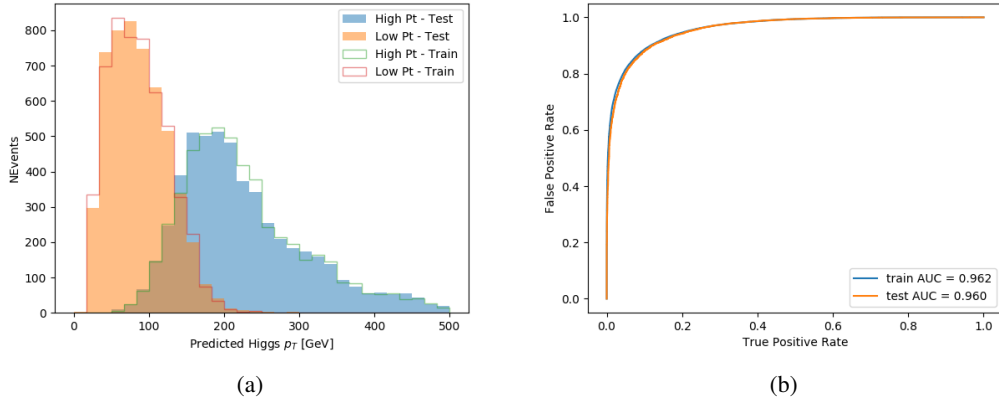


Figure C.27: (a) shows the reconstructed Higgs p_T for 2lSS events with truth $p_T > 150$ GeV and < 150 GeV, while (b) shows the ROC curve for those two sets of events.

1866 Based on the performance of the model, as shown Figures C.26 and C.27, the Higgs
 1867 momentum can be reconstructed with fairly high precision when its decay products are correctly
 1868 identified.

1869 C.4 Alternate b-jet Identification Algorithm

1870 The nominal analysis reconstructs the b-jets by considering different combinations of jets, and
 1871 asking a neural network to determine whether each combination consists of b-jets from top quark
 1872 decays. An alternate approach would be to give the neural network about all of the jets in an event
 1873 at once, and train it to select which two are most likely to be the b-jets from top decay. It was
 1874 hypothesized that this could perform better than considering each combination independently, as
 1875 the neural network could consider the event as a whole. While this is not found to be the case,
 1876 these studies are documented here as a point of interest and comparison.

1877 For these studies, the kinematics of the 10 highest p_T jets in each event are used for
 1878 training. This includes the vast majority of truth b-jets. Specifically the p_T , η , ϕ , E , and DL1r
 1879 score of each jet are used. For events with fewer than 10 jets, these values are substituted with 0.
 1880 The p_T , η , ϕ , and E of the leptons and E_T^{miss} are included as well. Categorical cross entropy is
 1881 used as the loss function.

Table 54: Accuracy of the NN in identifying b-jets from tops in 2lSS events for the alternate categorical method compared to the nominal method.

Channel	Categorical	Nominal
2lSS	70.6%	73.9%
3l	76.1%	79.8%

1882 C.5 Binary Classification of the Higgs p_T

1883 A two bin fit of the Higgs momentum is used because statistics are insufficient for any finer
 1884 resolution. This means separating high and low p_T events is sufficient for this analysis. As
 1885 such, rather than attempting to reconstruct the full Higgs p_T spectrum, a binary classification
 1886 approach is explored.

1887 A model is built to determine whether $t\bar{t}H$ events include a high p_T (>150 GeV) or low
 1888 p_T (<150 GeV) Higgs Boson. While this is now a classification model, it uses the same input
 1889 features described in section 18.5. Binary crossentropy is used as the loss function.

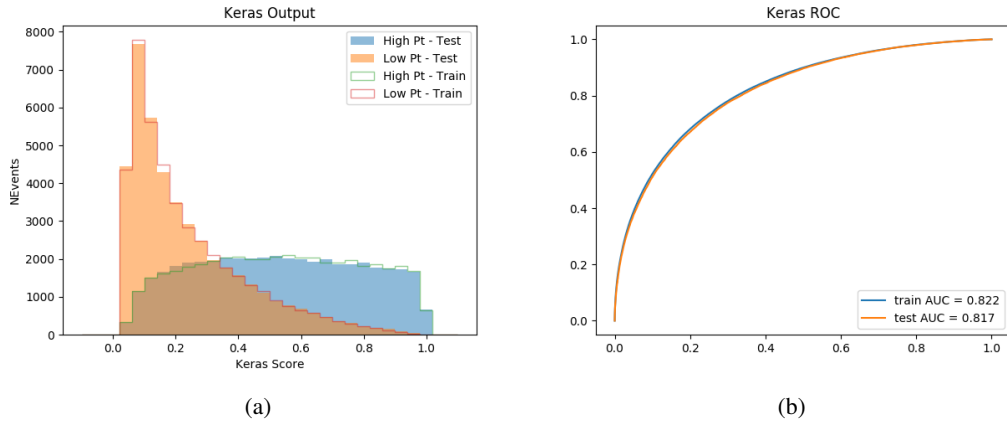


Figure C.28: Output distribution of the NN score for the binary high/low p_T separation model in the 2lSS channel.

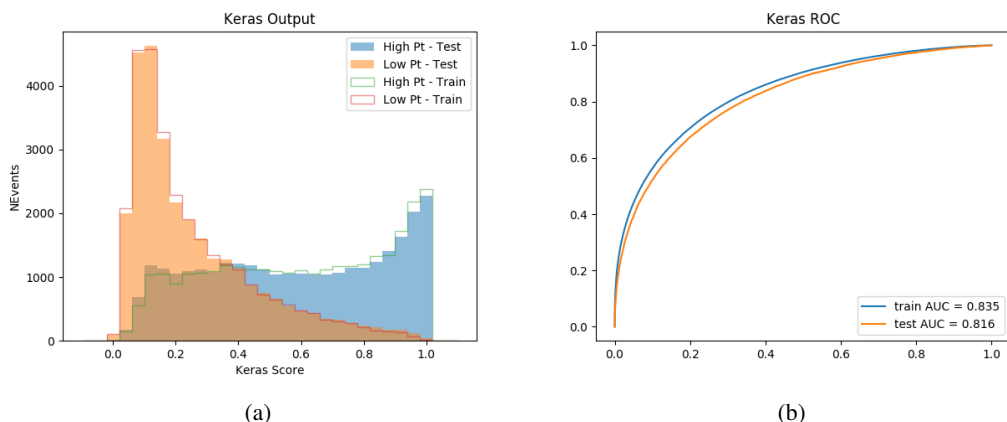


Figure C.29: Output distribution of the NN score for the binary high/low p_T separation model in the 3lS channel.

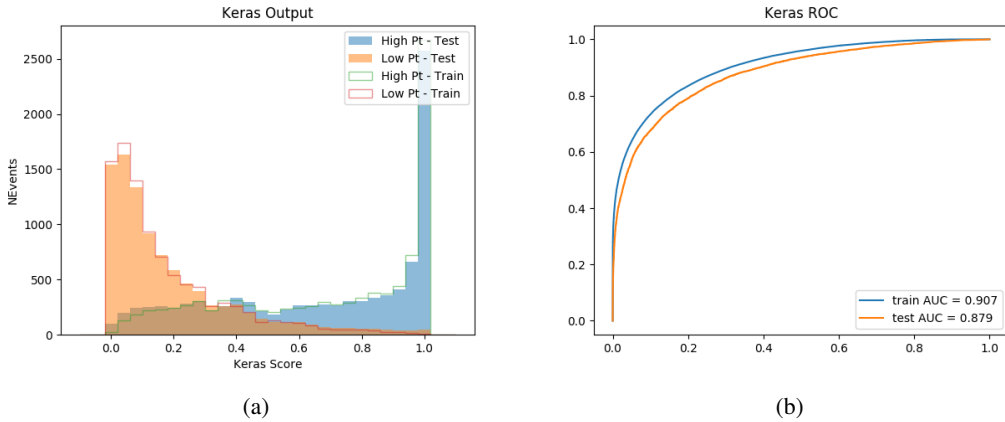


Figure C.30: Output distribution of the NN score for the binary high/low p_T separation model in the 3LS channel.

C.6 Impact of Alternative Jet Selection

1891 A relatively low p_T threshold of 15 GeV is used to determine jet candidates, as the jets originating
1892 from the Higgs decay are found to fall between 15 and 25 GeV a large fraction of the time. The
1893 impact of different jet p_T cuts on our ability to reconstruct the Higgs p_T is explored here.

The models are retrained in the 2LSS channel with the same parameters as those used in the nominal analysis, but the jet p_T threshold is altered. The performance of the Higgs p_T prediction models for jet p_T cuts of 20 and 25 GeV are shown below.

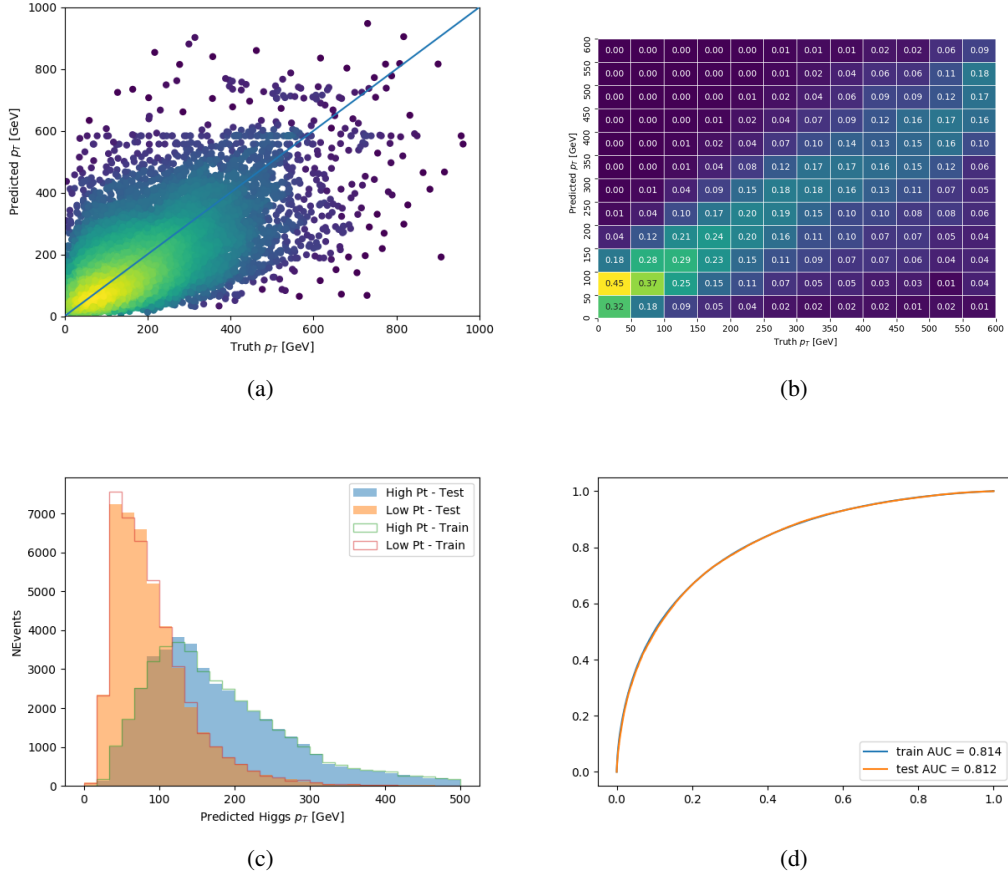
Jet $p_T > 20$ GeV

Figure C.31: Output of the model designed to predict the Higgs momentum in the 2LSS channel, with the jet p_T cutoff used is raised to 20 GeV.

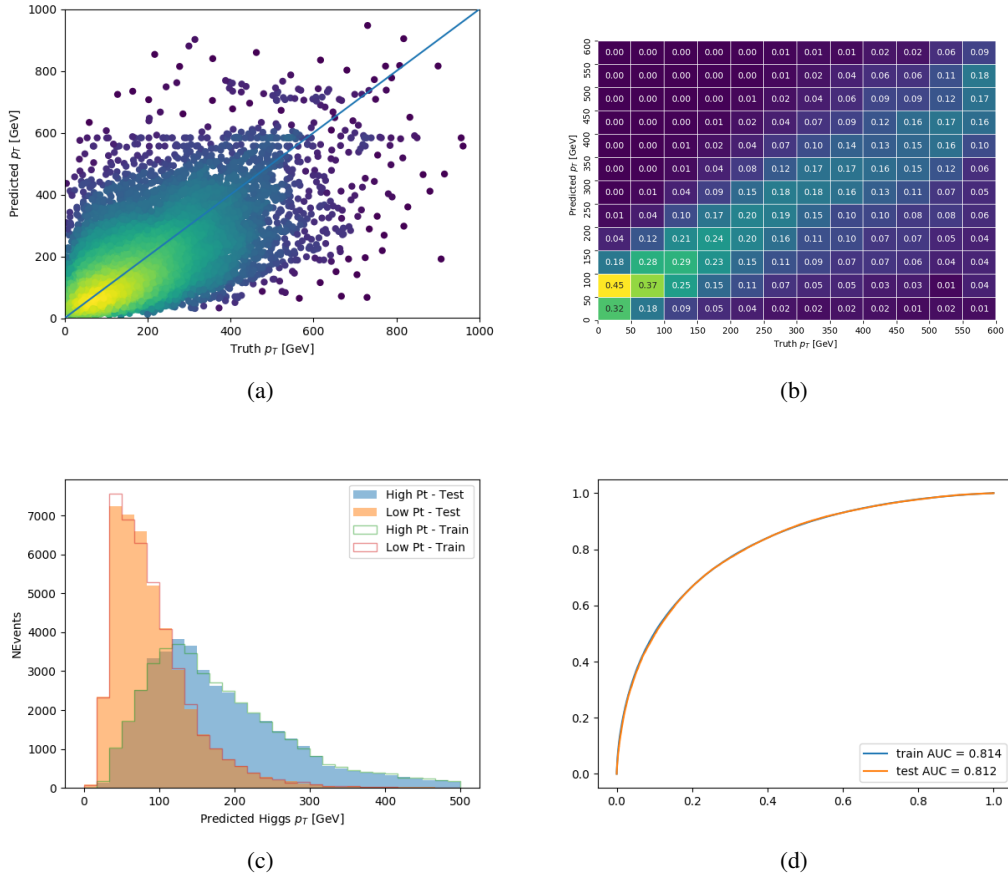
Jet $p_T > 25$ GeV

Figure C.32: Output of the model designed to predict the Higgs momentum in the 2LSS channel, with the jet p_T cutoff used is raised to 25 GeV.

1897 **D**